UNIVERSITÉ PARIS DIDEROT PARIS 7

IPN INSTITUT DE PHYSIQUE NUCLÉAIRE ORSAY

PNC ED517

THÈSE DE DOCTORAT

présentée en vue d'obtenir le grade de
Docteur, spécialité « Physique Théorique »

par

Sébastien GALAIS

SHOCK WAVE AND NEUTRINO SELF-INTERACTION EFFECTS UPON NEUTRINO FLAVOR CONVERSION IN THE SUPERNOVAE ENVIRONMENT

EFFETS DE L'ONDE DE CHOC ET DE L'AUTO-INTERACTION DES NEUTRINOS SUR LA CONVERSION DE SAVEUR DES NEUTRINOS DANS L'ENVIRONNEMENT DES SUPERNOVAE

Thèse soutenue le 3 octobre 2011 à l'Institut de Physique Nucléaire d'Orsay
devant le jury composé de :

Mme	CRISTINA VOLPE, Directeur de Recherche	Directrice de Thèse
M.	A. BAHA BALANTEKIN, Professeur	Rapporteur
M.	GIANLUIGI FOGLI, Professeur	Examinateur
M.	ELIGIO LISI, Directeur de Recherche	Rapporteur
M.	THOMAS PATZAK, Professeur	Président du jury

À mes parents

If, in some cataclysm, all scientific knowledge were to be destroyed, and only one sentence passed on to the next generation of creatures, what statement would contain the most information in the fewest words? I believe it is the atomic hypothesis (or atomic fact, or whatever you wish to call it) that all things are made of atoms - little particles that move around in perpetual motion, attracting each other when they are a little distance apart, but repelling upon being squeezed into one another. In that one sentence you will see an enormous amount of information about the world, if just a little imagination and thinking are applied.
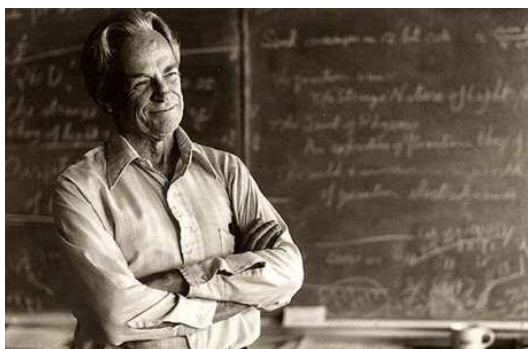
Richard P. Feynman

Remerciements/Acknowledgements

Je tiens tout d'abord à remercier Dominique Guillemaud-Mueller et Bachir Moussalam, respectivement directrice de l'IPN et responsable du groupe théorie, de m'avoir acueilli dans ce laboratoire pour pouvoir y effectuer ma thèse de doctorat.

Mes premiers remerciements vont à Cristina pour m'avoir supervisé durant ma thèse sur ce sujet très actif qu'est la physique des neutrinos. Je lui suis reconnaissant de m'avoir fait confiance, sans parfois en avoir le choix, sur des idées qui ont mené aux publications et au contenu de cette thèse.

Je tiens à remercier sincèrement Baha Balantekin et Eligio Lisi d'avoir été les rapporteurs de cette thèse, et Guianluigi Fogli et Thomas Patzak d'avoir accepté de faire partie de mon jury.

Dans le petit groupe de "neutrinos" que nous étions à l'IPN, je remercie les stagiaires que j'ai renconté sur mon chemin Daavid (maintenant thésard) et Dominik. Et je remercie encore plus Jim, post-doc à l'époque, pour son humour typiquement anglais et sa bonne humeur mais surtout pour son expertise en physique des neutrinos.

Dans le groupe théorie, je tiens à remercier chaleureusement ceux qui sont devenus maintenant des amis Jean-Paul, Jérôme, Marine et Anthea. La bonne humeur et les fous rires ont rythmé nos journées de "recherche". Je ne pourrais jamais oublier les parties de basket, le balançage de craies ou tout objet volant, la guerre de bureaux, les chansons, les sublimes gâteaux. En plus je n'aurai jamais pensé rencontrer un pote aussi taré que moi, JP tu te reconnaîtras. Ce fut donc un grand bonheur de squatter le même bureau que vous trois Jean-Paul, Jérôme et Anthea. Je souhaite aussi dire un grand merci à Marine pour sa bonne humeur et son sourire perpétuel.

Pendant ma thèse, j'ai aussi eu la chance de rencontrer des personnes que je n'oublierai pas. Je tiens à remercier Sophie, Sandra, Simon, Adrien pour leur sympathie et leur bonne humeur. C'est toujours agréable d'avoir du soutien entre thésards durant la thèse. Parmi les personnes que j'ai cotoyé durant mes études, je remercie énormément Mélanie, Yannis, Julien, David, Thomas et Erwan. On a bien rigolé ensemble et vous m'avez beaucoup appris. Je souhaite remercier plus particulièrement Mélanie, nos voyages autour du monde ne font que commencer...

Dans tout le personnel que compte l'IPN, je souhaite remercier sincèrement Christophe Diarra du service informatique qui a toujours su résoudre mes problèmes d'ordinateur et de grille avec une rapidité impressionnante. D'autre part, je dis un grand merci à notre ancienne secrétaire Nathalie Escoubeirou pour sa gentillesse et sa disponibilté pour résoudre les problèmes administratifs qui ne

sont pas mon fort.

Finalement je remercie très chaleureusement ma famille. Vous dire merci sur une page de mon mémoire de thèse ne représentera jamais assez. J'ai énormément apprécié et ai eu grand besoin de votre soutien durant ces 3 dernières années.

Merci à tous !

Paris, le 3 octobre 2011.

CONTENTS

LIST OF FIGURES

LIST OF TABLES

INTRODUCTION

$\mathcal{N}$ EUTRINO physics is nowadays a very active field both theoretically and experimentally. Neutrinos are indeed present in various fields of physics such as nuclear physics, particle physics, astrophysics, cosmology, physics beyond the Standard Model, etc. Historically, in 1930 Pauli proposed the existence of neutrinos to save energy conservation of β decay processes [1]. Neutrinos were finally directly observed by Cowan and Reines in 1956 [2, 3] in a nuclear reactor experiment based in Savannah River, South Carolina. Actually, Cowan and Reines measured electron antineutrinos which are the particles that are produced during the β^- decay in association with an electron. At the beginning of 1962, another flavor was discovered by Schwartz, Lederman and Steinberger at the accelerator of Brookhaven: the ν_μ neutrino. Finally, in 1989, the CERN particle accelerator "LEP" which studied the Z boson lifetime allowed to show that only three light neutrino families exist. Indeed the third neutrino ν_τ was identified in 2000 by the DONUT experiment at Fermilab.

Pontecorvo proposed the $\nu \leftrightarrow \bar{\nu}$ oscillations in a 1957 paper [4, 5]. In 1962 $\nu_e \leftrightarrow \nu_\mu$ oscillations were mentioned by Maki, Nakagawa and Sakata in the context of a model of leptons bound inside hadrons [6, 7]. These propositions were the first hypothesis of oscillations of particles in the leptonic sector. Oscillations between neutrinos were soon discovered in connection with the solar experiment by Davis et al. in 1968 [8, 9, 10] who measured a ν_e solar rate smaller than the one predicted by Bahcall et al. [11]. In parallel, another problem was found by looking at "atmospheric neutrinos" coming from the interaction of cosmic rays with atomic nuclei in the Earth's atmosphere. Actually, the first definitive evidence that neutrinos oscillate came from the atmospheric neutrino group Super-Kamiokande in 1998 [12]. Theoretically, Wolfenstein in 1978 and Mikheyev and Smirnov in 1986 discovered that neutrino oscillations in matter differ from the oscillations in vacuum in a very significant way. The most striking manifestation of the matter effects in neutrino oscillations is the presence of a resonance in the oscillation probability: the "MSW effect". This MSW phenomenon is considered to be the solution of the solar neutrino deficit which has been confirmed by the KamLAND experiment.

In the Universe, core-collapse supernova are also another source of neutrinos. Most of the energy produced in supernovae is radiated away in the form of an immense burst of neutrinos. The first experimental evidence of this phenomenon came in 1987, when neutrinos from supernova 1987A were detected by the Kamiokande II, IMB and Baksan detectors. These detections and the observation of solar neutrinos opened the large and very active field of neutrino astrophysics. In this field, neutrinos are studied for two aspects. The first is to search for neutrino effects in the supernova dynamics, because the mechanism leading to the supernova explosion is not yet clear and neutrinos may play an important role. The second aspect, which is the core of this PhD thesis, is to investigate the effects of the supernova environment upon the neutrino propagation

which lead to flavor conversions.

The present thesis focuses upon the recent developments that have been performed in the field of neutrino astrophysics. It has been shown in the last decade that the interaction of neutrinos with the neutrino background itself is very important for the flavor evolution in the supernova environment [13, 14, 15, 16, 17, 18, 19]. This neutrino self-interaction has completely changed the paradigm of supernova neutrino oscillations, leading to the appearance of collective phenomena. At the same time, the impressive progress achieved in the understanding of supernova explosion have allowed to show that the modification of the matter density profile induced by the presence of the shock [20] leads to new features for the MSW resonances in the neutrino propagation [21]. The first work of this thesis has consisted in studying the neutrino evolution within a realistic scenario, where the neutrino self-interaction and the shock wave are included, and in searching for their effects on the Diffuse Supernova Neutrino Background (DSNB). This is composed of all the neutrinos emitted from the core collapse supernovae in the observable Universe. The advantage of the DSNB compared to a supernova explosion is that the DSNB is an isotropic and time-independent source of neutrinos. Furthermore, the lastest bounds on the DSNB fluxes open up the potentiality of a DSNB signal in Super-Kamiokande detector [22] and in next-generation neutrino observatories [23].

As mentioned, the introduction of the neutrino self-interaction gives rise to collective phenomena that are unlike anything produced by interactions with ordinary matter. For the moment, these effects have been studied numerically in two and three flavors. The understanding of the underlying mechanisms is often based upon schematic analytical models [15] using the following assumptions:

1. the matter density profile is constant i.e. a maximal (resp. minimal) effective mixing angle equal to $\pi/4$ (resp. 0) is used,

2. the neutrino self-interaction has either no spatial dependence or a simplified one,

3. the neutrino and antineutrino spectra are represented by either a single energy or box-like spectra.

Our main goals in the second and third parts of this thesis are:

- to propose a new insight on the neutrino self-interaction effects by using the instantaneously diagonal basis that we called the "matter " basis,

- to search for the underlying effects of the collective phenomena engendered by the neutrino self-interaction with an exact treatment i.e. without the approximations mentioned above.

To reach these aims, we developed formal expressions to define the different quantities in the "matter" basis in the case where the propagation Hamiltonian includes the matter induced potential and the neutrino self-interaction. By applying our equations to the two flavors case, we have pointed out for the first time the importance of the derivative of the matter Dirac phase and we have also identified an exact analytical condition for the onset of bipolar oscillations. To complete the picture of a neutrino propagating in the supernova environment, we have made the conjecture and have proven, with complete numerical calculations using polarization vectors, that the spectral split phenomenon occurring at the end of the neutrino self-interaction region is actually a magnetic resonance phenomenon.

The present PhD thesis is organized as follows. In the first chapter, we introduce the theoretical framework for neutrino oscillations in vacuum, following the pioneering work of Pontecorvo. We study these oscillations within two and three flavors and also introduce the polarization vector formalism. Then we describe, for the two flavor case, the theoretical discovery of Mikheyev, Smirnov and Wolfenstein of the flavor resonance induced by the matter background in an astrophysical object such as the Sun. Thereafter we present the past experiments that measured the solar and atmospheric neutrinos leading to the solar and atmospheric evidence of neutrino oscillations. These pieces of evidence have allowed to determine neutrino oscillation parameters such as the mixing angles and mass squared differences. Finally we give a state of art of the latest measurements of the neutrino oscillation parameters.

The second chapter is dedicated to the neutrino propagation in a specific environment: core-collapse supernovae. We first give a description of the death of a massive star which gives birth to a supernova. We discuss the four phases that are the main sources of the neutrino emission. Then we briefly present the next-generation observatories under studies (MEMPHYS, LENA and Glacier) which will measure in the next years the neutrino fluxes coming from cosmic sources. To describe the flavor conversion occurring in supernovae, we come back to the MSW effect and consider the three flavors case. Indeed the matter density profile is such that the neutrino oscillations have to be studied by considering the three flavors. Finally, we present the recent developments in the field of neutrino astrophysics which are the analysis of the effects coming from the shock wave engendered by the explosion of the star and of the neutrino self-interaction which has to be included because of the high neutrino density that exists at the neutrino-sphere.

Chapter three corresponds to the first work of this thesis: the shock wave effects upon the Diffuse Supernova Neutrino Background (DSNB). So we first give an explanation of the DSNB which consists in the neutrino fluxes coming from all the supernovae existing in the Universe. Thereafter we present the theoretical model that we used and show our results about the inclusion of the neutrino self-interaction and of the shock wave in the calculation of the DSNB fluxes.

The last chapter is dedicated to the second and the third works of this thesis. We first derive all the equations and quantities that we used to define our view of the Hamiltonian in the matter basis which includes the neutrino self-interaction. Then we apply the formal model derived for two flavors and look at the informations that the matter basis gives us about the three main regimes: the synchronization, the bipolar oscillations and the spectral split. For the first two regimes, we investigate the effects of the presence of the matter Dirac phase $\widetilde{\beta}$ and for the spectral split, we relate it to a well known physical phenomenon using the polarization vector formalism: the magnetic resonance. Finally, we give a preliminary study of such phenomenon in the context of the $SU(3)$ group.

All the original results presented in this PhD thesis have been published in references [24, 25, 26]:

- Sebastien Galais, James Kneller, Cristina Volpe, and Jerome Gava, "Shockwaves in Supernovae: New Implications on the Diffuse Supernova Neutrino Background", Phys. Rev. D **81** (2010) 053002, [arXiv:0906.5294 [hep-ph]].

- S. Galais, J. Kneller, and C. Volpe, "The neutrino-neutrino interaction effects

in supernovae: the point of view from the matter basis", [arXiv:1102.1471 [astro-ph.SR]].

- Sebastien Galais and Cristina Volpe, "The neutrino spectral split in core-collapse supernovae: a magnetic resonance phenomenon", Phys. Rev. D **84**, (2011) 085005, [arXiv:1103.5302 [astro-ph.SR]].

1

Standard neutrino oscillations: theory and experiments

Contents

$\mathcal{T}$ HE idea of neutrino oscillations was first proposed by Pontecorvo in 1957 [4]. He was inspired by a previous discovery that K^0 and $\bar{K}^0$ are not identical particles. This observation led to a model describing the $K^0 - \bar{K}^0$ oscillations as a superposition of two particles K_1^0 and K_2^0. Pontecorvo applied this model to neutral particles: neutrinos and antineutrinos. Transitions between two neutrino families in terms of masses and mixings were introduced by Maki, Nakagawa and Sakata in 1962 [6], and the formalism of the oscillation hypothesis was developed by Pontecorvo in 1967 [27]. In section 1.1, we present the modern form of neutrino oscillations when they propagate in vacuum. We first derive the model for N neutrino flavors (and masses) and then apply the formalism to a two flavors case. Thereafter we explain the geometric representation of two neutrino flavor oscillations in vacuum using the polarization vector formalism. Finally, we apply the model of neutrino oscillations in vacuum to the three known active neutrinos ν_e, ν_μ and ν_τ.

Solar neutrinos are emitted from the deep interior of our star. Consequently, before being detected by different experiments on Earth, they travel through the Sun. In 1978, Wolfenstein [28] discovered that, in the case of two neutrino mixing, the mixing angle in vacuum is replaced by an effective mixing angle in matter which can be large even if the vacuum angle is very small. In 1985, Mikheyev and Smirnov [29, 30] discovered that a resonant flavor transition is possible when neutrinos propagate in a medium with varying density. Actually, it exists a region where the effective mixing angle is equal to the maximal mixing value of $\pi/4$. This mechanism is the so-called "Mikheyev-Smirnov-Wolfenstein (MSW) mechanism". Section 1.2 is dedicated to the description of the possible interactions between neutrinos and ordinary matter: coherent and incoherent forward scatterings. In fact, we will show that neutrino incoherent forward scattering can be not considered for the neutrino propagation if the matter density is sufficiently low, leaving the coherent forward scattering. From the coherent scattering, we derive the effective charged-current and neutral-current potentials in the mean field approximation. Adding the effective matter Hamiltonian to the vacuum Hamiltonian in the Schrödinger-like equation for neutrinos and antineutrinos, we calculate then the MSW resonance conditions. In addition, we discuss the adiabaticity of the propagation which can completely change the flavor conversion induced by the presence of matter. Finally, as for the vacuum oscillations we show the geometric correspondence of the MSW resonance in terms of polarization vectors. In section 1.3, we present the Solar neutrino deficit that has motivated the realization of many experiments (Homestake, Kamiokande, SuperKamiokande,...) and finally led to the discovery of the neutrino oscillation phenomenon.

Section 1.4 is dedicated to another source of neutrinos: the Earth's atmosphere. Indeed, we also receive neutrinos coming from our atmosphere which are the final particles of a series of processes induced by collisions of cosmic rays with the Earth atmosphere. Then we present the Super-Kamiokande experiment which has discovered in 1998 neutrino oscillations [12] and measured the related neutrino

oscillation parameters.

Some mass-mixing parameters relevant to neutrino astrophysics are still unknown for the moment. We mention the neutrino mass hierarchy problem in section 1.5 and the current limits on the third mixing angle θ_{13} in section 1.6. Finally, section 1.7 presents a recent state of art of the neutrino oscillation parameters from reference [31].

1.1 VACUUM OSCILLATIONS

Neutrinos produced by charged-current interactions are flavor eigenstates. But if we want to follow their propagation in vacuum, the easier basis is not the flavor one but the mass basis, which diagonalizes the Hamiltonian. It is always possible to define a unitary transformation U, called here the Maki-Nakagawa-Sakata-Pontecorvo (MNSP) matrix, to link the flavor and the mass basis. This allows us to express the flavor eigenstates $|\nu_\alpha\rangle$ with $\alpha = e, \mu, \tau$ as a linear combination of the mass eigenstates $|\nu_i\rangle$ with $i = 1, 2, 3$

$$|\nu_\alpha\rangle = \sum_i U^*_{\alpha i}|\nu_i\rangle, \tag{1.1}$$

where now we will implicitly sum over the number of neutrino mass species i. The equation for antineutrinos uses the complex conjugate of U, so $|\bar{\nu}_\alpha\rangle = U_{\alpha i}|\bar{\nu}_i\rangle$. We note that we would only observe a difference between neutrinos and antineutrinos in vacuum if U has complex elements (non-zero CP violating phases). Using eq. (1.1), the neutrino state at $t = 0$ can be written as $|\nu(0)\rangle = |\nu_\alpha\rangle = U^*_{\alpha i}|\nu_i\rangle$. After a time t, the neutrino state acquires a phase because its evolution is governed by the Schrödinger-like equation

$$\imath\frac{d\psi}{dt} = H\,\psi \quad \text{with} \quad \psi = \begin{pmatrix} |\nu_1\rangle \\ \vdots \\ |\nu_n\rangle \end{pmatrix}, \tag{1.2}$$

where the Hamiltonian H is diagonal i.e.

$$H = \text{diag}\left(E_1, \ldots, E_n\right). \tag{1.3}$$

So we have

$$|\nu(t)\rangle = U^*_{\alpha i}e^{-\imath E_i t}|\nu_i\rangle. \tag{1.4}$$

The probability amplitude to find the neutrino at the time t in a flavor state $|\nu_\beta\rangle$ is

$$\begin{aligned} \mathcal{A}(\nu_\alpha \to \nu_\beta) &= \langle\nu_\beta|\nu(t)\rangle = U^*_{\alpha i}e^{-\imath E_i t}\langle\nu_\beta|\nu_i\rangle = U_{\beta j}U^*_{\alpha i}e^{-\imath E_i t}\langle\nu_j|\nu_i\rangle \\ &= U_{\beta i}e^{-\imath E_i t}U^*_{\alpha i}. \end{aligned} \tag{1.5}$$

Finally, we obtain the transformation probability by squaring the amplitude of eq. (1.5). This will tell us the probability to find a neutrino in the flavor β while it was produced in the flavor α

$$\begin{aligned} P(\nu_\alpha \to \nu_\beta) &= |\mathcal{A}(\nu_\alpha \to \nu_\beta)|^2 = |U_{\beta i}e^{-\imath E_i t}U^*_{\alpha i}|^2 \\ &= \sum_i |U_{\beta i}|^2|U^*_{\alpha i}|^2 + 2\Re\left(\sum_{i<j} U_{\beta i}U^*_{\alpha i}U^*_{\beta j}U_{\alpha j}e^{-\imath(E_i - E_j)t}\right), \end{aligned} \tag{1.6}$$

where the summation is explicitly written. Since we are considering relativistic neutrinos of momentum p, we use the approximation

$$E_i = \sqrt{p^2 + m_i^2} \simeq p + \frac{m_i^2}{2p} \simeq p + \frac{m_i^2}{2E}, \tag{1.7}$$

and we rewrite eq. (1.6) as

$$P(\nu_\alpha \to \nu_\beta) = \sum_i |U_{\beta i}|^2|U^*_{\alpha i}|^2 + 2\Re\left(\sum_{i<j} U_{\beta i}U^*_{\alpha i}U^*_{\beta j}U_{\alpha j}e^{-\imath\frac{\Delta m_{ij}^2}{2E}t}\right), \tag{1.8}$$

in terms of the neutrino squared mass differences, $\Delta m_{ij}^2 = m_i^2 - m_j^2$. The final step in the standard derivation of the neutrino oscillation probability is based on the fact that the propagation time is not measured. What is known is the distance L between the source and the detector. Since ultrarelativistic neutrinos propagate almost at the speed of light, we can use the approximation $t \simeq L$, leading to

$$P(\nu_\alpha \to \nu_\beta) = \sum_i |U_{\beta i}|^2 |U_{\alpha i}^*|^2 + 2\, \Re \left(\sum_{i<j} U_{\beta i} U_{\alpha i}^* U_{\beta j}^* U_{\alpha j} e^{-i\frac{\Delta m_{ij}^2}{2E}L} \right). \qquad (1.9)$$

From this expression, we can define the phases of the neutrino oscillations

$$\phi_{ij} = -\frac{\Delta m_{ij}^2}{2E}L, \qquad (1.10)$$

and the oscillation lengths which are the distance where the phase ϕ_{ij} becomes equal to 2π

$$L_{ij}^{\text{osc}} = \frac{4\pi E}{\Delta m_{ij}^2}. \qquad (1.11)$$

The probability in eq. (1.9) satifies the two rules of the conservation of probability because of the unitarity evolution of states:

1. the sum of probabilities of a transition from a flavor α to all flavor β (including $\beta = \alpha$) is equal to unity

$$\sum_\beta P(\nu_\alpha \to \nu_\beta) = 1; \qquad (1.12)$$

2. the sum of probabilities of a transition from any flavor α (including $\alpha = \beta$) to a flavor β is equal to unity

$$\sum_\alpha P(\nu_\alpha \to \nu_\beta) = 1. \qquad (1.13)$$

These rules are useful if we want to focus on the survival probability of a flavor α i.e.$P(\nu_\alpha \to \nu_\alpha)$ and not on the transition probability to another flavor $P(\nu_\alpha \to \nu_\beta)$ with $\alpha \neq \beta$.

1.1.1 Two flavors case

In the two flavors case, we will only consider the mixing between ν_e and ν_μ. The mixing matrix U connecting the flavor and mass basis takes the general form (see appendix A.3.1)

$$U = \begin{pmatrix} 1 & 0 \\ 0 & e^{i\beta} \end{pmatrix} \begin{pmatrix} \cos\theta_0 & \sin\theta_0 \\ -\sin\theta_0 & \cos\theta_0 \end{pmatrix} \begin{pmatrix} e^{-i\alpha_1} & 0 \\ 0 & e^{-i\alpha_2} \end{pmatrix}, \qquad (1.14)$$

where θ_0 is the mixing angle in vacuum, β is a Dirac phase and α_i are Majorana phases. Using eqs. (1.9), (1.12) and (1.13), we obtain for the survival probability of the electron flavor

$$P(\nu_e \to \nu_e) = 1 - \sin^2(2\theta_0) \sin^2 \left(\frac{\Delta m_{21}^2}{4E}L \right). \qquad (1.15)$$

We remark that the Dirac and Majorana phases do not appear in eq. (1.15) because they do not lead to physical effects in neutrino oscillations. We observe that the survival probability of eq. (1.15) consists of two terms:

1. $\sin^2(2\theta_0)$ is the amplitude of the neutrino oscillations (see fig. 1.1) and does not depend on the distance L traveled by the neutrino. Then a maximal mixing ($\sin^2(2\theta_0) = 1$) corresponds to a vacuum angle equal to $45°$;

2. $\sin^2\left(\dfrac{\Delta m_{21}^2}{4E}L\right)$ is an oscillatory term (see fig. 1.1) which explains the denomination "neutrino oscillations". We notice that the period of the oscillations increases with the energy. Moreover we remark that no oscillations occur if neutrinos have degenerate (or zero) masses, i.e. $\Delta m_{21}^2 = 0$.

Because of the fact that we consider two neutrino species ν_1 and ν_2 in the mass basis (the U matrix is squared), we can have two mass hierarchies depending on the sign of Δm_{21}^2. These two scenarii (see fig. 1.2) are named "normal" ($\Delta m_{21}^2 > 0$) and "inverted" ($\Delta m_{21}^2 < 0$). But due to the form of the eq. (1.15) for the survival probability, the hierarchy is not observable for the two flavors case in vacuum.

In the two flavors case, we can explicitly write the oscillation length

$$L^{\text{osc}} = \frac{4\pi E}{\Delta m_{21}^2} = 2.47\,\text{m}\,\frac{E\,[\text{MeV}]}{\Delta m_{21}^2\,[\text{eV}^2]}. \tag{1.16}$$

For $L \gg L^{\text{osc}}$, the transition probability experiences very fast oscillations and so in the detector we would only observe the averaged probability

$$\langle P(\nu_e \to \nu_\mu)\rangle = \frac{1}{2}\sin^2(2\theta_0). \tag{1.17}$$

1.1.2 The polarization vector representation in two flavors

It is also possible to use the polarization vector representation to follow the evolution of a neutrino (see appendix B.1). The movement is a simple precession (see figure 1.3) of a polarization vector $\mathbf{P}$ around a fixed magnetic field $\mathbf{B}$ given by

$$\mathbf{B} = \frac{\Delta m_{21}^2}{2E}\begin{pmatrix} \sin(2\theta_0) \\ 0 \\ -\cos(2\theta_0) \end{pmatrix} \quad \text{and} \quad \mathbf{P} = \begin{pmatrix} 2\,\Re\left(\nu_e\nu_\mu^*\right) \\ -2\,\Im\left(\nu_e\nu_\mu^*\right) \\ |\nu_e|^2 - |\nu_\mu|^2 \end{pmatrix}, \tag{1.18}$$

and the equation that we have to solve is the gyroscopic equation

$$\frac{d\mathbf{P}}{dt} = \mathbf{B} \times \mathbf{P}. \tag{1.19}$$

In this geometric representation, if we want to look at the survival probability, the relation between survival probability and polarization vector projection on the z-axis is

$$P(\nu_e \to \nu_e) = \frac{1}{2}(P_z + 1). \tag{1.20}$$

This implies that a pure ν_e state corresponds to a polarization vector along the positive z-axis whereas a pure ν_μ state corresponds to a polarization vector along the negative z-axis.
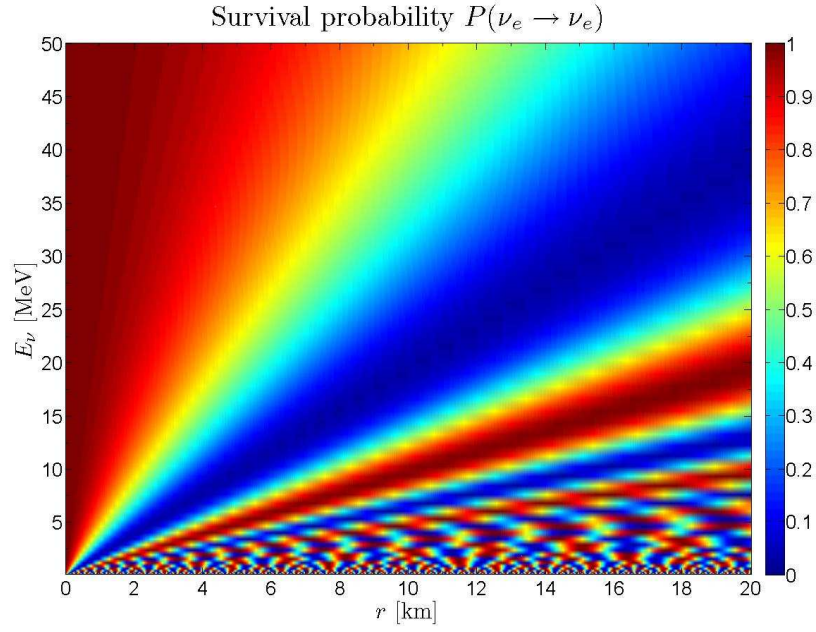
(a) Contour plot of the survival probability $P(\nu_e \to \nu_e)$ as a function of energy and distance.
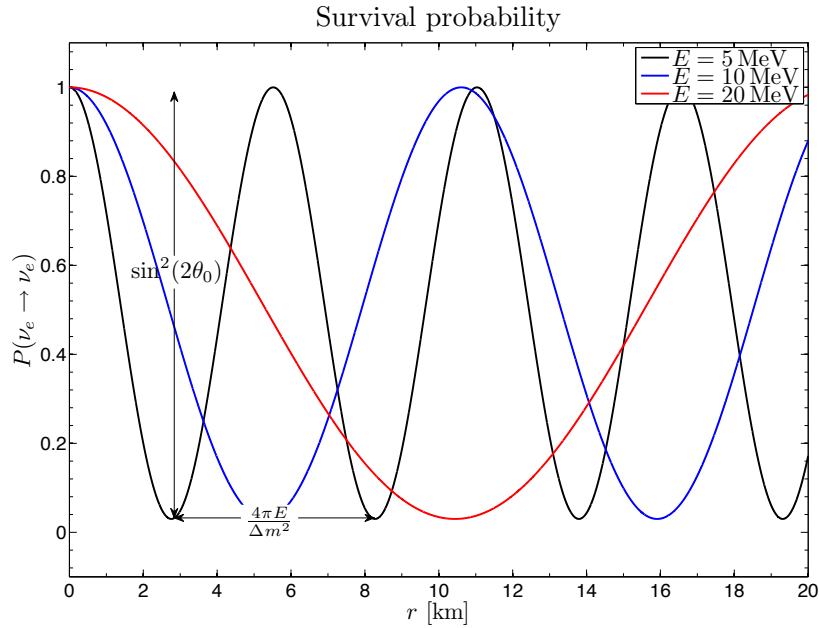
(b) Evolution of the survival probability with the distance for three energies $E = 5, 10$ and $20\,\text{MeV}$.

Figure 1.1 – *Both plots use for parameters $\Delta m_{21}^2 = 2.4 \times 10^{-3}\,\text{eV}^2$ and $\theta_0 = 40°$.*

In vacuum, because the magnetic field **B** is constant and does not move, the polarization vector **P** just precesses around **B**. Thus the projection on the z-axis, P_z, oscillates giving the expected survival probability plotted on figure 1.1. We note that neutrino oscillations are only possible if the vacuum angle θ_0 has a non-zero value. Otherwise, for $\theta_0 = 0°$, the magnetic field **B** is aligned with the z-axis i.e. $\mathbf{B} = B_z\,\mathbf{e}_z$ and because the polarization vector **P** is also initially aligned with the z-axis, the precession is impossible and the system is frozen.
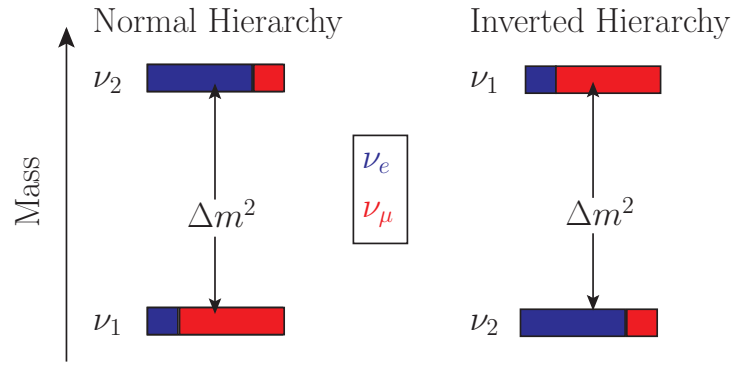
Figure 1.2 – *Two possible scenarii for the neutrino mass hierarchy depending on the sign of Δm_{21}^2: "normal" or "inverted".*
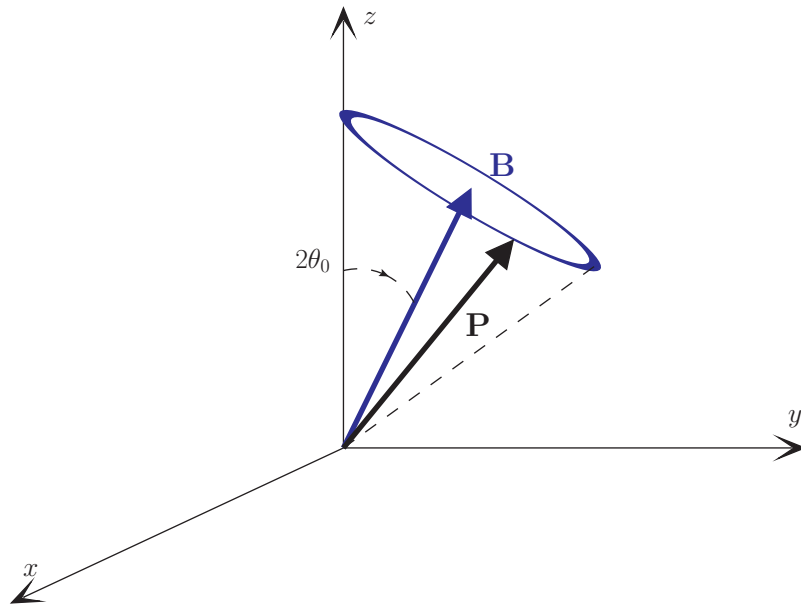
Figure 1.3 – *The solution of the Schrödinger-like equation of eq. (1.2) in vacuum is equivalent to determining the precession of a polarization vector associated to the neutrino flavor content, around a magnetic field given by the Hamiltonian (see eq. (1.18)).*

1.1.3 Three flavors case

The number of active neutrino species has been indirectly measured by the LEP using the invisible width of the Z^0 decay [32]. They obtained $N_\nu = 2.984 \pm 0.008$, proving the existence of three active flavors ν_e, ν_μ and ν_τ. In this case, the flavor eigenstates are related to the mass eigenstates through

$$\begin{pmatrix} \nu_e \\ \nu_\mu \\ \nu_\tau \end{pmatrix} = \begin{pmatrix} U_{e1} & U_{e2} & U_{e3} \\ U_{\mu 1} & U_{\mu 2} & U_{\mu 3} \\ U_{\tau 1} & U_{\tau 2} & U_{\tau 3} \end{pmatrix} \begin{pmatrix} \nu_1 \\ \nu_2 \\ \nu_3 \end{pmatrix}. \tag{1.21}$$

The most general lepton mixing matrix U, known as the MNSP matrix, is given in terms of three mixing angles θ_{12}, θ_{13} and θ_{23}, one Dirac phase δ and three Majorana

phases α_i [1]

$$
U = \begin{pmatrix} c_{12}\,c_{13} & s_{12}\,c_{13} & s_{13}\,e^{-\iota\delta} \\ -s_{12}\,c_{23} - c_{12}\,s_{23}\,s_{13}\,e^{\iota\delta} & c_{12}\,c_{23} - s_{12}\,s_{23}\,s_{13}\,e^{\iota\delta} & s_{23}\,c_{13} \\ s_{12}\,s_{23} - c_{12}\,c_{23}\,s_{13}\,e^{\iota\delta} & -c_{12}\,s_{23} - s_{12}\,c_{23}\,s_{13}\,e^{\iota\delta} & c_{23}\,c_{13} \end{pmatrix} \begin{pmatrix} e^{-\iota\alpha_1} & 0 & 0 \\ 0 & e^{-\iota\alpha_2} & 0 \\ 0 & 0 & e^{-\iota\alpha_3} \end{pmatrix} .
$$

$$(1.22)$$

where $c_{ij} = \cos\theta_{ij}$ and $s_{ij} = \sin\theta_{ij}$. The possible values for the mixing angles are within the range $[0, \pi/2]$ whereas for the phases we have $\delta, \alpha_i \in [-\pi, \pi]$.

Because Majorana phases do not affect neutrino oscillations, we will omit the matrix containing the Majorana phases. Inserting this matrix into eq. (1.9), we obtain the neutrino oscillations formulas in three flavors. By looking at the figure 1.4, representing the survival probability of the electron flavor as a function of the distance, we see that the survival probability is a combination of oscillations with different frequencies. For instance, on figure 1.4 b, we can distinguish an oscillation with a period of few hundred kilometers and another one with a period of tens kilometers at $E \sim \mathcal{O}(10)\,\mathrm{MeV}$. Contrary to the two flavors case, neutrino and antineutrino flavors do not follow the same evolution if $\delta \neq 0$.

In the three flavors case, atmospheric and solar experiments allow the presence of two hierarchies for neutrino masses (see fig. 1.5) depending on the sign of Δm_{31}^2. The sign of Δm_{21}^2 is already known because it comes from experiments which looked at neutrino oscillations enhanced by matter effect, which are sensitive to the hierarchy. We will explain in section 1.2.3 that the sign of the mass squared difference involved in a flavor conversion induced by the presence of ordinary matter can be found depending on the channel (neutrino or antineutrino) in which the flavor conversion occurs. However, for the moment, the value of Δm_{31}^2 is extracted from experiments mainly sensitive to neutrino oscillations in vacuum which, due to eq. (1.15), are only sensitive to $|\Delta m_{31}^2|$. Concerning notation and conventions, if the hierarchy is "normal" ($\Delta m_{31}^2 > 0$), then the solar mass squared difference $\Delta m_\odot^2$ is equal to Δm_{21}^2 and the atmospheric mass squared difference $\Delta m_\oplus^2$ is equal to Δm_{31}^2 whereas for the "inverted" hierarchy ($\Delta m_{31}^2 < 0$) we associate $\Delta m_\odot^2 = \Delta m_{21}^2$ and $\Delta m_\oplus^2 = \Delta m_{32}^2$.

1.2   OSCILLATIONS IN THE PRESENCE OF ORDINARY MATTER AND MIKHEYEV-SMIRNOV-WOLFENSTEIN EFFECT

In several cases, neutrinos travel through matter before being detected. For example, solar neutrinos are emitted from deep inside the Sun; in long-baseline accelerator and atmospheric experiments, neutrinos may also travel through Earth before detection. When active neutrinos propagate in matter, their evolution is affected by an effective potential due to the interactions with the medium through coherent forward scattering in charged-current and neutral-current processes (the corresponding Feynman diagrams are shown in fig. 1.6).

In section 1.2, we give a complete derivation of the neutrino incoherent and coherent forward scatterings. Thereafter, we introduce the effective matter Hamiltonian in the Schrödinger-like equation (eq. (1.2)) and examine, for the two flavors

---

1. Here we decide to express the U matrix with three Majorana phases but actually one of these phases depends on the others. Then we have only two independent Majorana phases.
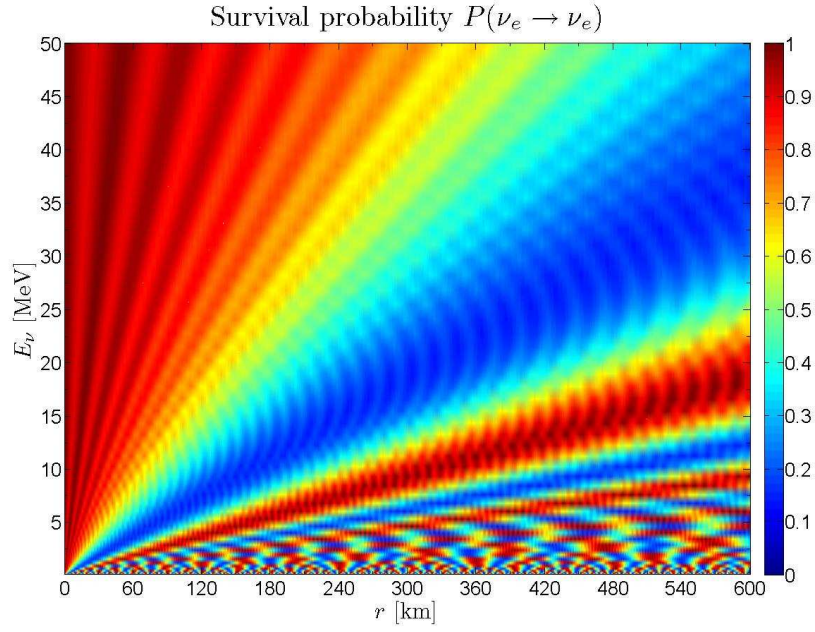
Survival probability $P(\nu_e \to \nu_e)$

(a) Contour plot of the survival probability $P(\nu_e \to \nu_e)$ as a function of energy and distance.

Survival probability
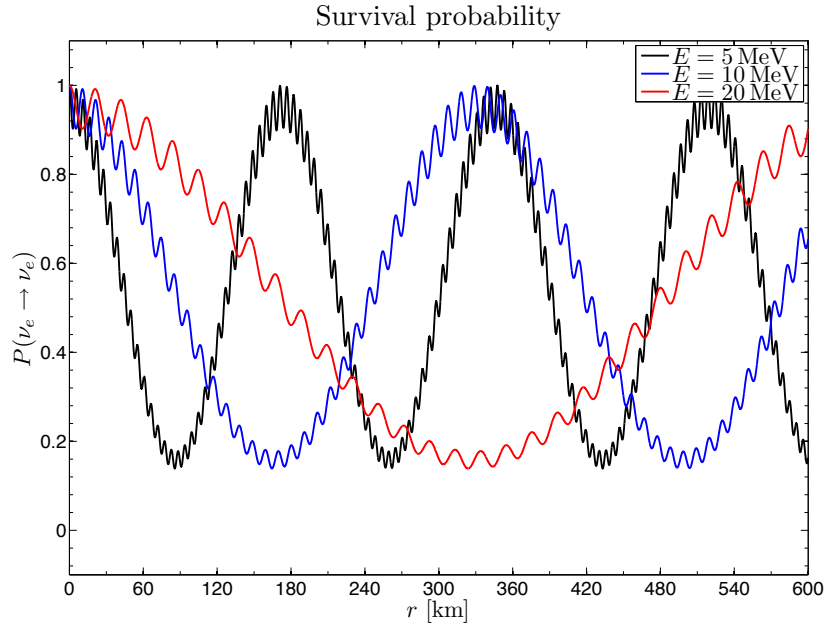
(b) Evolution of the survival probability with the distance for three energies $E = 5, 10$ and 20 MeV.

Figure 1.4 – *Both plots are obtained with the parameters $\Delta m_{21}^2 = 7.65 \times 10^{-5}\,\text{eV}^2$, $\Delta m_{31}^2 = 2.4 \times 10^{-3}\,\text{eV}^2$, $\theta_{12} = 33°$, $\theta_{13} = 9°$ and $\theta_{23} = 40°$.*

case, the impact upon the neutrino survival probability. The observed flavor conversion induced by the presence of the matter is known as the *MSW resonance*. We mention here that the MSW effect is the solution to the solar neutrino deficit problem and that MSW resonances can also occur in other astrophysical environments such as core-collapse supernovae. Then we describe another concept that can modify the neutrino evolution in matter: the adiabaticity. At the end of the section, we
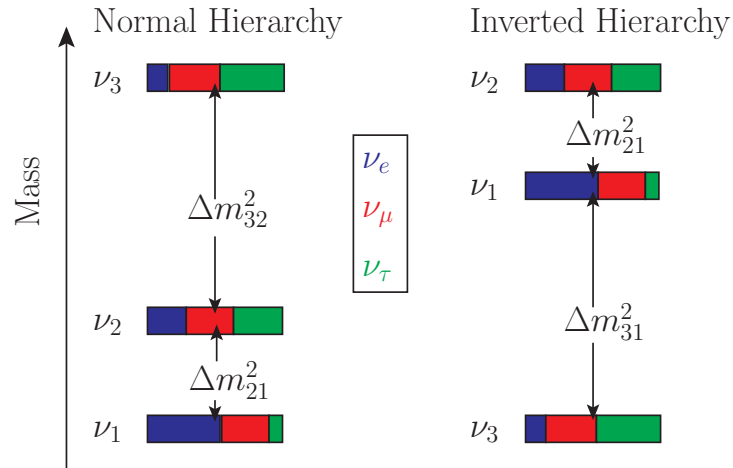
Figure 1.5 – *Two possible scenarii for the neutrino mass hierarchy depending on the sign of Δm_{31}^2: "normal" or "inverted". For each mass eigenstate, the colors (blue, red and green) represent the flavor content.*

explain the neutrino flavor conversion coming from the MSW resonance in terms of the polarization vectors formalism.

(a) Charged current interactions between electrons and neutrinos.

(b) Neutral current interactions between fermions and all neutrino flavors.
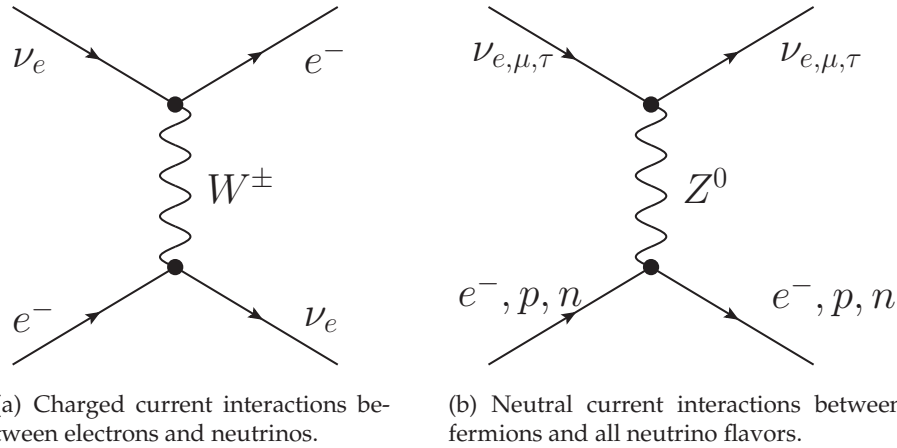
Figure 1.6 – *Neutrino scattering diagrams with ordinary matter via charged-current and neutral-current interactions.*

1.2.1   Neutrino incoherent forward scattering

As an example, we will estimate the cross section of the $\nu_e\,e$ scattering to see if neutrino incoherent forward scatterings are relevant for the matter density we are dealing with [33, 34]. The $\nu_e\,e$ scattering receives contribution both from charged and neutral-current interactions as shown in fig. 1.6. Since we work in the low energy limit, we will neglect the momentum dependence of the $W^\pm$ and Z^0 propagators and work in the four-Fermi interaction approximation, i.e.

$$\frac{-g^{\alpha\beta} + \frac{q^\alpha q^\beta}{m_{W,Z}^2}}{q^2 - m_{W,Z}^2 + \iota\epsilon} = \frac{g^{\alpha\beta}}{m_{W,Z}^2} \quad \text{and} \quad \frac{g^2}{8m_W^2} = \frac{G_F}{\sqrt{2}}, \tag{1.23}$$

where q is the momentum of the intermediate vector boson and G_F the Fermi constant.

For the charged-current diagram, the Feynman amplitude is given by

$$\mathcal{M}_{CC} = -\frac{G_F}{\sqrt{2}}\overline{\nu}_e(p')(\gamma_\alpha(1-\gamma^5))e(k)\overline{e}(k')(\gamma^\alpha(1-\gamma^5))\nu_e(p). \qquad (1.24)$$

Using the Fierz transformation, one obtains

$$\mathcal{M}_{CC} = -\frac{G_F}{\sqrt{2}}\overline{\nu}_e(p')(\gamma_\alpha(1-\gamma^5))\nu_e(p)\overline{e}(k')(\gamma^\alpha(1-\gamma^5))e(k). \qquad (1.25)$$

For the neutral-current diagram, the Feynman amplitude is given by

$$\mathcal{M}_{NC} = -\frac{G_F}{\sqrt{2}}\overline{\nu}_e(p')(\gamma_\alpha(1-\gamma^5))\nu_e(p)\overline{e}(k')(\gamma^\alpha(g_V^e - g_A^e\gamma^5))e(k). \qquad (1.26)$$

Adding the two contribution one thus obtains

$$\mathcal{M} = -\frac{G_F}{\sqrt{2}}\overline{\nu}_e(p')(\gamma_\alpha(1-\gamma^5))\nu_e(p)\overline{e}(k')(\gamma^\alpha(\underbrace{(1+g_V^e)}_{G_V} - \underbrace{(1+g_A^e)}_{G_A}\gamma^5))e(k). \qquad (1.27)$$

Now to calculate the total cross section, we average over the initial electron spin and sum over the final electron spin, so

$$\frac{1}{2}\sum_{\text{spin}}|\mathcal{M}|^2 = \frac{G_F^2}{4}N^{\lambda\rho}L_{\lambda\rho}, \qquad (1.28)$$

where

$$\begin{aligned}N^{\lambda\rho} &= \text{Tr}\left[\gamma^\rho(1-\gamma^5)\not{p}(1+\gamma^5)\gamma^\lambda\not{p}'\right]\\ &= 8\left(p^\rho p'^\lambda - g^{\rho\lambda}p.p' + p'^\rho p^\lambda - \imath\epsilon^{\rho\beta\lambda\delta}p_\beta p'_\delta\right),\end{aligned} \qquad (1.29)$$

and

$$\begin{aligned}L_{\lambda\rho} &= \text{Tr}\left[\gamma_\rho(G_V - G_A\gamma^5)(\not{k}+m_e)(G_V+G_A\gamma^5)\gamma_\lambda(\not{k}'+m_e)\right]\\ &= 4(G_V^2 + G_A^2)\left(k_\rho k'_\lambda - g_{\rho\lambda}k.k' + k'_\rho k_\lambda\right) - 8G_V G_A\imath\epsilon_{\rho\beta\lambda\delta}k^\beta k'^\delta\\ &\quad +4m_e^2(G_V^2 - G_A^2)g_{\rho\lambda}.\end{aligned} \qquad (1.30)$$

After contraction and using the momentum conservation $p+k = p'+k'$, that ensure $k.p = k'.p'$ and $k.p' = k'.p$, one obtains

$$N^{\lambda\rho}L_{\lambda\rho} = 64\left[(G_V+G_A)^2(p.k)^2 + (G_V-G_A)^2(p.k')^2 - m_e^2(G_V^2-G_A^2)p.p'\right], \qquad (1.31)$$

with

$$\begin{aligned}G_V - G_A &= 2\sin^2(\theta_W), &(1.32)\\ G_V + G_A &= 1 + 2\sin^2(\theta_W), &(1.33)\\ G_V^2 - G_A^2 &= 2\sin^2(\theta_W)(1 + 2\sin^2(\theta_W)). &(1.34)\end{aligned}$$

Now we decide to work in the frame in which the initial electron is at rest and choose the axes so that the incoming neutrino is traveling along the positive z direction

$$
p^\lambda = \begin{pmatrix} E_\nu \\ 0 \\ 0 \\ E_\nu \end{pmatrix}, \quad
k^\lambda = \begin{pmatrix} m_e \\ 0 \\ 0 \\ 0 \end{pmatrix}, \quad
p'^\lambda = \begin{pmatrix} E'_\nu \\ 0 \\ E'_\nu \sin\phi \\ E'_\nu \cos\phi \end{pmatrix}, \quad
k'^\lambda = \begin{pmatrix} E'_e \\ 0 \\ -p'_e \sin\chi \\ p'_e \cos\chi \end{pmatrix}.
$$
(1.35)

With the Mandelstam variables, it is straightforward to prove that

$$
s + t + u = 2m_e^2 \quad \Longrightarrow \quad E'_\nu = \frac{E_\nu m_e}{m_e + E_\nu(1 - \cos\phi)}.
$$
(1.36)

We now explicitly calculate eq. (1.31)

$$
N^{\lambda\rho} L_{\lambda\rho} = 64 m_e^2 \left[(1 + 2\sin^2(\theta_W))^2 E_\nu^2 + 4\sin^4(\theta_W) E_\nu'^2 \right],
$$
(1.37)

where we have dropped the last term which is proportional to m_e^3 so negligible for $E_\nu \gg m_e$. The total cross section is then equal to

$$
\sigma = \iint \frac{(2\pi)^4 \delta^4(p + k - p' - k')}{4 E_\nu m_e} \frac{d^3 p'}{(2\pi)^3 2E'_\nu} \frac{d^3 k'}{(2\pi)^3 2E'_e}
$$
$$
16 G_F^2 \, m_e^2 \left[(1 + 2\sin^2(\theta_W))^2 E_\nu^2 + 4\sin^4(\theta_W) E_\nu'^2 \right].
$$
(1.38)

By performing the integral over $d^3 k'$, one obtains

$$
\sigma = \frac{1}{16\pi^2 E_\nu m_e} \int \frac{d^3 p'}{4 E'_\nu E'_e} \delta(E_\nu + m_e - E'_\nu - E'_e)
$$
$$
16 G_F^2 \, m_e^2 \left[(1 + 2\sin^2(\theta_W))^2 E_\nu^2 + 4\sin^4(\theta_W) E_\nu'^2 \right].
$$
(1.39)

The integration over the azimuthal angle and the magnitude of p' give us

$$
\frac{d\sigma}{d\cos\phi} = \frac{G_F^2 m_e^2}{2\pi} \frac{\left[(1 + 2\sin^2(\theta_W))^2 E_\nu^2 + 4\sin^4(\theta_W) E_\nu'^2 \right]}{(m_e + E_\nu(1 - \cos\phi))^2}.
$$
(1.40)

The previous equation represents the differential cross section. If we want the total cross section, we have to do the integration over the angle ϕ. We finally obtain

$$
\sigma = \frac{G_F^2 m_e E_\nu}{2\pi} \left[(1 + 2\sin^2(\theta_W))^2 + \frac{4}{3}\sin^4(\theta_W) \right].
$$
(1.41)

We can follow the same procedure to find the total cross section of the process $\bar{\nu}_e + e^-$, $\nu_{\mu,\tau} + e^-$ and $\bar{\nu}_{\mu,\tau} + e^-$, the results are given in table 1.1.

With these cross sections, it is possible to estimate the mean free path of a neutrino in a medium with number density N of target particles by

$$
l = \frac{1}{N\sigma} \sim 10^{44} \, \text{cm}^{-2} \frac{1}{N \, (m_e E_\nu / \text{MeV}^2)}.
$$
(1.42)

In our supernova environment, we consider a typical density of $\rho_e \sim 10^{10} \, \text{g.cm}^{-3}$ at 10 km which will decrease as r^{-3}, so we have $N \sim 10^{34} \, \text{cm}^{-3}$. Now if we take

Process	Total cross section
$\nu_e + e^-$	$\dfrac{G_F^2 m_e E_\nu}{2\pi}\left[(1 + 2\sin^2(\theta_W))^2 + \dfrac{4}{3}\sin^4(\theta_W)\right]$
$\bar{\nu}_e + e^-$	$\dfrac{G_F^2 m_e E_\nu}{2\pi}\left[\dfrac{1}{3}(1 + 2\sin^2(\theta_W))^2 + 4\sin^4(\theta_W)\right]$
$\nu_{\mu,\tau} + e^-$	$\dfrac{G_F^2 m_e E_\nu}{2\pi}\left[(1 - 2\sin^2(\theta_W))^2 + \dfrac{4}{3}\sin^4(\theta_W)\right]$
$\bar{\nu}_{\mu,\tau} + e^-$	$\dfrac{G_F^2 m_e E_\nu}{2\pi}\left[\dfrac{1}{3}(1 - 2\sin^2(\theta_W))^2 + 4\sin^4(\theta_W)\right]$

Table 1.1 – *Total neutrino-electron elastic scattering cross sections for $\sqrt{s} \gg m_e$.*

a typical energy neutrino of 20 MeV, we obtain $l \sim 10^9$ cm. In our studies, this length corresponds roughly to ten times the distance reached by our calculations. This implies that we will only consider the coherent forward scatterings and not the incoherent ones.

The same calculation can be done for the neutrino-proton and neutrino-neutron elastic scattering cross sections. We would also conclude that the mean free path is much larger than the typical distance we are looking at. So we only take into account the coherent forward scatterings.

1.2.2   Neutrino coherent forward scatterings and effective potentials

1.2.2.1   Charged-current potential

We first calculate the charged-current potential V_{CC} for a ν_e propagating in a homogeneous and isotropic gas of unpolarized electrons. From the effective low energy charged-current weak interaction lagrangian in eq. (1.25), the effective charged-current Hamiltonian is

$$H^{CC}(x) = \frac{G_F}{\sqrt{2}}\overline{\nu}_e(x)(\gamma_\alpha(1 - \gamma^5))\nu_e(x)\overline{e}(x)(\gamma^\alpha(1 - \gamma^5))e(x). \qquad (1.43)$$

Then we do the average of the effective Hamiltonian over the electron background in the rest of the medium. This approximation is called the mean field approximation. The corresponding diagrams are showed in figure 1.7. In this framework, the four-momenta and helicities of the electron states are identical before and after the scattering because the interaction must leave the medium unchanged to contribute coherently to the neutrino potential.
The average of the effective Hamiltonian is given by

$$\langle H^{CC}(x)\rangle = \frac{G_F}{\sqrt{2}}\overline{\nu}_e(x)(\gamma_\alpha(1 - \gamma^5))\nu_e(x)\int d^3 p_e f(E_e, T)$$
$$\times \frac{1}{2}\sum_{h_e = \pm 1}\langle e^-(p_e, h_e)|\overline{e}(x)(\gamma^\alpha(1 - \gamma^5))e(x)|e^-(p_e, h_e)\rangle. \qquad (1.44)$$

(a) Charged-current interaction.   (b) Neutral-current interaction.
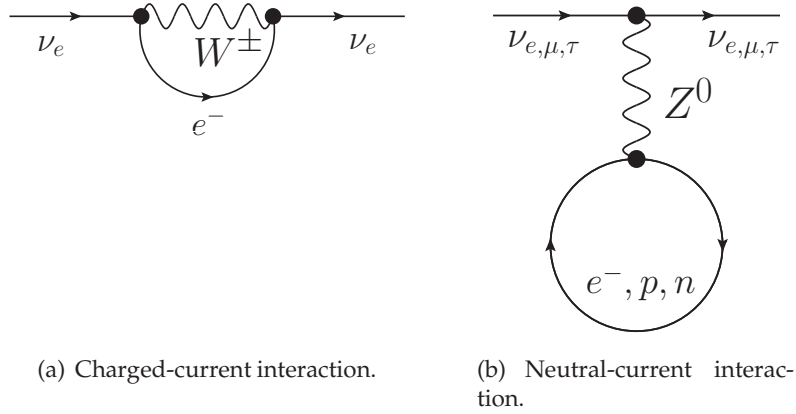
Figure 1.7 – *Neutrino forward scattering diagrams in the mean field approximation.*

For the electron background, we consider a finite normalization volume V with the one-electron states $|e^-(p_e, h_e)\rangle$

$$|e^-(p_e, h_e)\rangle = \frac{1}{2E_e V} a_e^{(h_e)\dagger}(p_e)|0\rangle \quad \text{and} \quad \langle e^-(p_e, h_e)| = \langle 0|a_e^{(h_e)}(p_e). \tag{1.45}$$

These definitions, with the discrete anticommutation relation

$$\left\{ a^{(h)}(p), a^{(h')\dagger}(p') \right\} = 2EV\delta_{\vec{p}\vec{p}'}\delta_{hh'}, \tag{1.46}$$

ensure the normalization

$$\langle e^-(p_e, h_e)|e^-(p_e, h'_e)\rangle = \delta_{h_e h'_e}. \tag{1.47}$$

The function $f(E_e, T)$ is the statistical distribution of the electron energy E_e, which depends on the temperature T and this quantity is normalized by

$$\int d^3p f(E_e, T) = N_e V, \tag{1.48}$$

where N_e is the electron density of the medium and so $N_e V$ is the total number of electrons.

By performing the average over the helicities of the electron matrix element one obtains

$$\frac{1}{2}\sum_{h_e=\pm 1} \langle e^-(p_e, h_e)|\bar{e}(x)(\gamma^\alpha(1-\gamma^5))e(x)|e^-(p_e, h_e)\rangle$$

$$= \frac{1}{4E_e V} \sum_{h_e=\pm 1} \overline{u_e^{(h_e)}}(p_e)(\gamma^\alpha(1-\gamma^5))u_e^{(h_e)}(p_e)$$

$$= \frac{1}{4E_e V}\text{Tr}\left[\left(\sum_{h_e=\pm 1} u_e^{(h_e)}(p_e)\overline{u_e^{(h_e)}}(p_e) \right) \gamma^\alpha(1-\gamma^5) \right]$$

$$= \frac{1}{4E_e V}\text{Tr}\left[(\not{p}_e + m_e)\gamma^\alpha(1-\gamma^5) \right]$$

$$= \frac{p_e^\alpha}{E_e V}. \tag{1.49}$$

Inserting this relation into the effective Hamiltonian, we obtain

$$\langle H^{CC}(x)\rangle = \frac{G_F}{\sqrt{2}V} \int d^3p_e f(E_e, T)\overline{\nu}_e(x)\frac{\not{p}_e}{E_e}(1-\gamma^5)\nu_e(x). \tag{1.50}$$

The integral over $d^3 p_e$ gives us

$$\int d^3 p_e f(E_e, T) \frac{\not{p}_e}{E_e} = \int d^3 p_e f(E_e, T) \left(\gamma^0 - \frac{\vec{p}_e \vec{\gamma}}{E_e} \right) = N_e V \gamma^0, \qquad (1.51)$$

where we have only a contribution from the first term because the second term is odd under the transformation $\vec{p}_e \rightarrow \vec{p}_e$. Finally, we use the left-handed projector $P_L = (1 - \gamma^5)/2$ to obtain the left-handed neutrinos and we have

$$\langle H^{CC}(x) \rangle = V_{CC} \bar{v}_{eL}(x) \gamma^0 v_{eL}(x), \qquad (1.52)$$

with the charged-current potential given by

$$V_{CC} = \sqrt{2} G_F N_e. \qquad (1.53)$$

1.2.2.2 Neutral-current potential

Analogously to the charged-current potential, one can find the neutral-current potential for a neutrino propagating in a medium with density $N_{\mathfrak{f}}$ of fermions $\mathfrak{f}$. From the effective low energy neutral-current weak interaction lagrangian in eq. (1.26), the effective neutral-current Hamiltonian is

$$H^{NC}(x) = \frac{G_F}{\sqrt{2}} \sum_{\alpha = e, \mu, \tau} \bar{v}_\alpha(x) (\gamma_\rho (1 - \gamma^5)) v_\alpha(x) \sum_{\mathfrak{f}} \bar{\mathfrak{f}}(x) (\gamma^\rho (g_V^{\mathfrak{f}} - g_A^{\mathfrak{f}} \gamma^5)) \mathfrak{f}(x). \qquad (1.54)$$

Now we do the same calculation that we have done for the charged-current potential and we obtain the neutral-current potential of any flavor v_α due to the coherent interaction with fermions $\mathfrak{f}$

$$V_{NC}^{\mathfrak{f}} = \sqrt{2} G_F N_{\mathfrak{f}} g_V^{\mathfrak{f}}. \qquad (1.55)$$

We use the table 1.2 for the values of constants $g_V^{\mathfrak{f}}$.

Fermions	g_V	g_A
v_e, v_μ, v_τ	$\frac{1}{2}$	$\frac{1}{2}$
e, μ, τ	$-\frac{1}{2} + 2 \sin^2 \theta_W$	$-\frac{1}{2}$
u, c, t	$\frac{1}{2} + \frac{4}{3} \sin^2 \theta_W$	$\frac{1}{2}$
d, s, b	$-\frac{1}{2} + \frac{2}{3} \sin^2 \theta_W$	$-\frac{1}{2}$

Table 1.2 – *Values of the vector constants $g_V^{\mathfrak{f}}$ and the axial constants $g_A^{\mathfrak{f}}$ for all fermions.*

Since the composition of the proton and the neutron are $p = uud$ and $n = udd$, we have

$$g_V^p = 2 g_V^u + g_V^d = \frac{1}{2} - 2 \sin^2 \theta_W \quad \text{and} \quad g_V^n = g_V^u + 2 g_V^d = -\frac{1}{2}. \qquad (1.56)$$

Because we are interested in astrophysical environments with low temperature and density where matter is composed of neutrons, protons and electrons. The electrical neutrality of the system implies an equal number density of protons and electrons, so only neutrons contribute leading to

$$V_{NC} = -\frac{1}{2} \sqrt{2} G_F N_n. \qquad (1.57)$$

1.2.2.3 Effective potential

Adding the two results of the previous sections, the effective neutrino Hamiltonian in matter is

$$H = \sum_{\alpha=e,\mu,\tau} V_\alpha \bar{\nu}_{\alpha L}(x) \gamma^0 \nu_{\alpha L}, \qquad (1.58)$$

with the potential

$$V_\alpha = \delta_{\alpha e} V_{CC} + V_{NC} = \sqrt{2} G_F \left(\delta_{\alpha e} N_e - \frac{N_n}{2} \right). \qquad (1.59)$$

It is now possible to write the effective matter Hamiltonian in flavor basis which will be added to the vacuum Hamiltonian

$$H^{\text{mat}} = \sqrt{2} G_F \begin{pmatrix} N_e - \frac{1}{2} N_n & 0 & 0 \\ 0 & -\frac{1}{2} N_n & 0 \\ 0 & 0 & -\frac{1}{2} N_n \end{pmatrix}. \qquad (1.60)$$

Since the contribution coming from the neutral current potential is the same for all flavors, it is proportional to the identity matrix and gives an unobservable common phase to the system. We can then remove this quantity and the effective matter Hamiltonian is just

$$H^{\text{mat}} = \sqrt{2} G_F \begin{pmatrix} N_e & 0 & 0 \\ 0 & 0 & 0 \\ 0 & 0 & 0 \end{pmatrix}. \qquad (1.61)$$

For the antineutrinos case, we just have to replace $N_e \rightarrow -N_e$.

1.2.3 Two flavors case and MSW resonance

Following references [28, 29, 30], we write the Schrödinger-like equation for neutrinos in the flavor basis

$$\iota \frac{\partial}{\partial x} \begin{pmatrix} \nu_e \\ \nu_\mu \end{pmatrix} = (H^{\text{vac}} + H^{\text{mat}}) \begin{pmatrix} \nu_e \\ \nu_\mu \end{pmatrix}, \qquad (1.62)$$

where the vacuum and matter Hamiltonians are given by

$$H^{\text{vac}} = \frac{\Delta m_{21}^2}{4E} \begin{pmatrix} -\cos(2\theta_0) & \sin(2\theta_0) \\ \sin(2\theta_0) & \cos(2\theta_0) \end{pmatrix} \quad \text{and} \quad H^{\text{mat}} = \begin{pmatrix} \sqrt{2} G_F N_e & 0 \\ 0 & 0 \end{pmatrix}, \qquad (1.63)$$

where Δm_{21}^2 is the mass squared difference and θ_0 is the vacuum mixing angle. In eq. (1.62), we changed the time derivative for a spatial derivative because we follow the evolution of relativistic neutrinos and antineutrinos with the distance. From there, we define the matter basis as the basis that instantaneously diagonalizes the Hamiltonian, i.e.

$$\widetilde{K} = \widetilde{U}^\dagger H \widetilde{U} = \begin{pmatrix} \widetilde{k}_1 & 0 \\ 0 & \widetilde{k}_2 \end{pmatrix}, \qquad (1.64)$$

where $\widetilde{k}_i$ are the instantaneous eigenvalues of H. From now on, the tilde means that the matrices, the quantities (eigenvalue, etc.) and the parameters (phases and angles) are those in the matter basis. $\widetilde{U}$ is an unitary matrix that relates the flavor states ν_α and the matter eigenstates $\widetilde{\nu}_i$

$$\begin{pmatrix} \widetilde{\nu}_1 \\ \widetilde{\nu}_2 \end{pmatrix} = \widetilde{U}^\dagger \begin{pmatrix} \nu_e \\ \nu_\mu \end{pmatrix} = \begin{pmatrix} \cos\widetilde{\theta} & -\sin\widetilde{\theta} \\ \sin\widetilde{\theta} & \cos\widetilde{\theta} \end{pmatrix} \begin{pmatrix} \nu_e \\ \nu_\mu \end{pmatrix}. \qquad (1.65)$$

In this unitary matrix, $\widetilde{\theta}$ is the matter (called also effective) mixing angle. Because in the supernovae and solar environments, the electron density is a function of the distance then the matter angle is also a function of the distance $\widetilde{\theta}(r)$. If we rewrite the evolution equation in the flavor basis in terms of the matter basis parameters, we have

$$
\begin{aligned}
\imath \frac{\partial}{\partial x} \begin{pmatrix} \nu_e \\ \nu_\mu \end{pmatrix} &= \widetilde{U}\widetilde{K}\widetilde{U}^\dagger \begin{pmatrix} \nu_e \\ \nu_\mu \end{pmatrix} \\
&= \frac{\delta \widetilde{k}_{12}}{2} \begin{pmatrix} \cos(2\widetilde{\theta}) & -\sin(2\widetilde{\theta}) \\ -\sin(2\widetilde{\theta}) & -\cos(2\widetilde{\theta}) \end{pmatrix} \begin{pmatrix} \nu_e \\ \nu_\mu \end{pmatrix},
\end{aligned}
\tag{1.66}
$$

where $\delta\widetilde{k}_{12} = \widetilde{k}_1 - \widetilde{k}_2$. By comparing the flavor Hamiltonian with the matter basis parameters in eq. (1.66) and the flavor Hamiltonian in eq. (1.62), we obtain the relation

$$
\tan(2\widetilde{\theta}) = \frac{\frac{\Delta m_{21}^2}{2E}\sin(2\theta_0)}{\sqrt{2}G_F N_e - \frac{\Delta m_{21}^2}{2E}\cos(2\theta_0)},
\tag{1.67}
$$

and

$$
\delta\widetilde{k}_{21} = \sqrt{\left(\frac{\Delta m_{21}^2}{2E}\sin(2\theta_0)\right)^2 + \left(\sqrt{2}G_F N_e - \frac{\Delta m_{21}^2}{2E}\cos(2\theta_0)\right)^2}.
\tag{1.68}
$$

For the survival probability, we still have the relation

$$
P(\nu_e \to \nu_e) = 1 - \sin^2(2\widetilde{\theta})\sin^2\left(\frac{\delta\widetilde{k}_{12}}{2}L\right),
\tag{1.69}
$$

where

$$
\sin^2(2\widetilde{\theta}) = \frac{\left(\frac{\Delta m_{21}^2}{2E}\sin(2\theta_0)\right)^2}{\left(\frac{\Delta m_{21}^2}{2E}\sin(2\theta_0)\right)^2 + \left(\sqrt{2}G_F N_e - \frac{\Delta m_{21}^2}{2E}\cos(2\theta_0)\right)^2}.
\tag{1.70}
$$

A maximum mixing corresponds to a matter angle equal to $\pi/4$, i.e. $\tan(2\widetilde{\theta}) \to \infty$. We see with eq. (1.67) that this condition is fulfilled when

$$
\sqrt{2}G_F N_e(r) = \frac{\Delta m_{21}^2}{2E}\cos(2\theta_0).
\tag{1.71}
$$

This condition is called the MSW resonance. A surprising result is that the transition probability can be large even if the vacuum angle is very small. The radius where the condition of eq. (1.71) is fulfilled is called "resonance radius" r_{res}, and is a function of the energy.

We see in the previous equation that the MSW condition in eq. (1.71) is fulfilled for neutrinos only in normal hierarchy where $\Delta m_{21}^2 > 0$, because by convention we use $\theta_0 \in [0, \pi/2]$. In the inverted hierarchy, the MSW condition is not fulfilled for neutrinos but it is the case for antineutrinos since $N_e \to -N_e$.

In addition to the matter angle we also have to look at the "adiabaticity" of the propagation.

1.2.4 Adiabaticity of the propagation

To understand what is the definition of "adiabaticity", let us write the evolution equation of the matter eigenstates

$$\imath\frac{\partial}{\partial x}\begin{pmatrix}\widetilde{\nu}_1\\\widetilde{\nu}_2\end{pmatrix}=\left(\widetilde{K}-\imath\widetilde{U}^\dagger\frac{\partial\widetilde{U}}{\partial x}\right)\begin{pmatrix}\widetilde{\nu}_1\\\widetilde{\nu}_2\end{pmatrix}=\begin{pmatrix}\widetilde{k}_1 & -\imath\dot{\widetilde{\theta}}\\\imath\dot{\widetilde{\theta}} & \widetilde{k}_2\end{pmatrix}\begin{pmatrix}\widetilde{\nu}_1\\\widetilde{\nu}_2\end{pmatrix}, \qquad (1.72)$$

where $\widetilde{K}$ is a diagonal matrix containing the eigenvalues $\widetilde{k}_1$ and $\widetilde{k}_2$, and the second term comes from the fact that the effective mixing angle is a function of the distance and then the mixing matrix $\widetilde{U}$ is also function of the distance. We write $\dot{\widetilde{\theta}}=\partial\widetilde{\theta}/\partial x$ for compactness. In this matter Hamiltonian $\widetilde{H}$, we define the non-adiabaticity parameter [35, 36, 29] to be

$$\Gamma=\frac{2\pi}{\delta\widetilde{k}_{12}}\dot{\widetilde{\theta}}. \qquad (1.73)$$

(Sometimes the inverse parameter is used, namely, the adiabaticity parameter $\gamma=\Gamma^{-1}$.)

We express eq. (1.73) in terms of the explicit potential using eq. (1.67) and we obtain

$$\Gamma=\frac{\pi\frac{\Delta m_{21}^2}{2E}\sin(2\theta_0)}{\delta\widetilde{k}_{21}}\dot{V}_{\text{CC}}. \qquad (1.74)$$

We see in eq. (1.72) that the Hamiltonian $\widetilde{H}$ in the matter basis is not diagonal so the states $\widetilde{\nu}_i$ can mix in their evolution. This effect depends on the size of the off-diagonal terms with respect to the diagonal ones. This gives us two scenarii: adiabatic and non-adiabatic propagation.

1.2.4.1 Adiabatic propagation

The adiabatic approximation corresponds to a density which is slowly changing so $|\Gamma|<1$. In that case, the transitions between matter states are suppressed and these states only acquire a phase because $\widetilde{H}$ is basically diagonal. Let's have a look at the evolution of a ν_e created at time $t=t_i$. Initially, ν_e is a superposition of matter eigenstates

$$\nu(t_i)=\nu_e=\cos\widetilde{\theta}_i\,\widetilde{\nu}_1+\sin\widetilde{\theta}_i\,\widetilde{\nu}_2. \qquad (1.75)$$

At a later time t_f, the neutrino state, in the adiabatic approximation, is

$$\nu(t_f)=\nu_e=\cos\widetilde{\theta}_i\,e^{-\imath\int_{t_i}^{t_f}\widetilde{k}_1(t')\,dt'}\,\widetilde{\nu}_1+\sin\widetilde{\theta}_i\,e^{-\imath\int_{t_i}^{t_f}\widetilde{k}_2(t')\,dt'}\,\widetilde{\nu}_2. \qquad (1.76)$$

Now we take into account that the mixing angle $\widetilde{\theta}$ changes with time and therefore $\widetilde{\theta}_f\neq\widetilde{\theta}_i$ and one obtains the transition probability

$$P(\nu_e\to\nu_\mu)=\frac{1}{2}-\frac{1}{2}\cos(2\widetilde{\theta}_i)\cos(2\widetilde{\theta}_f)-\frac{1}{2}\sin(2\widetilde{\theta}_i)\sin(2\widetilde{\theta}_f)\cos\phi, \qquad (1.77)$$

where

$$\phi=\int_{t_i}^{t_f}\widetilde{k}_{12}(t')\,dt'. \qquad (1.78)$$

At the production point, e.g. in the Sun or in a supernova, far above the MSW resonance i.e. $N_e^i\gg N_e^{\text{res}}$, the mixing angle is $\widetilde{\theta}_i=\pi/2$ and the third

term of eq. (1.77) is strongly suppressed. As the neutrino travel toward lower density regions, the matter angle decreases down to the vacuum value $\widetilde{\theta}_f = \theta_0$ for vanishing matter. On the way, it passes through $\widetilde{\theta} = \pi/4$ at the resonance which corresponds to the maximal mixing. So the transition probability is $P(\nu_e \rightarrow \nu_\mu) = \cos^2 \widetilde{\theta}_f \rightarrow \cos^2 \theta_0$. We remark that for a small vacuum angle, the transition between ν_e and ν_μ is almost complete. This effect is the well known MSW effect.

Figure 1.8 represents a simulation in a supernova environment where the adiabatic approximation is valid. We clearly see that the matter states do not mix (figure (b)) whereas the flavor ones do mix (figure (a)). We also have plotted the mixing angle $\widetilde{\theta}$ in figure (c) and the non-adiabatic parameter in figure (d). We see that the matter mixing angle is equal to $\pi/4$ at the distance where the mixing between ν_e and ν_μ is maximal i.e. $P(\nu_e \rightarrow \nu_e) = 0.5$).
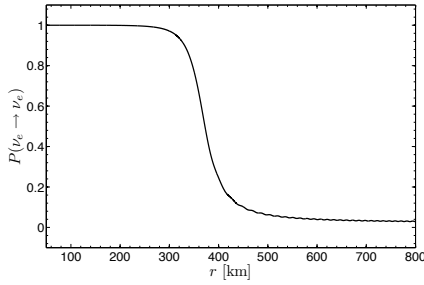
(a) Electron neutrino survival probability as a function of distance.
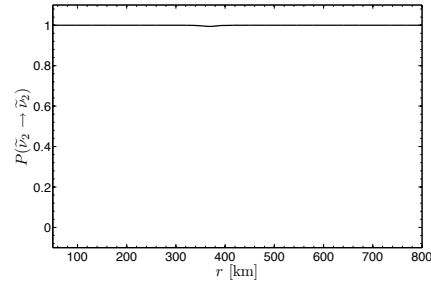
(b) Neutrino survival probability in the matter basis for state 2 ($\nu_e(r=0) \equiv \widetilde{\nu}_2(r=0)$) as a function of distance.
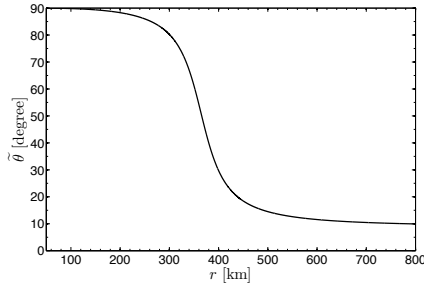
(c) Evolution of the matter angle $\widetilde{\theta}$ as a function of distance.
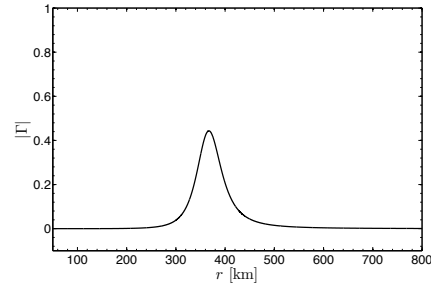
(d) Evolution of the non-adiabaticity parameter Γ as a function of distance.

Figure 1.8 – *Evolution of the survival probability in the flavor basis $P(\nu_e \rightarrow \nu_e)$ and in the matter basis $P(\widetilde{\nu}_2 \rightarrow \widetilde{\nu}_2)$, of the matter angle $\widetilde{\theta}$, and of the non-adiabaticity parameter Γ for a 5 MeV neutrino in an adiabatic propagation case. The numerical results presented have been obtained by using the vacuum oscillation parameters $\Delta m_{21}^2 = 2.4 \times 10^{-3}$ eV^2, $\theta_0 = 9°$, and the matter density profil $\rho_B = 1.5 \times 10^8 (10/x)$ g.cm^{-3} where x is the distance in the supernova in* km *unit.*

1.2.4.2 Non-adiabatic propagation

For a non-adiabatic propagation, the adiabatic approximation is no more valid because the off diagonals terms are comparable or larger than the diagonal ones i.e. $|\Gamma| \gtrsim 1$. So we have to take into account possible transition between $\widetilde{\nu}_1$ and $\widetilde{\nu}_2$. We define these transitions with P^{hop} which is the "hopping probability",

$$P(\nu_e \rightarrow \nu_e)$$
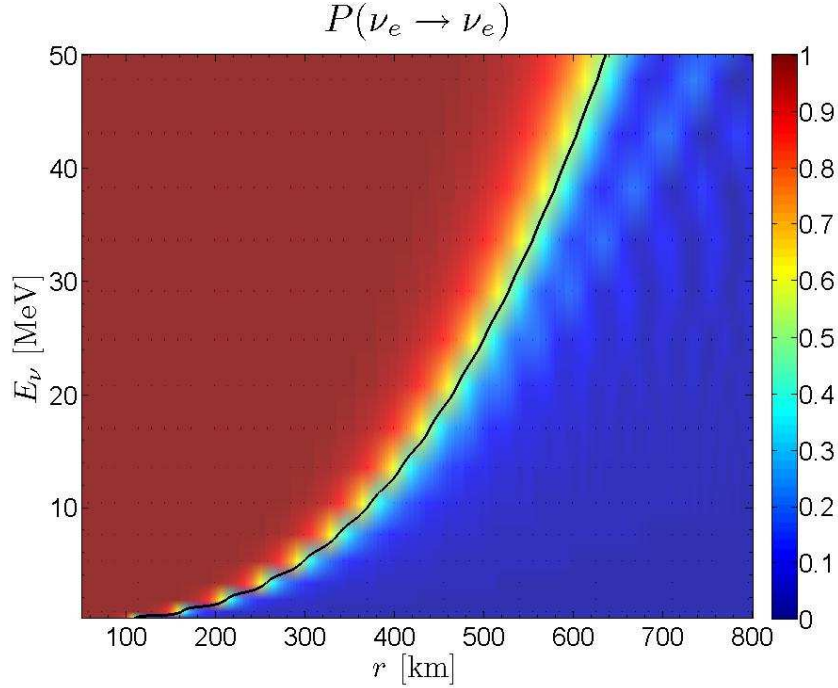
Figure 1.9 – *Contour plot of $P(\nu_e \rightarrow \nu_e)$ in matter in two flavors as a function of distance and energy. The solid black line corresponds to the location where the MSW conditions are fulfilled.*

$P^{\text{hop}} \equiv |\langle \widetilde{\nu}_2(r_+)|\widetilde{\nu}_1(r_-)\rangle|^2$. Here, $r_\pm$ refer to two faraway points on either side of the resonance position. We generalize the previous analysis to include possible transitions. The eq. (1.77) becomes, if we omit the oscillating term which average to zero,

$$
\begin{aligned}
\langle P(\nu_e \rightarrow \nu_\mu)\rangle &= \sum_i P(\nu_e \rightarrow \widetilde{\nu}_i)P(\widetilde{\nu}_i \rightarrow \nu_\mu) \\
&= (0\ 1)\begin{pmatrix} \cos^2\widetilde{\theta}_f & \sin^2\widetilde{\theta}_f \\ \sin^2\widetilde{\theta}_f & \cos^2\widetilde{\theta}_f \end{pmatrix}\begin{pmatrix} 1-P^{\text{hop}} & P^{\text{hop}} \\ P^{\text{hop}} & 1-P^{\text{hop}} \end{pmatrix}\begin{pmatrix} \cos^2\widetilde{\theta}_i & \sin^2\widetilde{\theta}_i \\ \sin^2\widetilde{\theta}_i & \cos^2\widetilde{\theta}_i \end{pmatrix}\begin{pmatrix} 1 \\ 0 \end{pmatrix} \\
&= \frac{1}{2} - \frac{1}{2}\cos(2\widetilde{\theta}_i)\cos(2\widetilde{\theta}_f)(1-2P^{\text{hop}}) \qquad (1.79)
\end{aligned}
$$

where P^{hop} is the "hopping probability". Because non-adiabatic effects are typically relevant only for a narrow range of r around the resonance point, we can use a linear density distribution over this small range [37]. Then the hopping probability is well modeled by the Landau-Zener approximation

$$P^{\text{hop}} \simeq e^{-\frac{\pi}{2}\Gamma_{\text{res}}^{-1}}, \qquad (1.80)$$

where Γ_{res}^{-1} is the non-adiabaticity parameter at the MSW resonance point. The Landau-Zener approximation is appropriate for a linear density change. This is a natural choice because it corresponds to the first term in a Taylor-series expansion about the resonance point.

In the case of a small vacuum mixing angle and $N_e^i \ll N_e^{\text{res}} \ll N_e^f$ (or $N_e^i \gg N_e^{\text{res}} \gg N_e^f$), eq. (1.79) reduces to

$$\langle P(\nu_e \rightarrow \nu_\mu)\rangle \simeq 1 - P^{\text{hop}}. \qquad (1.81)$$

In the adiabatic limit, one has $P^{\text{hop}} \simeq 0$ and we recover an almost complete flavor conversion. In the non-adiabatic limit, one has $P^{\text{hop}} \simeq 1$ and then the transition

probability is small if the vacuum angle is small too. If the vacuum angle is not so small, we can have some matter effects because the hopping probability has the form $P^{\text{hop}} \simeq \cos^2 \theta_0$.

As discussed in [37], for a medium with an arbitrary density profile, one can generalize the expression of the hopping probability

$$P^{\text{hop}} = \frac{e^{-\frac{\pi}{2}\Gamma^{-1}F} - e^{-\frac{\pi}{2}\Gamma^{-1}F/\sin^2\theta_0}}{1 - e^{-\frac{\pi}{2}\Gamma^{-1}F/\sin^2\theta_0}}, \tag{1.82}$$

where F depends on the density profile and the vacuum angle. The function F reduces to 1 for a linear density.

Figure 1.10 represents a simulation where the adiabatic approximation breaks down. We see that the flavor states do not mix (figure (a)) whereas the matter ones do mix (figure (a)). We also have plotted the mixing angle $\widetilde{\theta}$ in figure (c) and the non-adiabatic parameter in figure (d).
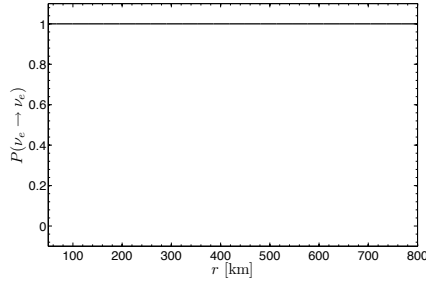
(a) Electron neutrino survival probability as a function of distance.
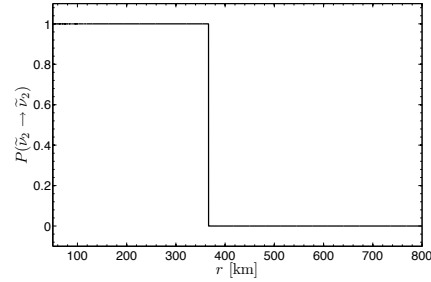
(b) Neutrino survival probability in the matter basis for state 2 ($\nu_e(r=0) \equiv \widetilde{\nu}_2(r=0)$) as a function of distance.
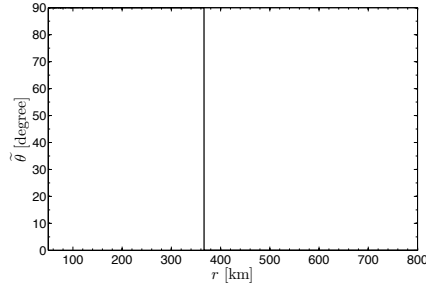
(c) Evolution of the matter angle $\widetilde{\theta}$ as a function of distance.
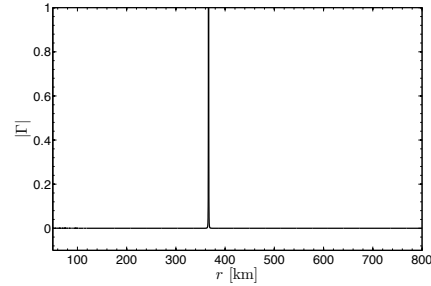
(d) Evolution of the non-adiabaticity parameter Γ as a function of distance.

Figure 1.10 – *Evolution of the survival probability in the flavor basis $P(\nu_e \to \nu_e)$ and in the matter basis $P(\widetilde{\nu}_2 \to \widetilde{\nu}_2)$, of the matter angle $\widetilde{\theta}$, and of the non-adiabaticity parameter Γ for a 5 MeV neutrino in the case of a non-adiabatic propagation. The numerical results presented have been obtained by using the vacuum oscillation parameters $\Delta m_{21}^2 = 2.4 \times 10^{-3}$ eV^2, $\theta_0 = 9°$, and the matter density profil $\rho_B = 1.5 \times 10^8 (10/x)$ g.cm^{-3} where x is the distance in the supernova in km unit.*

1.2.5 The geometric point of view

As explained in appendix B.1, the Schrödinger-like equation can be reexpressed in terms of a gyroscopic equation [38]. We construct the magnetic field **B** in the

flavor basis using the matter angle $\widetilde{\theta}$

$$\mathbf{B} = \delta\widetilde{k}_{21} \begin{pmatrix} \sin(2\widetilde{\theta}) \\ 0 \\ -\cos(2\widetilde{\theta}) \end{pmatrix}. \qquad (1.83)$$

At the beginning of the propagation, we are far away from the resonance region, $N_e \gg N_e^{\mathrm{res}}$, this implies that the matter angle is maximized to $\widetilde{\theta} = \pi/2$. In terms of vector representation, the magnetic field is aligned with z-axis. If we take the initial condition to be an electron neutrino then the neutrino polarization vector is initialized to

$$\mathbf{P} = \begin{pmatrix} 0 \\ 0 \\ 1 \end{pmatrix}. \qquad (1.84)$$

The polarization vector spins around the magnetic field with the angular velocity $\omega_{\mathbf{P}} = |\mathbf{B}| = |\delta\widetilde{k}_{21}|$ but because $\mathbf{B}$ is along the z-axis, $\mathbf{P}$ is stuck along this axis too and $P(\nu_e \to \nu_e) \simeq 1$ (see fig. 1.11 (a)).

As the neutrino propagates the density decreases and the matter angle also. In an adiabatic propagation, the matter angle decreases slowly and the polarization vector follows closely the magnetic field (as represented in fig. 1.11 (b)). The maximal mixing $\widetilde{\theta} = \pi/4$, where the MSW resonance occurs, corresponds to the complete disappearance of the z component of the magnetic field. In that configuration, $\mathbf{P}$ is contained in the (xOy) plane which corresponds in terms of probability to $P(\nu_e \to \nu_e) \simeq 0.5$. After the MSW region, the neutrino continues to propagate and the magnetic field tends to its limit position, the vacuum position, where $\widetilde{\theta} = \theta_0$. If θ_0 is small then $\mathbf{B}$ is very close to the z-axis (negative part) and $\mathbf{P}$, which has followed $\mathbf{B}$, is at the same position so $P(\nu_e \to \nu_e) \simeq 0$. The flavor conversion is then complete. In the case where θ_0 is not so small, then $\mathbf{P}$ is still close to $\mathbf{B}$ but the conversion is partial.

In a non-adiabatic propagation, the scenario is different in the sense that the magnetic field moves too rapidly compared to the angular velocity of the polarization vector, i.e. $|\dot{\widetilde{\theta}}/\delta\widetilde{k}_{21}| > 1$. So $\mathbf{P}$ follows the evolution of $\mathbf{B}$ but because the latter moves rapidly, $\mathbf{P}$ keeps away from $\mathbf{B}$ and the angle between these two vectors increases (as represented in fig. 1.11 (c)). When the magnetic field reaches its vacuum limit, there is a certain angle between $\mathbf{B}$ and $\mathbf{P}$ which depends on the value of Γ. If the amplitude of Γ is large and its width is narrow (as plotted on figure 1.10 d) then it is an extreme violation of the adiabaticity and the electron survival probability is unchanged i.e. $P(\nu_e \to \nu_e) \simeq 1$. Larger the width, smaller the angle between $\mathbf{B}$ and $\mathbf{P}$.

1.3   THE SOLAR EVIDENCE OF NEUTRINO FLAVOR CONVERSION

1.3.1   Solar neutrinos

The sun shines thanks to nuclear fusion via the ^{4}He reaction

$$4\,p + 2\,e \to {}^4\mathrm{He} + 2\nu_e. \qquad (1.85)$$

In absence of oscillations, the ν_e spectrum is shown in fig 1.12 [39]. The spectrum has a complex shape because the reaction chain proceeds in a sequence of steps with 2- and 3-body final states as shown in fig 1.13.

1.3.2 Solar neutrino experiments

1.3.2.1 The Homestake experiment

The first experiment which detected solar neutrinos is the Homestake experiment led by Davis [9, 10], using a radiochemical technique suggested by Pontecorvo. The ν_e's coming from the sun induce the reaction

$$\nu_e + {}^{37}\mathrm{Cl} \rightarrow {}^{37}\mathrm{Ar} + e, \tag{1.86}$$

producing the isotope ${}^{37}\mathrm{Ar}$. The Cl reaction was employed because its energy threshold, $E_{\nu_e} > 0.814$ MeV, is low enough to be sensitive to Boron ν_e.

The measured Cl rate $R^{\mathrm{exp}} = (2.56 \pm 0.23)\,\mathrm{SNU}$ [2] was found to be about 3 times lower than the predicted value $R^{\mathrm{BP00}} = (7.6 \pm 1.3)\,\mathrm{SNU}$ [3], suggesting for the first time the solar neutrino deficit.

1.3.2.2 Gallium experiments

The next radiochemical experiments, SAGE [40] and GALLEX [41] employed the reaction

$$\nu_e + {}^{71}\mathrm{Ga} \rightarrow {}^{71}\mathrm{Ge} + e, \tag{1.87}$$

which has the lowest threshold, $E_{\nu_e} > 0.233$ MeV. Then more than half of the ν_e-induced events are generated by pp neutrinos because the corresponding flux is very large.

The rate measured in Gallium experiments $R^{\mathrm{exp}} = (67.6 \pm 3.7)\,\mathrm{SNU}$ is about 2 times lower than the predicted value $R^{\mathrm{BP00}} = (128 \pm 9)\,\mathrm{SNU}$. So this result also confirm a solar neutrino deficit.

1.3.2.3 Water Čerenkov experiments: Kamiokande and Super-Kamiokande

In these two experiments [42, 43], solar neutrinos are detected via scattering on electrons, so the reaction is

$$\nu_{e,\mu,\tau} + e \rightarrow \nu_{e,\mu,\tau} + e. \tag{1.88}$$

In principle, this type of reaction has zero physical threshold but because of the presence of background coming from ${}^{222}\mathrm{Rn}$ in the water, external γ rays and muon-induced spallation products, they can only use data above the cut $T_e > 5.5$ MeV. This limit implies that Kamiokande and SuperKamiokande are sensitive to the ${}^{8}\mathrm{B}$ and hep components of the solar neutrino flux.

The main difference with other experiments is that the radiochemical experiments could just count neutrinos but not verify if they came from the Sun whereas

---

2. SNU $\equiv 10^{-36}$ interactions per target atom and per second.
3. BP means Bahcall and Pinsonneault, authors of a series of standard solar model.

water Čerenkov experiments could also check the direction of neutrinos because $T_e \gg m_e$. The detected electron keeps the initial direction of the neutrino.

The rate measured in SK $R^{\exp} = (2.35 \pm 0.06)$ SNU is about 2 times lower than the predicted value $R^{BP00} = (5.05 \pm 0.9)$ SNU.

1.3.2.4 The Sudbury Neutrino Observatory experiment

SNO [44] is a real-time heavy water (d_2O) Čerenkov experiment. SNO is the first solar neutrino appearance experiment because it can determine separately ν_e and $\nu_{\mu,\tau}$ fluxes by combining results from the charged-current reaction

$$\nu_e + d \rightarrow p + p + e, \tag{1.89}$$

whose threshold is $E_{\nu_e} > 6.9$ MeV, and from the neutral-current reaction

$$\nu_{e,\mu,\tau} + d \rightarrow \nu_{e,\mu,\tau} + p + n, \tag{1.90}$$

whose threshold is $E_{\nu_e} > 2.2$ MeV, in addition to the elastic reaction of eq. (1.88) which proceeds via both NC and CC.

SNO could statistically discriminate events because neutral-current events produce multiple γ rays and consequently a more isotropic Čerenkov light than the single electron produced in charged-current and elastic scattering events. SNO data imply for the ^8B flux:

$$\begin{aligned} F_{\nu_e} &= 1.59 \pm 0.08(\text{stat}) \pm 0.08(\text{syst})\ 10^6\ \text{cm}^{-2}.\text{s}^{-1}, & (1.91) \\ F_{\nu_{e,\mu,\tau}} &= 5.21 \pm 0.27(\text{stat}) \pm 0.38(\text{syst})\ 10^6\ \text{cm}^{-2}.\text{s}^{-1}. & (1.92) \end{aligned}$$

The total ^8B flux agrees with the value predicted by solar models, while the reduced ν_e flux gives a 5σ evidence for $\nu_e \rightarrow \nu_{\mu,\tau}$ transitions.

1.3.3 Solar neutrino problem

In all solar neutrino experiments, the detected fluxes were lower than the expected ones (calculated with the BP00 model) which suggest a problem in the solar neutrino model as shown on figure 1.14 [45]. Because of the behavior of the matter density profile in the Sun, the solar $\nu_e \leftrightarrow \nu_{\mu,\tau}$ oscillations depend on two oscillation parameters:

$$\Delta m_{\text{Sun}}^2 \equiv \Delta m_{12}^2 \quad \text{and} \quad \theta_{\text{Sun}} \equiv \theta_{12}. \tag{1.93}$$

A decade ago, the available data allowed different possible solutions, e.g. [46]:

1. the small mixing angle (SMA) MSW solution:

$$\Delta m_{\text{Sun}}^2 = (4 - 10) \times 10^{-6}\ \text{eV}^2 \quad \text{and} \quad \sin^2 2\theta_{\text{Sun}} = (2 - 10) \times 10^{-3}, \tag{1.94}$$

2. the large mixing angle (LMA) MSW solution:

$$\Delta m_{\text{Sun}}^2 = (1 - 10) \times 10^{-5}\ \text{eV}^2 \quad \text{and} \quad \sin^2 2\theta_{\text{Sun}} = 0.7 - 0.95, \tag{1.95}$$

3. the vacuum oscillation (VO) solution:

$$\Delta m_{\text{Sun}}^2 = \begin{cases} (4 - 6) \times 10^{-10}\ \text{eV}^2 \\ (6 - 8) \times 10^{-11}\ \text{eV}^2 \end{cases} \quad \text{and} \quad \sin^2 2\theta_{\text{Sun}} = 0.8 - 1.0. \tag{1.96}$$

Among these three solutions, the LMA scenario is the one that can successfully explain the data from both solar neutrinos and reactor antineutrinos as we will see with the reactor experiment KamLAND.

1.3.4 Reactor experiment KamLAND

KamLAND [47] is a Čerenkov scintillator which has been built to detect $\bar{\nu}_e$ emitted by terrestrial reactors using the reaction

$$\bar{\nu}_e + p \rightarrow e^+ + n. \tag{1.97}$$

The detector can see both the positron and the 2.2 MeV γ ray from neutron capture on proton. This experiment only analyzes $\bar{\nu}_e$ events with $E_{\bar{\nu}} > 3.4\,\text{MeV}$ in order to avoid background of $\bar{\nu}_e$ generated by the Earth (geoneutrinos). In presence of oscillations, the $\bar{\nu}_e$ flux can be predicted using the survival probability for antineutrinos

$$P(\bar{\nu}_e \rightarrow \bar{\nu}_e) = 1 - \sin^2 2\theta_{\text{Sun}} \sin^2 \frac{\Delta m_{\text{Sun}}^2 L}{4 E_{\bar{\nu}}}. \tag{1.98}$$

We see that like solar neutrino experiments, the effects of neutrino oscillations of the $\bar{\nu}_e$ flux depend on Δm_{Sun}^2 and θ_{Sun}.

The 2004 data showed 1609 events instead of the 2179 ± 89 signal events expected in absence of oscillations. $\bar{\nu}_e$ disappearance is observed at more than 5σ and with mass-mix parameters consistent with the LMA region. So in combination with the solar neutrino experiments, KamLAND enabled us to remove the degeneracy and to confirm that the LMA explanation is the solution to the solar neutrino deficit problem.

1.3.5 Solar neutrino parameters

We can create a global fit by combining the solar neutrino data and reactor antineutrino data. This fit gives us (see fig. 1.15)

$$\Delta m_{\text{Sun}}^2 = (7.58 \pm 0.21)\,10^{-5}\,\text{eV}^2 \quad \text{and} \quad \tan^2 \theta_{\text{Sun}} = 0.56^{+0.14}_{-0.09}. \tag{1.99}$$

1.4 THE ATMOSPHERIC EVIDENCE

The presence of $\nu_\mu \rightarrow \nu_\tau$ oscillations is named 'atmospheric' because it was established by the SuperKamiokande experiment which studied atmospheric neutrinos. Actually, SuperKamiokande was build to measure the decay of the proton into lighter energetic charged particles. This proton decay would be a proof for the Grand Unified Theories[4].

---

4. The name SuperKamiokande is composed of Kamioka, the location where the experiment is, and NDE which initially means "Nucleon Decay Experiment" and then "Neutrino Detection Experiment".

1.4.1 Where do they come from?

Atmospheric neutrinos are generated by collisions of cosmic rays [5] in the Earth atmosphere. The process to obtain atmospheric neutrino is the following [49]:

1. Cosmic rays hit the nuclei of air in the Earth atmosphere producing mostly pions $\pi^{\pm}$ and some kaons $K^{\pm}$,

2. Charged pions decay promptly and produce muons and muonic neutrinos

$$\pi^+ \rightarrow \mu^+ + \nu_\mu, \quad \pi^- \rightarrow \mu^- + \bar{\nu}_\mu. \tag{1.100}$$

The decay into electrons is suppressed by the ratio m_e^2/m_μ^2. The total flux of ν_μ, $\bar{\nu}_\mu$ is about $0.1/\text{cm}^2\text{s}$ at $E \sim$ GeV. The kaons decay like pions, except that the decay $K \rightarrow \pi + e^+ + \nu_e$ is significant.

3. The muons produced by pion decays could decay into

$$\mu^+ \rightarrow e^+ + \nu_e + \bar{\nu}_\mu, \quad \mu^- \rightarrow e^- + \bar{\nu}_e + \nu_\mu. \tag{1.101}$$

If all muons decay, one would obtain a flux of ν_μ and ν_e in proportion 2 : 1 with comparable energy $\gtrsim$ 100 MeV. However, muons with an energy above few GeV collide with Earth before producing neutrinos and so the flux ratio $\nu_\mu : \nu_e$ is larger than 2.

1.4.2 Super-Kamiokande anomaly

SuperKamiokande [12] detects atmospheric neutrinos through charged-current scattering on nucleons $\nu_l + N \rightarrow l + N'$. The charged lepton l produced in the reaction travels in water giving rise to a Čerenkov ring. Measuring the Čerenkov light, SK reconstructs the energy of the lepton E_l and its direction θ_l. At high energy, the scattered lepton keeps the direction of the neutrino and it is possible to find a relation between the zenith-angle θ_ν and the pathlength L

$$L = \underbrace{\sqrt{h^2 + 2hr_E + r_E^2 \cos^2 \theta_\nu} - r_E|\cos\theta_\nu|}_{\text{in the atmosphere}} + \underbrace{2r_E|\cos\theta_\nu|}_{\text{in the Earth, if } \cos\theta_\nu < 0}, \tag{1.102}$$

where $r_E = 6371$ km is the radius of the Earth and $h \sim (15-20)$ km is the height of the atmosphere i.e. the production layer for neutrinos. The three extreme cases are:

– downward going neutrinos ($\cos\theta_\nu = 1$) travel $L \sim h$,
– horizontal neutrinos ($\cos\theta_\nu = 0$) travel $L \sim \sqrt{2r_E h}$,
– upward going neutrinos ($\cos\theta_\nu = -1$) travel $L = 2r_E$.

To reconstruct the neutrino energy E_ν, the two quantities E_l and θ_l are not sufficient because the direction of the atmospheric neutrinos arriving in the detector is unknown. So pratically, SK group their data into big energy bins according to the topology of the events:

1. Fully contained electron and muon events correspond to the case where the lepton starts and ends inside the detector. These events are divided into
   – sub-GeV events with $E_l \lesssim 1.4$ GeV are produced by neutrinos with an energy of about a GeV,

---

5. composed by H ($\sim$ 82%), He ($\sim$ 12%) and heavier nuclei ($\sim$ 6%)

- multi-GeV events with $E_l \gtrsim 1.4$ GeV are produced by neutrinos with an energy of few GeV.

2. Partially contained muons describe a muon which is scattered inside the detector but escapes from it. Its energy cannot be measured. This class of events is conveniently grouped with the multi-GeV events,

3. Up-going stopping muons are produced in the rock below the detector and stops inside the detector so that its energy cannot be measured.

The SuperKamiokande data are shown in figure 1.16. The "multi-GeV μ + PC" data sample shows that a neutrino anomaly is present. Due to the spherical symmetry of the source, in absence of oscillations, the neutrino rate would be up/down symmetric, i.e. it would depend only on $|\cos\theta|$. The zenith-angle distribution of μ events is clearly asymmetric while e-like events are symmetric. Therefore the data can be interpreted assuming no conversion between ν_e and ν_μ, and an oscillation between ν_μ and ν_τ. We can assume, by neglecting Earth matter corrections,

$$P(\nu_e \rightarrow \nu_e) \simeq 1, \quad P(\nu_e \leftrightarrow \nu_\mu) \simeq 0, \tag{1.103}$$

and

$$P(\nu_\mu \rightarrow \nu_\tau) = 1 - \sin^2 2\theta_{\text{atm}} \sin^2 \frac{\Delta m_{\text{atm}}^2 L}{4E_\nu}. \tag{1.104}$$

Looking at the zenith-angle dependence, we see that the down-ward going neutrinos ($\downarrow$) are unaffected by oscillations while up-ward going neutrinos ($\uparrow$) feel almost averaged oscillations and their flux is reduced by a factor $1 - \frac{1}{2}\sin^2 2\theta_{\text{atm}}$. This must be equal to the up/down ratio $N_\uparrow/N_\downarrow = 0.5 \pm 0.05$, so we obtain $\sin^2 2\theta_{\text{atm}} = 1 \pm 0.1$. The mass squared difference Δm_{atm}^2 can be estimated with the multi-GeV neutrinos which have an energy $E_\nu \sim 3$ GeV. We see on fig. 1.16 b that oscillations begin around the horizontal direction where the path-length is $L \sim 1000$ km. Therefore $\Delta m_{\text{atm}}^2 \sim E_\nu/L \sim 3 \times 10^{-3}\,\text{eV}^2$. In conclusion, SuperKamiokande proved, by looking at the atmospheric neutrinos, that an oscillation occurs between the non-electron flavor neutrinos ν_μ and ν_τ. The parameters that are involved in this transformations completely differ from the solar parameters. Indeed, the ratio of the mass squared differences is $\Delta m_{\text{atm}}^2/\Delta m_{\text{Sun}}^2 \sim 10^2$ and the atmospheric angle θ_{atm} is larger than θ_{Sun} [6].

Historically, the deficit in the ratio between μ-like and e-like events gave the first proof for an atmospheric anomaly. Indeed the overall number of atmospheric ν_e and ν_μ cannot be precisely predicted but their ratio is normally close to 2 in absence of oscillations. The measurement of the double ratio,

$$\frac{(N_\mu/N_e)_{\text{exp}}}{(N_\mu/N_e)_{\text{Monte Carlo}}} \sim 0.65, \tag{1.105}$$

was considered as the main evidence of an oscillation involving μ neutrinos, although one could not distinguish $\nu_\mu \rightarrow \nu_\tau$ from $\nu_\mu \rightarrow \nu_e$ by the ratio alone.

---

6. The specific central value of the atmospheric angle $\theta_{\text{atm}} \simeq 45°$ has led to the construction of a lot of models such as the tribimaximal models which use the theory group.

1.5   THE NEUTRINO MASS HIERARCHY

If we assume that only three flavors exist for neutrinos, we have the relation for the mass squared differences

$$|\Delta m_{31}^2| \simeq |\Delta m_{32}^2| \gg \Delta m_{21}^2. \tag{1.106}$$

The problem with the three mass squared differences, known as the "hierarchy problem", is that the sign of Δm_{32}^2 is still unknown and then we have two possible schemes to order the neutrino masses as shown on figure 1.5. This hierarchy problem is crucial in the supernovae environment because it leads to MSW flavor conversion for supernova neutrinos or antineutrinos depending on $\Delta m_{31}^2 \lessgtr 0$. So, as we will see later in the thesis, neutrinos coming from supernovae could be used to distinguish between these two schemes.

1.6   THE THIRD MIXING ANGLE θ_{13}

In principle both atmospheric and solar data are sensitive to θ_{13} but the dominant bound on θ_{13} is given by the CHOOZ experiment which looked for disappearance of $\bar{\nu}_e$ emitted by nuclear reactors. The $\bar{\nu}_e$ emitted from the two reactors close to the CHOOZ experiment have an energy of few MeV. Because the experiment is located at a distance of 1 km from the reactors, CHOOZ is sensitive to Δm^2 down to 10^{-3} eV^2. This allows to probe all values of Δm^2 consistent with the atmospheric anomaly. The survival probability for an electron antineutrino is

$$P(\bar{\nu}_e \to \bar{\nu}_e) = 1 - \sin^2 2\theta_{13} \, \sin \frac{\Delta m_{23}^2 L}{4E_{\bar{\nu}}} - \cos^4 \theta_{13} \, \sin^2 2\theta_{12} \, \sin \frac{\Delta m_{12}^2 L}{4E_{\bar{\nu}}}. \tag{1.107}$$

In this formula, solar oscillations and Earth matter corrections can be neglected. Taking into account statistical and systematic errors [50], CHOOZ implies either $\Delta m_{atm}^2 < 0.7 \times 10^{-3}$ eV^2 for a maximal θ_{13} or $\sin^2 2\theta_{13} < 0.10$ for large Δm_{atm}^2. If one combines these results with the value of Δm_{atm}^2 obtained in SK and K2K experiments, we can conclude that $\sin^2 2\theta_{13} < 0.10$.

The mixing angle θ_{13} is currently a high-priority topic in the field of neutrino physics with five experiments addressing its measurement. These experiments are the reactor neutrino experiments Daya Bay [51], Double CHOOZ [52], RENO [53] searching for the $\bar{\nu}_e$ disappearance and the accelerator experiments NoνA [54] and T2K [55] looking at the $\nu_\mu \to \nu_e$ or $\bar{\nu}_\mu \to \bar{\nu}_e$ appearance. The latter two experiments are essential to search for the CP violating phase δ and the neutrino mass hierarchy, respectively.

Very recently, new results from the T2K collaboration [56] have changed this limit to $0.03(0.04) < \sin^2 2\theta_{13} < 0.28(0.34)$ for normal (inverted) hierarchy. These results are consistent with a non-zero value of θ_{13} at 90% CL. The non-zero value of θ_{13} has been already pointed out by making a combination of data in the works of Balantekin and Yilmaz [57] and Fogli et al. [58].

1.7   STATE OF ART OF THE NEUTRINO PARAMETERS

In this section, we summarize a complete analysis [31] which is a global neutrino oscillation data analysis within the three-flavor framework. This study

includes the latest results from the MINOS experiment, updating data of SuperKamiokande (SK I+II+III) and reactor data from KamLAND.

For the atmospheric sector (SK I+II+III and MINOS), combining these new data, global constraints are obtained on the atmospheric neutrino oscillation parameters Δm^2_{31} and θ_{23} that are shown on figure 1.17 and listed in table 1.3. This combination of the two experiments allows also an estimation of the third mixing angle θ_{13} as shown on figure 1.18.

The release of new solar data from the second and the third phase of the SK experiment, new data from the reactor experiment KamLAND and the new predictions for the reactor antineutrino fluxes enable us to give a better estimation of the solar parameters $\sin^2 \theta_{12}$ and Δm^2_{21}. This new determination is shown on figure 1.19. Now combining all the data mentioned before, it is possible to estimate a new bound for the value of θ_{13} as shown on figure 1.20.

Finally in table 1.3, the determination of all the neutrino oscillation parameters is summarized.

Oscillation parameters	Best fit $\pm 1\sigma$	2σ	3σ
Δm^2_{21}	$7.64^{+0.19}_{-0.18}$	$7.27 - 8.03$	$7.12 - 8.23$
Δm^2_{31}	2.45 ± 0.09 $- \left(2.34^{+0.10}_{-0.09} \right)$	$2.28 - 2.64$ $-(2.17 - 2.54)$	$2.18 - 2.73$ $-(2.08 - 2.64)$
$\sin^2 \theta_{12}$	0.316 ± 0.016	$0.29 - 0.35$	$0.27 - 0.37$
$\sin^2 \theta_{23}$	0.51 ± 0.06 0.52 ± 0.06	$0.41 - 0.61$ $0.42 - 0.61$	$0.39 - 0.64$
$\sin^2 \theta_{13}$	$0.017^{+0.007}_{-0.009}$ $0.020^{+0.008}_{-0.009}$	≤ 0.031 ≤ 0.036	≤ 0.040 ≤ 0.044

Table 1.3 – *Neutrino oscillation parameters summary. For Δm^2_{31}, $\sin^2 \theta_{23}$ and $\sin^2 \theta_{13}$ the upper (lower) row corresponds to normal (inverted) neutrino mass hierarchy [31].*

CONCLUSION

In this chapter, we have seen that the theoretical idea of Pontecorvo about the neutrino oscillations is realistic. Indeed the atmospheric anomaly observed by SuperKamiokande has proven that the model of vacuum mixing of neutrinos developed by Pontecorvo, Maki, Nakagawa and Sakata is the solution to this atmospheric neutrino anomaly. At the same time, the presence of oscillations between neutrino flavors shows us that neutrinos are not massless particles and so the Standard Model has to be extended to take into account this fact.

The solar anomaly identified by different experiments (SNO, Homestake, etc.) and the measurements of the KamLAND experiment have confirmed that the presence of matter on the way of solar neutrinos to Earth has a significant impact

on the neutrino flavor conversion. This matter induces a flavor conversion visible by a strong disappearance in the electron neutrino flux detected on Earth. This effect is known as the "MSW effect" which is established to be the solution to the solar neutrino problem.

Nowadays, all the terrestrial experiments have allowed physicists to measure the neutrino oscillation parameters such as the mixing angles and the mass squared differences. But in the three flavors scheme, two parameters are not still completely known. The CHOOZ experiment established bounds for the value of θ_{13} allowing this mixing angle to be zero. At the same time, the sign of the mass squared difference Δm_{31}^2 is still unknown which leads to two possible hierarchies for the mass ordering namely normal $\Delta m_{31}^2 > 0$ and inverted $\Delta m_{31}^2 < 0$.
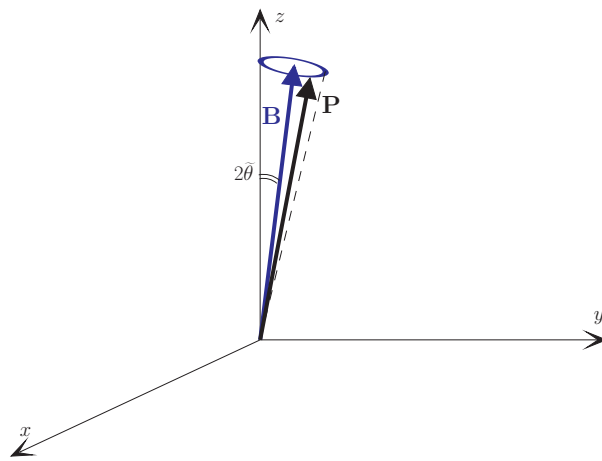
(a) Starting configuration.
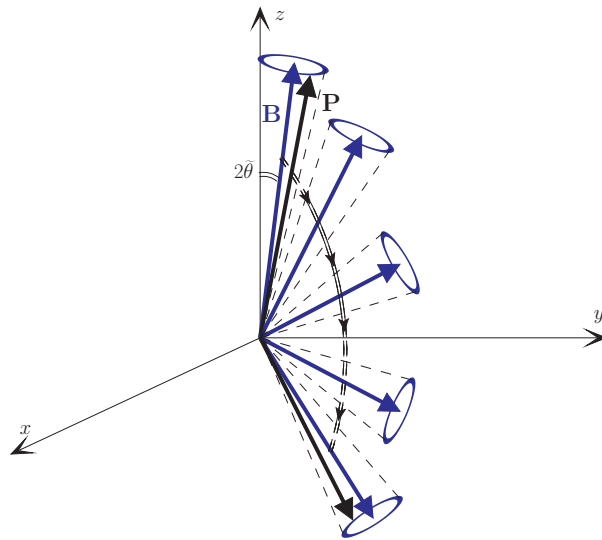
(b) Evolution in an adiabatic case.
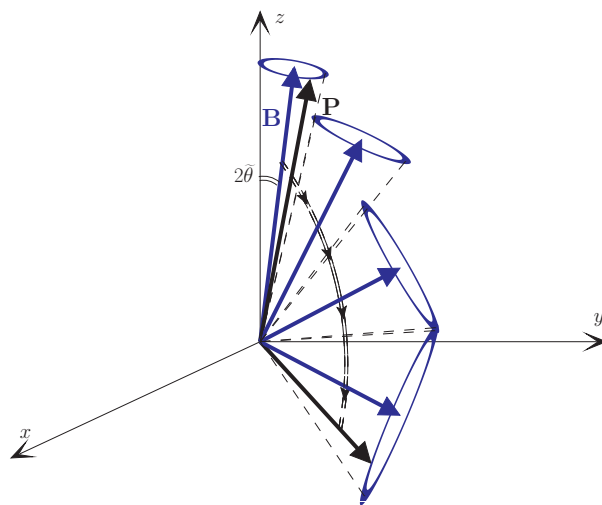
(c) Evolution in a non-adiabatic case.

Figure 1.11 – *Evolution of the polarization vector around a magnetic field in the flavor basis in the region where the MSW resonance occurs. Every neutrino starts in (a) and finishes in (b) for an adiabatic propagation or in (c) for a non-adiabatic propagation.*
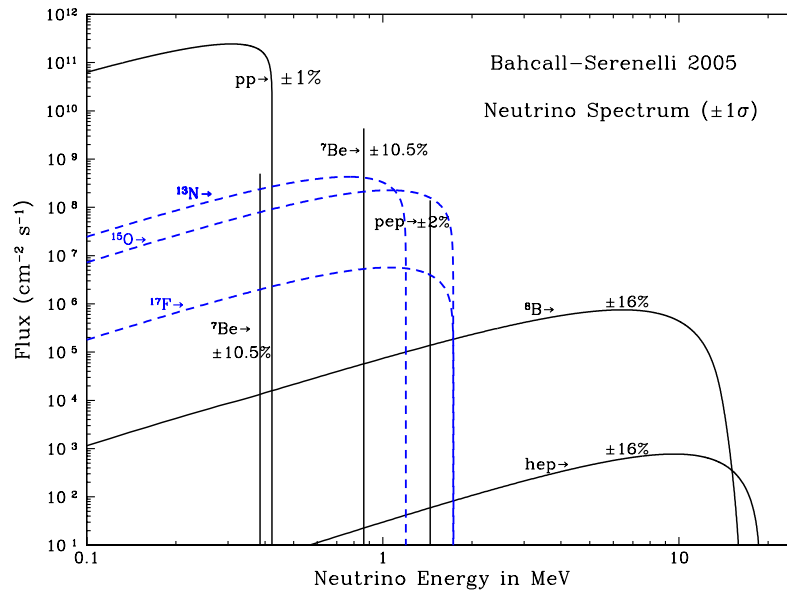
Figure 1.12 – *Expected electron neutrino spectrum emitted from the Sun by various processes according to Bahcall and Serenelli model [39].*
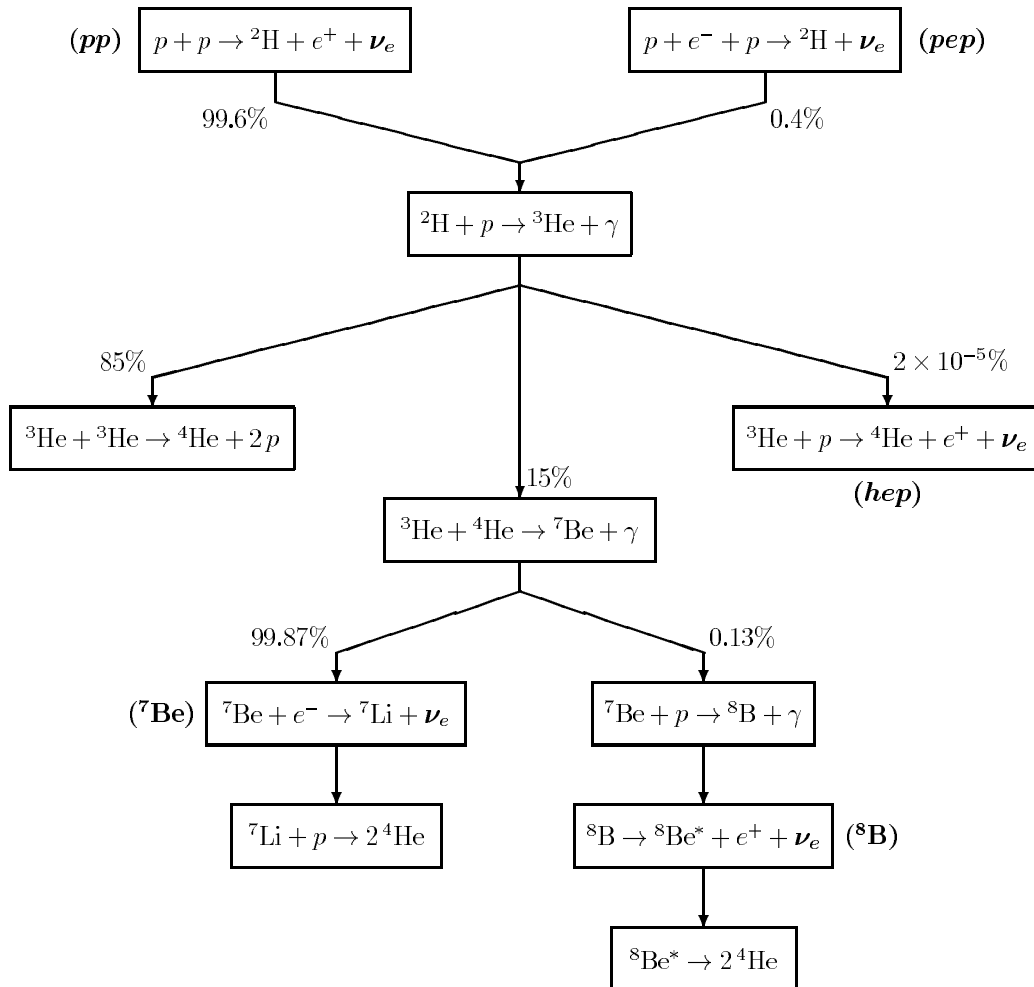
Figure 1.13 – *The $4\,p + 2\,e \rightarrow {}^4He + 2\nu_e$ chain producing the solar neutrino fluxes shown in figure 1.12.*
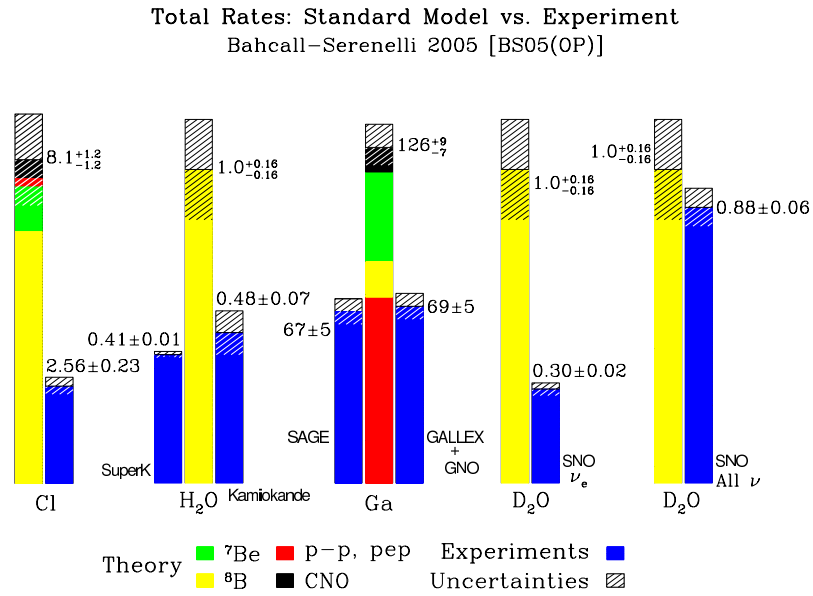
Figure 1.14 – *Comparison between the prediction of the model BS05 for the solar neutrino rates and the measurement in detectors [45].*
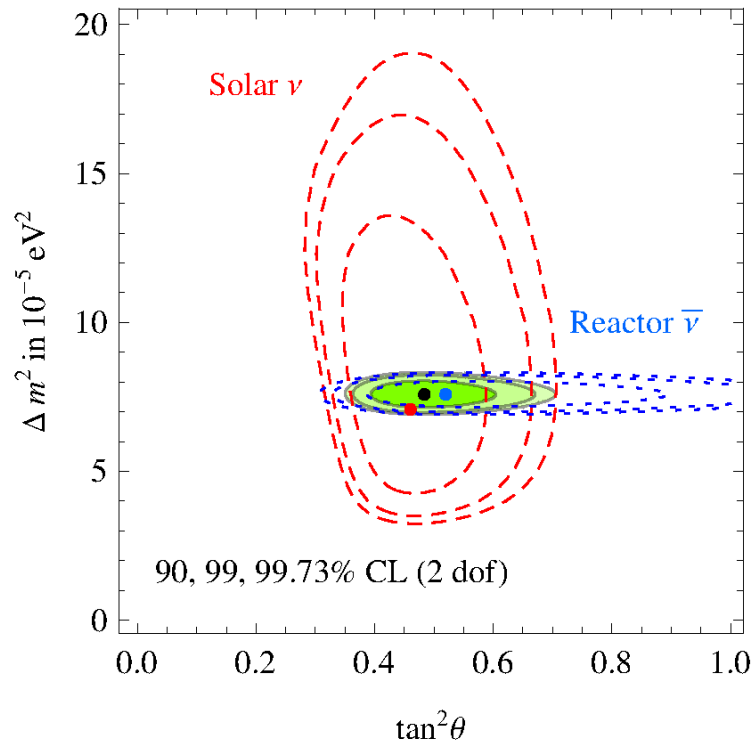
Figure 1.15 – *Best-fit regions at 90, 99 and 99.73% CL obtained fitting solar ν data (red dashed contours), reactor ν̄ data (blue dotted contours) and all data (shaded region). Dots indicate the best fit points [48].*
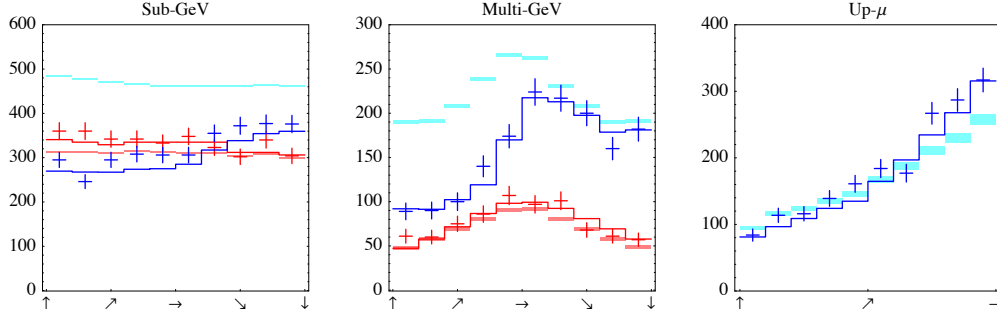
Figure 1.16 – *Main SK data: number of $e^{\pm}$ (red) and of $\mu^{\pm}$ (blue) events as a function of direction of scattered lepton. The horizontal axis is $\cos\theta$ ranging between -1 (up-going events) and $+1$ (down-going events). The crosses are the data and their errors, the thin lines are the best-fit oscillation expectation, and the thick lines are the no-oscillation expectation. Data in the multi-GeV muon samples are very asymmetric while data in the electron samples (in red) are compatible with no oscillations [48].*
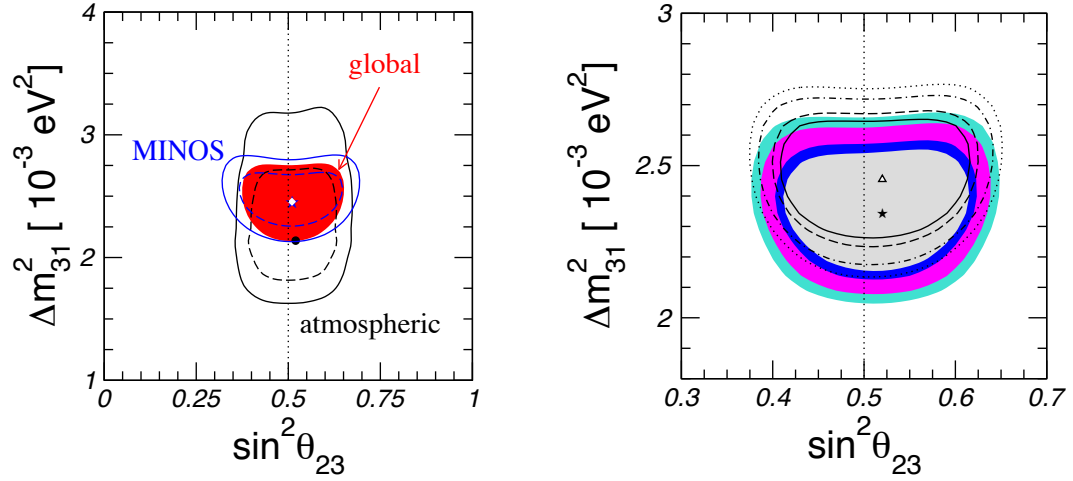
(a) Interplay of atmospheric (black) and MINOS (blue) data and the combination (red/shaded region) for normal hierarchy at 90% CL (dashed) and 3σ (solid) [31].

(b) Combined allowed regions for normal (black curves) and inverted hierarchy (colored regions) at 90%, 95%, 99%, 99.73% CL [31].

Figure 1.17 – *Determination of the atmospheric oscillation parameters.*
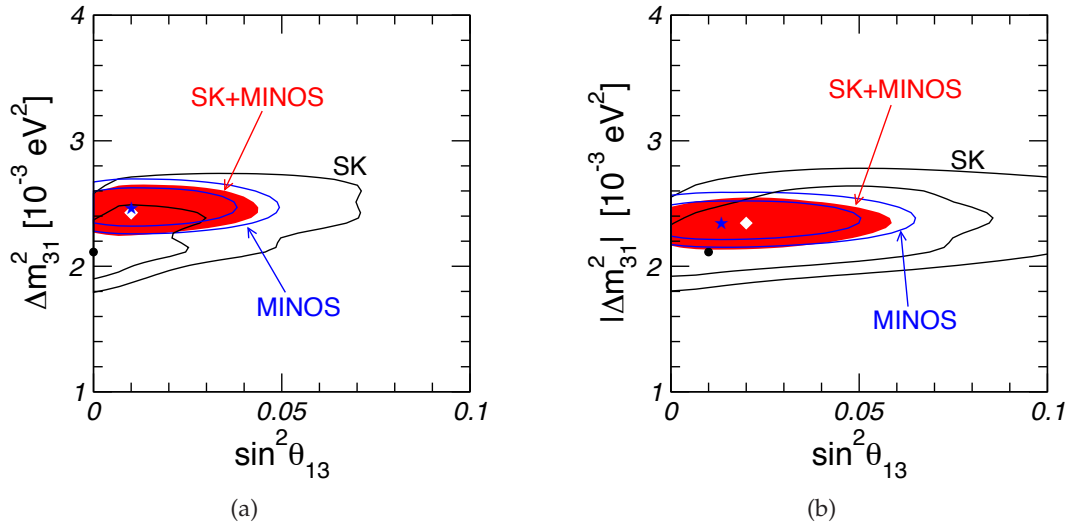
Figure 1.18 – *Allowed regions at 1σ and 90% CL in the plane of $\sin^2\theta_{13}$ and Δm^2_{31} for NH (left) and IH (right). Combined data is shown as shaded/red region at 90% CL. The black dot, blue star, white diamond correspond to the best fit points of SK, MINOS, SK+MINOS, respectively [31].*
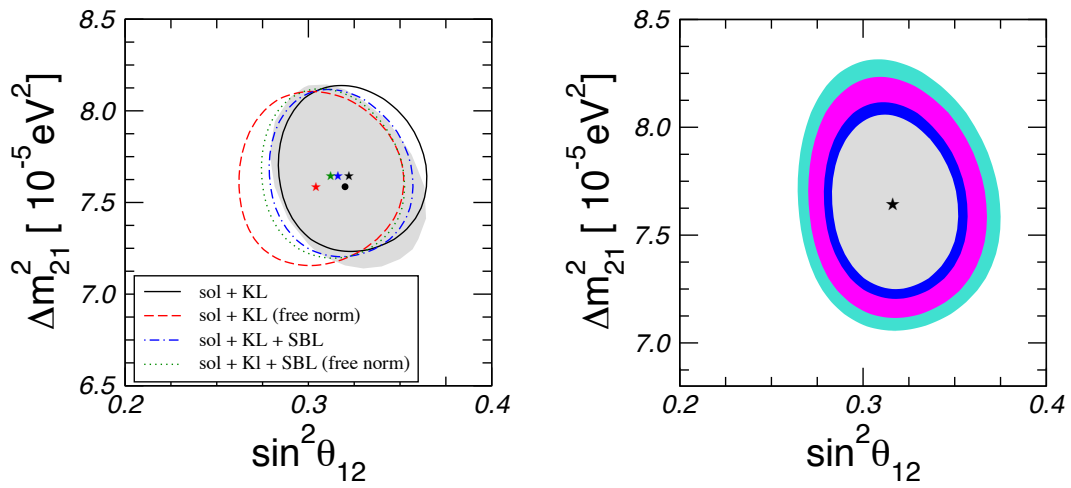
(a) 2σ allowed regions in the $\sin^2\theta_{12} - \Delta m^2_{21}$ plane form the analysis of solar + KamLAND data minimizing over θ_{13}. The different curves show the results obtained using different assumptions for reactor data, as indicated in the legend. For comparison we show as grey-shaded area the region obtained in the previous solar + KamLAND data analysis [31].

(b) Region allowed at 90%, 95%, 99%, 99.73% CL in the recommended analysis of solar + KamLAND data including SBL reactor results [31].

Figure 1.19 – *2σ allowed regions from the solar + KamLAND neutrino data.*

(a) Normal Hierarchy.

(b) Inverted Hierarchy.
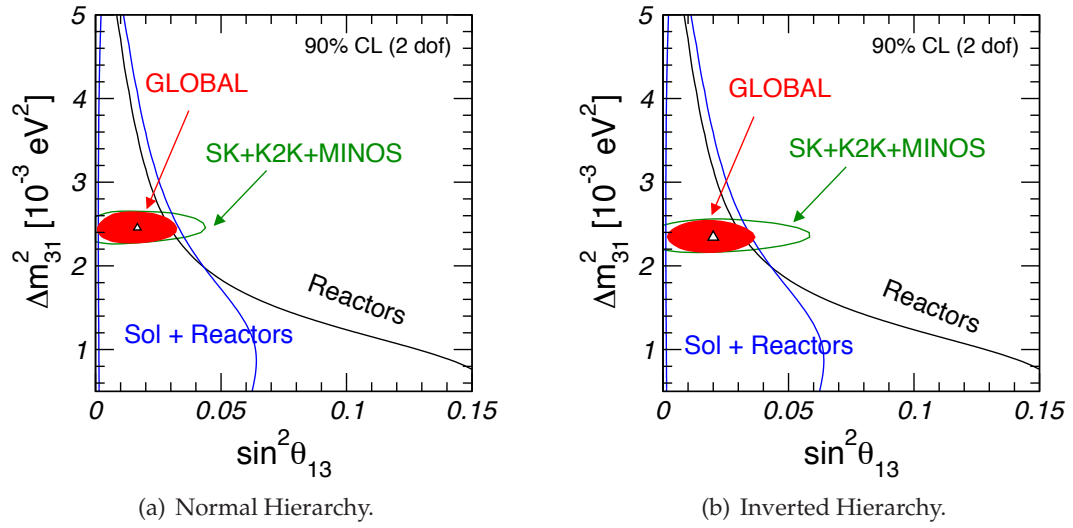
Figure 1.20 – *Illustration of the interplay of the global data on the* $\sin^2 \theta_{13}$ *bound [31].*

NEUTRINO PROPAGATION IN CORE-COLLAPSE SUPERNOVAE

2

CONTENTS

$\mathcal{T}$HE main topic of this thesis is the study of the neutrino propagation in the environment of core-collapse supernovae. In this chapter, we first describe in section 2.1 the composition and the evolution of the stars which lead to core-collapse supernovae. Actually, during the different burning stages which occur in the star compression, electron neutrinos are created and emitted because of electron capture. The star explosion and the birth of the proto-neutron star continue to emit neutrinos and antineutrinos through others reactions like positron capture and electron-positron annihilation. Then we explain the supernova dynamics which enables the emission of neutrinos and antineutrinos of all flavors during four phases (collapse, neutronization burst, accretion and cooling of the

proto-neutron star) and we show the parametrization of the neutrino spectra, namely the Fermi-Dirac distribution, and of the matter density profile that we used in the three works done in this thesis. Finally, we make a comment on the cross sections $\sigma_{\bar{\nu}_e p}$ and $\sigma_{\nu_e n}$ used for the calculation of the electron fraction Y_e [59]. The electron fraction is related to the possibility that the nucleosynthesis occurs inside supernovae [60, 61, 62, 63, 64]. Indeed, the nucleosynthesis is the formation of the nuclei heavier than iron and supernovae, through the rapid neutron-capture process (r-process), can be a possible location. Here we point out the fact that if one wants to look for neutrino oscillation effects upon Y_e, one should already pay attention to the approximation used for the cross sections [65] because it has a non negligible impact on the electron fraction.

After, we present in the section 2.2 three next-generation observatories [23] that are considered in the LAGUNA [1] design study: MEMPHYS [66], LENA [67] and Glacier [68]. The aims of these experiments is to search for:
  – the proton decay to directly test physics at GUT scale,
  – the unknown third mixing angle θ_{13} and the CP violating phase δ to provide an explanation of the matter-antimatter asymmetry in the Universe,
  – neutrinos from astrophysical objects as well as from the Early Universe to give us information on processes happening in the Universe such as the mechanisms driving the explosion of stars.

Thereafter, in section 2.3, we apply the MSW resonance to three flavors because in the supernova environment the matter density profile allows to have two resonances (High and Low) related to the mixing angles θ_{12} and θ_{13}. We will show that actually these resonances can be modeled by two independent resonances in a two flavors scenario. This spatial independence, i.e. without interference, is called the factorization of the MSW resonances. Next we study a case in section 2.4 where the factorization is impossible, the one of the neutrino propagation in supernova in presence of the shock waves. This shock engendered by the rebounce of the collapse on the iron core present inside the star creates multiple H-resonances which cannot be modeled by the factorization approximation due to their nearness. We first describe how the shock waves affect the matter density profile (forward and reverse shocks [20]) and the consequences of the H-resonances, namely the phase effects [21].

Finally, in section 2.5, we present a new feature which exists in supernovae environment: the neutrino self-interaction. The complexity and the richness engendered by this new interaction has led to a vast literature on the topic [69, 70, 71, 13, 72, 14, 15, 16, 17, 73, 74, 75, 76, 77, 18, 19, 78, 79, 16, 80, 81, 82, 83, 84, 85, 24, 25, 26, 86, 87, 88, 89, 90, 91]. At the emission, the neutrino and antineutrino densities are so high that the interactions of neutrino with themselves engender effects which are dominant in the first 200 km of the propagation. This neutrino self-interaction makes the oscillation equations non-linear and leads to surprising collective phenomena in the environment of core-collapse supernovae. The main new aspects are the multi-angle and multi-energy effects on the neutrino propagation. We first calculate the effective neutrino self-interaction Hamiltonian in the mean field approximation and include it in the Schrödinger-like equation following the bulb model of [19]. After, we present a well known approximation used for the

---

1. Large Apparatus studying Grand Unification and Neutrino Astrophysics.

neutrino propagation: the single-angle approximation. This approximation corresponds to an angular independence of the neutrinos and is less demanding numerically while keeping the main features of the multi-angle neutrino self-interaction Hamiltonian. Finally, we present three main regimes in the electron neutrino and antineutrino survival probabilities which are: the synchronization region, the bipolar oscillations and the spectra split phenomenon.

2.1 DESCRIPTION OF A SUPERNOVA

2.1.1 Supernova types

Supernovae (SN) are divided in two types (type I and II) depending on the presence of hydrogen lines in their spectra [92]. The type SNI does not show hydrogen lines whereas SNII does. Also SNIa ends with a thermonuclear explosion, while SNIb, Ic and II that end with a core-collapse explosion.

When a supernova of type Ia explodes, the total energy released is approximatively 3×10^{51} erg. Roughly 1% of this energy is carried by neutrinos, which thus do not play a crucial role in the supernova dynamics. Considering the core-collapse explosion, we can separate SNIb, SNIc and SNII. Due to their affiliation to type I, SNIb-c do not show hydrogen lines and silicon lines. SNIb present helium lines while SNIc do not. The differences in the supernova spectra is a consequence of the loss of different envelope layers during their evolution. SNIb ejects the hydrogen layer and SNIc also loses its helium layer. The common point of SNIb-c and SNII is that they are the result of the same explosion mechanism coming from the death of a massive star with $M \gtrsim 8M_\odot$. For this kind of supernova, the total energy released is about 10^{53} erg. Neutrinos carry approximatively 99% of this energy (the rest is released as kinetic energy and as light) so they can play an important role in the explosion process.

Detecting supernova neutrinos is important because:
– neutrinos emerge from the deepest regions of the star, being only sensitive to weak interaction. They are so the only probe of the inner layers of the star and can shed light on the explosion mechanism.
– neutrinos escape quickly from the star after collapse, while photons remain trapped in the envelope due to their electromagnetic interaction, and escape later. Therefore neutrinos are the first signal of supernovae explosion.
– neutrino oscillations in core-collapse supernovae are another way to probe oscillation parameters and possibly to distinguish between the two possible hierarchies (normal and inverted) by detecting neutrino fluxes on Earth.

2.1.2 Core-collapse dynamics

Evolution of the progenitor star

During the life of the star, two forces are always in competition: the gravitational force and the thermal pressure. The gravitational force tends to collapse the star and the thermal pressure produced by nuclear fusion tends to expand it. The hydrogen initially present in the star merge to form helium. When there is no more hydrogen, the gravitational force becomes stronger and starts to contract the star. Consequently, the density and the temperature increase which allows the helium to burn via nuclear fusion. This process stabilize the collapse. This mechanism repeats itself, producing carbon, neon, oxygen and silicon. Because it is harder and harder to start each new fusion, the combustion lasts less and less time as the fuel becomes heavier (see table 2.1 for details).

When the stage of iron is reached, then its ignition will never occur because iron is the nucleus with the largest binding energy. At this moment, the star has an

Stage	Time scale	Fuel	Product	Central T (10^9 K)	Central ρ (g/cm^3)	L (s.u.)	Neutrino losses (s.u.)
H	11 My	H	He	0.035	5.8	28000	1800
He	2 My	He	C, O	0.18	1390	44000	1900
C	2000 y	Ne	Ne, Mg	0.81	2.8×10^7	72000	3.7×10^5
Ne	0.7 y	Ne	O, Mg	1.6	1.2×10^7	75000	1.4×10^8
O	2.6 y	O, Mg	Si, S, Ar, Ca	1.9	8.8×10^6	75000	9.1×10^8
Si	18 d	Si, S, Ar, Ca	Fe, Ni, Cr, Ti,...	3.3	4.8×10^7	75000	1.3×10^{11}
Fe	~ 1 s	Fe, Ni, Cr, Ti,...	Neutron star	> 7.1	$> 7.3 \times 10^9$	75000	$> 3.6 \times 10^{15}$

Table 2.1 – *Evolution of a 15 $M_\odot$ star [93]. "s.u." stands for solar units, luminosity are normalized to the ones of the Sun $L_\odot = 3.839 \times 10^{33}$ erg/s and neutrino losses are normalized to emission of the Sun which is 2×10^{38} neutrinos per second.*

onion-shell structure as shown in figure 2.1. More precisely, stars with $M > 11\,M_\odot$ have a core mainly composed of iron and nickel whereas the stars with a mass in the range $[8, 11]\,M_\odot$ have an oxygen-neon-magnesium core. Then the future of the star is guided by the iron core mass compared to the Chandrasekhar limit. Stars with an iron core mass lower than this limit end with a white dwarf where the electron degeneracy pressure stabilizes the collapse. For stars with $M > M_{\rm Ch} \simeq 1.2 - 1.5 M_\odot$, the electron pressure cannot compensate the gravitational force and the star finishes in a neutron star or a black hole.
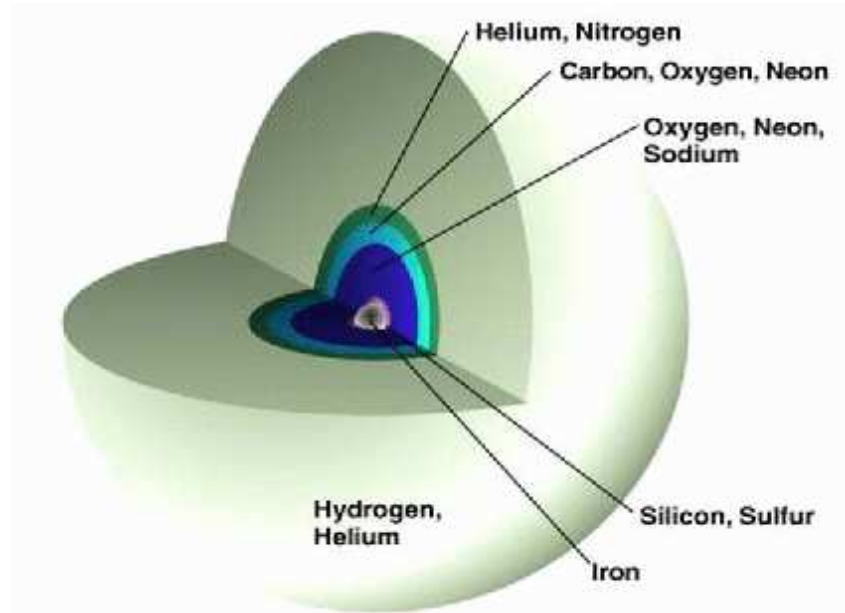
Figure 2.1 – *Schematic picture of the onion-shell structure.*

Stellar collapse

At the end of the burning stages, the heart of the star is an iron white dwarf with a mass roughly equal to 1.5 $M_\odot$, a central density $\rho \sim 3.7 \times 10^7$ g.cm^{-3}, a central temperature $T \sim 0.69$ MeV and a ratio of electron per baryon (electron fraction) of $Y_e \simeq 0.42$. At this step, the electron degeneracy pressure can no longer compensate

the gravitational force, because of the stability of the iron, and the star starts to collapse. Due to this compression, the density and the temperature rise, leading to new processes. Most of these reactions bring into play electrons so they participate to the acceleration of the collapse of the star. The two main processes are:

1. *Electron capture:* electrons that are present in the star are captured by heavy elements to produce lighter elements and electron neutrinos.

$$e^- + (Z, A) \rightarrow \nu_e + (Z - 1, A). \tag{2.1}$$
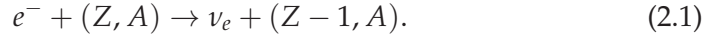
As we see in eq. (2.1), this reaction will also produce electron neutrinos and so it is one of the causes of the energy loss carried by neutrinos.

2. *Nuclei photodissociation:* the high temperature reached due to the collapse induces a photodissociation of the iron core which is an important source of energy loss. The reaction is an absorption of high energy photons by iron nuclei to give helium and neutrons.

$$^{58}\text{Fe} + \gamma \rightarrow 13\,^4\text{He} + 4n - 124.4\,\text{MeV}. \tag{2.2}$$
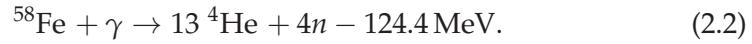
This reaction also consumes about 124.4 MeV of energy which reduces the electron pressure because this energy is taken from them.

Neutrino-sphere

Due to the loss of energy induced by the processes cited previously, the density of the star continues to increase. At some point, the density will be so high (about 10^{12} g.cm^{-3}) that the environment will become opaque to neutrinos and they will be trapped in some layers. The main source of the opacity is neutral-current interaction of neutrinos with heavy elements. In opposition to the beginning of the collapse where they were immediately emitted, they have to interact several times before being able to escape the core freely. This diffusion time creates an effective confinement of neutrinos around the core. The outer surface of this effective region is called the "neutrino-sphere" and its radius is noted as R_ν. A good approximation is to consider the volume inside the neutrino-sphere opaque to neutrinos and the outside transparent. This approximation of a sharp neutrino-sphere will be used in our calculations in chapters 3 and 4.

Core bounce and shock wave

Due to the reduction of the electron degeneracy pressure, the star continues to collapse. We can then consider that the core is composed of two parts: the inner core which collapse subsonically and the outer core which collapse supersonically. The collapse still infer the growth of the density in the inner core. At the moment where the nuclear matter density is reached ($\rho \sim 2 \times 10^{14}$ g.cm^{-3}), the inner core is transformed into a macroscopic state of nuclear matter. The repulsion of nucleons makes the inner core incompressible and causes a rise in pressure and a rebound. The sound waves created by the rebound are trapped by the infall of the outer core and then are accumulated until the sonic point is reached. This accumulation generates a discontinuity in the flow (density, pressure,...) i.e. a shock wave which propagates into the outer regions of the star.

Deleptonization and cooling

The propagation of the shock wave into the outer regions of the star dissociates nuclei into free nucleons. As the cross section of electron on protons is larger than the one on nuclei, a large amount of ν_e are created through the inverse beta decay reaction (neutronization)

$$e^- + p \to n + \nu_e. \tag{2.3}$$

Because these electron neutrinos are produced by the passing of the shock wave, the emission is restricted to a short moment ($\lesssim 1\,\mathrm{s}$) where the production is huge. This rise of the emission, luminosity goes up to $10^{54}\,\mathrm{erg.s}^{-1}$, is called the "neutronization burst" or "the prompt neutrino brust" (see fig. 2.2).

At this point, the shock wave has left behind it a proto-neutron star (PNS) which will turn later into a neutron star or a black hole. The PNS is composed of a cold inner part below the region where the shock was formed and a hotter mantle composed by shocked nuclear elements. In this mantle, electrons are not quite degenerate and some positrons can be created. These positrons will engender two new reactions that produce neutrinos and antineutrinos of all flavors

$$e^+ + n \to \bar{\nu}_e + p \quad \text{and} \quad e^+ + e^- \to \nu_\alpha + \bar{\nu}_\alpha. \tag{2.4}$$

Also an accretion takes place around the PNS. The gravitational energy released will also produce thermal neutrinos. This phase lasts approximatively 1 s (see fig. 2.2). In the accretion and cooling phase of the mantle, there is an equipartition of the emitted luminosity of all flavors. The average luminosity per flavor is about $L \sim 10^{52}\,\mathrm{erg.s}^{-1}$.

At the Kelvin-Helmhotz cooling phase, the PNS evolves to a cold and deleptonized neutron star. This cooling stage of the PNS is the last phase of neutrino emission. This step is characterized by an exponential decrease of the luminosity but still an equipartition of it.
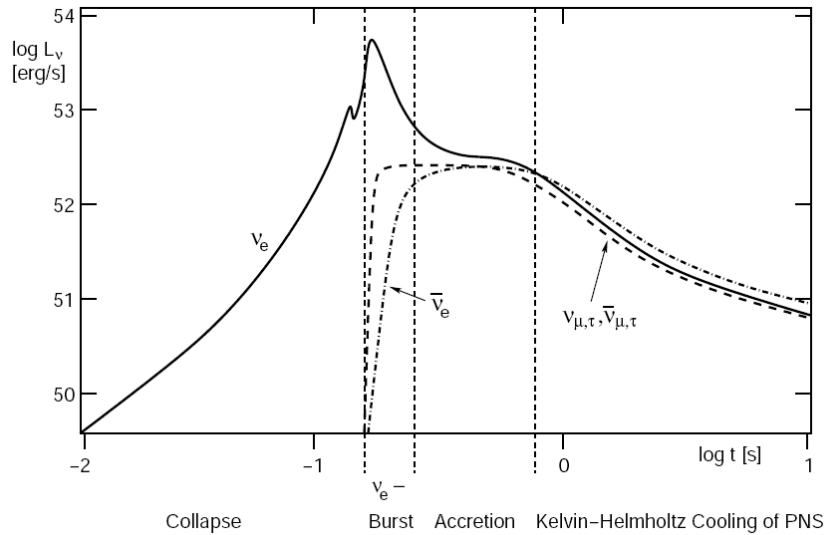
Figure 2.2 – *Neutrino luminosity for different emission phases [94].*

2.1.3 Neutrino spectra

The energy released by the collapse is given by the gravitational binding energy of the compact star before and after the compactification. In a Newtonian description, one obtains

$$\Delta E = \left(-\frac{G_N M^2}{R}\right)_{\text{star}} - \left(-\frac{G_N M^2}{R}\right)_{\text{NS}}, \tag{2.5}$$

where G_N is the gravitational constant, M the mass of the object (star or NS) and R the radius of the considered object. Considering that the difference of the radii is $R_{\text{star}} \sim 10^{10}$ cm $\gg R_{\text{NS}} \sim 10^6$ cm and of the mass is $M_{\text{star}} \sim 10 \times M_{\text{NS}}$, we can omit the first term of eq. (2.5) and one finds

$$\Delta E = 5.2 \times 10^{53} \,\text{erg} \left(\frac{10\,\text{km}}{R_{\text{NS}}}\right) \left(\frac{M_{\text{NS}}}{1.4\,M_\odot}\right)^2. \tag{2.6}$$

For a neutron star with a radius of 10 km and a mass of 1.4 $M_\odot$, one obtains $\Delta E = 5.2 \times 10^{53}$ erg. Because 99% of the energy is released by neutrinos, the total luminosity available for neutrinos and antineutrinos of all flavors is approximatively $L \sim 6 \times 10^{52}$ erg.s^{-1} during 10 s. We assume an equipartition of this energy among all the neutrino and antineutrino flavors so we have 6 degrees of freedom. As we have seen before, all the neutrinos are trapped inside the neutrino-sphere. The PNS, inside the neutrino-sphere, is maintained by its thermal pressure as long as the matter near its surface is not degenerate. Using the virial theorem, because we have a lot of particles in interaction, we have a relation between the mean kinetic energy of a typical nucleon near the PNS surface and the potential gravitational energy

$$2\langle E_{\text{kin}}\rangle + \langle E_G\rangle = 0 \quad \Rightarrow \langle E_{\text{kin}}\rangle = -\frac{1}{2}\langle E_G\rangle \simeq \frac{1}{2} G_N \frac{M m_N}{R}. \tag{2.7}$$

This equation gives us a typical value for the temperature of the order of 10 MeV. This temperature will therefore characterize the temperature of the neutrinos released.

The different processes which take place during the cooling phase thermalize the neutrinos when they will be emitted from the neutrino-sphere. Due to the existence of different interaction depending on the flavor of neutrinos, they are not emitted with the same temperature. Concerning electronic flavor, neutrinos and antineutrinos are trapped inside the neutrino-sphere mainly because of β reactions: neutron capture for ν_e and proton capture for $\bar{\nu}_e$. In addition, since the PNS will become a neutron star, there are more neutrons than protons inside the core and this difference will increase with time. Therefore, electron neutrinos have a higher absorption rate than electron antineutrinos and they are trapped longer which means a larger radius for their neutrino-sphere. There is an inverse relation between the neutrino-sphere radius and the temperature of neutrinos. A larger radius corresponds to a lower temperature, so ν_e will always have a lower average energy than $\bar{\nu}_e$. For the muon and tau flavors, the scheme is a bit more complex. ν_x neutrinos do not experience charged-current interactions because of the absence of μ and τ in the medium. But they will have a lot of neutral-current interactions during their propagation. Following the terminology of [95], before the number sphere, non-electron neutrinos are kept in thermal equilibrium by the following pair processes:
  – bremsstrahlung: $N + N \leftrightarrow N + N + \nu + \bar{\nu}$,
  – neutrino annihilation: $\nu_e + \bar{\nu}_e \leftrightarrow \nu + \bar{\nu}$,

– electron-positron annihilation: $e^+ + e^- \leftrightarrow \nu + \bar{\nu}$.

From this distance, ν_x's are no longer in thermal equilibrium but they are still exchanging energy with the medium via scatterings on nuclei $N + \nu \rightarrow N + \nu$ and leptons $e^\pm + \nu \rightarrow e^\pm + \nu$. These two reactions are very different because the cross section with nuclei is much larger than the one with $e^\pm$, and there are more nucleons in the medium, but at the same time the energy exchanged with $e^\pm$ is much larger than the recoil of nucleons. The radius where the scatterings with electrons and positrons stop is called the energy-sphere. After this sphere, ν_x's only interact with nucleons, exchanging little energy in their reactions. This last scatterings define the transport-sphere where non-electron neutrinos can stream freely. The average energy of ν_x emerging the star is found to be larger than the one of $\bar{\nu}_e$.

All these reactions and scatterings imply a hierarchy of the average energies which is

$$\langle E_{\nu_e} \rangle < \langle E_{\bar{\nu}_e} \rangle < \langle E_{\nu_x} \rangle. \tag{2.8}$$

The typical values obtained in numerical simulations are

$$\langle E_{\nu_e} \rangle \approx 10 - 12\,\text{MeV}, \quad \langle E_{\bar{\nu}_e} \rangle \approx 15 - 18\,\text{MeV}, \quad \langle E_{\nu_x} \rangle \approx 18 - 24\,\text{MeV}. \tag{2.9}$$

Neutrinos emitted at their neutrino-sphere are almost in thermal equilibrium, so we can assume that their initial flux F_ν^0 follow a Fermi-Dirac distribution (see figure 2.3) defined as

$$F_\nu^0(E_\nu) = \frac{L_\nu^0}{T_\nu^4 F_3(\eta_\nu)} \frac{E_\nu^2}{1 + e^{E_\nu/T_\nu - \eta_\nu}}, \tag{2.10}$$

where L_ν^0 is the initial luminosity, E_ν is the neutrino energy, T_ν is its temperature and η_ν is an effective degeneracy parameter or chemical potential. The functions $F_n(\eta_\nu)$ are the Fermi integral (without the Γ function normalization)

$$F_n(\eta_\nu) = \int_0^\infty \frac{x^n}{1 + e^{x - \eta_\nu}}\, dx. \tag{2.11}$$
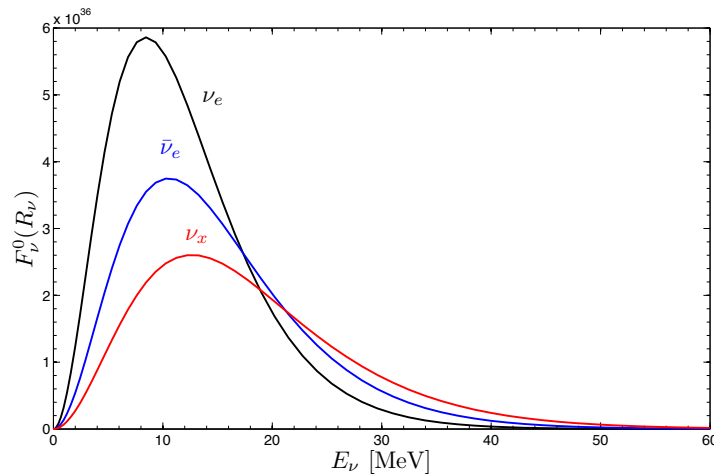
Figure 2.3 – *Neutrino fluxes at the neutrino-sphere given by eq. (2.10) with $\langle E_{\nu_e} \rangle = 12\,\text{MeV}, \langle E_{\bar{\nu}_e} \rangle \approx 15\,\text{MeV}, \langle E_{\nu_x} \rangle \approx 18\,\text{MeV}$ and $\eta_\nu = 0$.*

A simple relation can be found between the average energy and the temperature using the Fermi integrals

$$F_2(\eta_\nu)\langle E_\nu \rangle = F_3(\eta_\nu)T_\nu. \tag{2.12}$$

In figure 2.4, we see that during the cooling phase we can consider an equipartition of the luminosity for each neutrino flavors. Also the evolution of the average energy is shown in the bottom panel and we see that the hierarchy for the average energies is conserved.
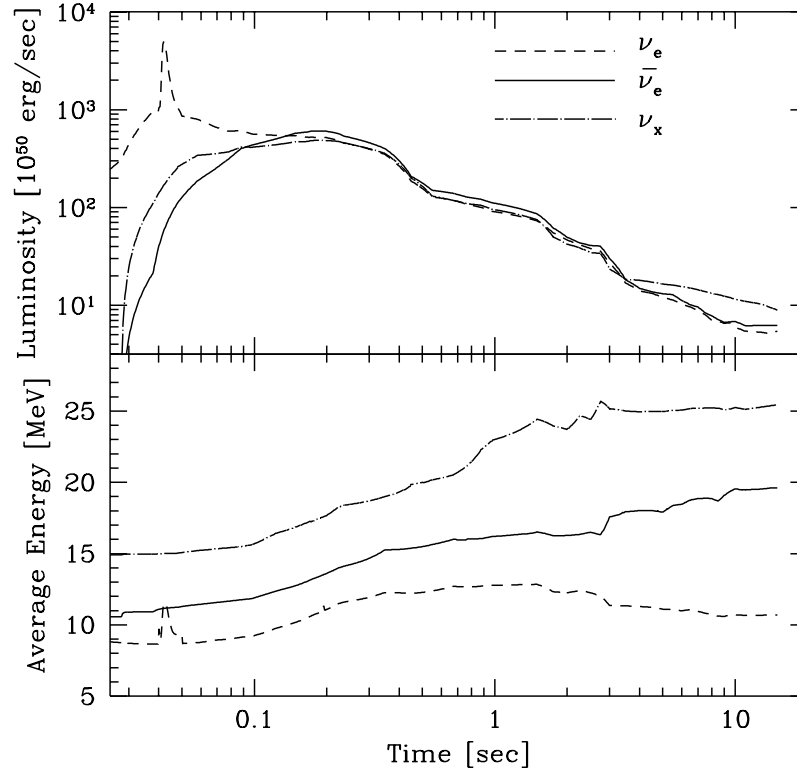
Figure 2.4 – *Time evolution of neutrino luminosity and average energy. Dashed lines are for ν_e, solid lines for $\bar{\nu}_e$ and dot-dashed lines for ν_x (i.e. $\nu_{\mu,\tau}$ and $\bar{\nu}_{\mu,\tau}$). Taken from [96].*

2.1.4 Matter density profile

As we have seen in section 1.2, the evolution of neutrinos in a medium is characterized by the neutrino parameters (distribution, energy, flavor,...) and by the properties of the medium (variation, composition,...). In this section, we focus on the matter density profile N_e.

Figure 2.5 shows typical density $\rho(t,r)$ and electron fraction $Y_e(t,r)$ profiles for a supernova progenitor and after the core bounce. On this figure, we also see the regions corresponding to the H and L-resonances where a flavor conversion occurs. These resonances are the matching MSW resonances explained in chapter 1 but when three flavors are considered. The H-resonance is related to the mixing angle θ_{13} and the L-resonance is still related to the mixing angle θ_{12}. Approximatively the

baryon density follows a power law

$$\rho_B(r) = \frac{\rho_0}{m_n} \left(\frac{10}{r\,[\text{km}]}\right)^n, \tag{2.13}$$

where ρ_0 is the baryon density at the neutrino-sphere, r is the distance in km, $n \simeq 3$ and m_n the neutron mass. In figure 2.6, we present some density profiles used in
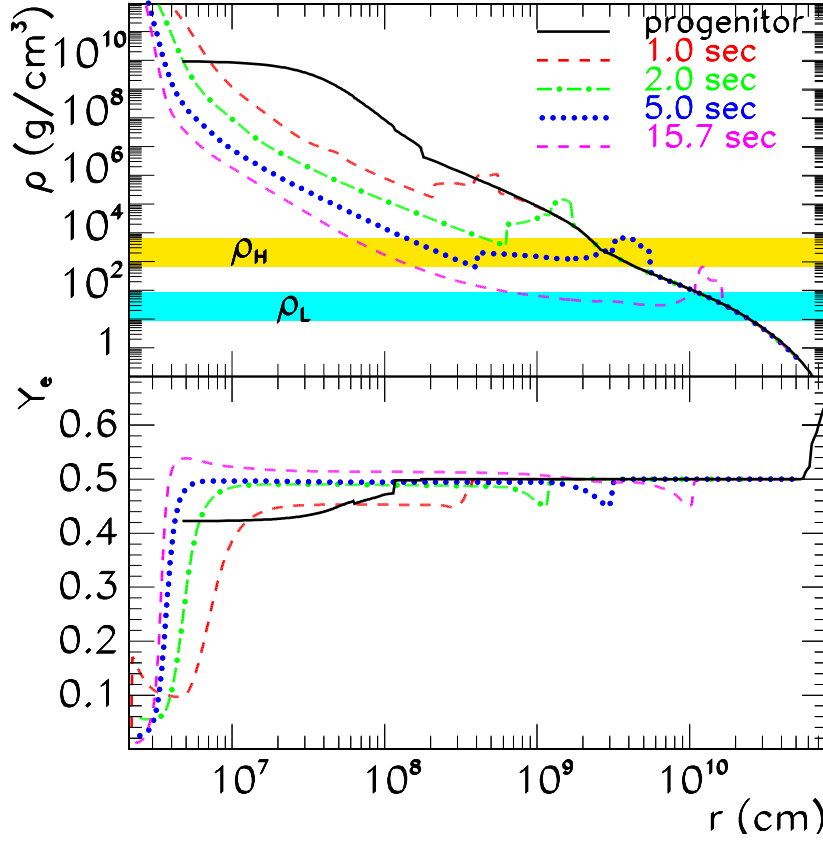
Figure 2.5 – *Density (top) and electron fraction (bottom) profiles for the supernova progenitor and after the core bounce taken from [97]. The region in yellow corresponds to the H-resonance and the one in blue to the L-resonance.*

the literature. By changing the matter density profile, the locations of the MSW resonances are shifted. In this thesis, we use a density profile as defined in eq. (2.13) with the parameter $\rho_0 = 1.5 \times 10^8$ g.cm^{-3} [89, 98, 91] for the calculations shown in chapters 3 and 4.

The effective potential V_{CC} that is taken into account to reproduce the coherent forward scattering of neutrinos with ordinary matter is related to the baryon density by

$$V_{CC} = \sqrt{2}G_F\rho_e = \sqrt{2}G_F Y_e\rho_B, \tag{2.14}$$

where Y_e is the neutron to proton ratio also known as the electron fraction. Typically, the electron fraction is taken to be equal to 0.5 because it is the value reached by numerical simulations in the MSW regions.

2.1.5   Electron fraction Y_e

One of the open questions in nuclear astrophysics is to find where nuclei heavier than iron are produced. A possible site for the nucleosynthesis is the supernova
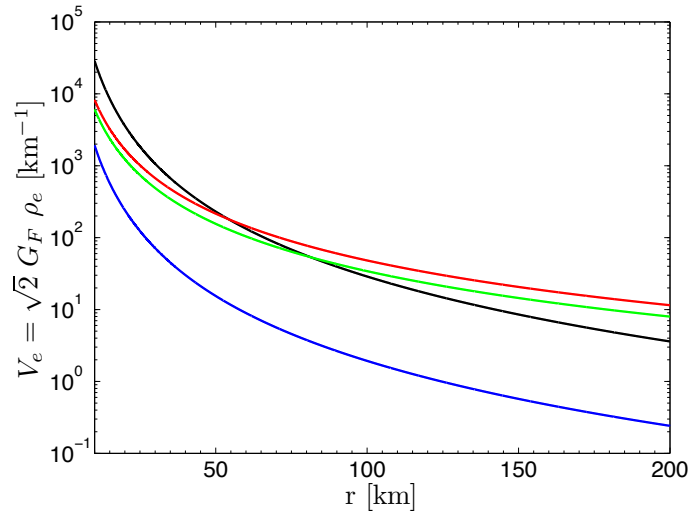
Figure 2.6 – *Electron density profiles as a function of distance for different parametrizations. The black line corresponds to the density profile used in [24, 25, 26, 89, 98, 91], the blue is used in [82, 18, 19], the red is used in [83, 85, 99] and finally the green line is used in [17, 100].*

environment, outside the PNS [60, 61, 62, 63, 64]. The processes that can engender heavy nuclei is related to a rapid capture of neutrons called the "r-process" [101]. However neutrino oscillations can affect the ratio of protons/neutrons (electron fraction Y_e) because of the interactions of neutrinos with nucleons. So first we need to determine the cross sections of electron neutrinos on neutrons and electron antineutrinos on protons which are present in the reaction rates involved in the calculation of the electron fraction.

Cross sections

As we have said, the neutron to proton ratio is affected by the free nucleon captures

$$\nu_e + n \rightleftharpoons p + e^- \quad \text{and} \quad \bar{\nu}_e + p \rightleftharpoons n + e^+. \tag{2.15}$$

Here we would like to point out a work [65] where the precise quasielastic cross sections on nucleons is calculated and we will show that the use of precise cross sections instead of simplified formulas has a huge impact of Y_e. Most of the time, a low energy approximation is used to calculate the nucleon capture

$$\sigma_{\nu_e}(E_\nu) \simeq 9.52 \times 10^{-44} \left(\frac{E_\nu + \Delta_{np}}{\text{MeV}} \right)^2 \text{cm}^2, \tag{2.16}$$

$$\sigma_{\bar{\nu}_e}(E_{\bar{\nu}}) \simeq 9.52 \times 10^{-44} \left(\frac{E_{\bar{\nu}} - \Delta_{np}}{\text{MeV}} \right)^2 \text{cm}^2, \tag{2.17}$$

where $\Delta_{np} = m_n - m_p \approx 1.293\,\text{MeV}$ is the neutron proton mass difference. As it is written in [65], "it is not recommended for analysis of supernova neutrinos, nor for precise studies of reactor $\bar{\nu}_e$". So we follow the work of Vissani and Strumia to obtain the precise quasielastic scatterings.

The differential cross section at tree level in the weak interaction, averaged (summed) over initial (final) polarizations is given by [65]

$$\frac{d\sigma}{dt} = \frac{G_F^2 \cos^2\theta_C}{2\pi(s - m_p^2)^2} |\mathcal{M}^2|, \tag{2.18}$$

where G_F is the Fermi constant, $\cos\theta_C = 0.9746 \pm 0.0008$ is the cosine of the Cabibbo angle and $\mathcal{M}$ has the current-current structure

$$\mathcal{M} = \bar{v}_{v_e}\gamma^a(1-\gamma_5)v_e \cdot \bar{u}_n\left(f_1\gamma_a + g_1\gamma_a\gamma_5 + \imath f_2\sigma_{ab}\frac{q^b}{2M} + g_2\frac{q_a}{M}\gamma_5\right)u_p, \qquad (2.19)$$

where $q = p_v - p_e = p_n - p_p$ and $M = (m_p + m_n)/2 \approx 938.9$ MeV. After calculations, one finds

$$|\mathcal{M}^2| = A(t) - (s-u)B(t) + (s-u)^2 C(t), \qquad (2.20)$$

where $s = (p_v + p_p)^2$, $t = (p_v - p_e)^2$, $u = (p_v - p_n)^2$ are the usual Mandelstam variables and

$$
\begin{aligned}
16\,A \;=\; & (t-m_e^2)\left[4|f_1^2|(4M^2+t+m_e^2) + 4|g_1^2|(-4M^2+t+m_e^2)\right.\\
& \left. +|f_2^2|\left(\frac{t^2}{M^2}+4t+4m_e^2\right) + \frac{4m_e^2 t|g_2^2|}{M^2} + 8\,\mathfrak{R}\,(f_1^* f_2)\,(2t+m_e^2) + 16m_e^2\,\mathfrak{R}\,(g_1^* g_2)\right]\\
& -\Delta_{np}^2\left[\left(4|f_1^2|+t\frac{|f_2^2|}{M^2}\right)(4M^2+t-m_e^2) + 4|g_1^2|(4M^2-t+m_e^2)\right.\\
& \left. +\frac{4m_e^2|g_2^2|(t-m_e^2)}{M^2} + 8\,\mathfrak{R}\,(f_1^* f_2)\,(2t-m_e^2) + 16m_e^2\,\mathfrak{R}\,(g_1^* g_2)\right]\\
& -32m_e^2 M\Delta_{np}\,\mathfrak{R}\,(g_1^*(f_1+f_2)), \qquad (2.21)
\end{aligned}
$$

$$16\,B \;=\; 16t\,\mathfrak{R}\,(g_1^*(f_1+f_2)) + \frac{4m_e^2\Delta_{np}\left(|f_2^2| + \mathfrak{R}\,(f_1^* f_2 + 2g_1^* g_2)\right)}{M}, \qquad (2.22)$$

$$16\,C \;=\; 4(|f_1^2| + |g_1^2|) - t\frac{|f_2^2|}{M^2}. \qquad (2.23)$$

The adimensional form factors f_i, g_i are real functions of the transferred 4-momentum $t = q^2 < 0$. They can be approximated with

$$\{f_1, f_2\} = \frac{\{1-(1+\xi)t/4M^2, \xi\}}{(1-t/4M^2)(1-t/M_V^2)^2}, \quad g_1 = \frac{g_1(0)}{(1-t/M_A^2)^2}, \quad g_2 = \frac{2M^2 g_1}{m_\pi^2 - t}, \quad (2.24)$$

where $g_1(0) = -1.270 \pm 0.003$, $M_V^2 = 0.71$ GeV^2, $M_A^2 \approx 1$ GeV^2. Finally $\xi = \kappa_p - \kappa_n = 3.706$ is the difference between the proton and neutron anomalous magnetic moments in units of the nuclear magneton ($\kappa_p = 1.792$, $\kappa_n = -1.913$). The expressions for $v_e n$ scattering are obtained by exchanging $p_v \leftrightarrow -p_e$, and $m_p \to m_n$ in the flux factor. In fact, in the expression of $|\mathcal{M}^2|$ we have to do the transformation $s - u \to u - s$.

To find the total cross section, one needs to know the cross section in terms of the neutrino and electron energy in the rest frame of the proton, E_v and E_e. Inserting

$$s - m_p^2 = 2m_p E_v, \qquad s - u = 2m_p(E_v + E_e) - m_e^2, \qquad t = m_n^2 - m_p^2 - 2m_p(E_v - E_e),$$

the total cross section $\sigma_{\bar{v}_e p}(E_v)$ is

$$\sigma(E_v) = \int_{E_2}^{E_1}\frac{d\sigma}{dE_e}(E_v, E_e) = \int_{E_2}^{E_1} 2m_p\frac{d\sigma}{dt} \quad \text{if } E_v \geq E_{\text{thr}} \equiv \frac{(m_n+m_e)^2 - m_p^2}{2m_p}. \quad (2.25)$$

The allowed values of the electron energy E_e, $E_1 \leq E_e \leq E_2$, correspond to the possible scattering angles θ^{CM} in the center of mass (CM) frame

$$E_{1,2} = E_v - \frac{m_n^2 - m_p^2 - m_e^2}{2m_p} - \frac{1}{m_p}E_v^{\text{CM}}(E_e^{\text{CM}} \pm p_e^{\text{CM}}), \qquad (2.26)$$

where the energy and momenta in the CM have the standard expressions

$$E_\nu^{CM} = \frac{s - m_p^2}{2\sqrt{s}}, \qquad E_e^{CM} = \frac{s - m_n^2 + m_e^2}{2\sqrt{s}}, \qquad p_e^{CM} = \frac{\sqrt{[s - (m_n - m_e)^2][s - (m_n + m_e)^2]}}{2\sqrt{s}}.$$
(2.27)

For the neutrino reaction, one has just to replace $m_n \leftrightarrow m_p$ in all formulas above except for Δ_{np}, which remains the same, and E_{thr}, which is equal to 0 for ν_e. As discussed in [65], to use the most precise cross sections, one has also to consider the two corrections

1. the radiative corrections to both cross sections, well approximated as

$$d\sigma(E_\nu, E_e) \rightarrow d\sigma(E_\nu, E_e) \left[1 + \frac{\alpha}{\pi}\left(6.00 + \frac{3}{2}\log\frac{m_p}{2E_e} + 1.2\left(\frac{m_e}{E_e}\right)^{1.5}\right)\right],$$
(2.28)

where α is the fine-structure constant. This one-loop correction is valid at $E_\nu \ll m_p$, when the final state positron (electron) is the only radiator, and in the hypothesis that all the energy E_e in electrons and bremsstrahlung photons is detected.

2. the $\sigma(\nu_e n \rightarrow pe)$ needs to be multiplied by the Sommerfeld factor that accounts for final-state interactions

$$F(E_e) = \frac{\eta}{1 - \exp(-\eta)}, \quad \text{with } \eta = \frac{2\pi\alpha}{\sqrt{1 - m_e^2/E_e^2}}.$$
(2.29)

In figure 2.7 a, we clearly see that the approximated formula (eq. (2.17)) is not a good approximation for supernova neutrinos which have an energy in the range $[0, 100]$ MeV. The overestimation of the approximated cross section is plotted on figure 2.8 a. We see that the discrepancy between the "naive" and the precise cross section increases with the energy. For a typical Fermi-Dirac distribution of the neutrino fluxes picked at ~ 20 MeV which is the case in our calculations (it is due to the average energies), the approximated cross section induces an error of 20%. On the contrary, the approximated formula (eq. (2.16) and figure 2.7 b) agrees pretty well with the exact cross section as shown on figure 2.8 b.
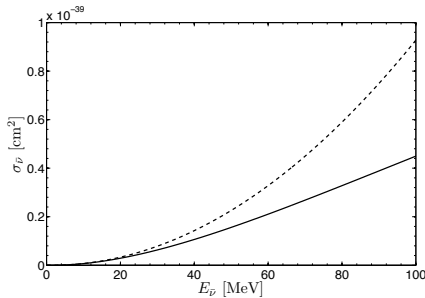
(a) $\sigma_{\bar{\nu}_e p}$ as a function of the antineutrino energy for the approximated (dashed) and precise (solid) scattering formulas.
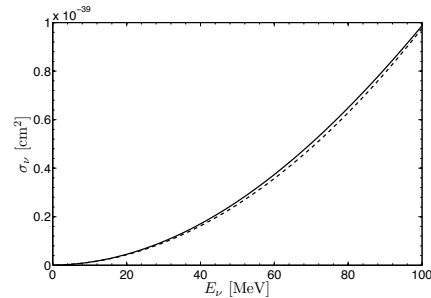
(b) $\sigma_{\nu_e n}$ as a function of the neutrino energy for the approximated (dashed) and precise (solid) scattering formulas.

Figure 2.7 – *Precise and approximated cross sections of the reactions $\nu_e + n \rightleftharpoons p + e^-$ and $\bar{\nu}_e + p \rightleftharpoons n + e^+$.*

Electron fraction calculation
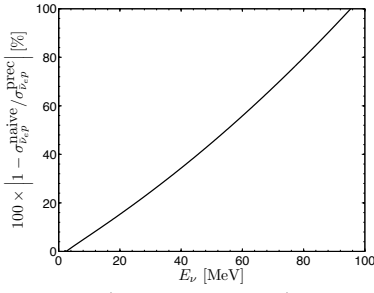
(a) Ratio $100 \times \left| 1 - \sigma_{\bar{\nu}_e p}^{\text{naive}} / \sigma_{\bar{\nu}_e p}^{\text{prec}} \right|$ as a function of the antineutrino energy.
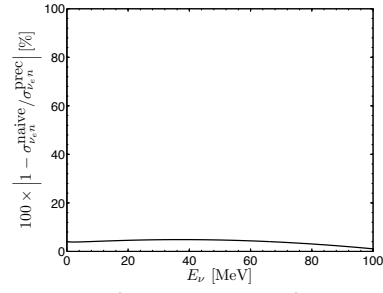
(b) Ratio $100 \times \left| 1 - \sigma_{\nu_e n}^{\text{naive}} / \sigma_{\nu_e n}^{\text{prec}} \right|$ as a function of the neutrino energy.

Figure 2.8 – *Percentage difference between the precise and approximated cross sections for the reaction $\nu_e + n \rightleftharpoons p + e^-$ (right) and $\bar{\nu}_e + p \rightleftharpoons n + e^+$ (left).*

The electron fraction Y_e, is the net number of electrons (number of electrons minus the number of positrons) per baryon

$$Y_e = \frac{n_{e^-} - n_{e^+}}{n_B}, \tag{2.30}$$

where n_{e^-}, n_{e^+}, and n_B are number densities of electrons, positrons, and baryons, respectively. In an environment where no heavy nuclei are present (atomic weight $A > 2$), the electron fraction is reduced to

$$Y_e = X_p + \frac{1}{2}X_\alpha + \sum_h \left(\frac{Z_h}{A_h} \right) X_h \simeq X_p + \frac{1}{2}X_\alpha, \tag{2.31}$$

where X_i is the mass fraction of a i element. The rate of change of X_i is guided by the rate of the reactions

$$\nu_e + n \rightarrow p + e^- \quad , \qquad \lambda_{\nu_e} = \int \sigma_{\nu_e n} F_{\nu_e} dE_{\nu_e}, \tag{2.32}$$

$$e^+ + n \rightarrow p + \bar{\nu}_e \quad , \qquad \lambda_{e^+} = \int \sigma_{e^+ n} F_{e^+} dE_{e^+}, \tag{2.33}$$

$$\bar{\nu}_e + p \rightarrow n + e^+ \quad , \qquad \lambda_{\bar{\nu}_e} = \int \sigma_{\bar{\nu}_e p} F_{\bar{\nu}_e} dE_{\bar{\nu}_e}, \tag{2.34}$$

$$e^- + p \rightarrow n + \nu_e \quad , \qquad \lambda_{e^-} = \int \sigma_{e^- p} F_{e^-} dE_{e^-}, \tag{2.35}$$

where σ are the total cross sections for the considered reaction and F_α are the flux of electronic neutrinos and antineutrinos, electrons and positrons. Because of the large binding energy, we consider that alpha particles interact very weakly with neutrinos. The evolutions of the mass functions are

$$\frac{dX_p}{dt} = -(\lambda_{\bar{\nu}_e} + \lambda_{e^-})X_p + (\lambda_{\nu_e} + \lambda_{e^+})X_n = -\lambda_p X_p + \lambda_n X_n \quad \text{and} \quad \frac{dX_\alpha}{dt} = 0. \tag{2.36}$$

So using the constraint $X_p + X_\alpha + X_n = 1$, one obtains

$$\frac{dY_e}{dt} = \lambda_n - (\lambda_p + \lambda_n)Y_e + \frac{1}{2}(\lambda_p - \lambda_n)X_\alpha. \tag{2.37}$$

We limit our calculations to the freeze-out model in which $dY_e/dt = 0$, so the equilibrium value of the electron fraction is

$$Y_e = \frac{\lambda_n}{\lambda_p + \lambda_n} + \frac{1}{2}\frac{\lambda_p - \lambda_n}{\lambda_p + \lambda_n}X_\alpha. \tag{2.38}$$

At high temperatures, alpha particles are absent and the second term of eq. (2.38) can be dropped. In the region just below where the alpha particles are formed approximately one second after the bounce, the temperature is less then ~ 1 MeV. Here both the electron and positron capture rates are very small and Y_e can be approximated as

$$Y_e = \frac{1}{1 + \lambda_{\bar{\nu}_e}/\lambda_{\nu_e}}. \tag{2.39}$$

The aim of searching for effects coming from neutrino oscillations on the electron fraction is to reduce Y_e. In the outer regions of the star where heavy elements can be produced, we need to have $Y_e < 0.5$ so that the rate λ_p is larger than λ_n and much more neutrons are created which enhance the environment in neutrons. Consequently, the enhancement in neutrons allows the nucleosynthesis (i.e. the creation of heavier nuclei) by the r-process. It has been shown in [59] that the effects induced by the MSW resonances change Y_e by ± 0.1.

On figure 2.9 a, we show that the electron fraction at the neutrino-sphere is more or less close to 0.5 for typical values of the average energies $\langle E_{\nu_e} \rangle \sim 12$ MeV and $\langle E_{\bar{\nu}_e} \rangle \sim 15$ MeV. So neutrino oscillation effects can make Y_e lower than 0.5 and enrich the medium in neutrons. The main problem that we show in figure 2.9 b is the increase of the initial electron fraction by using the precise quasielastic cross sections instead of the approximative formulas. As a consequence, because the effects of neutrino oscillations are not so large, it is more difficult to decrease Y_e below 0.5 for typical values of $\langle E_{\nu_e} \rangle$ and $\langle E_{\bar{\nu}_e} \rangle$.

2.2 NEXT-GENERATION OBSERVATORIES UNDER STUDIES

The feasibility of a next generation neutrino observatory in Europe is being considered within the LAGUNA design study. To accommodate giant neutrino detectors and shield them from cosmic rays, a new very large underground infrastructure is required. Seven potential candidate sites in different parts of Europe and at several distances from CERN are being studied: Boulby (UK), Canfranc (Spain), Fréjus (France/Italy), Pyhäsalmi (Finland), Polkowice-Sieroszowice (Poland), Slanic (Romania) and Umbria (Italy). The aim of the construction of these next-generation observatories are:

– an improvement in the sensitivity to search for proton decays to possibly test physics at the GUT scale,
– the measurement, with unprecedented sensitivity of the last unknown mixing angle θ_{13}, so as to unveil possible CP violation in the leptonic sector and provide an explanation of the matter-antimatter asymmetry in the Universe,
– the detection of neutrinos emitted from astrophysical objects (supernovae,...) and from diffuse sources (Diffuse supernova Neutrino Background, ...) to give information on processes happening in the Universe and on the mechanisms which give rise to star explosion,
– precision studies of terrestrial, solar and atmospheric neutrinos.

Here we present the three detector options that are currently being studied: MEMPHYS [66], LENA [67] and Glacier [68].
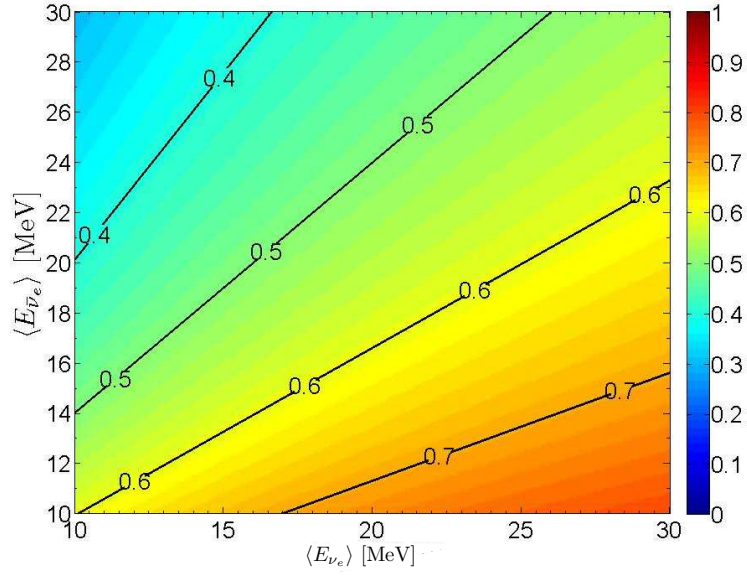
(a) Y_e at the neutrino-sphere with the approximative cross sections.
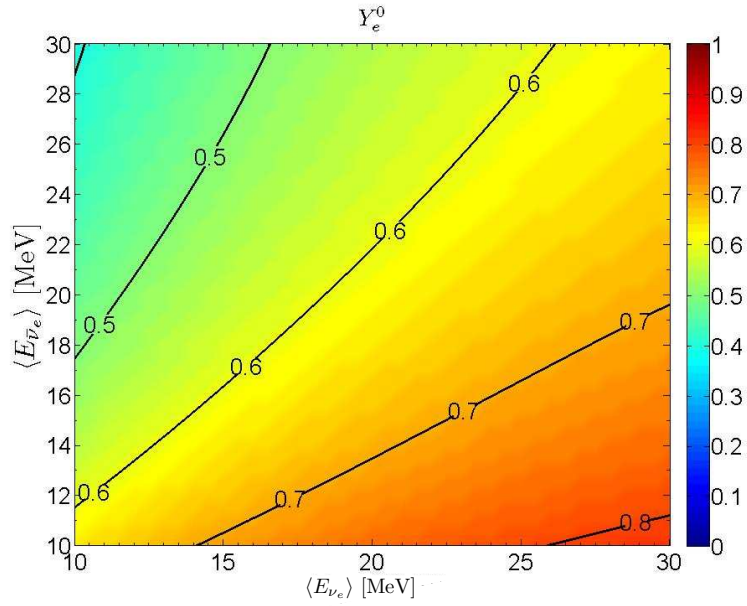
(b) Y_e at the neutrino-sphere with the precise cross sections.

Figure 2.9 – *Y_e at the neutrino-sphere with the approximative and precise cross sections.*

2.2.1 MEMPHYS

The MEMPHYS detector (fig. 2.10) is an extrapolation of the water Čerenkov SuperKamiokande detector to a fiducial mass of 730 kTon or 440 kTon. It is composed of up to 5 or 3 shafts containing separate tanks. Each shaft has 65 m diameter and 65 m height. The combination of the shafts represents an increase of a factor 8 with respect to SuperKamiokande [102]. The main detection channel is the usual one in water Čerenkov detectors i.e.

$$\bar{\nu}_e + p \rightarrow n + e^+. \tag{2.40}$$
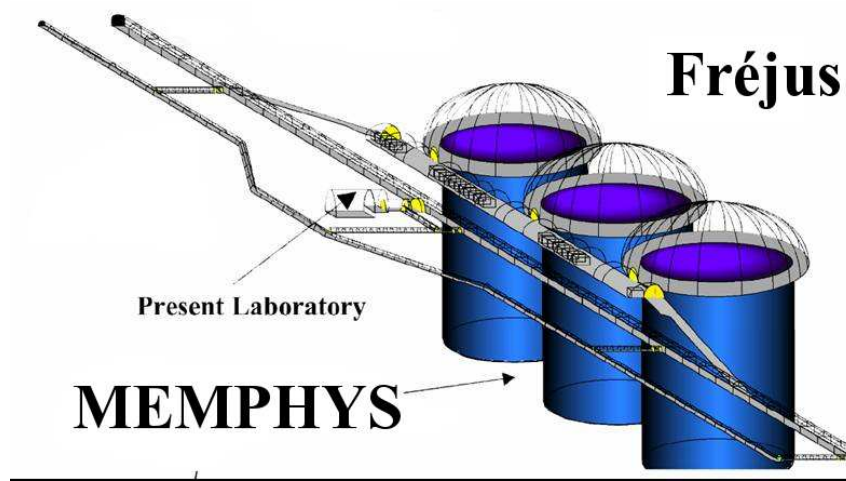
Figure 2.10 – *Layout of the MEMPHYS detector in the future Fréjus laboratory [23].*

Then we can estimate the number of target protons [2] as

$$N_{\text{targets}} = m_{\text{water}} \, \mathcal{N}_A \, \frac{M_{\text{H}_2}}{M_{\text{H}_2\text{O}}} \simeq 2.97 \times 10^{34} \text{ target protons.} \tag{2.41}$$

2.2.2 LENA

The LENA detector (fig. 2.11) is a liquid scintillator detector, cylindrical in shape with a height of about 100 m and 30 m diameter. The inner volume corresponding to a radius of 13 m contains approximatively $5 \times 10^4 \, \text{m}^3$ of liquid scintillator. The outer part is filled with water, acting as a veto for identifying muons entering the detector from outside. The fiducial volume (1 m distance to the inner tank walls) represents 88% of the total detector volume i.e. 44 kTon. The organic liquid scintillator mixtures under consideration are both linear-alkyl-benzene (LAB) and phenyl-o-xylylethane (PXE with an admixture of non-scintillating dodecane). In our study, we assume the liquid scintillator material to be pure phenyl-o-xylylethane, a mixture of 20% PXE ($C_{16}H_{18}$) and 80% Dodecane ($C_{12}H_{26}$). The mass density of the two constituents are $\rho_1 = 986 \, \text{g.L}^{-1}$ and $\rho_2 = 749 \, \text{g.L}^{-1}$ respectively [23]. The detection channel is the same as for water Čerenkov detectors and the number of proton targets is

$$\begin{aligned} N_{\text{targets}} = \quad & 0.2 \left[m_{\text{liquid}} \, \rho_1 \, \mathcal{N}_A \, \frac{M_{\text{H}_{18}}}{M_{\text{C}_{16}\text{H}_{18}}} \right] + 0.8 \left[m_{\text{liquid}} \, \rho_2 \, \mathcal{N}_A \, \frac{M_{\text{H}_{26}}}{M_{\text{C}_{12}\text{H}_{26}}} \right] \\ & \simeq 2.89 \times 10^{33} \text{ target protons.} \end{aligned} \tag{2.42}$$

2.2.3 Glacier

GLACIER (fig. 2.12) is the foreseen extrapolation up to 100 kTon of the liquid Argon Time Projection Chamber technique. The detector is mechanically subdivided into two parts, the liquid Argon tank and the inner detector instrumentation. The basic idea behind the detector is to use a single 100 kTon boiling liquid Argon cryogenic tank with cooling directly performed with liquid Argon (self-refrigerating). Events are reconstructed by using the ionization in liquid. The signal

---

2. $\mathcal{N}_A$ is the Avogadro number.

Cavern
height: 115 m, diameter: 50 m
shielding from cosmic rays: ~4,000 m.w.e.

Muon Veto
plastic scintillator panels (on top)
Water Cherenkov Detector
3,000 phototubes
100 kt of water
reduction of fast
neutron background

Steel Cylinder
height: 100 m, diameter: 30 m
70 kt of organic liquid
30,000 – 50,000 phototubes

Buffer
thickness: 2 m
non-scintillating organic liquid
shielding from external radioactivity

Nylon Vessel
separating buffer liquid
and liquid scintillator

Target Volume
height: 100 m, diameter: 26 m
50 kt of liquid scintillator

Figure 2.11 – *Schematic view of the LENA detector [67].*
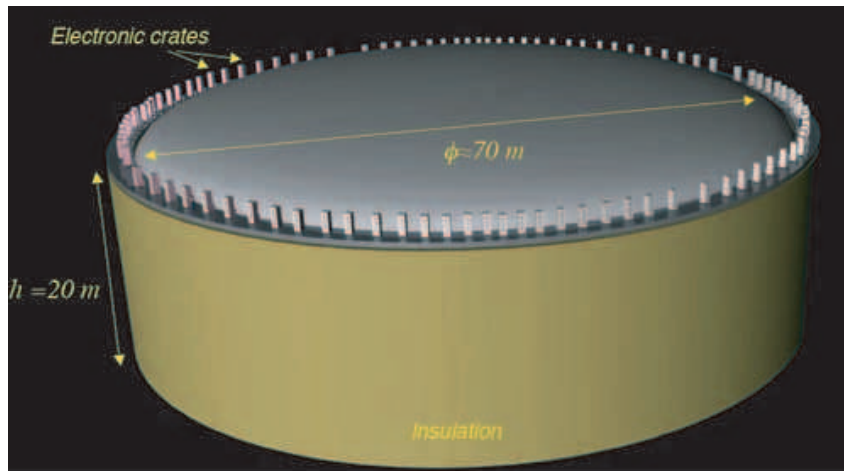
Figure 2.12 – *Artistic view of a 100 kTon single-tank liquid Aron TPC detector [23].*

from scintillation and Čerenkov light readout complete the information contributing to the event reconstruction. The main detection channel is the scattering of electron neutrinos on Argon nuclei

$$\nu_e + {}^{40}A \rightarrow {}^{40}K^* + e^-. \tag{2.43}$$

Here the number of target corresponds to the number of Argon nuclei i.e. $N_{\text{targets}} \simeq 6.02 \times 10^{34}$ targets.

2.3 THREE FLAVORS OSCILLATIONS AND FACTORIZATION OF THE MSW RESONANCES

We extend the results of section 1.2 and analyze the case where we consider all the three possible active flavors ν_e, ν_μ and ν_τ. The supernova environment and moreover the matter density profile inside supernovae enable to have another MSW resonance in addition to the one present in the Sun. Then we still have the MSW resonance related to the parameters Δm^2_{Sun} and θ_{Sun} that we call the L-resonance and a new resonance, the H-resonance, related to the parameters Δm^2_{atm} and θ_{atm}. We will see that the large difference between the two mass squared differences Δm^2_{Sun} and Δm^2_{atm} creates a large spatial gap between the H and L-resonances. This gap allows us to consider the two MSW resonances independently, this very good approximation is named the factorization of the resonances.

The Hamiltonian in the flavor basis H is a sum of the vacuum Hamiltonian and the matter Hamiltonian. It has the form

$$H = H^{\text{vac}} + H^{\text{mat}}. \tag{2.44}$$

The explicit elements of the vacuum Hamiltonian H^{vac}, in terms of the three mass squared differences Δm^2_{ij} $(i, j = 1, 2, 3)$, are (without CP violation phases)

$$H^{\text{vac}}_{ee} = \frac{1}{4E}(-\Delta m^2_{21}c^2_{13}C_{12} + (\Delta m^2_{31} + \Delta m^2_{32})s^2_{13}), \tag{2.45}$$

$$H^{\text{vac}}_{e\mu} = \frac{1}{4E}c_{13}(\Delta m^2_{21}c_{23}S_{12} + (\Delta m^2_{31} + \Delta m^2_{32} + \Delta m^2_{21}C_{12})s_{13}s_{23}), \tag{2.46}$$

$$H^{\text{vac}}_{e\tau} = \frac{1}{4E}c_{13}((\Delta m^2_{31} + \Delta m^2_{32} + \Delta m^2_{21}C_{12})c_{23}s_{13} - \Delta m^2_{21}S_{12}s_{23}), \tag{2.47}$$

$$H^{\text{vac}}_{\mu\mu} = \frac{1}{4E}(-0.125\Delta m^2_{21}c^2_{12}(-2 - 2C_{13} + 2C_{13}C_{23} - 6C_{23}) - \Delta m^2_{21}c^2_{23}s^2_{12}$$
$$+((\Delta m^2_{31} + \Delta m^2_{32})c^2_{13} + \Delta m^2_{21}s^2_{12}s^2_{13})s^2_{23} - \Delta m^2_{21}S_{12}s_{13}S_{23}), \tag{2.48}$$

$$H^{\text{vac}}_{\mu\tau} = \frac{1}{8E}(-2\Delta m^2_{21}C_{23}S_{12}s_{13} - \Delta m^2_{21}C_{12}s^2_{13}S_{23}$$
$$+((\Delta m^2_{31} + \Delta m^2_{32})c^2_{13} - C_{12}\Delta m^2_{21})S_{23}), \tag{2.49}$$

$$H^{\text{vac}}_{\tau\tau} = \frac{1}{4E}((\Delta m^2_{31} + \Delta m^2_{32})c^2_{13}c^2_{23}$$
$$+\Delta m^2_{21}(-C_{12}c^2_{23}s^2_{13} + C_{12}s^2_{23} + S_{12}s_{13}S_{23})), \tag{2.50}$$

with $c_{ij} = \cos\theta_{ij}$, $s_{ij} = \sin\theta_{ij}$, $C_{ij} = \cos 2\theta_{ij}$ and $S_{ij} = \sin 2\theta_{ij}$, and $\Delta m^2_{ij} = m^2_i - m^2_j$. We have demonstrated in section 1.2.2.3 the expression of the matter-interaction Hamiltonian which includes the coherent forward scattering in eq. (1.61). In a three flavors scenario, we know that two hierarchies are possible: normal and inverted (see figure 1.5). Here we give a complete explanation and explicit formulas for the normal hierarchy. The calculations for the inverted hierarchy follow the same procedure and so we will only give the corresponding results in tables.

Following the work in [103], the expressions of the matter angles are

$$\tan^2\widetilde{\theta}_{12} = -\frac{\delta\widetilde{k}_{13}\left[(H_{\mu\mu} - \widetilde{k}_2)(H_{\tau\tau} - \widetilde{k}_2) - |H_{\mu\tau}|^2\right]}{\delta\widetilde{k}_{23}\left[(H_{\mu\mu} - \widetilde{k}_1)(H_{\tau\tau} - \widetilde{k}_1) - |H_{\mu\tau}|^2\right]}, \tag{2.51}$$

$$\sin^2 \widetilde{\theta}_{13} = \frac{(H_{\mu\mu} - \widetilde{k}_3)(H_{\tau\tau} - \widetilde{k}_3) - |H_{\mu\tau}|^2}{\delta\widetilde{k}_{13}\,\delta\widetilde{k}_{23}}, \tag{2.52}$$

$$\tan^2 \widetilde{\theta}_{23} = \left| \frac{H_{\mu\tau}\,H_{\tau e} - H_{\mu e}(H_{\tau\tau} - \widetilde{k}_3)}{H_{\tau\mu}\,H_{\mu e} - H_{\tau e}(H_{\mu\mu} - \widetilde{k}_3)} \right|^2. \tag{2.53}$$

At the beginning of the propagation where $N_e \gg N_e^{\text{res}}$, the eigenvalues $\widetilde{k}_i$ tend to their limits

$$\widetilde{k}_1 \;\to\; \frac{H_{\mu\mu} + H_{\tau\tau}}{2} - \sqrt{|H_{\mu\tau}|^2 + \frac{(H_{\mu\mu} - H_{\tau\tau})^2}{4}} + \mathcal{O}(1/V_{\text{CC}}), \tag{2.54}$$

$$\widetilde{k}_2 \;\to\; \frac{H_{\mu\mu} + H_{\tau\tau}}{2} + \sqrt{|H_{\mu\tau}|^2 + \frac{(H_{\mu\mu} - H_{\tau\tau})^2}{4}} + \mathcal{O}(1/V_{\text{CC}}), \tag{2.55}$$

$$\widetilde{k}_3 \;\to\; H_{ee} + \mathcal{O}(1/V_{\text{CC}}). \tag{2.56}$$

With these expressions of the eigenvalues $\widetilde{k}_i$, we estimate the values of the matter angles at the neutrino-sphere using eqs. (2.51), (2.52) and (2.53) which are given in table 2.2.

	Matter angles	Normal Hierarchy	Inverted Hierarchy
Neutrino	$\widetilde{\theta}_{12}$	$\pi/2$	$\pi/2$
	$\widetilde{\theta}_{13}$	$\pi/2$	0
	$\widetilde{\theta}_{23}$	θ_{23}	θ_{23}
Antineutrino	$\widetilde{\bar{\theta}}_{12}$	0	0
	$\widetilde{\bar{\theta}}_{13}$	0	$\pi/2$
	$\widetilde{\bar{\theta}}_{23}$	θ_{23}	θ_{23}

Table 2.2 – *Values of the neutrino matter angles $\widetilde{\theta}_{12}$, $\widetilde{\theta}_{13}$ and $\widetilde{\theta}_{23}$ and of the antineutrino matter angles $\widetilde{\bar{\theta}}_{12}$, $\widetilde{\bar{\theta}}_{13}$ and $\widetilde{\bar{\theta}}_{23}$ for normal and inverted hierarchies at very high densities. The maximization $\widetilde{\theta} = \pi/2$ and the minimization $\widetilde{\theta} = 0$ of certain angles is induced by the presence of the effective matter potential $V_{\text{CC}} = \sqrt{2}G_F N_e$.*

The explicit values of the matter angles allow us to determine in which matter state the flavors begin, using $\nu_\alpha = \sum_i \widetilde{U}_{\alpha i}\widetilde{\nu}_i$. The initial matter eigenstates and the correspondent flavor states are given in table 2.3 for neutrinos and antineutrinos.

From table 2.2, we see that for normal hierarchy the vacuum limits for matter angles can be reached if the matter angles $\widetilde{\theta}_{12}$ and $\widetilde{\theta}_{13}$ cross on their way the maximal mixing value $\pi/4$ because their vacuum limits are respectively $\theta_{12} \simeq \pi/5$ and $\theta_{13} \leq \pi/20$. Thus there will be two resonances associated to $\widetilde{\theta}_{12}$ and $\widetilde{\theta}_{13}$ with the corresponding mass differences Δm_{ij}^2. To know which eigenvalues will play a role for the two resonances, we look at the evolution equation of matter states and the

		Normal Hierarchy			Inverted Hierarchy		
		$\widetilde{\nu}_1$	$\widetilde{\nu}_2$	$\widetilde{\nu}_3$	$\widetilde{\nu}_1$	$\widetilde{\nu}_2$	$\widetilde{\nu}_3$
Neutrino	ν_e			1	1		
	ν_μ	c_{23}	s_{23}		c_{23}		s_{23}
	ν_τ	s_{23}	c_{23}		s_{23}		c_{23}

		Normal Hierarchy			Inverted Hierarchy		
		$\widetilde{\nu}_1$	$\widetilde{\nu}_2$	$\widetilde{\nu}_3$	$\widetilde{\nu}_1$	$\widetilde{\nu}_2$	$\widetilde{\nu}_3$
Antineutrino	$\bar{\nu}_e$	1					1
	$\bar{\nu}_\mu$		c_{23}	s_{23}	c_{23}	s_{23}	
	$\bar{\nu}_\tau$		s_{23}	c_{23}	s_{23}	c_{23}	

Table 2.3 – *Initial composition of the flavor states ν_e, ν_μ and ν_τ in terms of the matter eigenstates $\widetilde{\nu}_1$, $\widetilde{\nu}_2$ and $\widetilde{\nu}_3$ for neutrinos and antineutrinos at very high densities, and for both hierarchies: normal and inverted. These compositions directly reflect the initial values of the matter angles.*

Hamiltonian in the matter basis $\widetilde{H}$ which is given by

$$
\imath \frac{\partial}{\partial x} \begin{pmatrix} \widetilde{\nu}_1 \\ \widetilde{\nu}_2 \\ \widetilde{\nu}_3 \end{pmatrix} = \left(\widetilde{K} - \imath \widetilde{U}^\dagger \frac{\partial \widetilde{U}}{\partial x} \right) \begin{pmatrix} \widetilde{\nu}_1 \\ \widetilde{\nu}_2 \\ \widetilde{\nu}_3 \end{pmatrix}
$$
$$
= \begin{pmatrix} \widetilde{k}_1 & \imath \frac{\delta \widetilde{k}_{12}}{2\pi} \Gamma_{12} & \imath \frac{\delta \widetilde{k}_{13}}{2\pi} \Gamma_{13} \\ -\imath \frac{\delta \widetilde{k}_{12}}{2\pi} \Gamma_{12}^* & \widetilde{k}_2 & \imath \frac{\delta \widetilde{k}_{23}}{2\pi} \Gamma_{23} \\ -\imath \frac{\delta \widetilde{k}_{13}}{2\pi} \Gamma_{13}^* & -\imath \frac{\delta \widetilde{k}_{23}}{2\pi} \Gamma_{23}^* & \widetilde{k}_3 \end{pmatrix} \begin{pmatrix} \widetilde{\nu}_1 \\ \widetilde{\nu}_2 \\ \widetilde{\nu}_3 \end{pmatrix}, \qquad (2.57)
$$

where $\widetilde{K} = \mathrm{diag}\left(\widetilde{k}_1, \widetilde{k}_2, \widetilde{k}_3 \right)$, $\delta \widetilde{k}_{ij} = \widetilde{k}_i - \widetilde{k}_j$ and $\widetilde{U}$ is the unitary matrix that relates the flavor and the matter states. The eq. (2.57) defines three functions Γ_{ij} which are the non-adiabaticity parameters for three flavor neutrino oscillations. By expressing the Γ_{ij}'s in terms of the eigenvalues and the matter angles (and their derivatives) one finds

$$
\Gamma_{12} = -\frac{2\pi}{\delta \widetilde{k}_{12}} \left(\frac{d\widetilde{\theta}_{12}}{dx} + \widetilde{s}_{13} \frac{d\widetilde{\theta}_{23}}{dx} \right), \qquad (2.58)
$$

$$
\Gamma_{13} = -\frac{2\pi}{\delta \widetilde{k}_{13}} \left(\widetilde{c}_{12} \frac{d\widetilde{\theta}_{13}}{dx} - \widetilde{s}_{12}\widetilde{c}_{13} \frac{d\widetilde{\theta}_{23}}{dx} \right), \qquad (2.59)
$$

$$
\Gamma_{23} = -\frac{2\pi}{\delta \widetilde{k}_{23}} \left(\widetilde{s}_{12} \frac{d\widetilde{\theta}_{13}}{dx} + \widetilde{c}_{12}\widetilde{c}_{13} \frac{d\widetilde{\theta}_{23}}{dx} \right). \qquad (2.60)
$$

From the expression of Γ_{ij}'s and the values given in table 2.2, we conclude that the resonance associated to $\widetilde{\theta}_{12}$ connect states 1 and 2, and the one associated to $\widetilde{\theta}_{13}$ connect states 2 and 3.

The fact that the hierarchy of the mass squared differences is $\Delta m_{21}^2 \ll \Delta m_{32}^2$ implies that the two resonances are well separated. This spatial separation is called the factorization approximation [104]. For each resonance the system is considered as a mixture between two states $\widetilde{\nu}_i$ and $\widetilde{\nu}_j$ and the third one, $\widetilde{\nu}_k$, is decoupled. The factorization approximation and the fact that only two neutrino matter eigenstates are involved in each resonances allow us to apply the resonance condition for two neutrino flavors to three flavors, then one obtains the two conditions

$$\frac{\Delta m_{21}^2}{2E} \cos 2\theta_{12} = \sqrt{2} G_F N_e(r), \tag{2.61}$$

$$\frac{\Delta m_{32}^2}{2E} \cos 2\theta_{13} = \sqrt{2} G_F N_e(r). \tag{2.62}$$

The resonance associated to θ_{13} is called the "High" resonance because it appears the first, at high density. The other one, related to θ_{12}, is called the "Low" resonance. As for the two flavors case (see section 1.2.3), we define two "hopping" probabilities, one for the H-resonance P_H and one for the L-resonance P_L. Because the high resonance connects states 2 and 3 and the low resonance connects states 1 and 2, the expressions for the matrices containing these probabilities are

$$R^L = \begin{pmatrix} 1 - P_L & P_L & 0 \\ P_L & 1 - P_L & 0 \\ 0 & 0 & 1 \end{pmatrix}, \tag{2.63}$$

$$R^H = \begin{pmatrix} 1 & 0 & 0 \\ 0 & 1 - P_H & P_H \\ 0 & P_H & 1 - P_H \end{pmatrix}. \tag{2.64}$$

In the factorization approximation and considering a "2 + 1" propagation, the survival probability for an electron neutrino is

$$P(\nu_e \to \nu_e) = \left(|U_{e1}|^2 \; |U_{e2}|^2 \; |U_{e3}|^2 \right) R^L R^H \begin{pmatrix} |\widetilde{U}_{e1}|^2 \\ |\widetilde{U}_{e2}|^2 \\ |\widetilde{U}_{e3}|^2 \end{pmatrix}. \tag{2.65}$$

In the normal hierarchy scenario, one obtains

$$P(\nu_e \to \nu_e) = P_L P_H |U_{e1}|^2 + (1 - P_L) P_H |U_{e2}|^2 + (1 - P_H) |U_{e3}|^2. \tag{2.66}$$

While in the inverted hierarchy scenario, the survival probability becomes

$$P(\nu_e \to \nu_e) = P_L |U_{e1}|^2 + (1 - P_L) |U_{e2}|^2. \tag{2.67}$$

For antineutrinos, we have to consider that they can experience the H-resonance only in inverted hierarchy. By considering the expression of the antineutrino non-adiabaticity parameters $\bar{\Gamma}_{ij}$ (same as in eq. (2.60) but with a bar over all quantities) and the matter angle values at the neutrino-sphere given in table 2.2, we deduce that the H-resonance associated to $\widetilde{\bar{\theta}}_{13}$ connects states 1 and 3. The matrix containing the hopping probability is written as

$$\bar{R}^H = \begin{pmatrix} 1 - \bar{P}_H & 0 & \bar{P}_H \\ 0 & 1 & 0 \\ \bar{P}_H & 0 & 1 - \bar{P}_H \end{pmatrix}. \tag{2.68}$$

In this expression, $\bar{P}_H$ is the probability associated to the H-resonance. Then the survival probability for an electron antineutrino is in normal hierarchy

$$P(\bar{\nu}_e \rightarrow \bar{\nu}_e) \quad = \quad |\bar{U}_{e1}|^2. \tag{2.69}$$

In inverted hierarchy one obtains

$$P(\bar{\nu}_e \rightarrow \bar{\nu}_e) \quad = \quad \bar{P}_H \, |\bar{U}_{e1}|^2 + (1 - \bar{P}_H) \, |\bar{U}_{e3}|^2. \tag{2.70}$$

On figure 2.13, we show the locations of the H and L-resonances, in the neutrino and/or antineutrino channel, depending on the considered mass hierarchy.
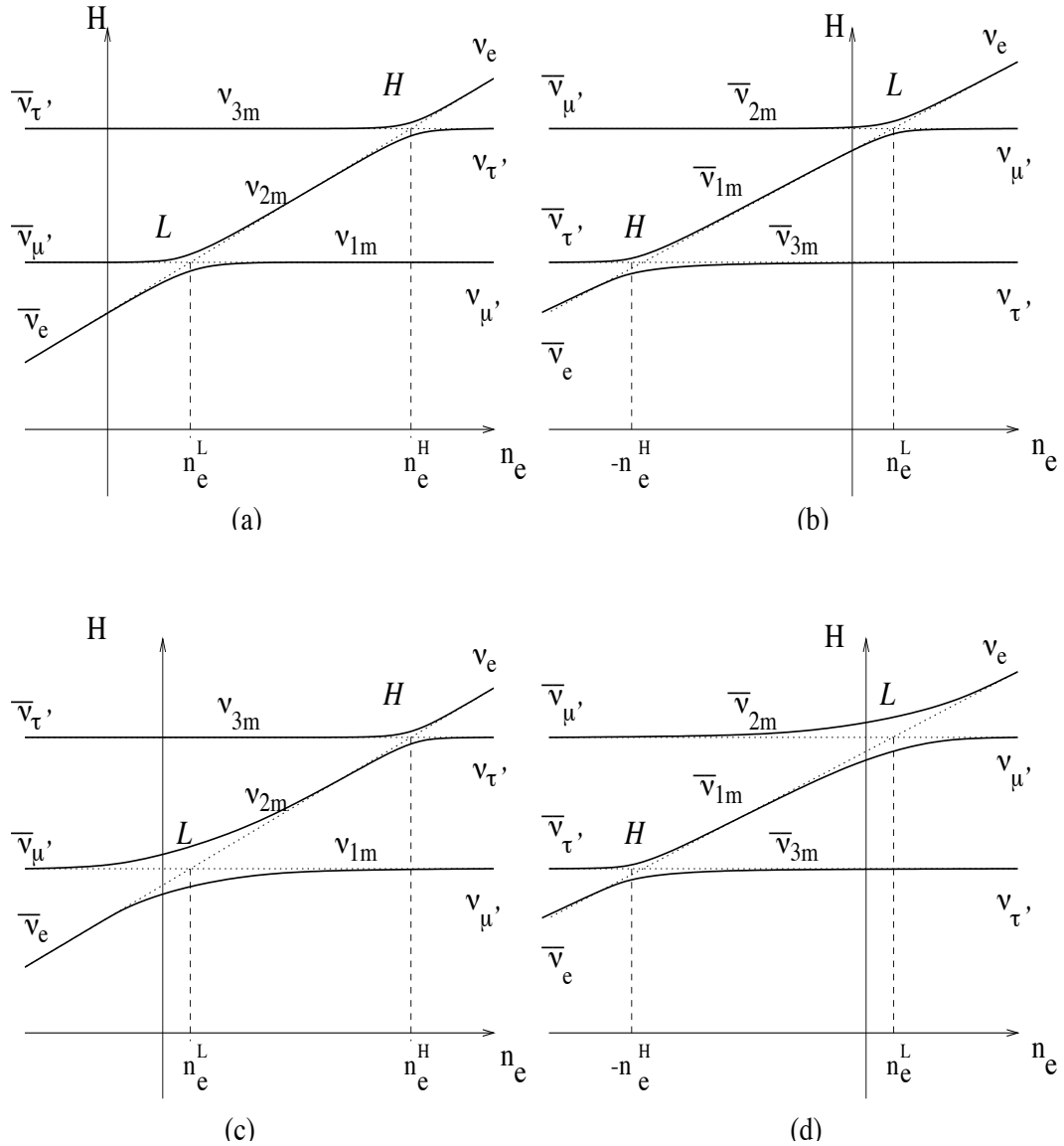
Figure 2.13 – *The level crossing diagrams for (a) the normal hierarchy and small θ_{Sun}, (b) the inverted hierarchy and small θ_{Sun}, (c) the normal hierarchy and large θ_{Sun}, (d) the inverted hierarchy and largeθ_{Sun}. Solid lines show the eigenvalues of the effective Hamiltonian as a function of the electron number density. The dashed lines correspond to energies of flavor levels ν_e, $\nu_{\mu'} = c_{23}\nu_\mu - s_{23}\nu_\tau$ and $\nu_{\tau'} = s_{23}\nu_\mu + c_{23}\nu_\tau$. The part of the plot with $n_e < 0$ corresponds to the antineutrino channel. Taken from [104].*

Adiabaticity of the propagation

An insightful study of the effects of the progenitor was made by Lunardini and Smirnov [105]. By adopting an inverse power law profile and one can distinguish, for the H-resonance, three regimes in the parameter space of θ_{13}:

1. The adiabatic regime where

$$\sin^2 \theta_{13} \gtrsim 10^{-4} \left(\frac{E}{10 \, \mathrm{MeV}} \right)^{2/3}. \tag{2.71}$$

   In this regime, we have $P_H = 0$ for the normal hierarchy or $\bar{P}_H = 0$ for the inverted hierarchy.

2. The non-adiabatic regime where

$$\sin^2 \theta_{13} \lesssim 10^{-6} \left(\frac{E}{10 \, \mathrm{MeV}} \right)^{2/3}. \tag{2.72}$$

   In this regime, we have $P_H = 1$ for the normal hierarchy or $\bar{P}_H = 1$ for the inverted hierarchy.

3. The transition regime where

$$\sin^2 \theta_{13} \sim (10^{-6} - 10^{-4}) \left(\frac{E}{10 \, \mathrm{MeV}} \right)^{2/3}. \tag{2.73}$$

   In this regime, P_H (or $\bar{P}_H$) takes an intermediate value.

The L-resonance is directly related to the solar MSW resonance and is adiabatic so a good approximation is to take $P_L = 0$.

Fluxes on Earth

By using the factorization method explained previously, we can calculate the flux of electron neutrinos received on Earth and coming from a supernova. In most of the studies, it is considered that ν_μ and ν_τ have the same fluxes at the neutrino-sphere. This is due to the fact that they are emitted at the neutrino-sphere with the same average energies i.e. $\langle E_{\nu_\mu} \rangle = \langle E_{\nu_\tau} \rangle$. So at the beginning of the propagation, ν_e's are distributed according to a flux $F^0_{\nu_e}$, ν_μ and ν_τ's are distributed according to another flux $F^0_{\nu_x}$ with $x = \mu, \tau$.

To calculate the electron neutrino flux on Earth, we just have to multiply the initial fluxes by the survival and transition probabilities. Then at a distance r from the supernova, the electron fluxes are [104]

$$\begin{aligned} F_{\nu_e}(r) &= P(\nu_e \to \nu_e) \, F^0_{\nu_e} + (P(\nu_e \to \nu_\mu) + P(\nu_e \to \nu_\tau)) \, F^0_{\nu_x} \\ &= p \, F^0_{\nu_e} + (1-p) \, F^0_{\nu_x}, \end{aligned} \tag{2.74}$$

and

$$F_{\bar{\nu}_e}(r) = \bar{p} \, F^0_{\bar{\nu}_e} + (1 - \bar{p}) \, F^0_{\bar{\nu}_x}. \tag{2.75}$$

The expressions of p and $\bar{p}$ depend on the hierarchy. The explicit expressions are given in eqs. (2.66) and (2.67) for neutrinos and in eqs. (2.69) and (2.70) for antineutrinos.

2.4 SHOCK WAVE EFFECTS UPON NEUTRINO FLAVOR CONVERSION

In the previous section, we focused on neutrino flavor conversion (MSW resonances) with a static matter density profile. Actually at the end of the life of a star, shock waves are engendered by the rebounce of the falling matter on the iron core. As a result, the matter density profile is not static but dynamic [20]. The dynamic of the density profile also reveals a much more complex shape. We will see that this dynamic shape engenders multiple H-resonances which give rise to a new effect: the phase effects [21]. These phase effects correspond to interferences between the multiple H-resonances where the factorization approximation breaks down.

The modified density profile taken from [20] has been used in [90] to study how the shock wave can affect the neutrino propagation and in the first work [24] of this thesis to explore the consequences on the diffuse supernova neutrino background.

2.4.1 Shock waves in supernovae

The dynamic density profile that we used in our calculations is extracted from a hydrodynamic code [20] based on Woodward and Colella's piecewise parabolic method [106]. In this code, the progenitor profile has a spherical symmetry so the density profile is in 1D. As we can see on figure 2.14, the initial density profile is divided in three pieces: the dense core (A), the standing accretion shock (B) and the collapsing progenitor (C). To drive the explosion, the neutrino heating is imitated by inserting energy which is proportional to the density of the material (falling as r^{-2}) and decreases exponentially with time t over a time scale $\tau = 0.5$ s.
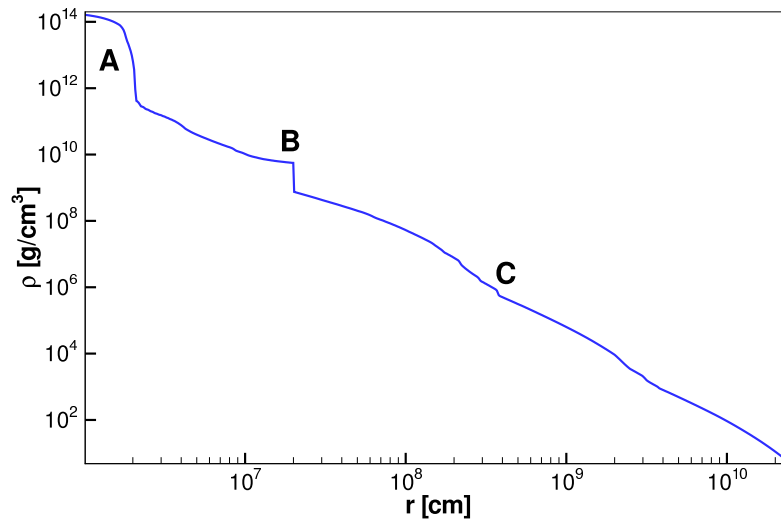
Figure 2.14 – *The initial, $t = 0$, density profile used in our supernova calculations. The dense core (A) inside 20 km contains approximatively 3 $M_\odot$. The slow, outward-moving standing accretion shock (B) is located at 200 km. Above that we have a collapsing, 13.2 $M_\odot$, progenitor (C). Taken from [20].*

The forward shock

After the revival induced by the introduction of the heating, the shock propagates out through the star. As we see on figure 2.15, the forward shock is defined by a significant jump in the density profile. The consequence of this modification is the increase of the steepness of the density profile compared to the part before the forward shock. The steepness of the profile has an impact on the adiabaticity (as shown in section 1.2.4) seen by neutrinos. Indeed, neutrinos which feel the density profile before the arrival of the forward shock are prone to an adiabatic conversion whereas the ones which arrive during the forward shock feel a non-adiabatic propagation. As a result, the survival probabilities and the fluxes are completely different according to time.
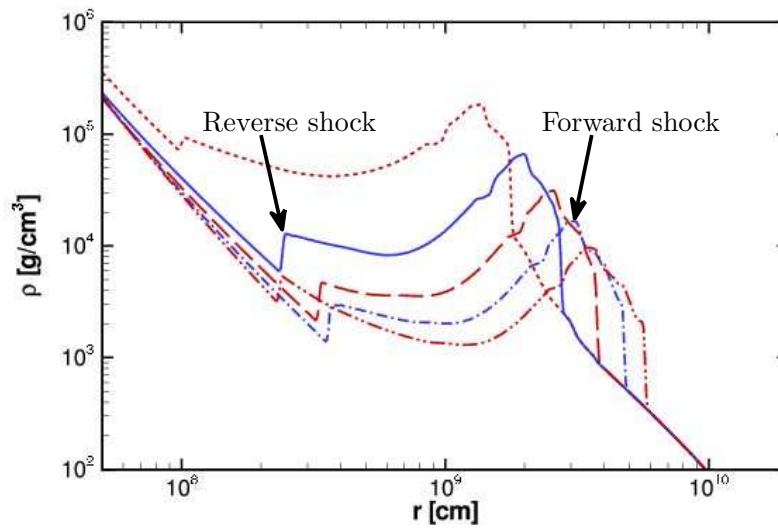
Figure 2.15 – *The density as a function of the radius in a 1D supernova model at $t = 1$ s (dotted line), $t = 1.5$ s (solid), $t = 2$ s (long dashed), $t = 2.5$ s (dash-dot) and $t = 3$ s (dash double-dot). The forward and the reverse shocks are indicated by arrows. Taken from [20].*

The reverse shock

The heating that regenerated the forward shock continues to accelerate the material above the PNS even after the shock has been revived and is moving outwards. Then a wind is created with a velocity that increases with radius. A reverse shock is thus formed when the material velocity is larger than the local sound speed. In opposition to the forward shock, the reverse shock is not present in the initial profile, it develops afterwards. Also, the energy deposit has to be large otherwise the wind is not enough strong and the reverse shock cannot develop.

The reverse shock is characterized by a small jump in the profile as shown on figure 2.15. This jump is smaller than the one induced by the forward shock. In the simulations used, because the energy deposit decreases exponentially with time, the strength of the created wind also decreases gradually. Consequently, the outward motion of the reverse shock slows and can eventually be stopped. After it stalls, the reverse shock moves back towards the core.

2.4.2 Multiple H-resonances and phase effects

As mentioned, the presence of the forward shock in the density has dramatic consequences on the adiabaticity of the propagation. The propagation passes from an adiabatic to a non-adiabatic evolution. Moreover, as shown on figure 2.16, between the forward and reverse shock, the density profile has a specific shape that enables neutrinos to experience more than one MSW resonance because they encounter the density corresponding to the fulfillment of the MSW condition more than once.
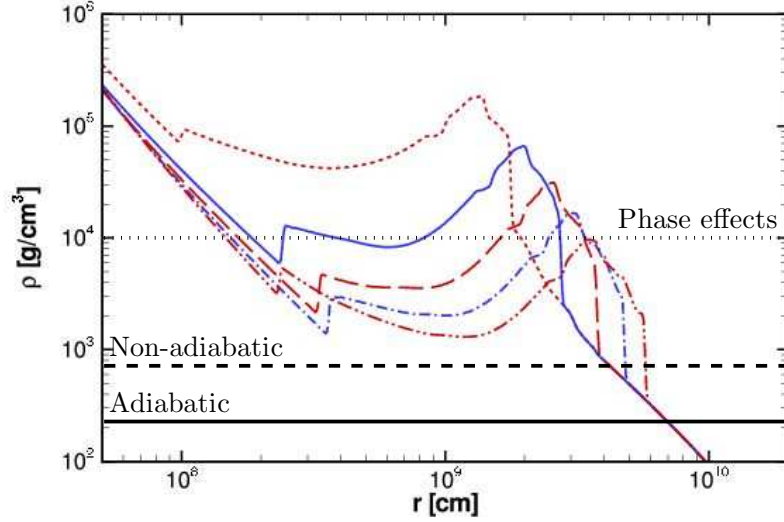
Figure 2.16 – *Evolution of the density profile as a function of the distance and with time. The induced modification of the adiabaticity of the propagation is indicated. By taking the solid blue line as reference, the MSW resonance density can imply an adiabatic propagation (solid black line), a non-adiabatic propagation (dashed black line) and phase effects (dotted black line).*

As an example, for a neutrino with an energy of 20 MeV, the density value that gives rise to MSW H-resonance (see eq. (1.71)) is

$$\rho = \frac{|\Delta m^2_{31}|}{2\sqrt{2}G_F Y_e\, E} \cos 2\theta_{13}\, m_n \simeq 10^4 \text{ g.cm}^{-3}, \tag{2.76}$$

where the mass difference is $|\Delta m^2_{31}| = 2.4 \times 10^{-3}$ eV^2, the electron fraction is equal to $Y_e = 0.5$ and the vacuum mixing angle $\theta_{13} = 9°$. We remark on figure 2.16 that this neutrino crosses the density profile 5 times at $t = 1.5$ s. The main difference with the density profile considered without the shock is the interference among multiple resonances. While the separation between H and L-resonances is legitimate because of their spatial gap, we cannot study the multiple resonances engendered by the shock independently. The coherence between the neutrino matter eigenstates is maintained and we have to compute the amplitudes of neutrino flavor conversions at the H-resonances to keep track of the relative phases. This gives rise to the "phase effects" that we explain following the work of Dasgupta and Dighe in [21].

Analytical treatment

To simplify the approach, we only consider that a neutrino with an energy E propagating through the supernova encounters twice the density ρ_R corresponding to its H-resonance. These two resonances $R_{1,2}$ are located at $x = x_{1,2}$. We also assume that the propagation of neutrino matter eigenstates is adiabatic everywhere except in the region (x_{1-}, x_{1+}) and (x_{2-}, x_{2+}) around the resonance points. Far away before the H-resonance, where $x \ll x_1$ and $\rho(x) \gg \rho_R$, the heavier matter eigenstate ν_H is approximatively equal to the electronic flavor eigenstate ν_e. So initially, we have

$$\nu_e(x \ll x_1) \approx \nu_H. \tag{2.77}$$

ν_H propagates adiabatically till it reaches the resonance region x_1. Just after the resonance point, at x_{1+}, ν_e is a linear combination of the heavy and light matter eigenstates ν_H and ν_L (considering a semi-adiabatic propagation)

$$\nu_e(x_{1+}) = \cos \chi_1 \nu_H + \sin \chi_1 \nu_L, \tag{2.78}$$

where $P_1 = \sin^2 \chi_1$ would be the jump probability at R_1 if the resonance was isolated. Between the two points x_{1+} and x_{2-}, the matter eigenstates only acquire a relative phase and then before the resonance R_2, we have

$$\nu_e(x_{2-}) = \cos \chi_1 \nu_H + \sin \chi_1 \exp \left(\imath \int_{x_1}^{x_2} \frac{\Delta \tilde{m}^2}{2E} dx \right) \nu_L, \tag{2.79}$$

where $\Delta \tilde{m}^2$ is the mass squared difference between ν_H and ν_L given by eq. (1.68) with $\Delta \tilde{m}^2 \equiv 2E \, \delta \tilde{k}_{12}$. As for the resonance R_1, the resonance R_2 may be parametrized as

$$\begin{pmatrix} \nu_H(x_{2+}) \\ \nu_L(x_{2+}) \end{pmatrix} = \begin{pmatrix} \cos \chi_2 & \sin \chi_2 \\ -\sin \chi_2 & \cos \chi_2 \end{pmatrix} \begin{pmatrix} \nu_H(x_{2-}) \\ \nu_L(x_{2-}) \end{pmatrix}. \tag{2.80}$$

Like P_1, $P_2 = \sin^2 \chi_2$ would be the jump probability at R_2 if the resonance was isolated.

At a distance $x \gg x_{2+}$, the matter eigenstates become the mass eigenstates and decohere from one another. Then the survival probability for a ν_e is

$$P(\nu_e \to \nu_e) = \cos^2(\chi_1 - \chi_2) - \sin 2\chi_1 \sin 2\chi_2 \sin^2 \left(\int_{x_1}^{x_2} \frac{\Delta \tilde{m}^2}{4E} dx \right). \tag{2.81}$$

The last term $\sin^2 \left(\int_{x_1}^{x_2} \Delta \tilde{m}^2 / 4E dx \right)$ is the oscillatory term that gives rise to oscillations in the survival probability pattern (see figure 2.17 b).

From eq. (2.81), we can extract conditions about the presence of phase effects in the survival probability behavior. First, if one of the resonances involved in the multiple resonances is completely adiabatic then its related angle is $\chi_i = 0$. As a result, the term $\sin 2\chi_i$ is zero and thus the contribution of the oscillatory term vanishes. It is also the case if one resonance is completely non-adiabatic. Then we have $\chi_i = \pi/2$ and we obtain the same consequence because $\sin 2\chi_i = 0$. So, in order to see the effects of the interference term, we need the resonances to be semi-adiabatic. This is possible for a range of values of $\sin^2 \theta_{13} \sim (10^{-6} - 10^{-4}) (E/10 \, \mathrm{MeV})^{2/3}$ as mentioned in section 2.3.

Secondly the loss of coherence between matter eigenstates is another reason of the
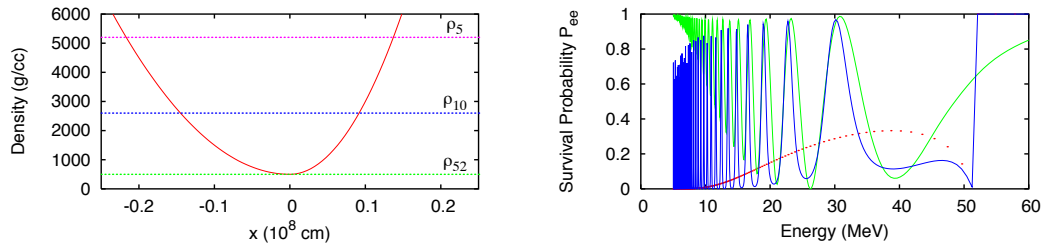
(a) Density profile $\rho(x) = a + (b_1\Theta(x) + b_2\Theta(-x))x^2$ with $a = 500\,\text{g.cm}^{-3}$, $b_1 = 10^5\,\text{g.cm}^{-3}.(10^8\,\text{cm})^{-2}$ and $b_2 = 2.5 \times 10^5\,\text{g.cm}^{-3}.(10^8\,\text{cm})^{-2}$. The horizontal lines are the resonance densities for three energies (5, 10, 52 MeV) taking $\theta = 1.1\,°$.

(b) Survival probability $P(\nu_e \rightarrow \nu_e)$ as a function of the energy for $\theta = 5.7\,°$. The convention for the lines is the same as that used in figure (a).

Figure 2.17 – *Simplified density profile (a) used in [21] to reproduce the phase effects (b).*

absence of phase effects. The decoherence between two matter eigenstates can be due to the separation of the wave packets or the finite energy resolution of a detector. The expression of the distance over which the wave packets separate, the coherence length L_{coh}, is [107]

$$L_{\text{coh}} \sim \frac{4\sqrt{2}\sigma E^2}{\Delta m^2},\qquad(2.82)$$

where σ is the width of the wave packet at source. Taking $\sigma \sim 10^{-9}$ cm near the neutrino-sphere [108] in the energy range [5, 80] MeV, we find $L_{\text{coh}} \sim 10^8 - 10^{10}$ km. If the distance separating two resonances is larger than L_{coh} then the resonances may be taken to be incoherent. Since the distances involved are of the order of 10^9 km (see fig. 2.16), the coherence between eigenstates is conserved and multiple resonances can induce phase effects in the survival probability pattern.

2.5 NEUTRINO SELF-INTERACTION

In the section 2.1.2, we have seen that during the collapse of a star producing a supernova, 99% of its energy is released by neutrinos. Close to the neutrino-sphere, where neutrinos start to stream freely, the neutrino density is so high compared to the matter density that the neutrino self-interactions become dominant in comparison with the neutrino-matter interactions. We first introduce the theoretical framework of neutrino self-interaction in the bulb model. Then we calculate the neutrino self-interaction Hamiltonian in the mean field approximation. We also present another approximation that we used in our calculations and works: the single-angle approximation. This neutrino self-interaction implies features that are completely new in the neutrino propagation: the synchronization region, the bipolar oscillations and the spectral split phenomenon. Finally, we shortly present these new features because they are the subject of chapter 4 where another approach to these features is studied.

2.5.1 Neutrino self-interaction effective Hamiltonian

Neutrinos (and antineutrinos) interact with each other via a neutral-current interaction mediated by the Z^0 boson (see fig.2.18). Because we are dealing with en-

ergies that are much lower than the mass of the Z^0 boson, the effective Hamiltonian of the neutrino self-interaction is

$$H_{\nu\nu}^{NC} = \frac{G_F}{\sqrt{2}} \sum_{\alpha=e,\mu,\tau} \overline{\nu}_{\alpha L} \gamma^\mu \nu_{\alpha L} \sum_{\beta=e,\mu,\tau} \overline{\nu}_{\beta L} \gamma_\mu \nu_{\beta L}, \tag{2.83}$$

where $\nu_{\alpha L} = (1 - \gamma^5)\nu_\alpha$ are the left-handed fermions.
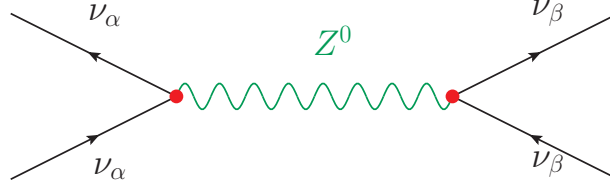
Figure 2.18 – *Neutrino-neutrino scattering Feynman diagrams mediated with the Z^0 boson. α and β represent all the possible flavors for neutrinos namely e, μ and τ.*

Contrary to the matter interaction, the propagation of neutrinos is now affected by the other flavors present in the medium. This new interaction implies that the Hamiltonian becomes non-linear because neutrinos interact with themselves. Also the oscillation of a particular neutrino is affected by ν_e's, ν_μ's and ν_τ's when it travels. The background composed of all possible neutrinos is much more complex because neutrinos can oscillate and then modify the flavor content of this gas. The density and the composition of the medium evolve with the distance from the neutrino-sphere. This new feature in the neutrino propagation was first pointed out by Pantaleone and Samuel [109, 70].

For the calculation of the effective Hamiltonian, we only consider two flavors (e and μ) for simplicity but the demonstration can be extended to the three flavors case. We approximate the left-handed current $\overline{\nu}_{\alpha L} \gamma^\mu \nu_{\alpha L}$ by its background value $\langle \overline{\nu}_{\alpha L} \gamma^\mu \nu_{\alpha L} \rangle$. This approach is similar to the mean field approximation already used for the derivation of the effective matter Hamiltonian (see section 1.2.2). By applying the approximation to our Hamiltonian, all the possible contractions are

$$\begin{aligned}
\overline{\nu}_{\alpha L} \gamma^\mu \nu_{\beta L}\, \overline{\nu}_{\gamma L} \gamma_\mu \nu_{\delta L} \quad \rightarrow \quad & \overline{\nu}_{\alpha L} \gamma^\mu \nu_{\beta L} \langle \overline{\nu}_{\gamma L} \gamma_\mu \nu_{\delta L} \rangle + \langle \overline{\nu}_{\alpha L} \gamma^\mu \nu_{\beta L} \rangle \overline{\nu}_{\gamma L} \gamma_\mu \nu_{\delta L} \\
& + \overline{\nu}_{\alpha L} \gamma^\mu \nu_{\delta L} \langle \overline{\nu}_{\gamma L} \gamma_\mu \nu_{\beta L} \rangle + \langle \overline{\nu}_{\alpha L} \gamma^\mu \nu_{\delta L} \rangle \overline{\nu}_{\gamma L} \gamma_\mu \nu_{\beta L} \\
& - \langle \overline{\nu}_{\alpha L} \gamma^\mu \nu_{\beta L} \rangle \langle \overline{\nu}_{\gamma L} \gamma_\mu \nu_{\delta L} \rangle + \langle \overline{\nu}_{\alpha L} \gamma^\mu \nu_{\delta L} \rangle \langle \overline{\nu}_{\gamma L} \gamma_\mu \nu_{\beta L} \rangle.
\end{aligned} \tag{2.84}$$

The first two terms in eq. (2.84) are the Hartree part of a Hartree-Fock approximation. The third and fourth terms are 'exchange interactions' and enter additively because of the Fermi statistics. The last two terms contribute to the vacuum energy. One subtlety is that the off-diagonal backgrounds $\langle \overline{\nu}_{eL} \gamma_\mu \nu_{\mu L} \rangle$ and $\langle \overline{\nu}_{\mu L} \gamma_\mu \nu_{eL} \rangle$ cannot be set to zero because neutrinos are not massless and they can mix. Even if at the neutrino-sphere these terms vanish, they can become non-zero during the evolution of neutrinos in the supernova medium.

By considering the complete system composed of ν_e and ν_μ, the expressions for the neutrino background is

$$\langle \overline{\nu}_{\alpha L} \gamma_\mu \nu_{\beta L} \rangle (\mathbf{x}, t) = \sum_{j \neq i} \overline{\nu}_{\alpha L}^{(j)} \gamma_\mu \nu_{\beta L}^{(i)}, \tag{2.85}$$

where $\mathbf{x}$ and t are the space and time dependence. In practice, the system has symmetries which simplify the analysis. For example, if we consider a homogeneous isotropic gas in a large box of volume V then the spatial component of the lepton current is zero and only the temporal component remains. One obtains

$$\langle \overline{\nu}_{\alpha L} \gamma_\mu \nu_{\beta L} \rangle = \frac{1}{V} \int_V d^3x \, \overline{\nu}_{\alpha L} \gamma_0 \nu_{\beta L}. \tag{2.86}$$

The flavor-diagonal currents are number densities since

$$\frac{1}{V} \int_V d^3x \, \overline{\nu}_{eL} \gamma_0 \nu_{eL} = \rho_{\nu_e}(t) - \rho_{\bar{\nu}_e}(t), \tag{2.87}$$

$$\frac{1}{V} \int_V d^3x \, \overline{\nu}_{\mu L} \gamma_0 \nu_{\mu L} = \rho_{\nu_\mu}(t) - \rho_{\bar{\nu}_\mu}(t). \tag{2.88}$$

To express the effective Hamiltonian, we need to take into account the differential number of neutrinos $dn_{\nu_\alpha}(\mathbf{q})$ for a momentum $\mathbf{q}$. Also in a non homogeneous, still isotropic, environment we add a geometric factor $(1 - \hat{\mathbf{q}}.\hat{\mathbf{q}}')$ [3] to take into account that neutrinos interact with themselves with a certain angle. To compact the notation we use the density matrices (see appendix B.2) defined as

$$\rho_{\nu_\underline{\alpha}}(t) = \begin{pmatrix} |\nu_e|^2 & \nu_e \nu_\mu^* \\ \nu_e^* \nu_\mu & |\nu_\mu|^2 \end{pmatrix} \quad \text{and} \quad \rho_{\bar{\nu}_\underline{\alpha}}(t) = \begin{pmatrix} |\bar{\nu}_e|^2 & \bar{\nu}_e \bar{\nu}_\mu^* \\ \bar{\nu}_e^* \bar{\nu}_\mu & |\bar{\nu}_\mu|^2 \end{pmatrix}, \tag{2.89}$$

where $\underline{\alpha}$ specifies the initial condition at $t = 0$ at the neutrino-sphere. It corresponds to a neutrino (or antineutrino) born with a certain flavor $\alpha = e, \mu$. Finally, the effective Hamiltonian representing the neutrino-neutrino forward scattering in two flavors is

$$H_{\nu\nu}^{\text{NC}} = \sqrt{2} G_F \sum_{\alpha=e,\mu} \left[\iint (1 - \hat{\mathbf{q}}.\hat{\mathbf{q}}') \rho_{\nu_\underline{\alpha}}(\mathbf{q}') dn_{\nu_\underline{\alpha}}(\mathbf{q}') \, dq' - \int (1 - \hat{\mathbf{q}}.\hat{\mathbf{q}}') \rho_{\bar{\nu}_\underline{\alpha}}^*(\mathbf{q}') dn_{\bar{\nu}_\underline{\alpha}}(\mathbf{q}') \, dq' \right]. \tag{2.90}$$

For the three flavors case, the expression of the effective Hamiltonian is exactly the same. One just has to extend the sum from $\alpha = e, \mu$ to $\alpha = e, \mu, \tau$.

2.5.2 The bulb model

In reference [19], Duan et al. introduced the neutrino bulb model used also in this thesis. To simplify the numerical calculations of the flavor transformations of neutrinos and antineutrinos, this model approximates the physical and geometric conditions of the post-bounce supernova. The assumptions are

1. The neutron star emits neutrinos uniformly and isotropically from the surface of the neutrino-sphere of radius R_ν.

2. At any point outside the neutrino-sphere, the physical conditions (such as baryon density ρ_B, temperature T,...) depend only on the distance r from this point to the center of the neutron star.

3. Neutrinos are emitted from the neutrino-sphere in a pure flavor eigenstates and with Fermi-Dirac or power law type energy spectra.

As illustrated in figure 2.19, the neutrino bulb model has some symmetries. The spherical symmetry of the object allows us to only study the physical conditions along one radial direction which we choose to be the z-axis. Also from the

---

3. A hatted vector $\hat{\mathbf{q}}$ denotes the direction of the vector $\mathbf{q}$

geometric picture, we remark a cylindrical symmetry for the neutrino flux at any given point on the z-axis. As a consequence, neutrino beams with the same polar angle with respect to the z-axis and with the same initial physical properties should be equivalent. They will have the same evolution stories. Alternatively, a beam can be specified by the polar angle $\Theta = \widehat{COB}$, the angle between the z-axis and the beam $\theta = \widehat{CPB}$, or the emission angle at the neutrino-sphere $\theta_0 = \widehat{OBA}$ since $\theta_0 = \Theta + \theta$. At a given point P on the z-axis, the neutrino flux has a cylindrical symmetry defined by its opening angle θ. This angle is restricted in the range $[0, \arcsin(R_\nu/r)]$ where $\theta = 0$ is equivalent to an emission angle θ_0 equal to 0 and $\theta = \arcsin(R_\nu/r)$ corresponds to $\theta_0 = \pi/2$. Because of the assumptions 1 and 2 in the neutrino bulb model, all the neutrino beams with the same emission angle θ_0 and the same initial properties must be equivalent.

Figure 2.19 – *Geometric picture of the neutrino bulb model. A neutrino (solid line) is emitted from the point B on the neutrino-sphere with polar angle Θ. The beam intersects the z-axis at point P with angle θ. Because neutrinos are emitted from a radius R_ν, point P only sees neutrinos traveling within the cone delimited by the dashed line. The main characteristic of the neutrino beam is its emission angle θ_0, defined with respect to the normal direction at the point of emission.*

At any given radius $OP = r$, all the geometric properties of a neutrino beam may be calculated using r and θ_0. Defining the two distances

$$AP = l = r\cos\theta \quad \text{and} \quad AB = l_0 = R_\nu \cos\theta_0, \tag{2.91}$$

where $l - l_0 = BP$ is the total propagation distance along the neutrino beam, we find the identity

$$\frac{\sin\theta}{R_\nu} = \frac{\sin\Theta}{l - l_0} = \frac{\sin\theta_0}{r}. \tag{2.92}$$

In eq. (2.90), the differential number density of neutrinos dn_{ν_α} is also present so we need to calculate it at a radius r. The calculation for antineutrinos is similar. The differential number density of neutrinos $dn_{\nu_\alpha}(\mathbf{q})$ has contribution from all ν_α with energy q which propagate in directions within the range between $\hat{\mathbf{q}}$ and $\hat{\mathbf{q}} + d\hat{\mathbf{q}}$. We now define the number flux of ν_α as $j_{\nu_\alpha}(q)$. The corresponding number of neutrinos emitted at the neutrino-sphere radially through the spherical differential area per unit time is (figure 2.20)

$$dN_{\nu_\alpha} = j_{\nu_\alpha}(q)\, R_\nu^2 \sin\Theta d\Theta d\Phi. \tag{2.93}$$

Regarding to the point P, we only take into account the neutrino beam inside the cone defined by its opening angle θ so emitted with an angle θ_0. Then we have

Figure 2.20 – *Geometric picture of the neutrino bulb model in 3D.*

to multiply the differential number of neutrinos dN_{ν_α} by a factor $\cos\theta_0$, eq. (2.93) becomes

$$dN_{\nu_\alpha} = j_{\nu_\alpha}(q)\,\cos\theta_0\,R_\nu^2\sin\Theta d\Theta d\Phi. \tag{2.94}$$

Here we have looked at the differential number of neutrinos from the point of view of the star, it is also possible to calculate it from the point P. The neutrino-sphere is located at a distance $(l - l_0)$ to the point P, so the expression of the differential number of neutrinos is

$$dN_{\nu_\alpha} = j_{\nu_\alpha}(q)\,(l - l_0)^2\sin\theta d\theta d\phi = (l - l_0)^2\,dn_{\nu_\alpha}. \tag{2.95}$$

As a result, the differential number density of neutrinos dn_{ν_α} is

$$dn_{\nu_\alpha} = \frac{j_{\nu_\alpha}(q)\,\cos\theta_0\,R_\nu^2\sin\Theta d\Theta d\Phi}{(l - l_0)^2} = j_{\nu_\alpha}(q)\,\sin\theta d\theta d\phi. \tag{2.96}$$

By considering the isotropy at the neutrino-sphere, the number of ν_α with energy q emitted per unit time is

$$
\begin{aligned}
N_{\nu_\alpha} &= \int_0^{2\pi}\int_0^1 d(\cos\theta_0)\,d\phi \int dN_{\nu_\alpha}\\
&= 2\pi\int_0^1\int_0^{2\pi}\int_{-1}^1 j_{\nu_\alpha}(q)\,R_\nu^2\,d(\cos\Theta)\,d\Phi\,\cos\theta_0 d(\cos\theta_0)\\
&= 4\pi^2 j_{\nu_\alpha}(q)\,R_\nu^2.
\end{aligned}\tag{2.97}
$$

This flux can be also expressed as

$$N_{\nu_\alpha} = F_{\nu_\alpha}(q), \tag{2.98}$$

where $F_{\nu_\alpha}(q)$ is a Fermi-Dirac distribution as defined in eq. (2.10). Therefore one has

$$j_{\nu_\alpha}(q) = \frac{F_{\nu_\alpha}(q)}{4\pi^2 R_\nu^2}. \tag{2.99}$$

With these formulas, we now reexpress eq. (2.90) in terms of the opening angle θ and the energy q of neutrino beams. The density matrices are then $\rho_\nu(\mathbf{q}) = \rho_\nu(q,\theta)$

and we note that for an arbitrary function $A(\theta)$

$$
\int \hat{\mathbf{q}}.\hat{\mathbf{q}}' A(\theta') \, d\hat{\mathbf{q}}' = \int \begin{pmatrix} \sin\theta\cos\phi \\ \sin\theta\sin\phi \\ \cos\theta \end{pmatrix} . \begin{pmatrix} \sin\theta'\cos\phi' \\ \sin\theta'\sin\phi' \\ \cos\theta' \end{pmatrix} A(\theta') \, d(\cos\theta')d\phi
$$

$$
= 2\pi \int \cos\theta\cos\theta' A(\theta') \, d(\cos\theta'). \qquad (2.100)
$$

We can rewrite eq. (2.90) as

$$
H_{\nu\nu} = \frac{\sqrt{2}G_F}{2\pi R_\nu^2} \sum_{\alpha=e,\mu,\tau} \int d(\cos\theta')dq' \, (1 - \cos\theta\cos\theta')
$$

$$
\left[\rho_{\nu_\alpha}(q',\theta')F_{\nu_\alpha}(q') - \rho^*_{\bar{\nu}_\alpha}(q',\theta')F_{\bar{\nu}_\alpha}(q') \right]. \qquad (2.101)
$$

This Hamiltonian is called the multi-angle neutrino self-interaction Hamiltonian because it takes into account the momentum q and the emission angle (rather the opening angle θ) of the neutrino beam at the interaction point P. Numerically speaking, to solve the propagation of one neutrino, we must consider due to multi-angle neutrino self-interaction Hamiltonian

1. neutrinos and antineutrinos,
2. all the flavors as initial condition,
3. all energies,
4. all angles within the cone.

Obviously, solving the multi-angle neutrino self-interaction Hamiltonian is extremely demanding so we use an approximation called the single angle approximation [19] which still conserves the main and most interesting behaviors of the neutrino survival and transition probabilities.

2.5.3   The single angle approximation

In the single angle approximation, we assume that the flavor evolution history of a neutrino is trajectory independent i.e. $\rho_\nu(q,\theta) = \rho_\nu(q)$. In addition, all neutrinos emitted with an angle θ are assumed to have the same evolution history as the ones emitted e.g. radially, i.e. $\theta = 0$. Therefore, we can factorize the density matrices in eq. (2.101) and the spatial dependence is reduced to

$$
\int_{\theta_{max}}^{0} (1 - \cos\theta') \, d(\cos\theta') = \frac{1}{2}(1 - \cos\theta_{max})^2
$$

$$
= \frac{1}{2}\left(1 - \sqrt{1 - \left(\frac{R_\nu}{r}\right)^2}\right)^2. \qquad (2.102)
$$

In the context of the single angle approximation, the self-interaction Hamiltonian is

$$
H_{\nu\nu} = \frac{\sqrt{2}G_F}{2\pi R_\nu^2} D\left(\frac{R_\nu}{r}\right) \sum_{\alpha=e,\mu,\tau} \iint \left[\rho_{\nu_\alpha}(q')F_{\nu_\alpha}(q') - \rho^*_{\bar{\nu}_\alpha}(q')F_{\bar{\nu}_\alpha}(q') \right] dq'. \ (2.103)
$$

where $D(R_\nu/r)$ is the geometrical factor

$$
D\left(\frac{R_\nu}{r}\right) = \frac{1}{2}\left(1 - \sqrt{1 - \left(\frac{R_\nu}{r}\right)^2}\right)^2. \qquad (2.104)
$$

For large value of the radius r, the geometrical factor varies like $D(R_\nu/r) \sim r^{-4}$. In comparison, the matter density profile in the supernova environment decreases as r^{-3}. So the strength of the neutrino self-interaction decreases faster than the matter interaction strength as shown on figure 2.21.
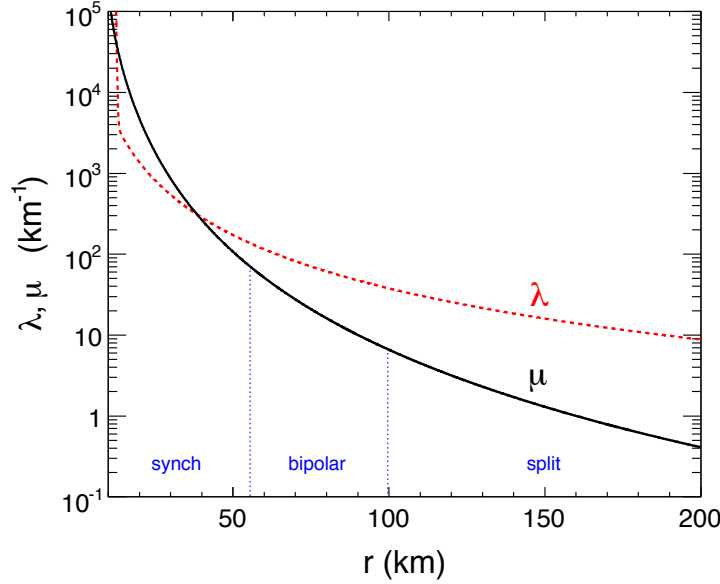
Figure 2.21 – *Radial profiles of the neutrino self-interaction parameter $\mu(r) = \sqrt{2}G_F(N + \overline{N})$ and of the matter interaction parameter $\lambda(r) = \sqrt{2}G_F N_e$. Picture taken from [17].*

2.5.4 Three regimes identified

By including the neutrino self-interaction discussed before, the Schrödinger-like equation for a neutrino propagating in a supernova environment is

$$\imath\frac{\partial}{\partial x}\psi = \left(H^{\text{vac}} + H^{\text{mat}} + H^{\nu\nu}\right)\psi, \tag{2.105}$$

where $H^{\text{vac}} = UKU^\dagger$ is the vacuum Hamiltonian (eq. (1.63)), $H^{\text{mat}} = \sqrt{2}G_F N_e \delta_{\alpha e}$ is the matter interaction Hamiltonian (eq. (1.63)) and $H^{\nu\nu}$ is the neutrino self-interaction Hamiltonian (eq. (2.101) or eq. (2.103)). In a two flavor calculation with $\psi = (\nu_e, \nu_\mu)^T$, a complete simulation in the first hundred kilometers gives us for the neutrino and antineutrino survival probabilities the behavior plotted on figure 2.22 and 2.23. To be sure that, in these regions, we are only focusing on the neutrino self-interaction effects, we chose a matter density profile $N_e(r)$ giving rise to MSW resonances far away from the region where such effects take place. With our matter density profile, the MSW H-resonance occurs at around 200 km for a 20 MeV neutrino energy. We also note that the neutrino self-interaction effects are only visible in inverted hierarchy when equipartition of the luminosity is assumed.

In this paragraph, we explain quantitatively the different regions that have been identified [77, 15, 110] in the survival probabilities without going into details. A qualitative explanation of the neutrino self-interaction effects will be given in
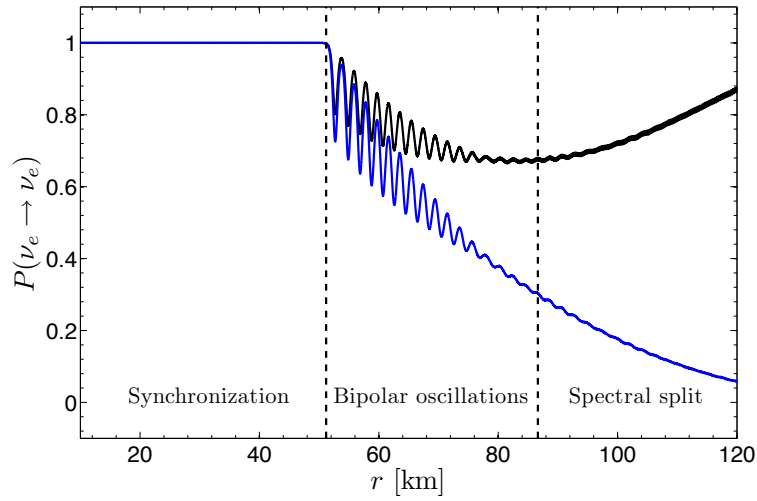
(a) Neutrino survival probability $P(\nu_e \rightarrow \nu_e)$.
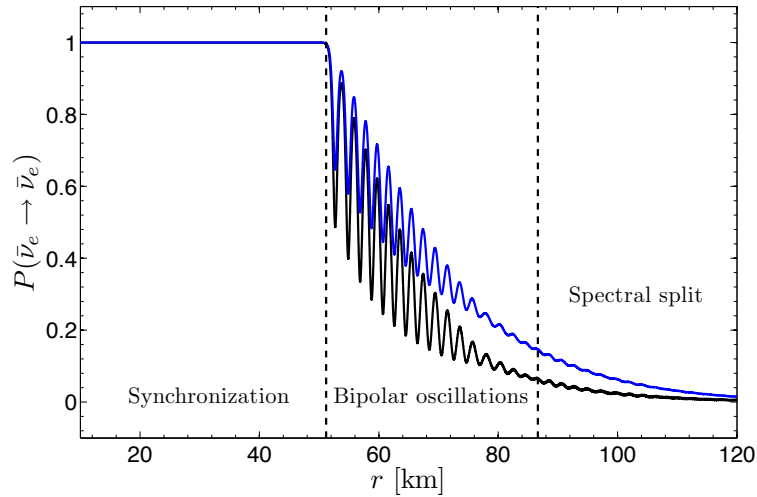
(b) Antineutrino survival probability $P(\bar{\nu}_e \rightarrow \bar{\nu}_e)$.

Figure 2.22 – *Neutrino and antineutrino survival probabilities including the neutrino self-interaction in the single-angle approximation as a function of the distance and the energy from the neutrino-sphere. The results correspond to an inverted hierarchy and $\theta_{13} = 9°$.*

chapter 4.

The synchronized region

When we look at the final survival probabilities on figure 2.22 and 2.23, we distinctly see that in the range from the neutrino-sphere (10 km) to $\sim$ 50 km, neutrinos and antineutrinos are immobilized to their initial condition and $P(\nu_e \rightarrow \nu_e) = P(\bar{\nu}_e \rightarrow \bar{\nu}_e) = 1$ [77]. This part of the propagation is called the "synchronized region" because the effect does not depend on the energy and thus all neutrino energies are synchronized. Actually, the survival probabilities oscillate just below 1, but these variations are non visible due to their smallness.
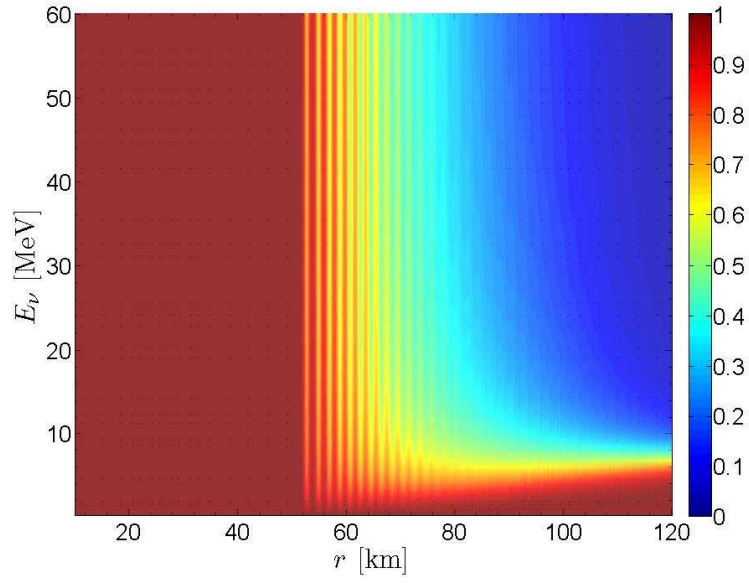
(a) Neutrino survival probability $P(\nu_e \rightarrow \nu_e)$.
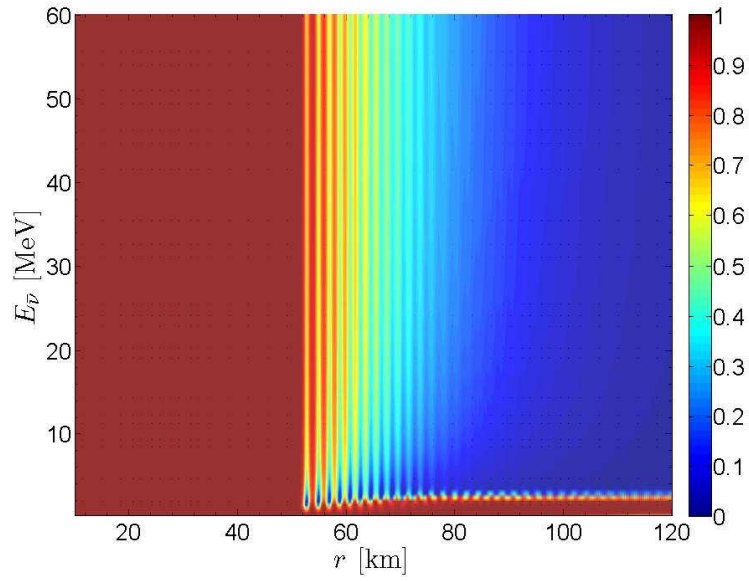
(b) Antineutrino survival probability $P(\bar{\nu}_e \rightarrow \bar{\nu}_e)$.

Figure 2.23 – *Contour plot of the neutrino and antineutrino survival probabilities including the neutrino self-interaction in the single-angle approximation as a function of the distance and of the neutrino energy from the neutrino-sphere. The results correspond to an inverted hierarchy and $\theta_{13} = 9°$.*

Bipolar oscillations

After the synchronized region, in the range $[50, 87\,\text{km}]$, collective flavor conversion occurs between ν_e's and ν_x's. By considering the presence of a constant electron density profile, some quantities are invariant such as the lepton flavor number [15, 111, 112, 113]. This invariant implies that the conversion in the bipolar region is done via the process $\nu_e \bar{\nu}_e \rightarrow \nu_x \bar{\nu}_x$. Also contrary to the synchronization, the bipolar oscillations are energy dependent. The oscillations and the conversion

from the electronic to the other flavor is more or less rapid (see fig. 2.22).

Spectral split

At the end of the bipolar oscillations, a surprising phenomenon takes place: the "spectral split" [15, 111, 25, 26, 112, 113]. The effect is represented on figures 2.22 and 2.23 by an extreme behavior. For a neutrino with an energy $E < E_C \sim 7\,\text{MeV}$, the survival probability goes up to 1. Thus we recover the initial condition for the flavor content that we had at the neutrino-sphere. On the contrary, for a neutrino with an energy $E > E_C$, a total flavor conversion happens and so $P(\nu_e \to \nu_e) \to 0$. This impact on the probabilities is more apparent on the neutrino fluxes (see fig. 2.24). This phenomenon implies a sharp split in the fluxes. The electron flux after the collective effects is composed of the initial electron flavor $F_{\nu_e}^0$ (from 0 to E_C) and the initial muon flavor $F_{\nu_x}^0$ (from E_C to ∞). For antineutrinos, there is also a sharp split but it appears at very small energy ($\sim 2\,\text{MeV}$). So the electron antineutrino flux has almost completely been swapped with the muon flux. A good approximation for the fluxes is to consider:

$$F_{\nu_e} = \begin{cases} F_{\nu_e}^0 \text{ for } E < E_C \\ F_{\nu_x}^0 \text{ for } E > E_C \end{cases} \quad \text{and} \quad F_{\bar{\nu}_e} = F_{\bar{\nu}_x}^0. \tag{2.106}$$

Here we mention the fact that when the equipartition of luminosity is not assumed, the spectral split phenomenon becomes more complex giving rise to multiple spectral splits [85]. Actually, one obtains a second split for neutrinos and antineutrinos at a higher energy. Then the approximation of eq. (2.106) becomes

$$F_{\nu_e} = \begin{cases} F_{\nu_e}^0 \text{ for } E < E_{C1} \text{ and } E > E_{C2} \\ F_{\nu_x}^0 \text{ for } E_{C1} < E < E_{C2} \end{cases} \quad \text{and} \quad F_{\bar{\nu}_e} = \begin{cases} F_{\bar{\nu}_e}^0 \text{ for } E < E_{C3} \\ F_{\bar{\nu}_x}^0 \text{ for } E > E_{C3} \end{cases}. \tag{2.107}$$

CONCLUSION

We have showed that the core-collapse supernovae of type II are also another interesting source of neutrinos and antineutrinos. This type of supernovae releases 99% of its energy through the emission of neutrinos. This large source of neutrinos has led to the study of new neutrino observatories with the LAGUNA project[4]. The principal goal of LAGUNA is to assess the feasibility of a new pan-European research infrastructure able to host the next generation, very large volume, deep underground neutrino observatory such as MEMPHYS, LENA and Glacier.

In the supernova environment, because of the matter density profile, another resonance occurs related to the atmospheric neutrino oscillation parameters in addition to the "solar" resonance when we treat the problem with three flavors. We have seen that the large difference existing between the atmospheric and solar mass squared differences leads to the factorization approximation where the resonances are treated independently. This approximation makes the problem easier and allows us to predict the location of the resonances by applying the resonance conditions that we found for the two flavors case.

---

4. http://www.laguna-science.eu
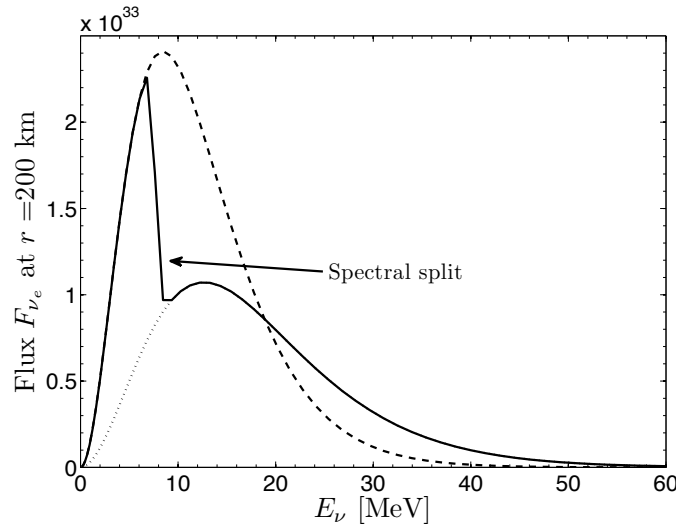
(a) Neutrino flux as a function of the neutrino energy.
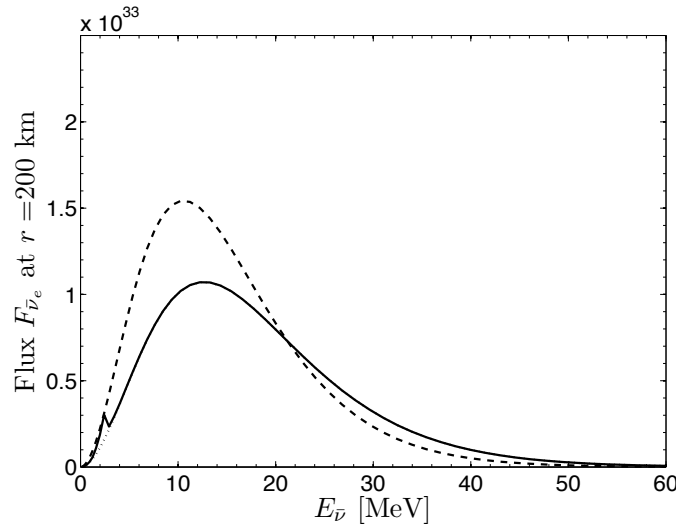
(b) Antineutrino flux as a function of the antineutrino energy.

Figure 2.24 – *Neutrino and antineutrino fluxes after the neutrino self-interaction effects ($\sim$ 200 km) as a function of the energy in the single-angle approximation. The spectral split phenomenon is clearly obvious at $\sim$ 7 MeV for neutrinos and at $\sim$ 3 MeV for antineutrinos. The dashed lines correspond to the initial electron fluxes (neutrinos and antineutrinos), the dotted lines to the initial muon fluxes and the solid lines to the electronic fluxes at $r \sim$ 200 km. The results correspond to an inverted hierarchy, $\theta_{13} = 9°$ and a total luminosity of 4×10^{51} erg.s^{-1}.*

The impressive progress that has been achieved in the last few years makes now possible the realistic study of the neutrino propagation in the supernovae with the presence of the shock wave engendered by the explosion of the star. We showed in section 2.4 that the modification of the density profile from a static to a dynamic profile creates multiple H-resonances that cannot be treated with the factorization approximation. The interference between the multiple H-resonances are visible in the electron neutrino survival probabilities as fast oscillations. The effects of such phenomenon will be studied in the next chapter with the application to the detection of the Diffuse Supernova Neutrino Background.

At the same time, the introduction of the neutrino self-interaction in the neu-
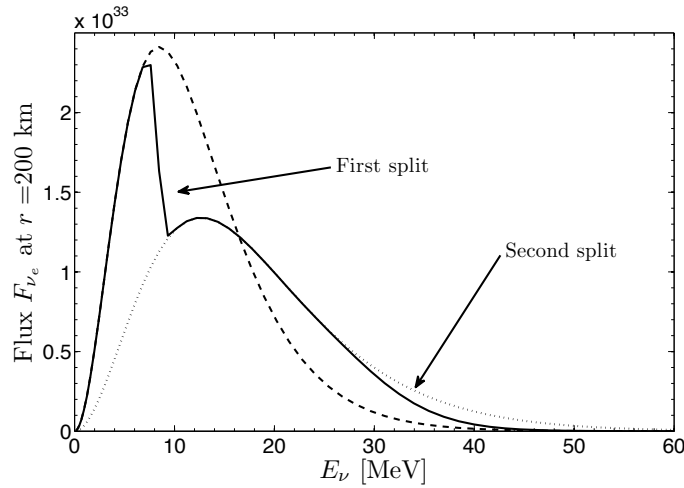
(a) Neutrino flux as a function of the neutrino energy.
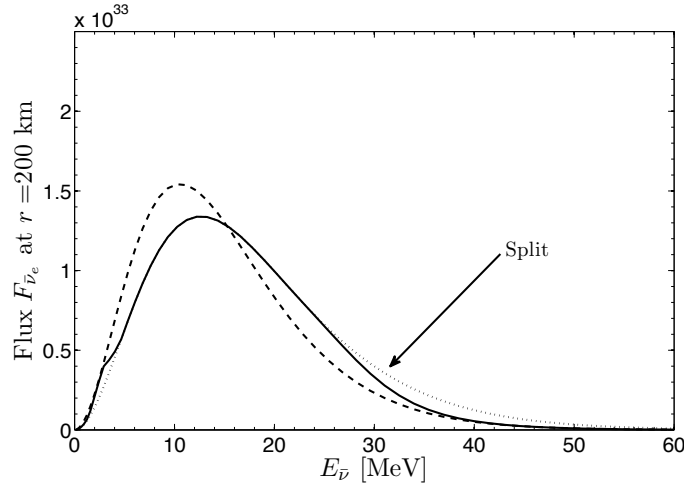
(b) Antineutrino flux as a function of the antineutrino energy.

Figure 2.25 – *Neutrino and antineutrino fluxes after the neutrino self-interaction effects ($\sim$ 200 km) as a function of the energy in the single-angle approximation. The spectral splits are visible at $\sim$ 8 and $\sim$ 35 MeV for neutrinos and at $\sim$ 3 and $\sim$ 30 MeV for antineutrinos. The dashed lines correspond to the initial electron fluxes (neutrinos and antineutrinos), the dotted lines to the initial muon fluxes and the solid lines to the electronic fluxes at $r \sim$ 200 km. The results correspond to an inverted hierarchy, $\theta_{13} = 9°$ and the total luminosity is distributed as $L_{\nu_e} = L_{\bar{\nu}_e} = 10^{51}$ erg.s^{-1} and $L_{\nu_x} = 1.25 \times 10^{51}$ erg.s^{-1}.*

trino propagation inside the supernova has completely changed the known features of the propagation. Indeed, the addition of this new Hamiltonian has revealed new effects much more complex due to their collective nature. These effects are studied very actively in the neutrino astrophysics community and has led to a fruitful literature on this topic. In this chapter, we gave a qualitative introduction to the subject which will be studied in details in chapter 4.

SHOCK WAVE EFFECTS UPON THE DIFFUSE SUPERNOVA NEUTRINO BACKGROUND

3

$\mathcal{T}$HE goal of the first work of this thesis published in [24] is to combine the neutrino self-interaction and the shock wave effects and investigate these effects upon the Diffuse Supernova Neutrino Background (DSNB). This work represents the first realistic study of the neutrino oscillation effects upon DSNB including a dynamic density profile coming from an astrophysical model [20] and a complete calculation for the neutrino propagating in the supernova environment [90].

We first explain in section 3.1 in what consists the DSNB and our motivations about the fact that the DSNB could be detected by the next-generation observatories in the next decade. Then, we present the theoretical model that we used to describe the DSNB fluxes received on Earth whose the main ingredients are the star formation rate and the supernova neutrino spectra. To look for the neutrino self-interaction effects, we also use analytical formulas to calculate the neutrino and antineutrino survival probabilities. These analytical formulas are used to mimic the MSW H and L-resonances but without the phase effects induced by the shock waves because these formulas describe the resonances with independent hopping probabilities. So using the analytical probabilities and turning on or off the neutrino

self-interaction we can search for effects coming from the interaction of neutrinos with themselves.

By keeping the neutrino self-interaction turned on, we present our numerical predictions on the DSNB fluxes and the number of events per kTon per year with the analytical formulas and with the full numerical calculation where the shock wave effects are included. This allows us to search for effects coming from the presence of the shock because shock waves are only considered in the numerical model. Finally, we explain some of the interesting numerical results that we obtained with the assistance of a simple model that we built to account for the shock.

3.1 WHAT IS THE DIFFUSE SUPERNOVA NEUTRINO BACKGROUND?

The diffuse supernova neutrino background (DSNB), sometimes referred to "supernova relic neutrinos", is the flux of neutrinos and antineutrinos emitted by all core collapse supernovae in the causally-reachable Universe. In opposition to standard core collapse supernovae where the received neutrino flux is localized and lasts a finite time, the DSNB flux is isotropic and time-independent. The DSNB results from the neutrino spectrum emitted by newly-formed neutron stars convolved with the rapid redshift evolution of the supernova rate. While the estimated rate of supernovae is 1-3 per century, this DSNB is a guaranteed steady source of supernova neutrinos. Even if the probability of detecting a single neutrino from a distant supernova is infinitesimally small, the number of supernovae per year is astronomically large, yielding to a nonzero rate.

We know that we can potentially discover a DSNB signal in SuperKamiokande detector [22] (see figure 3.1) and in next-generation neutrino observatories (see section 2.2) since current bounds on the DSNB are only a factor of ~ 2 above typical predictions. Most of studies of DSNB limits are focused on detection via $\bar{\nu}_e$ scattering off protons at water Čerenkov detectors and at large liquid scintillator for ν_e and $\bar{\nu}_e$. The current limits from the SK and SNO data at 90% CL are listed in table 3.1. Moreover, we clearly see on figure 3.1 that for antineutrinos, a detectable window is possible for $\bar{\nu}_e$ between the reactor and atmospheric electron antineutrinos. The combination of limits and detection windows encourage us to look for neutrino oscillation effects on the DSNB waiting for a larger neutrino flux coming from a Supernova.

	$\Phi_{\bar{\nu}_e}$	Φ_{ν_e}	$\Phi_{\bar{\nu}_\mu + \bar{\nu}_\tau}$	$\Phi_{\nu_\mu + \nu_\tau}$
$E_\nu > 19.3\,\mathrm{MeV}$	1.2	73.3-154	$(1.0 - 1.4) \times 10^3$	$(1.3 - 1.8) \times 10^3$
$22.9 < E_\nu < 36.9\,\mathrm{MeV}$		70		

Table 3.1 – *Current limit bounds for the detection of a DSNB signal [114, 115, 116]. The fluxes are given in number of particles per* $\mathrm{cm}^2.\mathrm{s}$.

3.2 DESCRIPTION OF THE THEORETICAL MODEL

3.2.1 How do we model the DSNB fluxes arriving on Earth?

The DSNB flux spectrum at Earth is calculated from the neutrino emission at the supernova's neutrino-sphere $F_{\nu_\alpha}(E'_{\nu_\alpha})$ and the evolving core collapse supernova rate $R_{\mathrm{SN}}(z)$ as

$$F_{\nu_\alpha}(E_{\nu_\alpha}) = \int dz \left| \frac{dt}{dz} \right| (1+z) R_{\mathrm{SN}}(z)\, F_{\nu_\alpha}(E'_{\nu_\alpha}), \qquad (3.1)$$

where z is the redshift, $E'_{\nu_\alpha} = (1+z)E_{\nu_\alpha}$ is the neutrino energy at the emission and E_{ν_α} on Earth, $R_{\mathrm{SN}}(z)$ is the core collapse supernova rate per unit comoving volume and $F_{\nu_\alpha}(E'_{\nu_\alpha})$ the spectra emitted by the supernova for a flavor α. In the following simulations, we assume that all the supernovae, considered in the DSNB flux calculation, are equal and so emit the same energy spectrum.
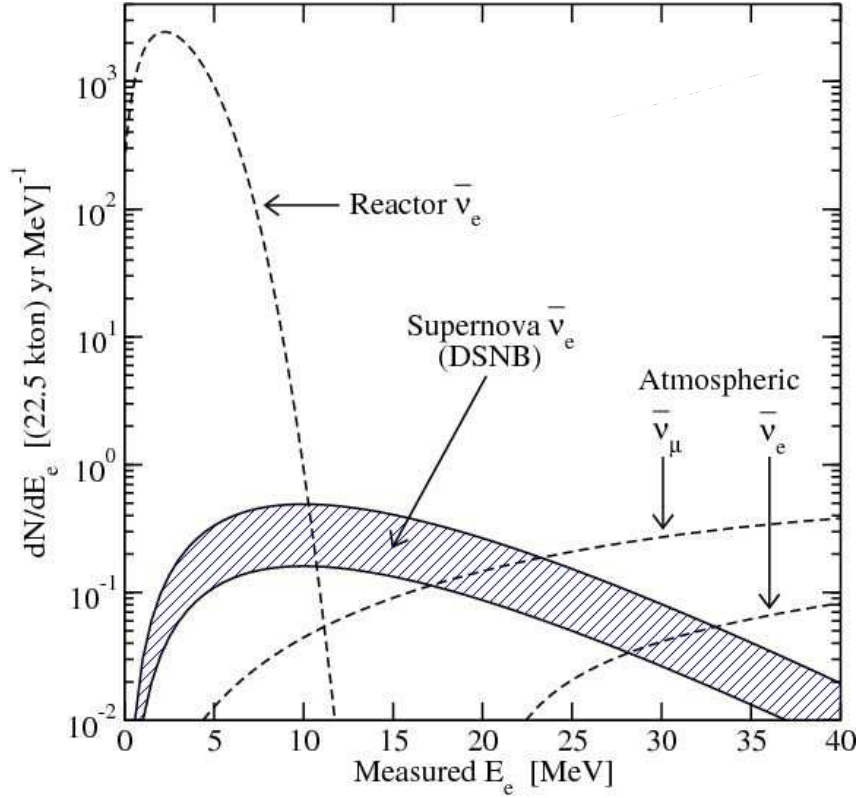
Figure 3.1 – *Expected detection rates in SuperKamiokande. The DSNB signal could be cleanly detected at a reasonable rate. Taken from [117].*

From the Friedmann equation for a flat universe, one finds for the redshift evolution with time

$$\frac{dz}{dt} = -H_0(1+z)\sqrt{\Omega_M(1+z)^3 + \Omega_\Lambda}, \tag{3.2}$$

where $\Omega_{M,\Lambda}$'s are dimensionless densities defined by the ratio of the density $\rho_{M,\Lambda}$ over the critical density $\rho_c = 3H_0^2/(8\pi G)$. Ω_M is the density of matter and Ω_Λ the density of the vacuum. Their values within the ΛCDM model are

$$\Omega_\Lambda \simeq 0.7 \quad \text{and} \quad \Omega_M \simeq 0.3, \tag{3.3}$$

and the Hubble constant H_0 is taken to be

$$H_0 = 70\,h_{70}\,\text{km.s}^{-1}.\text{Mpc}^{-1}, \tag{3.4}$$

where h_{70} is the normalized dimensionless Hubble constant with $h_{70} \simeq 1$. This Hubble constant is one of the most important quantity in the Standard Cosmological Model because it gives the present rate of expansion of the Universe. Its inverse, called the "Hubble time", gives the time scale of the age of the Universe

$$H_0^{-1} \simeq 13.965\,\text{Gyr.} \tag{3.5}$$

If it is expressed in distance units, the inverse of the Hubble constant is called the "Hubble distance" and it represents the scale of the dimensions of the observable Universe

$$H_0^{-1} \simeq 4.28\,\text{Gpc.} \tag{3.6}$$

We use the parameters defined in eqs. (3.3) and (3.4) in our calculations.

3.2.2 The cosmic supernova rate and star formation rate

Supernovae are infrequent in the Milky Way but not in the Universe. Since massive stars have lifetimes that are very short on cosmological timescales, their cosmic birth and death rates are equal. The cosmic star formation rate has been measured precisely, using a great variety of techniques, principally based on the emission of massive stars. The cosmic supernova rate (SN) R_{SN} is related to the star formation rate [118] (SFR) R_{SF} through the initial mass function (IMF) $\phi(M)$ which described the differential mass distribution of stars at formation [119]. Here we assume that all stars with a mass larger than $8M_\odot$ give rise to a core collapse supernova and die on a timescale much shorter than the Hubble time, and that the IMF is independent of redshift z. This assumptions give the following relation between R_{SN} and R_{SF}

$$R_{SN}(z) = R_{SF}(z) \frac{\int_{8M_\odot}^{125M_\odot} \phi(M)\, dM}{\int_{0.1M_\odot}^{125M_\odot} \phi(M) M\, dM}. \tag{3.7}$$

For the IMF, we adopt the functions from [119]

$$\phi(M) \propto \begin{cases} M^{-1.50}, & 0.1M_\odot < M < 0.5M_\odot \\ M^{-2.25}, & M > 0.5M_\odot \end{cases} . \tag{3.8}$$

Thus we obtain, by inserting eq. (3.8) in eq. (3.7),

$$R_{SN}(z) \simeq 0.0132\, R_{SF}(z)\, M_\odot^{-1}. \tag{3.9}$$

For the SFR, we use the estimations from Yüksel et al. [118] where they compile measurements and observations of the color-selected Lyman Break Galaxies (LGB) and the Lyman α Emitters (LAE), and the *Swift* Gamma-Ray Bursts (GRB) data (see figure 3.2).

In reference [118], the star formation rate is estimated using a continuous form of a broken power law

$$R_{SF}(z) = R_{SF}(0) \left[(1+z)^{3.4\eta} + \left(\frac{1+z}{B}\right)^{-0.3\eta} + \left(\frac{1+z}{C}\right)^{-3.5\eta} \right]^{1/\eta}, \tag{3.10}$$

where the normalization at $z = 0$ is $R_{SF}(0) = 0.02\, M_\odot.\text{year}^{-1}.\text{Mpc}^{-3}$ and we use $\eta \simeq -10$ to smooth the transitions. The factors B and C correspond to the breaks $z_1 = 1$ and $z_2 = 4$ respectively. Then we obtain the values $B = (1+z_1)^{1+3.4/0.3} \simeq 5161$ and $C = (1+z_1)^{(0.3+3.4)/3.5}(1+z_2)^{1-0.3/3.5} \simeq 9$. This parametrization of eq. (3.10) of the star formation rate is the one that we use in our simulations.

3.2.3 Supernova neutrino emission spectra

To calculate the neutrino and antineutrino fluxes emitted by the Supernova in the presence of a dynamic electron density profile, we follow the procedure used by Gava et al. [90]. Reference [90] provides a calculation combining the neutrino self-interaction and shock wave effects and studying their impacts on a supernova
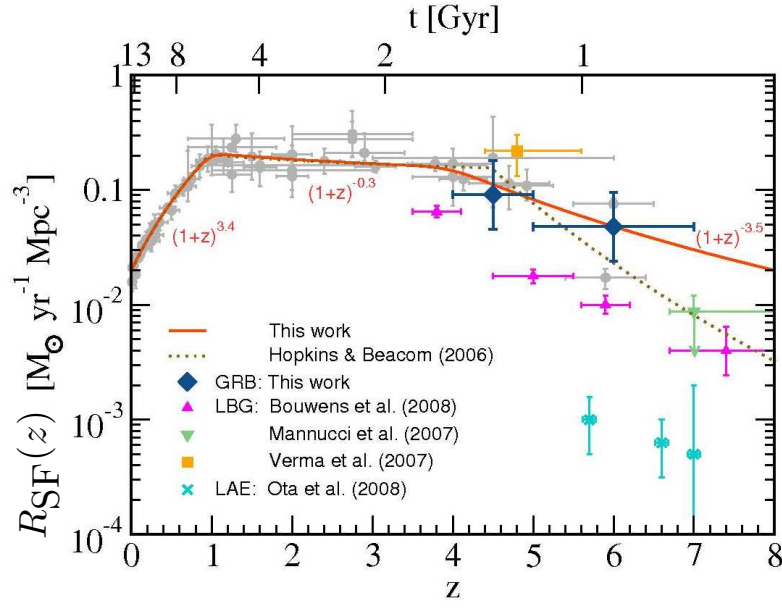
Figure 3.2 – *The cosmic star formation history. The compiled SFR data (light circles) and fit (dotted line) of Hopkins & Beacom (2006) are shown, as well as newer high-z data. The results of the work, as inferred using bright Swift gamma-ray bursts, are shown with dark diamonds. The solid line is the new high-z fit given in eq. (3.10). Taken from [118].*

signal on Earth. The propagation of neutrinos in matter is divided in two steps. First, we determine the neutrino wave functions up to some radius using density profiles at different times during the supernova explosion for one static density profile i.e. without shock waves. The Hamiltonian of the system that we need to solve is

$$H = H^{\text{vac}} + H^{\text{mat}} + H^{\nu\nu}, \tag{3.11}$$

where the vacuum Hamiltonian H^{vac} is given by eqs. 2.45 to 2.50, the matter induced Hamiltonian H^{mat} given by eq. (1.61) is an inverse power-law (see section 2.1.4 and figure 2.6) and the neutrino self-interaction Hamiltonian is taken in the single-angle approximation (see eq. (2.103)). Secondly, we determine the neutrino evolution through the rest of the supernova mantle, where the shock affects the propagation, by solving the evolution operator equations as described in [20]. The final neutrino wave functions of the first step are the initial neutrino wave functions of the second step. The 1D density profiles used include both the forward and reverse shock (see figure 2.15). These profiles are the dynamic continuity of the profile used in the first step.

The results published in this work of the thesis [24] are obtained with the oscillation parameters

$$\Delta m_{12}^2 = 8 \times 10^{-5} \, \text{eV}^2 \quad \text{and} \quad \Delta m_{23}^2 = \pm 3 \times 10^{-3} \, \text{eV}^2, \tag{3.12}$$

$$\sin^2 2\theta_{12} = 0.83, \quad \sin^2 2\theta_{23} = 1 \quad \text{and} \quad \sin^2 2\theta_{13} \leq 4 \times 10^{-4}. \tag{3.13}$$

The Dirac CP violating phase is taken to be zero. Note that the existence of CP violating effects in supernova has been established by Balantekin et al. in [98] and further studied in references [89, 91]. The mass hierarchy taken is the inverted

hierarchy because otherwise there are no effects from the neutrino self-interaction in the normal hierarchy. For the third mixing angle θ_{13}, two values are explored. A large one, $\sin^2 \theta_{13} = 10^{-4}$, to obtain an adiabatic flavor conversion for the H-resonance which will be the resonance modified by the shock. The other value, $\sin^2 \theta_{13} = 10^{-8}$, is much smaller and implies a non-adiabatic conversion for the H-resonance. For the luminosities at the neutrino-sphere, the equipartition among all neutrino flavors and an exponential decrease are assumed.

$$L_\nu = L_0 \, e^{-t/\tau} \quad \text{with } L_0 = 10^{52} \, \text{erg.s}^{-1} \text{ and } \tau = 3.5 \, \text{s}. \tag{3.14}$$

These assumptions are used because we focus on the cooling phase where equipartition of the luminosity is a good approximation (see section 2.1.2). The average energies taken follow the usual hierarchy i.e. $\langle E_{\nu_e} \rangle < \langle E_{\bar{\nu}_e} \rangle < \langle E_{\nu_x} \rangle$ with values 12, 15 and 18 MeV respectively. As a result, the emission spectra $F_{\nu_\alpha}(E'_{\nu_\alpha})$ that we integrate in eq. (3.1) contain an addition of three effects:

1. neutrino self-interaction. We sometimes turn it off to explore the effects coming from the self-interaction alone,

2. adiabatic or non-adiabatic MSW resonances. The L-resonance is always adiabatic for neutrinos but we consider the H-resonance to be adiabatic or not depending on the value of θ_{13}. If θ_{13} is large (L), i.e. equal to $\sin^2 2\theta_{13} = 4 \times 10^{-4}$, then the conversion is adiabatic otherwise θ_{13} is small (S), i.e. equal to $\sin^2 2\theta_{13} = 4 \times 10^{-8}$, and the flavor conversion at the H-resonance is non-adiabatic,

3. multiple H-resonances and phase effects due to the presence of the shock.

As mentioned, we also compare the results extracted from a full numerical calculation with analytical formulas that are often used. In these analytical formulas, the conversion at the MSW resonances are modeled in a three flavors scenario by hopping probabilities (see section 2.3) and consequently do not include the phase effects. So using the analytical formulas corresponds to consider the absence of the shock. Then this allows us to explore the shock waves effects upon the propagation of neutrinos.

The neutrino and antineutrino fluxes after the neutrino self-interaction and the MSW resonances, for a given neutrino energy E, are given by

$$
\begin{aligned}
F_{\nu_e}(E) &= p \, F_{\nu_e}^0(E) + (1 - p) \, F_{\nu_x}^0(E), \tag{3.15} \\
F_{\bar{\nu}_e}(E) &= \bar{p} \, F_{\bar{\nu}_e}^0(E) + (1 - \bar{p}) \, F_{\bar{\nu}_x}^0(E). \tag{3.16}
\end{aligned}
$$

where $F_{\nu_e,\nu_x,\bar{\nu}_e,\bar{\nu}_x}^0(E)$ are the fluxes at the neutrino-sphere assuming a Fermi-Dirac distribution and the same average energies for the μ and τ flavors. The probabilities p and $\bar{p}$ are the two survival probabilities for the electron flavor and are found to be in normal hierarchy [20]

$$
\begin{aligned}
p &= (|U_{e1}|^2 P_L + |U_{e2}|^2 (1 - P_L))(P_H(1 - P_{SI}) + (1 - P_H)P_{SI}) \\
&\quad + |U_{e3}|^2 (P_H P_{SI} + (1 - P_H)(1 - P_{SI})), \tag{3.17} \\
\bar{p} &= |U_{e1}|^2 (\bar{P}_H \bar{P}_{SI} + (1 - \bar{P}_H)(1 - \bar{P}_{SI})) \\
&\quad + |U_{e3}|^2 (\bar{P}_H(1 - \bar{P}_{SI}) + (1 - \bar{P}_H)\bar{P}_{SI}). \tag{3.18}
\end{aligned}
$$

and in inverted hierarchy

$$
\begin{aligned}
p &= (|U_{e1}|^2 P_L + |U_{e2}|^2 (1 - P_L))(P_H P_{SI} + (1 - P_H)(1 - P_{SI})) \\
&\quad + |U_{e3}|^2 (P_H(1 - P_{SI}) + (1 - P_H)P_{SI}), \tag{3.19}
\end{aligned}
$$

$$\begin{aligned}\bar{p} &= |U_{e1}|^2(\bar{P}_H(1-\bar{P}_{SI}) + (1-\bar{P}_H)\bar{P}_{SI}) \\ &+ |U_{e3}|^2(\bar{P}_H\bar{P}_{SI} + (1-\bar{P}_H)(1-\bar{P}_{SI})).\end{aligned} \qquad (3.20)$$

The hopping (or crossing) probability which models the H-resonance is for neutrinos in normal hierarchy P_H or for antineutrinos in inverted hierarchy $\bar{P}_H$. These probabilities can take two values. If the conversion is adiabatic or absent (because of the hierarchy) then $P_H = 0$ otherwise it is non-adiabatic and $P_H = 1$. The crossing probability for the L-resonance is always for neutrinos and adiabatic so we assume $P_L = 0$. Finally P_{SI} and $\bar{P}_{SI}$ account for the self-interaction effects and are only present in inverted hierarchy. We use the following approximation

$$P_{SI} = \Theta(E - E_C) \quad \text{and} \quad \bar{P}_{SI} = 1, \qquad (3.21)$$

where the step energy E_C is taken to be $E_C = 7$ MeV.

Before looking at the numerical results of the shock waves effects upon the DSNB, let us have a look at the shock waves effects upon the neutrino propagation as discussed in section 2.4.2 but with a realistic dynamic density profile.

3.2.4 Effects of multiple H-resonances with a realistic dynamic density profile

On figure 3.3, we show the typical behavior of the $\bar{\nu}_e$ survival probability for the H-resonance in the MSW region in presence of a shock wave. As explained in section 2.4.2, the adiabaticity of the conversion depends on the density at which the resonance occurs for one energy because the steepness of the density profile is modified by the shock. On figure 3.3, we can distinguish 3 phases.

Below 20 MeV, antineutrinos feel the phase effects due to the multiple H-resonances. It is characterized by fast oscillations in the survival probability and so a semi-adiabaticity in average. In terms of density, antineutrinos in that energy range resonate at a density similar to the dotted line on figure 2.16. Then they will encounter the fulfillment of the MSW conditions several times leading to phase effects.

Between 20 and 45 MeV, the survival probability is equal to $P(\bar{\nu}_e \rightarrow \bar{\nu}_e) \lesssim 0.1$ which is a non-adiabatic propagation. After the neutrino self-interaction, the $\bar{\nu}_e$ flux has been completely swapped with the $\bar{\nu}_x$ flux and so the electron antineutrino survival probability is $P(\bar{\nu}_e \rightarrow \bar{\nu}_e) \sim 0$. This flux is now the initial flux before the MSW region and because the survival probability stays very small, lower than 0.1, it is by definition a non-adiabatic propagation. This adiabaticity will change later because, at $t = 2$ s, the forward shock has not reached yet the density resonance for these energies. The corresponding density is plotted as a dashed line on figure 2.16.

Finally, for energies above 45 MeV, the survival probability goes up to ~ 0.6 leading to a semi adiabatic propagation. These energies resonate at a density similar to the solid line of figure 2.16.

The effects described before have an important impact on the survival probability and consequently on the final flux measured on Earth because we remind that the flux at a distance r from the neutrino-sphere is $F_{\bar{\nu}_e} = P(\bar{\nu}_e \rightarrow \bar{\nu}_e) F^0_{\bar{\nu}_e} + (1 - P(\bar{\nu}_e \rightarrow \bar{\nu}_e)) F^0_{\bar{\nu}_x}$. The possible observability of the effects have been studied Gava

et al. in [90]. Here our aim is to continue the exploration and see if such effects are also important for the diffuse supernova neutrino background
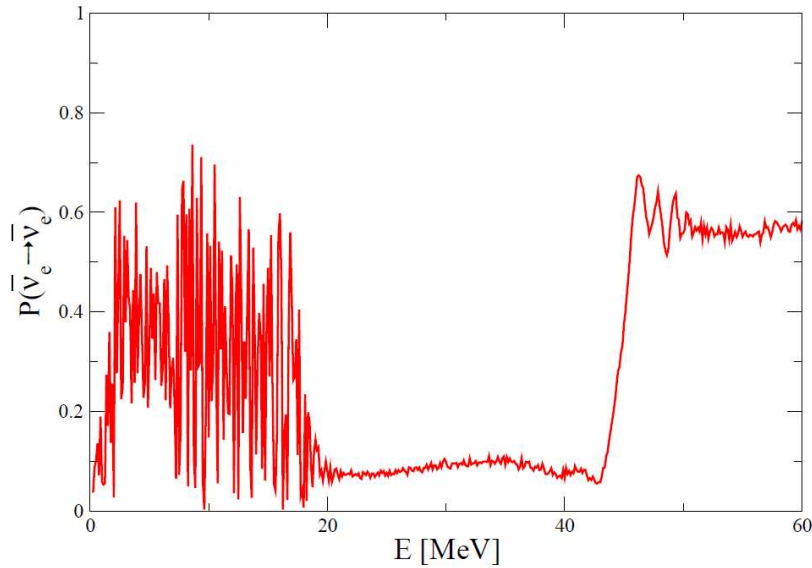
Figure 3.3 – *Electron antineutrino survival probability at the edge of the 1D core collapse supernova at $t = 2$ s. Phase effects are visible as fast oscillations in the range $[2, 20]$ MeV. Taken from [20].*

3.3 RESULTS

Using the analytical formulas and the full simulations described above, we investigate the shock wave effects upon the DSNB fluxes and consequently on the expected event rates in water Čerenkov, scintillator and liquid Argon detectors such as the next-generation observatories MEMPHYS [66], LENA [67] and Glacier [68] (for further details on these experiments, see section 2.2).

3.3.1 Numerical predictions

DSNB fluxes

Not all the possible scenarii are interesting when we study the effects of the shock wave on the H-resonance. Indeed, we focus on the normal hierarchy for ν_e and the inverted hierarchy for $\bar{\nu}_e$ because that is where they can experience a flavor conversion due to the H-resonance. Then in these two cases, we modify the value of θ_{13} to generate an adiabatic conversion with $\sin^2 2\theta_{13} \in [0.19, 10^{-5}]$ (noted L for "Large"), or a non-adiabatic conversion with $\sin^2 2\theta_{13} < 10^{-5}$ (noted S for "Small"). The DNSB (or relic) fluxes on Earth are plotted on figure 3.4.

Before going into details, we just note that the full numerical calculation and the analytical formulas are in agreement for the S case because neutrinos (or antineutrinos, depending on the hierarchy) feel a non-adiabatic propagation and so there are no effects coming from the presence of the shock wave. Thus the dotted line on figure 3.4 is valid for a complete numerical calculation or for a propagation using analytical formulas. The curves on figure 3.4 look like Fermi-Dirac distributions but with lower average energies compared to the typical fluxes emitted by a

(a) Relic ν_e flux on Earth in normal hierarchy.   (b) Relic $\bar{\nu}_e$ flux on Earth in inverted hierarchy.
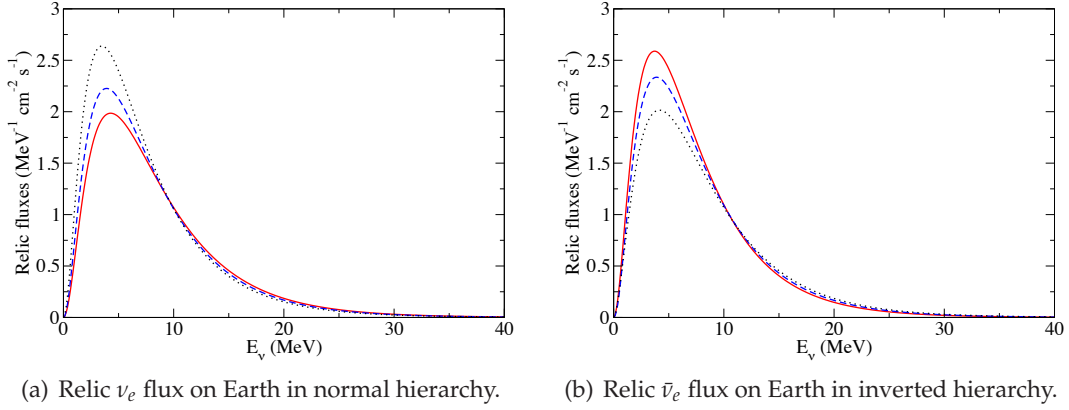
Figure 3.4 – *DSNB fluxes on Earth as a function of neutrino energy. The dashed line shows the results of the full numerical calculation with neutrino self-interaction, shock wave and large θ_{13} i.e. $\sin^2 2\theta_{13} \in [0.19, 10^{-5}]$. The dotted line is obtained using the analytical formulas of eqs. (3.18) and (3.20) including neutrino self-interaction (but no shock wave) and a small θ_{13} i.e. $\sin^2 2\theta_{13} < 10^{-5}$ whereas the solid line is obtained with analytical formulas and a large θ_{13}. Note that in the case S the analytical and numerical results are the same.*

supernova where $\langle E_\nu \rangle \in [12, 25]$ MeV. The "compression" of the distribution is due to the fact that the neutrino energy received on Earth E_{Earth} is redshifted and does not correspond to the emission energy E_{SN}.

In order to explore the effects on DSNB event rates in detectors, we consider the following detection windows:

$$[19.3 - 30] \text{ MeV and } [9.3 - 25] \text{ MeV for } \bar{\nu}_e,$$
$$[17.5 - 41.5] \text{ MeV and } [4.5 - 41.5] \text{ MeV for } \nu_e.$$

The two detection windows for antineutrinos are the one from the SK detector, as in reference [114], and the one expected in LENA detector, as in reference [67]. For neutrinos, the detection windows are taken from the GLACIER detector [23]. So first, let us have a look at the fluxes in this energy region. To better see the effects coming from the shock, we plot on figure 3.5 the ratio of the relic fluxes with case L over case S knowing that the case S is the same with analytical formulas or a full numerical approach. We note that these ratios are directly sensitive to the shock because the shock affects the neutrino propagation only for case L.

First, figures 3.4 and 3.5 show that there is a difference between the L case with the shock (solid for $\bar{\nu}_e$ and dashed for ν_e on fig. 3.5) and without the shock (dotted for $\bar{\nu}_e$ and dash-dotted for ν_e on fig. 3.5). We see a change of about $10-20\%$ in the fluxes coming from the addition of the shock in the numerical calculation. The first conclusion is a significant impact of the shock wave on the DSNB fluxes. Secondly, on figure 3.5, the presence of the shock wave reduces the flux ratio ($E_\nu \gtrsim 10$ MeV) and so the difference between case S and L. This decrease induces a reduction of the sensitivity to θ_{13} because the two cases are less distinguishable.

Even if the sensitivity to the third mixing angle θ_{13} is reduced in the numerical calculation, there is still a significant impact coming the presence of the shock. This result is at variance with [120] where it was found that the shock wave effects were
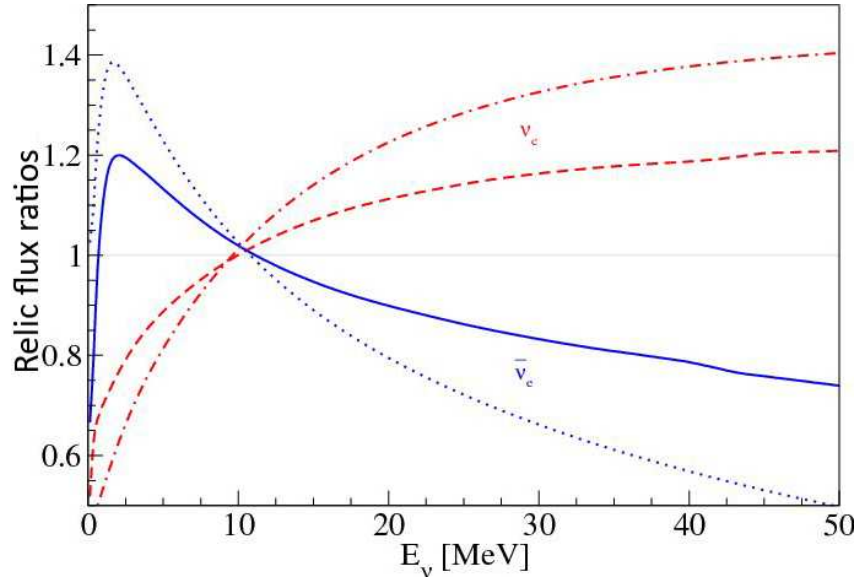
Figure 3.5 – *Relic electron (anti)neutrino flux ratios on Earth, with case L over case S, as a function of neutrino energy. The results for neutrinos are in normal hierarchy, the dot-dashed line represents analytical formulas (self-interaction + no shock) and the dashed line is the full numerical calculation (self-interaction + shock). On the contrary, the results for antineutrinos are in inverted hierarchy, the dotted line represents analytical formulas (self-interaction + no shock) and the solid line is the full numerical calculation (self-interaction + shock).*

negligible. Such a difference might be due to the fact that, as stated in [121, 122, 20], the shocks in hydrodynamical profiles are "softened" due to numerical artifacts and are not as steep as they should be. Since the adiabaticity is inversely proportional to the density derivative, a softened shock is more adiabatic than a non-softened shock. This is why the choice for a "large" θ_{13}, as in reference [120], seems to give an adiabatic result. To compensate for the softness of the shocks in hydroprofiles one must either steepen the shock feature by hand or use a value of θ_{13} as close as possible to the threshold $\sin^2 2\theta_{13} > 10^{-5}$ but without making the adiabaticity of the progenitor too small, as for example in [20].

DSNB event rates

Now we investigate the effects of the multiple H-resonances, i.e. the difference between numerical and analytical results, on the DSNB event rates.

Table 3.2 presents all the event rates obtained per kTon.year. The results include the neutrino self-interaction and are based upon a large θ_{13}. By considering the inverted hierarchy for antineutrinos, we extract that the presence of the shock wave gives an increase of 7-18% on the event rates. In opposition, in normal hierarchy, the neutrino event rates decrease in $\sim 10\%$. Then we recover what we found by examining the DSNB fluxes, the presence of the shock wave implies a significant impact (increase or decrease) of about $10 - 20\%$. On the other hand, numerical and analytical results are equal in the normal hierarchy for $\bar{\nu}_e$. This is normal because antineutrinos do not experience neutrino self-interaction and MSW H-resonances in normal hierarchy. However, for ν_e's and inverted hierarchy, a discrepancy of

about 20% between the two calculations appears. We have found that such a difference is a combined effect of the $V_{\mu\tau}$ refractive index [1] with neutrino self-interaction.

Case	Windows	Numerical	Analytical
$\bar{\nu}_e$ events			
IH	19.3-30 MeV	0.078	0.066
IH	9.3-25 MeV	0.211	0.196
NH	19.3-30 MeV	0.066	0.066
NH	9.3-25 MeV	0.196	0.196
ν_e events			
NH	17.5-41.5 MeV	0.066	0.074
NH	4.5-41.5 MeV	0.106	0.116
IH	17.5-41.5 MeV	0.059	0.075
IH	4.5-41.5 MeV	0.099	0.117

Table 3.2 – *Comparison between numerical (with shock wave effects) and analytical (without shock wave effects) DSNB events rates for the case of a large θ_{13} (L). The neutrino self-interaction is included in all cases. The event rates for $\bar{\nu}_e + p$ and $\nu_e + {}^{40}Ar$ scatterings are given per kTon.year for different experimental windows relevant for water Čerenkov, scintillator and argon detectors.*

Table 3.3 presents all the DSNB event rates obtained with the full numerical simulation per kTon.year for a large and small value of θ_{13} to show the sensitivity to this unknown neutrino parameter. The results shown can include (with $\nu\nu$) or not the neutrino self-interaction (without $\nu\nu$).

The combination of tables 3.2 and 3.3 a shows that we still have a reduction of the sensitivity to the third mixing angle in the antineutrino channel. The difference between the S case and the analytical L case is $\sim -26\%$ whereas the difference between the S case and the numerical L case is reduced of $\sim -12\%$. The same conclusion is found for the neutrino channel by comparing tables 3.2 and 3.3 c.

Finally, by looking at table 3.3 a, an unpredictable result appears. The event rates obtained with or without the neutrino self-interaction are the same. This shows that the spectral swap induced by the neutrino self-interaction (see figure 2.22 and section 2.5.4) is completely washed-out by the presence of the shock. We have a loss of sensitivity to the collective effects in that case.

Table 3.3 b presents the DSNB event rates for electron antineutrinos in the case where there are no effects coming from the shock waves and the neutrino self-interaction. Indeed the assumption of the equipartition of the total luminosity among all flavors ensures that the flux swap does not occur in normal hierarchy and the fact that we are in normal hierarchy implies that the H-resonances take place for neutrinos.

Next, table 3.3 d presents the DSNB event rates for electron neutrinos in the case where the possible effects come from the neutrino self-interaction. Indeed in inverted hierarchy the H-resonances occur for antineutrinos.

---

1. This refractive index appears when we go to the one loop corrections for the matter Hamiltonian which becomes $H^{\mathrm{mat}} = \sqrt{2}\,G_F\,N_e(\delta_{e\alpha} + Y_e^{\mathrm{eff}}\,\delta_{\tau\alpha}/Y_e)$ where $\alpha \in \{e, \mu, \tau\}$ and $Y_e^{\mathrm{eff}} = 5.4 \times 10^{-5}$.

(a)

N_{events}	Inverted hierarchy: with $\nu\nu$ (without $\nu\nu$)		
	Window	L	S
$\bar{\nu}_e$	19.3-30 MeV	0.078 (0.078)	0.089 (0.066)
$\bar{\nu}_e$	9.3-25 MeV	0.211 (0.210)	0.224 (0.196)

(b)

N_{events}	Normal hierarchy: with/without $\nu\nu$	
	Window	L or S
$\bar{\nu}_e$	19.3-30 MeV	0.066
$\bar{\nu}_e$	9.3-25 MeV	0.196

(c)

N_{events}	Normal hierarchy: with/without $\nu\nu$		
	Window	L	S
ν_e	17.5-41.5 MeV	0.066	0.058
ν_e	4.5-41.5 MeV	0.106	0.096

(d)

N_{events}	Inverted hierarchy: with $\nu\nu$ (without $\nu\nu$)	
	Window	L or S
ν_e	17.5-41.5 MeV	0.059 (0.058)
ν_e	4.5-41.5 MeV	0.099 (0.096)

Table 3.3 – *DSNB event rates for $\bar{\nu}_e + p$ and $\nu_e + {}^{40}Ar$ scatterings per kTon.year from our numerical calculations for different detection windows. The experimental windows are relevant for water Čerenkov, scintillator and argon detectors. The calculations are given for a large (L) and small (S) value of θ_{13}, including shock wave effects, and with/without the neutrino self-interaction ($\nu\nu$).*

Before going on to explain why the sensitivity to the neutrino self-interaction is lost, in the presence of the shock wave (see table 3.3 a), we use these calculations to predict - on average - 343 events over 10 years in a detector like MEMPHYS, 91 events in LENA and 62 events in GLACIER.

3.3.2 A simplified model to account for the shock wave effects

We have built up a simplified model corresponding to our calculation. For any given energy, the time-integrated $\bar{\nu}_e$ spectra are

$$F_{\bar{\nu}_e} = \int_0^\infty dt \left(\bar{p}(t) F_{\bar{\nu}_e}^0 + (1 - \bar{p}(t)) F_{\bar{\nu}_x}^0 \right), \tag{3.22}$$

where $F_{\bar{\nu}_\alpha}^0$ are the spectra at the neutrino-sphere. As a example, two survival probabilities $\bar{p}(E, t)$, extracted from the full numerical simulation, are plotted on figure 3.6, with the neutrino self-interaction and on figure 3.7, without collective effects, for two energies of 10 and 30 MeV as a function of time.

From these two survival probabilities, we can divide the time dependence of neutrino evolution identifying four typical periods (see figure 3.8). At around a certain time t_s, the shock wave reaches the H-resonance region and the propagation goes from adiabatic to non-adiabatic. The non-adiabatic propagation persists till a time t_p and switches to a period where the survival probabilities oscillate rapidly
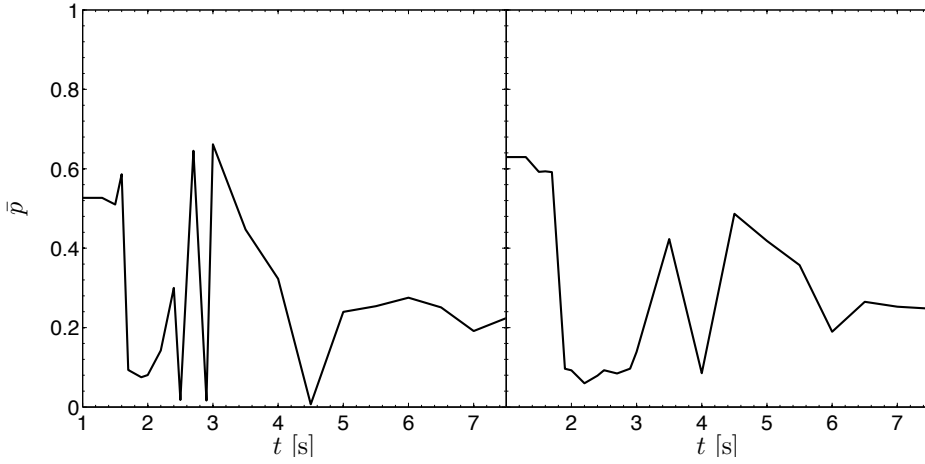
Figure 3.6 – *Electron antineutrino survival probability $\bar{p}(E,t)$ as a function of time. These probabilities are for a neutrino energy of 10 (left) and 30 MeV (right) and include the neutrino self-interaction. They are taken from a calculation where the density profile is taken from 1D hydrodynamical calculation of reference [20] and the antineutrino propagation includes mixing, coupling to matter and the shock wave. The results correspond to inverted hierarchy and a large θ_{13}.*
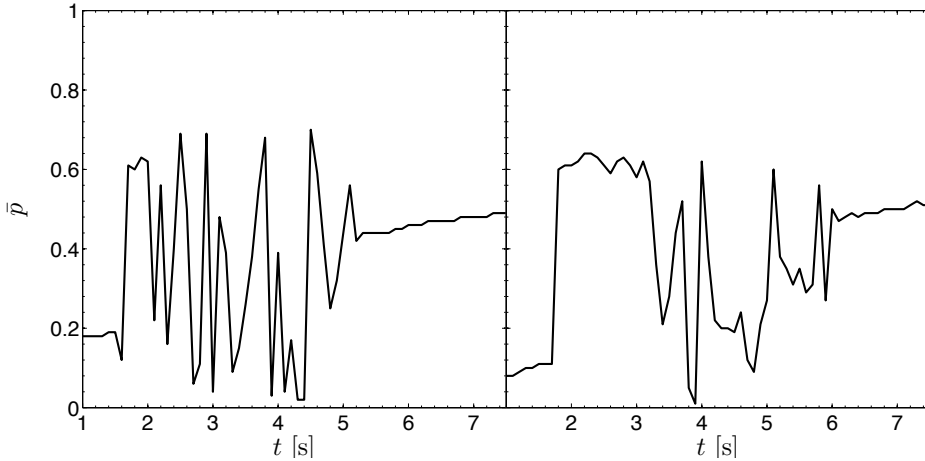
Figure 3.7 – *Same as figure 3.6 but the neutrino self-interaction is not included.*

due to the phase effects generated by the interference of the multiple H-resonances. These eventually cease whereupon neutrino propagation enters a postshock regime (t_∞) that may be semi-adiabatic depending on the postshock profile.

The simplified model is constructed as follows. We divide the integral of eq. (3.22) into four integrals. The transition times, t_s, t_p and t_∞, taken from the numerical results are shown on figure 3.9 as a function of neutrino energy. The curves have been fitted with polynomials given by

$$t_{s,p}(E) = \sum_{i=0}^{5} a_i.E^i,$$ (3.23)

$$t_\infty(E) = 3.75 + 9.5 \times 10^{-2}\, E - 5 \times 10^{-4}\, E^2.$$ (3.24)

with the coefficients listed in table 3.4.
We then approximate $\bar{p}(E,t)$ by doing the time average of $\bar{p}(E,t)$ for each energy within each domain and after we again perform another average on the energy
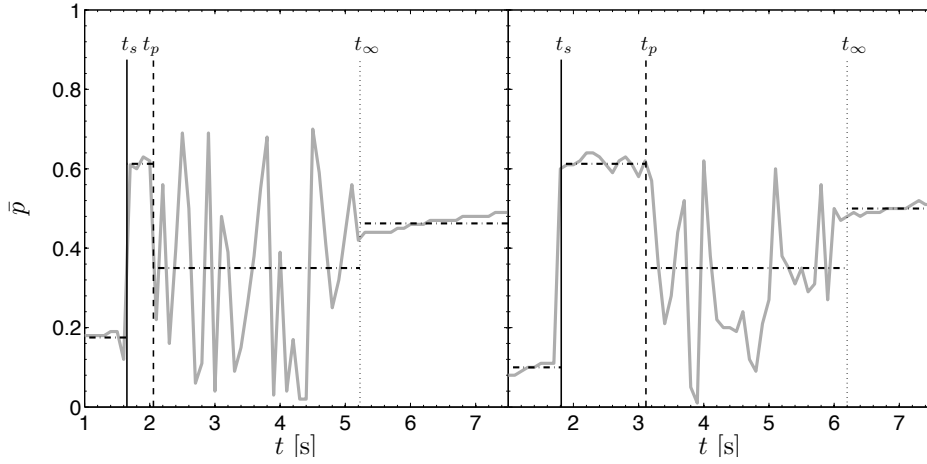
Figure 3.8 – *Same as figure 3.7 with indications of the location of the three times t_s, t_p and t_∞. The probability averages are also shown in each domain to explain the procedure of the simple model proposed to include shock wave effects (see text).*

	a_0	a_1	a_2	a_3	a_4	a_5
t_s	1.02×10^{-2}	1.72×10^{-1}	-6.88×10^{-3}	1.4×10^{-4}	-1.2×10^{-6}	4.2×10^{-9}
t_p	9.83×10^{-2}	1.39×10^{-1}	-2.47×10^{-3}	4.0×10^{-5}	-4.4×10^{-7}	1.9×10^{-9}

Table 3.4 – *Coefficients for the polynomial fit of eq. (3.23).*
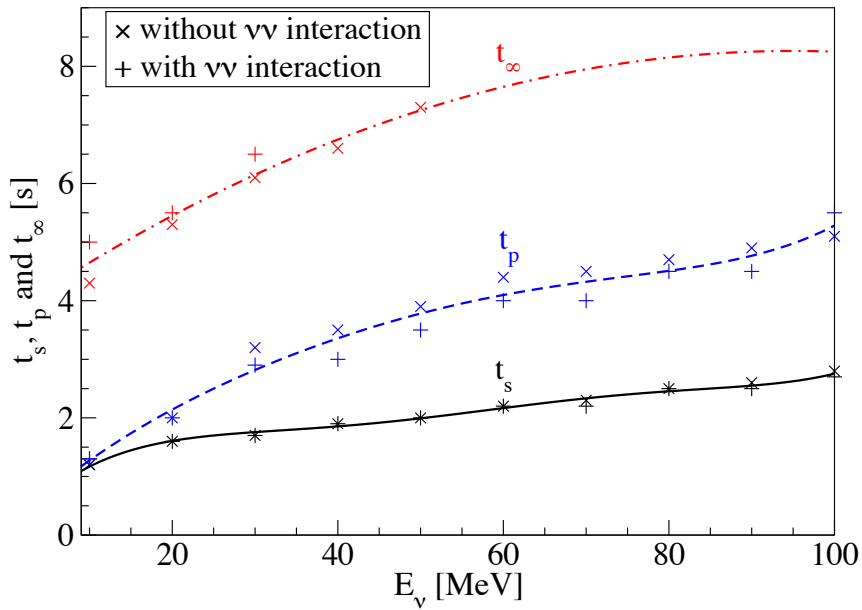
Figure 3.9 – *Numerical results of the three times characterizing the neutrino evolution in the supernova mantle obtained in presence of a shock and with/without the $\nu\nu$ interaction: the shock time t_s, the phase effects time t_p and the postshock time t_∞. The corresponding analytical fits of eqs. (3.23) and (3.24) are also shown.*

$\langle \bar{p}(E, t) \rangle_E$. Then the survival probability is energy-independent within each domain. The obtained averages are listed in table 3.5.

Before giving an explanation to the loss of sensitivity to the collective effects

Interval	$0 \rightarrow t_s$	$t_s \rightarrow t_p$	$t_p \rightarrow t_\infty$	$t_\infty \rightarrow \infty$
With $\nu\nu$	0.5436	0.0634	0.3092	0.2548
Without $\nu\nu$	0.1611	0.6356	0.3531	0.4835

Table 3.5 – *Averages of the survival probability $\bar{p}(t)$ of electron antineutrinos from the full numerical calculation including mixing, coupling to matter and the shock wave. The neutrino self-interaction is included (with νν) or not (without νν). Different time intervals are shown (see figure 3.8).*

using this simplified model, we first look at the quality of the results obtained with the simple model. We have done two calculations with a large θ_{13}: the first calculation uses the complete simulation and the second calculation uses the simplified model. On figure 3.10, we plot the ratio of these two calculations for two cases: with and without the neutrino self-interaction. We see that the difference between the full simulation and the simple model does not exceed 3%. So even if the model that we present is simplified, it accounts pretty well for the results of the full simulation.
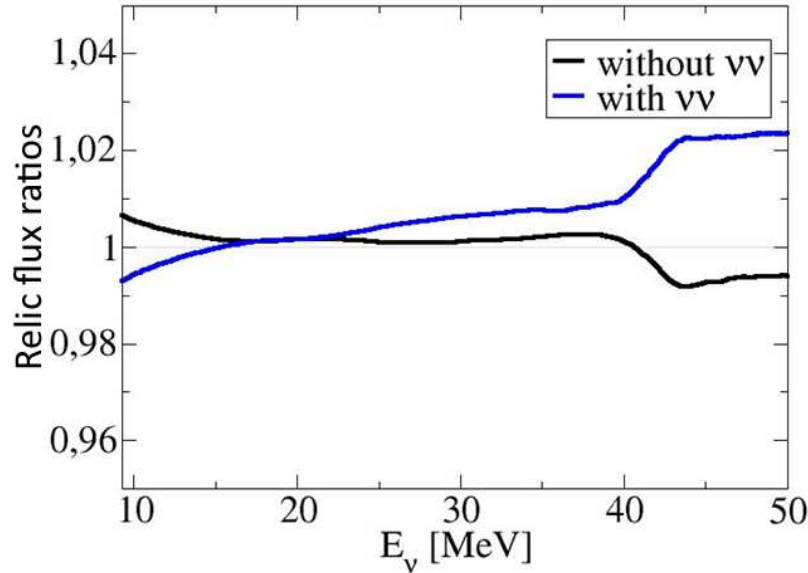
Figure 3.10 – *Ratios of the numerical results obtained with the full simulation over the simple model. The black line corresponds to calculations including the neutrino self-interaction whereas the blue line does not include the neutrino self-interaction.*

Explanation of the loss of sensitivity to collective effects using the simple model

With this simplified model, it is now possible to explain the loss of sensitivity to collective effects observed. Indeed, when computing the DSNB relic fluxes for a large value of θ_{13} and a given hierarchy, the effect of the shock leads to a time-integrated spectra that is composed of a mixture of pre-shock and post-shock fluxes. Due to the value of the cooling time $\tau = 3.5$ s we have selected and the fact that the luminosity decreases exponentially (eq. (3.14)), the time-integrated spectra is principally a sum of the three integrals between 0 and t_s, t_s and t_p, and t_p and t_∞. Also the arrival of the shock in the H-resonance region, $t \sim 2$ s for the hydro model used, implies that the mixture of the pre-shock and the shock is almost

exactly 50:50. In addition to this, we have the relations

$$\bar{p}_{\nu\nu}(0 \to t_s) \simeq \bar{p}_{\cancel{\nu\nu}}(t_s \to t_p), \tag{3.25}$$
$$\bar{p}_{\nu\nu}(t_s \to t_p) \simeq \bar{p}_{\cancel{\nu\nu}}(0 \to t_s), \tag{3.26}$$
$$\bar{p}_{\nu\nu}(t_p \to t_\infty) \simeq \bar{p}_{\cancel{\nu\nu}}(t_p \to t_\infty). \tag{3.27}$$

These approximate equalities come from the fact that the inclusion of the neutrino self-interaction completely swap the $\bar{\nu}_e$ and the $\bar{\nu}_x$ fluxes (see eq. (2.106)). So an adiabatic (non-adiabatic) propagation with the neutrino self-interaction included is equivalent to a non-adiabatic (adiabatic) propagation without the neutrino self-interaction. And for the phase effects region, the survival probabilities are almost equal because, on average, the phase effects induce a semi-adiabatic propagation.

It is because the composition is so close to equality and because we have the relations eqs. (3.25), (3.26) and (3.27) that switching on or off the neutrino self-interaction has little impact for the $\bar{\nu}_e$ DSNB rates in the case of a large θ_{13} and inverted hierarchy (see table 3.3 a). But if we change τ or alter the time at which the shock reaches the H-resonances then we alter the mixture of pre-shock and shock fluxes that make the time-integrated spectra and thus might recover some sensitivity to the collective effects. To properly examine the sensitivity of our results to possible changes of the cooling time and/or the arrival time of the shock we use the simplified model.

Robustness of the results

Using the model described above, we investigate the loss of sensitivity by changing the cooling time τ and the arrival time of the shock. The ratio of the results with an altered τ relative to the rate at $\tau = 3.5$ s is shown in figure 3.11. The additional τ factor accounts for the change in the integrated luminosity. For reasonable cooling times between 2.5 and 4.5 s, the DSNB event rates with and without neutrino self-interaction, differ at most by $2 - 3\%$. This first result confirms the loss of sensitivity to collective effects even with a smaller or larger cooling time.

Now by introducing a temporal offset Δt to all the times, we change the time arrival of the shock in the H-resonance region. Then the new times are now $t_s + \Delta t, t_p + \Delta t, t_\infty + \Delta t$. The ratio of the rates with non-zero Δt relative to the rate with no offset are shown in figure 3.12. For reasonable values ($\Delta t = \pm 1$ s) the difference does not exceed 4% from the rates listed in table 3.3. Thus we conclude that the loss of sensitivity to the collective effects is robust and is not an effect of the coincidence of our original choice of cooling time and the density profiles adopted.

CONCLUSION

In this chapter, we presented the results that we obtained in the work [24] where we have performed the first dynamic calculation of the DSNB fluxes arriving on Earth including the neutrino self-interaction. Our simulations have showed that the presence of the shock waves induces considerable effects if the third mixing angle θ_{13} is larger than the threshold $\sin^2 2\theta_{13} = 10^{-5}$. These effects are twofold. First the shock waves reduce the sensitivity to the oscillation parameters (θ_{13} in particular). Second there is a loss of sensitivity to the collective effects introduced by the neutrino self-interaction for the inverse hierarchy and a large θ_{13}.
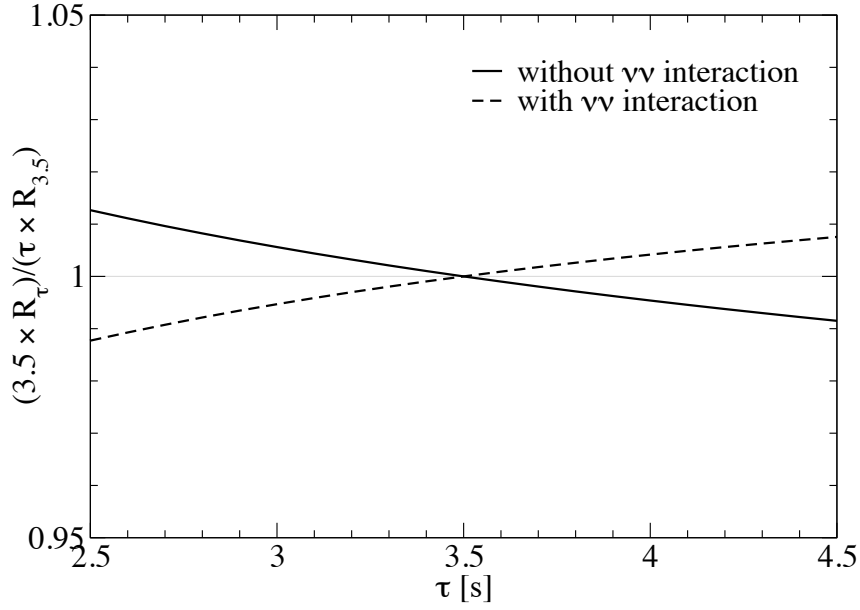
Figure 3.11 – *The ratio of the $\bar{\nu}_e$ DNSB event rate with altered cooling time τ relative to the rate with $\tau = 3.5\,s$ for the inverted hierarchy and large θ_{13} (case L) either with or without the neutrino self-interaction effects ($\nu\nu$). This calculation employs the simplified model proposed.*
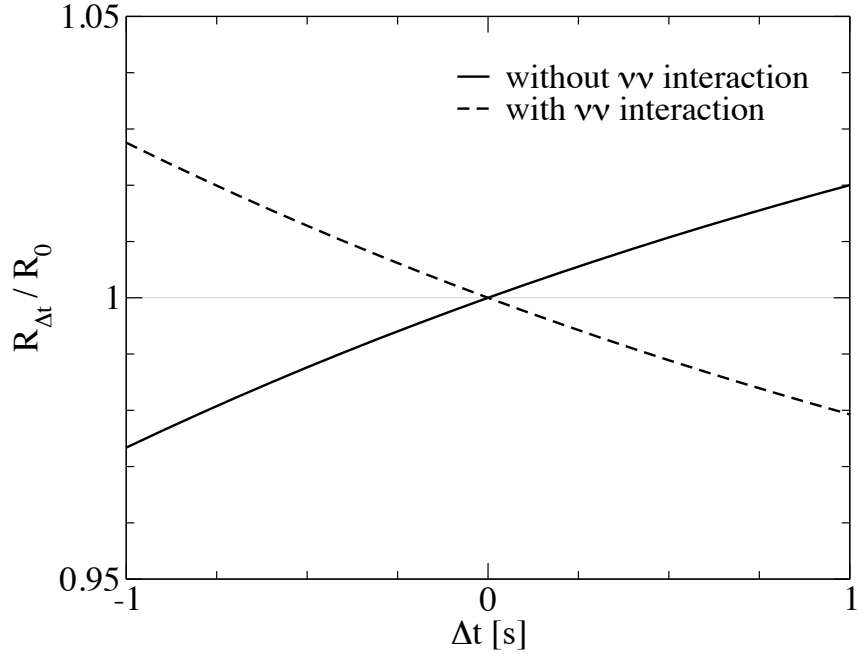
Figure 3.12 – *The ratio of the $\bar{\nu}_e$ DNSB event rate when an offset Δt time is introduced relative to the rate with zero offset for the inverted hierarchy and large θ_{13} (case L) either with or without the neutrino self-interaction effects ($\nu\nu$). This calculation employs the simplified model proposed.*

The first result is the consequence of the modification of the density profile. Indeed, if we take a small value for θ_{13} then the propagation is totally non-adiabatic whereas the propagation becomes adiabatic for a large value. The dynamic density

profile induced by the shock waves makes the adiabaticity of the propagation much more complex. The adiabaticity evolves with time and is a sequence of adiabatic, non-adiabatic and semi-adiabatic propagations. As a result, the difference between the fluxes with a small θ_{13} and with a large θ_{13} is reduced.

To find the origin of the loss of sensitivity to collective effects, we built up a simplified model to account for the shock. With this simple model, we have shown that the DSNB flux arriving on Earth consists in an integral of a sum of three periods. Each neutrino passes from an adiabatic to a non-adiabatic propagation to finally ends in a semi-adiabatic evolution. For antineutrinos, the neutrino self-interaction just swaps the electron and the muon neutrino fluxes for all energies. So an adiabatic propagation (non-adiabatic) without the self-interaction is equivalent to a non-adiabatic propagation (adiabatic) with the self-interaction and the semi-adiabatic evolutions are equal in both cases. Thus performing the integral with or without neutrino self-interaction gives the same results. So both cases are indistinguishable. By using our simple model, we have also demonstrated that the loss of sensitivity to collective effects and to θ_{13} are robust against variations of the cooling time τ and of the details of the density profiles (time arrival).

Our numerical results have also shown that the use of analytical formulas without the shock effects can significantly overestimate (or underestimate) the fluxes and event rates which will be possibly detected in the future terrestrial experiments.

In summary, the presence of the shock waves introduces important modifications of the DSNB fluxes and event rates and need to be considered in future modeling and simulations. To assist further efforts to this end we have proposed a simplified procedure to quantitatively capture the relevant shock wave effects, both in the DSNB fluxes and in the associated event rates in observatories on Earth.

A NEW INSIGHT ON NEUTRINO SELF-INTERACTION EFFECTS

<div style="text-align:right">4</div>

*T*HE aim of the second work [25] of this thesis is to gather further insight the neutrino self-interaction effects using the point of view of the instantaneously diagonal basis that we called for simplicity the 'matter' basis. In section 4.1, we describe our generalization of this matter basis when the flavor Hamiltonian is arbitrary but can be computed as well as its derivative. Indeed, our derivations show that for the calculations of the quantities present in the matter Hamiltonian $\widetilde{H}$, e.g. the non-adiabaticity parameters, we need to know the first derivative of the flavor Hamiltonian H. So in section 4.1.2.1, we give the first derivative of the flavor Hamiltonian in the case where it is composed of the vacuum Hamiltonian H^{vac}, the matter induced Hamiltonian H^{mat} and the neutrino self-interaction Hamiltonian $H^{\nu\nu}$. We calculate the derivative of the neutrino self-interaction Hamiltonian in the multi-angle case for completeness but focus on the derivative of its single-angle

approximation that we use in our work. Then, for the third work [26] of this thesis, we also need to compute the second derivative of the flavor Hamiltonian H. We decide to give in section 4.1.2.2 this second derivative for the multi-angle case and the single-angle approximation because the calculations rely on results of the first derivative calculated before.

Thereafter, we focus on the application of the previous formal equations to the two neutrino flavors case. We mention that our calculations published in [25] treat the problem exactly i.e. in presence of matter and within the single-angle approximation. Our expectations are that the matter basis will give more informations about the underlying effects that are responsible to the end of the synchronization regime and to the bipolar oscillations. We show that the neutrino self-interaction Hamiltonian implies a non-zero matter phase $\widetilde{\beta}$ that has a significant impact on the neutrino evolution in the supernova and is the key point to the onset of the bipolar oscillations.

After, we present our work published in reference [26] which consists in the first demonstration that the spectral split phenomenon corresponds actually in the polarization vector formalism to a well known phenomenon in physics: the magnetic resonance. To prove our conjecture, we derive some relevant quantities such as the magnetic fields, the rotation frequencies, etc. Then with these quantities, we show that the flavor basis corresponds to the laboratory frame of the magnetic resonance phenomenon and the matter basis is - in average - the comoving frame. This correspondence allows us to define two magnetic resonance criteria and to look for their fulfillment in the neutrino evolution in the supernova. Finally, we discuss the adiabaticity of the neutrino propagation in the first hundred kilometers in the supernova where the dominant effects come from the neutrino self-interaction.

In conclusion, we present the preliminary results that we obtained when we extend the results and particularly the idea of point of view of the matter basis to the three flavors case. We show the complete derivation of the six matter angles and phases. Then we go into the polarization vector formalism and show that the 8D magnetic field can be approximated by three 3D magnetic fields. Applying the results of the two flavors case of section 4.3 to one of these 3D magnetic fields, we present our preliminary results about the correspondence between the spectral split phenomenon and the magnetic resonance phenomenon in the three flavors case.

4.1 THE MATTER BASIS GENERALIZED FOR AN ARBITRARY HAMILTONIAN

In this first section, our goal is to make no assumptions about the entries of the Hamiltonian of the flavor basis H but only that the Hamiltonian and its derivatives can be computed. Also the calculations are done assuming an arbitrary number of flavor families. With this arbitrary Hamiltonian we derive quantities, such as the matter Hamiltonian $\widetilde{H}$ and the generalized non-adiabaticity parameters Γ, of the instantaneously diagonal basis that we call the *matter* basis.

4.1.1 From the flavor to the matter basis

The Hamiltonian H in the flavor basis can be composed of multiple terms. Here we decide to consider H as arbitrary. The eigenvalues of H are $\widetilde{k}_i$ with $i \in \mathbb{N}^*$. For two and three flavor cases, the expressions for the eigenvalues are well known [123, 124] and one may also find an algebraic solution for $N = 4$. For $N \geq 5$, the Abel-Ruffini theorem indicates that no general algebraic formulas exists.

Once the eigenvalues are found, one can determine the unitary transformation $\widetilde{U}$ that relates the Hamiltonian in the flavor basis H to the matrix $\widetilde{K}$ which has the eigenvalues $\widetilde{k}_i$ on the diagonal, i.e.

$$\widetilde{U}^\dagger H \widetilde{U} = \widetilde{K} = \text{diag}\left(\widetilde{k}_1, \ldots, \widetilde{k}_n\right). \tag{4.1}$$

We remind that in our notations, the tilde means that the eigenvalues as well as the matrices and the parameters (phases and angles) of the $\widetilde{U}$ matrix are those in matter basis. If the eigenvalues are non-degenerate then we can derive the identity that the elements of $\widetilde{U}$ satisfy

$$\widetilde{U}^*_{\alpha i} \widetilde{U}_{\beta i} = \frac{C^{(i)}_{\alpha\beta}}{\sum_\gamma C^{(i)}_{\gamma\gamma}}, \tag{4.2}$$

where $C^{(i)}$ is the cofactor matrix of $H - \widetilde{k}_i$ and so

$$|\widetilde{U}_{\beta i}|^2 = \frac{C^{(i)}_{\beta\beta}}{\sum_\gamma C^{(i)}_{\gamma\gamma}}. \tag{4.3}$$

Note that both equations are independent of the Majorana phases $\widetilde{\alpha}$'s. The denominator of eqs. (4.2) and (4.3) is the trace of the cofactor matrix $H - \widetilde{k}_i$ which is basis independent, so that

$$\sum_\gamma C^{(i)}_{\gamma\gamma} = \sum_j C^{(i)}_{jj}[\widetilde{K} - \widetilde{k}_i] = \prod_{j \neq i}(\widetilde{k}_j - \widetilde{k}_i). \tag{4.4}$$

In practice we use eq. (4.2) to relate the elements in a column to one specific element $\widetilde{U}_{\beta i}$, then use eq. (4.3) to evaluate $\widetilde{U}_{\beta i}$. However, since the N Majorana phases $\widetilde{\alpha}_i$ do not appear in eqs. (4.2) and (4.3), we have no way to determine them and can make any choice including zeros and functions of the position.

Once $\widetilde{U}$ is found, a change of basis can be made using $\widetilde{U}$, to give the Schrödinger-like equation in the matter basis

$$
\imath \frac{d\widetilde{\psi}}{dx} = \left(\widetilde{K} - \imath \widetilde{U}^{\dagger} \frac{d\widetilde{U}}{dx} \right) \widetilde{\psi} = \widetilde{H} \, \widetilde{\psi} \quad \text{with} \quad \widetilde{\psi} = \begin{pmatrix} \widetilde{\nu}_1 \\ \vdots \\ \widetilde{\nu}_n \end{pmatrix}, \tag{4.5}
$$

where $\widetilde{H}$ is the matter basis Hamiltonian and $\widetilde{\nu}_i$ are the matter eigenstates. The term $\widetilde{U}^{\dagger} d\widetilde{U}/dx$ appears because the matter eigenvalues are functions of position, which requires that $\widetilde{U}$ also be a function of position. In order to evaluate $\widetilde{H}$ we need to compute $\widetilde{U}^{\dagger} d\widetilde{U}/dx$. In fact, if we differentiate the eigen-equation $H\widetilde{U} = \widetilde{U}\widetilde{K}$ and multiply the result by $\widetilde{U}^{\dagger}$, we derive the result that

$$
\widetilde{U}^{\dagger} \frac{dH}{dx} \widetilde{U} + \left[\widetilde{K}, \widetilde{U}^{\dagger} \frac{d\widetilde{U}}{dx} \right] = \frac{d\widetilde{K}}{dx}. \tag{4.6}
$$

The commutator vanishes for the diagonal elements of this equation, because $\widetilde{K}$ is diagonal. Thus we find the result that

$$
\frac{d\widetilde{k}_i}{dx} = \left(\widetilde{U}^{\dagger} \frac{dH}{dx} \widetilde{U} \right)_{ii}. \tag{4.7}
$$

By considering the off-diagonal elements of eq. (4.6), the following equation is deduced

$$
\left(\widetilde{U}^{\dagger} \frac{dH}{dx} \widetilde{U} \right)_{ij} + \left[\widetilde{K}, \widetilde{U}^{\dagger} \frac{d\widetilde{U}}{dx} \right]_{ij} = 0 \quad \text{with} \quad i \neq j. \tag{4.8}
$$

Again, since $\widetilde{K}$ is diagonal, the off-diagonal elements of the commutator have a compact form

$$
\left(\widetilde{U}^{\dagger} \frac{d\widetilde{U}}{dx} \right)_{ij} = -\frac{1}{\delta \widetilde{k}_{ij}} \left(\widetilde{U}^{\dagger} \frac{dH}{dx} \widetilde{U} \right)_{ij}, \tag{4.9}
$$

where $\delta \widetilde{k}_{ij} = \widetilde{k}_i - \widetilde{k}_j$.

The remaining missing pieces of $\widetilde{H}$ are the diagonal terms of $\widetilde{U}^{\dagger} d\widetilde{U}/dx$. Because of the Majorana phase ambiguity there is no unique expression for these terms but, by using eq. (4.2), we can eliminate the ambiguity from all elements of a column of $\widetilde{U}$ bar one, $\widetilde{U}_{\beta i}$. Using the identity

$$
\widetilde{U}^{\dagger} \frac{d\widetilde{U}}{dx} = -\frac{d\widetilde{U}^{\dagger}}{dx} \widetilde{U}, \tag{4.10}
$$

we derive that

$$
\begin{aligned}
\left(\widetilde{U}^{\dagger} \frac{d\widetilde{U}}{dx} \right)_{ii} &= \frac{1}{2|\widetilde{U}_{\beta i}|^2} \sum_{\alpha \neq \beta} \left[\widetilde{U}_{\alpha i}^{*} \widetilde{U}_{\beta i} \frac{d}{dx} \left(\widetilde{U}_{\beta i}^{*} \widetilde{U}_{\alpha i} \right) - \widetilde{U}_{\beta i}^{*} \widetilde{U}_{\alpha i} \frac{d}{dx} \left(\widetilde{U}_{\alpha i}^{*} \widetilde{U}_{\beta i} \right) \right] \\
&\quad + \frac{1}{2|\widetilde{U}_{\beta i}|^2} \left(\widetilde{U}_{\beta i}^{*} \frac{d\widetilde{U}_{\beta i}}{dx} - \widetilde{U}_{\beta i} \frac{d\widetilde{U}_{\beta i}^{*}}{dx} \right).
\end{aligned} \tag{4.11}
$$

The first term of eq. (4.11) is well defined because it is independent of the $\widetilde{\alpha}$'s while the Majorana phase ambiguity is entirely contained in the second term. Introducing the variable Q_i to represent the first term in eq. (4.11), and using eq. (4.2), we find

$$\imath Q_i = \Xi \sum_{\alpha \neq \beta} \left(C_{\alpha\beta}^{(i)} \frac{dC_{\beta\alpha}^{(i)}}{dx} - C_{\beta\alpha}^{(i)} \frac{dC_{\alpha\beta}^{(i)}}{dx} \right), \tag{4.12}$$

with $\Xi = \left[2|\widetilde{U}_{\beta i}|^2 \left(\mathrm{Tr}\left[C^{(i)} \right] \right)^2 \right]^{-1}$. This leaves the second term in eq. (4.11). If the phase of $\widetilde{U}_{\beta i}$ is chosen to be solely the Majorana phase i.e $\arg(\widetilde{U}_{\beta i}) = -\widetilde{\alpha}_i$ - since there are $N-1$ Dirac phases, β will be fixed to the electron flavor for all i - then

$$\frac{1}{2|\widetilde{U}_{\beta i}|^2} \left(\widetilde{U}_{\beta i}^* \frac{d\widetilde{U}_{\beta i}}{dx} - \widetilde{U}_{\beta i} \frac{d\widetilde{U}_{\beta i}^*}{dx} \right) = -\imath \frac{d\widetilde{\alpha}_i}{dx}. \tag{4.13}$$

Thus we obtain the result that the diagonal elements of $\widetilde{U}^\dagger \, d\widetilde{U}/dx$ are

$$\left(\widetilde{U}^\dagger \frac{d\widetilde{U}}{dx} \right)_{ii} = \imath Q_i - \imath \frac{d\widetilde{\alpha}_i}{dx}. \tag{4.14}$$

Inserting eq. (4.14) into the matter basis Hamiltonian of eq. (4.5) we obtain our final result that $\widetilde{H}$ can be written as

$$\widetilde{H} = \begin{pmatrix} \widetilde{k}_1 + Q_1 - \frac{d\widetilde{\alpha}_1}{dx} & \imath \frac{(\delta\widetilde{k}_{12}+\delta Q_{12})}{2\pi} \Gamma_{12} & \imath \frac{(\delta\widetilde{k}_{13}+\delta Q_{13})}{2\pi} \Gamma_{13} & \cdots \\ -\imath \frac{(\delta\widetilde{k}_{12}+\delta Q_{12})}{2\pi} \Gamma_{12}^* & \widetilde{k}_2 + Q_2 - \frac{d\widetilde{\alpha}_2}{dx} & \imath \frac{(\delta\widetilde{k}_{23}+\delta Q_{23})}{2\pi} \Gamma_{23} & \cdots \\ -\imath \frac{(\delta\widetilde{k}_{13}+\delta Q_{13})}{2\pi} \Gamma_{13}^* & -\imath \frac{(\delta\widetilde{k}_{23}+\delta Q_{23})}{2\pi} \Gamma_{23}^* & \widetilde{k}_3 + Q_3 - \frac{d\widetilde{\alpha}_3}{dx} & \cdots \\ \vdots & \vdots & \vdots & \ddots \end{pmatrix}, \tag{4.15}$$

with $\delta Q_{ij} = Q_i - Q_j$. We have introduced the Γ_{ij} functions which are the generalized non-adiabaticity parameters for neutrino oscillations with arbitrary potentials. Note that, in the MSW case, the Γ only depend upon the derivative of the matter angles. The generalized non-adiabaticity parameters are defined as

$$\begin{align} \Gamma_{ij} &= -\frac{2\pi e^{\imath\delta\widetilde{\alpha}_{ij}}}{(\delta\widetilde{k}_{ij} + \delta Q_{ij})} \left(\widetilde{U}^\dagger \frac{d\widetilde{U}}{dx} \right)_{ij} \tag{4.16} \\ &= \frac{2\pi e^{\imath\delta\widetilde{\alpha}_{ij}}}{\delta\widetilde{k}_{ij} (\delta\widetilde{k}_{ij} + \delta Q_{ij})} \left(\widetilde{U}^\dagger \frac{dH}{dx} \widetilde{U} \right)_{ij}, \tag{4.17} \end{align}$$

where we have substituted in, the results from eq. (4.9). Note that in eq. (4.17), the Γ_{ij} functions are directly related to the first derivative of the flavor Hamiltonian H. So we need to find an analytical expression for it.

4.1.2 The Hamiltonian first and second derivatives

4.1.2.1 First derivatives

We now apply the Γ_{ij} expressions given by eq. (4.17) to our case of interest. The first derivative of the flavor Hamiltonian has two contributions, one from the

matter induced potential Hamiltonian H^{mat} (eq. (1.61)) and the other one from the neutrino self-interaction Hamiltonian $H^{\nu\nu}$ (eq. (2.101)) since the vacuum term is a constant. As discussed in chapter 2, in our calculations we use realistic density profiles form supernova simulations. These have an inverse power law dependence for the matter density profile. Therefore its derivative is just [1]

$$H^{\text{mat}} \propto x^{-n} \quad \Rightarrow \quad \dot{H}^{\text{mat}} \propto -n\, x^{-(n+1)}. \tag{4.18}$$

For the neutrino self-interaction Hamiltonian in the multi-angle case $H^{\nu\nu}_{\text{ma}}$ (eq. (2.101)), the Hamiltonian reads

$$
\begin{aligned}
H^{\nu\nu}_{\text{ma}} = \; & \frac{\sqrt{2}G_F}{2\pi R_\nu^2} \sum_\alpha \int_0^\infty \int_{\cos\theta_{max}}^1 dq'\, d\cos\theta'\, h(\theta') \\
& [\rho_{\nu_\alpha}(q',\theta')F_{\nu_\alpha}(q') - \rho^*_{\bar{\nu}_\alpha}(q',\theta')F_{\bar{\nu}_\alpha}(q')],
\end{aligned}
\tag{4.19}
$$

with

$$\cos\theta_{max} = \sqrt{1 - (R_\nu/x)^2} \quad \text{and} \quad h(\theta') = 1 - \cos\theta\cos\theta'. \tag{4.20}$$

We remind that ρ_{ν_α} are the density matrices (eq. (2.89)), F_{ν_α} the neutrino flux at the neutrino-sphere (eq. (2.10)) for a neutrino born with the flavor α and q' is the neutrino energy. Using the Leibniz Integral Rule

$$\frac{\partial}{\partial z}\int_{a(z)}^{b(z)} f(y,z)dx = \int_{a(z)}^{b(z)} \frac{\partial f(y,z)}{\partial z}dx + f(b(z),z)\frac{\partial b(z)}{\partial z} - f(a(z),z)\frac{\partial a(z)}{\partial z}, \tag{4.21}$$

and the Liouville Von-Neumann equation (see appendix B.2), the derivative of eq. (4.19) is

$$\dot{H}^{\nu\nu}_{\text{ma}} = \frac{\sqrt{2}G_F}{2\pi R_\nu^2} \sum_\alpha \int_0^\infty dq'\, (R(\theta',q') - S(x)\,T(q')), \tag{4.22}$$

with the functions

$$
\begin{aligned}
R(\theta',q') = \; & -\int_{\cos\theta_{max}}^1 d\cos\theta'\, h(\theta') \\
& \left[[H,\rho_{\nu_\alpha}(q',\theta')]\, F_{\nu_\alpha}(q') + [\bar{H},\rho_{\bar{\nu}_\alpha}(q',\theta')]^*\, F_{\bar{\nu}_\alpha}(q') \right],
\end{aligned}
\tag{4.23}
$$

$$S(x) = \frac{R_\nu^2}{x^3\, f(x)}, \tag{4.24}$$

$$T(q') = h(\theta_{max})[\rho_{\nu_\alpha}(q',\theta_{max})F_{\nu_\alpha}(q') - \rho^*_{\bar{\nu}_\alpha}(q',\theta_{max})F_{\bar{\nu}_\alpha}(q')], \tag{4.25}$$

with $\bar{H}$ indicating the Hamiltonian for antineutrinos. In the case of antineutrinos, eqs. (4.23) and (4.25) holds but by replacing $H \leftrightarrow \bar{H}$ and $\nu \leftrightarrow \bar{\nu}$.

Most of the numerical studies, including ours, use the single-angle approximation of the Hamiltonian $\dot{H}^{\nu\nu}_{\text{ma}}$. In such approximation, $H^{\nu\nu}_{\text{sa}}$ (eq. (2.103)) factors as

$$H^{\nu\nu}_{\text{sa}} = F(x)_{\text{sa}} G(\rho)_{\text{sa}}, \tag{4.26}$$

with the geometrical factor

$$F(x)_{\text{sa}} = \frac{\sqrt{2}G_F}{2\pi R_\nu^2}\frac{1}{2}(1 - f(x))^2 \quad \text{with} \quad f(x) = \sqrt{1 - \left(\frac{R_\nu}{x}\right)^2}, \tag{4.27}$$

---

1. From now on we indicate differentiation by $\dot{f} = df/dx$ for compactness.

where R_ν is the radius of the neutrino-sphere and x the distance from it. The non-linear contribution is given by

$$G(\rho)_{\mathrm{sa}} = \sum_\alpha \int dq' \, [\rho_{\nu_\alpha}(q') F_{\nu_\alpha}(q') - \rho^*_{\bar{\nu}_\alpha}(q') F_{\bar{\nu}_\alpha}(q')]. \tag{4.28}$$

The corresponding derivative $\dot{H}^{\nu\nu}_{\mathrm{sa}}$ includes contributions from both the derivative of the geometrical factor and the density matrices, i.e.

$$\dot{H}^{\nu\nu}_{\mathrm{sa}} = \dot{F}(x)_{\mathrm{sa}} G(\rho)_{\mathrm{sa}} + F(x)_{\mathrm{sa}} \dot{G}(\rho)_{\mathrm{sa}}, \tag{4.29}$$

where the calculation of $\dot{F}(x)$ is straightforward

$$\dot{F}(x)_{\mathrm{sa}} = -\frac{\sqrt{2} G_F}{2\pi R^2_\nu} R^2_\nu x^{-3} \frac{1 - f(x)}{f(x)}, \tag{4.30}$$

and the one for the non-linear term is obtained using again the Liouville Von-Neumann equation. We obtain

$$\dot{G}(\rho)_{\mathrm{sa}} = -\imath \sum_\alpha \int [[H, \rho_{\nu_\alpha}(q')] F_{\nu_\alpha}(q') + [\bar{H}, \rho_{\bar{\nu}_\alpha}(q')]^* F_{\bar{\nu}_\alpha}(q')] dq'. \tag{4.31}$$

4.1.2.2 Second derivatives

In our third work [26], we have established a connection between the spectral split and magnetic resonance for which we need the second derivative of the Hamiltonian. Therefore we give here the second derivative of the flavor Hamiltonian $\ddot{H}$ using some of the previous results.

As for the first derivative, the second derivative has only contribution of the matter induced potential Hamiltonian H^{mat} and of the neutrino self-interaction Hamiltonian $H^{\nu\nu}$ since the vacuum term is a constant. Still using an inverse power law for the matter density profile, its second derivative is [2]

$$H^{\mathrm{mat}} \propto x^{-n} \quad \Rightarrow \quad \ddot{H}^{\mathrm{mat}} \propto n(n+1) \, x^{-(n+2)}. \tag{4.32}$$

For the neutrino self-interaction Hamiltonian in the multi-angle case $H^{\nu\nu}_{\mathrm{ma}}$, the second derivative depends on the functions $R(\theta', q')$, $S(x)$ and $T(q')$ defined in eqs. (4.22), (4.23), (4.24) and (4.25) as

$$\ddot{H}^{\nu\nu}_{\mathrm{ma}} = \frac{\sqrt{2} G_F}{2\pi R^2_\nu} \sum_\alpha \int_0^\infty dq' \, \left(\dot{R}(\theta', q') - \dot{S}(x) \, T(q') - S(x) \, \dot{T}(q') \right). \tag{4.33}$$

Its evaluation requires the first derivatives of the R, T and S functions. For $\dot{R}$ we get the following equation

$$\dot{R}(\theta', q') = \int_{\cos\theta_{max}}^1 d\cos\theta' \, \left(R_1(\theta', q') + R_2(\theta', q') \right) + R_3(\theta', q'), \tag{4.34}$$

where

$$R_1(\theta', q') = -\imath h(\theta') \left([\dot{H}, \rho_{\nu_\alpha}(q', \theta')] \, F_{\nu_\alpha}(q') + \left[\dot{\bar{H}}, \rho_{\bar{\nu}_\alpha}(q', \theta') \right]^* F_{\bar{\nu}_\alpha}(q') \right), \tag{4.35}$$

---

2. From now on we indicate differentiation by $\ddot{f} = d^2 f / dx^2$ for compactness.

$$R_2(\theta', q') = h(\theta') \left(- [H, [H, \rho_{\nu_\alpha}(q', \theta')]] \, F_{\nu_\alpha}(q') + [\bar{H}, [\bar{H}, \rho_{\bar{\nu}_\alpha}(q', \theta')]]^* \, F_{\bar{\nu}_\alpha}(q') \right),$$
(4.36)

$$R_3(\theta', q') = \imath S(x) h(\theta_{max}) \left([H, \rho_{\nu_\alpha}(q', \theta')] \, F_{\nu_\alpha}(q') + [\bar{H}, \rho_{\bar{\nu}_\alpha}(q', \theta')]^* \, F_{\bar{\nu}_\alpha}(q') \right). \tag{4.37}$$

For the derivative of the function $S(x)$, one obtains

$$\dot{S}(x) = R_\nu^2 \left[-\frac{3}{x^4 f(x)} - \frac{R_\nu^2}{x^6 f(x)^3} \right], \tag{4.38}$$

and finally the derivative of the $T(q')$ function reads

$$\dot{T}(q') = T_1(q') + T_2(q'), \tag{4.39}$$

with

$$T_1(q') = -\cos\theta \, S(x) \left[\rho_{\nu_\alpha}(q', \theta_{max}) F_{\nu_\alpha}(q') - \rho_{\bar{\nu}_\alpha}^*(q', \theta_{max}) F_{\bar{\nu}_\alpha}(q') \right], \tag{4.40}$$

$$T_2(q') = -\imath h(\theta_{max}) \left[[H, \rho_{\nu_\alpha}(q', \theta_{max})] \, F_{\nu_\alpha}(q') + [\bar{H}, \rho_{\bar{\nu}_\alpha}(q', \theta_{max})]^* \, F_{\bar{\nu}_\alpha}(q') \right]. \tag{4.41}$$

As for the first derivative, while we give equations for the multi-angle case for completeness, we derive the expression of the second derivative of the neutrino self-interaction Hamiltonian in the single-angle approximation since this is the approximation that we will employ. By using the factorization of eq. (4.26), the formal expression of $\ddot{H}_{sa}^{\nu\nu}$ is

$$\ddot{H}_{sa}^{\nu\nu} = \ddot{F}(x)_{sa} G(\rho)_{sa} + 2\dot{F}(x)_{sa} \dot{G}(\rho)_{sa} + F(x)_{sa} \ddot{G}(\rho)_{sa}. \tag{4.42}$$

The expressions of $\dot{F}(x)_{sa}$ and $\dot{G}(\rho)_{sa}$ are given by eqs. (4.30) and (4.31). The second derivative of the geometrical factor $F(x)$ is obvious

$$\ddot{F}(x)_{sa} = \frac{\sqrt{2} G_F R_\nu^2}{2\pi x^6} \left(f(x)^{-2} + (1 - f(x)) f(x)^{-3} + 3R_\nu^{-2} x^2 (1 - f(x)) f(x)^{-1} \right), \tag{4.43}$$

and the second derivative of the function $G(\rho)_{sa}$ containing the density matrices is

$$\ddot{G}(\rho)_{sa} = -\imath \sum_\alpha \int \left[\left([\dot{H}, \rho_{\nu_\alpha}(q')] - \imath \, [H, [H, \rho_{\nu_\alpha}(q')]] \right) F_{\nu_\alpha} \right.$$
$$\left. \left([\dot{\bar{H}}, \rho_{\bar{\nu}_\alpha}(q')] - \imath \, [\bar{H}, [\bar{H}, \rho_{\bar{\nu}_\alpha}(q')]] \right)^* F_{\bar{\nu}_\alpha} \right] dq'. \tag{4.44}$$

Thereafter we apply all these formal expressions and the polarization vector formalism (see appendix B.1) to the two flavors case to gain further understanding of the neutrino self-interaction effects in supernovae and of the three regimes: synchronization, bipolar oscillations and spectral split phenomenon. We stress that our works are based upon an exact treatment in the single-angle approximation i.e. without using the simplifications often employed in the toy models proposed in the literature [15]. The approximation usually made are three:

1. the matter density profile is constant and a maximal (or minimal) effective mixing angle is used,

2. the neutrino self-interaction has either no spatial dependence or a simplified one,

3. the neutrino and antineutrino spectra are represented by either a single energy or a box-like spectra.

4.2 AN APPLICATION TO TWO NEUTRINO FLAVORS

Let us now apply the results obtained in section 4.1 and in particular eqs. (4.15) and (4.17) to the case of two neutrino flavors. For the unitary matrix $\widetilde{U}$, it is well known that in vacuum the Dirac phase β can be absorbed by redefining the charged fermion fields in the standard model lagrangian. This possibility indicates that their absolute values cannot affect observables, however, once this is done, we have removed this degree of freedom. Here we cannot ignore the possibility that this phase could reappear in matter. As a result, we use the general parametrization of the mixing matrix $\widetilde{U}$ (see eq. (A.23))

$$\widetilde{U} = \begin{pmatrix} 1 & 0 \\ 0 & e^{\imath\widetilde{\beta}} \end{pmatrix} \begin{pmatrix} \cos\widetilde{\theta} & \sin\widetilde{\theta} \\ -\sin\widetilde{\theta} & \cos\widetilde{\theta} \end{pmatrix} \begin{pmatrix} e^{-\imath\widetilde{\alpha}_1} & 0 \\ 0 & e^{-\imath\widetilde{\alpha}_2} \end{pmatrix}, \tag{4.45}$$

where the phase $\widetilde{\beta}$ is the Dirac phase in matter and $\widetilde{\alpha}_i$ are the Majorana phases in matter. With this parametrization the elements of the flavor Hamiltonian H describing e.g. neutrino propagation in Supernova including neutrino mixing, coupling to matter and the neutrino self-interaction are given by

$$H = \begin{pmatrix} H_{ee} & H_{e\mu} \\ H_{\mu e} & H_{\mu\mu} \end{pmatrix} = \begin{pmatrix} \widetilde{k}_1 \cos^2\widetilde{\theta} + \widetilde{k}_2 \sin^2\widetilde{\theta} & -\delta\widetilde{k}_{12}\, e^{-\imath\widetilde{\beta}} \cos\widetilde{\theta}\sin\widetilde{\theta} \\ -\delta\widetilde{k}_{12}\, e^{\imath\widetilde{\beta}} \cos\widetilde{\theta}\sin\widetilde{\theta} & \widetilde{k}_1 \sin^2\widetilde{\theta} + \widetilde{k}_2 \cos^2\widetilde{\theta} \end{pmatrix}. \tag{4.46}$$

We note that the Majorana phases do not appear in these expressions. From eq. (4.46), it is very simple to derive several different relationships between the matter angle $\widetilde{\theta}$ and the elements of the flavor basis Hamiltonian H e.g.

$$\sin^2\widetilde{\theta} = \frac{H_{ee} - \widetilde{k}_1}{\widetilde{k}_2 - \widetilde{k}_1} \quad \text{and} \quad \cos^2\widetilde{\theta} = \frac{H_{\mu\mu} - \widetilde{k}_1}{\widetilde{k}_2 - \widetilde{k}_1}. \tag{4.47}$$

For the Dirac phase $\widetilde{\beta}$ we derive the expression

$$\tan\widetilde{\beta} = \imath \left(\frac{H_{e\mu} - H_{\mu e}}{H_{e\mu} + H_{\mu e}} \right) = -\frac{\Im\left(H_{e\mu}\right)}{\Re\left(H_{e\mu}\right)}, \tag{4.48}$$

where $\Re\left(c\right)$ and $\Im\left(c\right)$ are the real and imaginary part of a complex c.

From this equation we immediately see that when the off-diagonal elements of H are independent of position then $\widetilde{\beta}$ is simply the same as in vacuum. Also, if the off-diagonal term $H_{e\mu} \in \mathbb{R}$ during the propagation then the Dirac phase $\widetilde{\beta}$ stays equal to zero.

By differentiating $\widetilde{U}$ and multiplying by $\widetilde{U}^\dagger$ one finds the detailed expression

$$\widetilde{U}^\dagger \frac{d\widetilde{U}}{dx} = \imath \begin{pmatrix} \sin^2\widetilde{\theta} & -\frac{\sin 2\widetilde{\theta}}{2} e^{\imath\delta\widetilde{\alpha}_{12}} \\ -\frac{\sin 2\widetilde{\theta}}{2} e^{-\imath\delta\widetilde{\alpha}_{12}} & \cos^2\widetilde{\theta} \end{pmatrix} \dot{\widetilde{\beta}} + \begin{pmatrix} 0 & e^{\imath\delta\widetilde{\alpha}_{12}} \\ -e^{-\imath\delta\widetilde{\alpha}_{12}} & 0 \end{pmatrix} \dot{\widetilde{\theta}}$$
$$-\imath \begin{pmatrix} \dot{\widetilde{\alpha}}_1 & 0 \\ 0 & \dot{\widetilde{\alpha}}_2 \end{pmatrix}, \tag{4.49}$$

so, following eq. (4.15), the full two flavor Hamiltonian in the matter basis $\widetilde{H}$

$$\widetilde{H} = \begin{pmatrix} \widetilde{k}_1 + Q_1 - \dot{\widetilde{\alpha}}_1 & \imath\frac{(\delta\widetilde{k}_{12} + \delta Q_{12})}{2\pi} \Gamma_{12} \\ -\imath\frac{(\delta\widetilde{k}_{12} + \delta Q_{12})}{2\pi} \Gamma_{12}^* & \widetilde{k}_2 + Q_2 - \dot{\widetilde{\alpha}}_2 \end{pmatrix}, \tag{4.50}$$

explicitly reads

$$\widetilde{H} = \begin{pmatrix} \widetilde{k}_1 + \dot{\widetilde{\beta}}\sin^2\widetilde{\theta} - \dot{\widetilde{\alpha}}_1 & -e^{\imath\delta\widetilde{\alpha}_{12}}\left(\dot{\widetilde{\beta}}\frac{\sin 2\widetilde{\theta}}{2} + \imath\dot{\widetilde{\theta}}\right) \\ -e^{-\imath\delta\widetilde{\alpha}_{12}}\left(\dot{\widetilde{\beta}}\frac{\sin 2\widetilde{\theta}}{2} - \imath\dot{\widetilde{\theta}}\right) & \widetilde{k}_2 + \dot{\widetilde{\beta}}\cos^2\widetilde{\theta} - \dot{\widetilde{\alpha}}_2 \end{pmatrix}, \tag{4.51}$$

where $\delta\widetilde{\alpha}_{12} = \widetilde{\alpha}_1 - \widetilde{\alpha}_2$. From the diagonal elements of $\widetilde{H}$ we read off the Q_i's to be (see eq. (4.12))

$$Q_1 = \dot{\widetilde{\beta}}\sin^2\widetilde{\theta}, \tag{4.52}$$
$$Q_2 = \dot{\widetilde{\beta}}\cos^2\widetilde{\theta}, \tag{4.53}$$

and from the off-diagonal entries we derive that the generalized non-adiabaticity parameter is

$$\Gamma_{12} = -\frac{2\pi\, e^{\imath\delta\widetilde{\alpha}_{12}}}{\delta\widetilde{k}_{12} + \delta Q_{12}}\left(\dot{\widetilde{\theta}} - \imath\frac{\sin 2\widetilde{\theta}}{2}\dot{\widetilde{\beta}}\right), \tag{4.54}$$

and observe that it depends both on the derivative of the matter angle $\widetilde{\theta}$, as in the MSW case, and on the derivative of the matter phase $\widetilde{\beta}$. From eq. (4.54) one notes that the Γ_{12} is defined up to the Majorana phases. As we have explained before, we are free to choose what we want for $\widetilde{\alpha}_i$ and decided to take $\widetilde{\alpha}_1 = \widetilde{\alpha}_2 = 0$. In order for the imaginary component of Γ_{12} to be non-zero we require that the off-diagonal elements of H rotate in the Argand plane. Neutrino self-interaction gives exactly such a term because the flavor basis Hamiltonian includes contributions from the density matrices i.e. $H \sim \rho$.

In order to compute the expressions of the RHS of eqs. (4.52) and (4.53), we find for the derivative of the Dirac phase $\widetilde{\beta}$

$$\dot{\widetilde{\beta}} = \frac{\Im\left(H_{e\mu}\right)\Re\left(\dot{H}_{e\mu}\right) - \Re\left(H_{e\mu}\right)\Im\left(\dot{H}_{e\mu}\right)}{|H_{e\mu}|^2}, \tag{4.55}$$

where we use the formulas derived in eqs. (4.29), (4.30) and (4.31) to evaluate $\Re\left(\dot{H}_{e\mu}\right)$ and $\Im\left(\dot{H}_{e\mu}\right)$. We also find an expression for the first derivative of the matter angle $\widetilde{\theta}$ which is

$$\dot{\widetilde{\theta}} = \frac{\left(\dot{H}_{ee} - \dot{H}_{\mu\mu}\right)\delta\widetilde{k}_{12} - \left(H_{ee} - H_{\mu\mu}\right)\delta\dot{\widetilde{k}}_{12}}{4\delta\widetilde{k}_{12}|H_{e\mu}|}. \tag{4.56}$$

In eq. (4.56), the term $\delta\dot{\widetilde{k}}_{12}$ can be calculated in two ways. We can differentiate eq. (4.46) and find

$$\dot{\widetilde{k}}_1 = \cos^2\widetilde{\theta}\,\dot{H}_{ee} + \sin^2\widetilde{\theta}\,\dot{H}_{\mu\mu} - \cos\widetilde{\theta}\sin\widetilde{\theta}\left(e^{\imath\widetilde{\beta}}\dot{H}_{e\mu} + e^{-\imath\widetilde{\beta}}\dot{H}_{\mu e}\right), \tag{4.57}$$
$$\dot{\widetilde{k}}_2 = \sin^2\widetilde{\theta}\,\dot{H}_{ee} + \cos^2\widetilde{\theta}\,\dot{H}_{\mu\mu} + \cos\widetilde{\theta}\sin\widetilde{\theta}\left(e^{\imath\widetilde{\beta}}\dot{H}_{e\mu} + e^{-\imath\widetilde{\beta}}\dot{H}_{\mu e}\right), \tag{4.58}$$

or directly estimate this term with eq. (4.7) and obtain

$$\delta\dot{\widetilde{k}}_{12} = \left(\widetilde{U}^\dagger\frac{dH}{dx}\widetilde{U}\right)_{11} - \left(\widetilde{U}^\dagger\frac{dH}{dx}\widetilde{U}\right)_{22}. \tag{4.59}$$

We checked that eqs. (4.57) and (4.58) and eq. (4.59) are consistent.

4.2.1 Correspondence between flavor survival probabilities and matter survival probabilities

Before going into details for the three regimes identified in the survival probabilities (see figure 2.22), we want to emphasize an equivalence that exists between the neutrino survival probabilities in the flavor and the matter basis. This equivalence allows us then to study the neutrino self-interaction in the flavor basis or the matter basis because the impacts seen in the survival probabilities are the same in both basis. Of course the amplitudes of the wave functions in both basis are completely different and consequently the underlying dynamics is not the same.

As it has discussed in section 1.2.3, the presence of the matter potential induces a maximization (or minimization) of the matter angle $\widetilde{\theta}$. For neutrinos, we have $\widetilde{\theta} \simeq 0$ in inverted hierarchy, which is the hierarchy we are interested in [3]. This extreme value of the effective angle will only change when the MSW region is reached by the neutrino. Therefore for our study of the neutrino self-interaction effects, i.e. before the MSW region, $\widetilde{\theta} \simeq 0$ is a good approximation. We note that for our calculations of the next sections, and published in [25, 26], we do not take this approximation for the matter angle but we calculate the exact value of $\widetilde{\theta}$ using eq. (4.47). The transformation from the flavor basis to the matter basis at high matter density is

$$\psi = \widetilde{U}\widetilde{\psi} \quad \Rightarrow \quad \begin{pmatrix} \nu_e \\ \nu_\mu \end{pmatrix} = \begin{pmatrix} 1 & 0 \\ 0 & e^{i\widetilde{\beta}} \end{pmatrix} \begin{pmatrix} \widetilde{\nu}_1 \\ \widetilde{\nu}_2 \end{pmatrix}. \tag{4.60}$$

Then we find for the survival probabilities the relation $P(\nu_e \to \nu_e) = P(\widetilde{\nu}_1 \to \widetilde{\nu}_1)$. We have the same explanation for antineutrinos but with $\widetilde{\theta} \simeq \pi/2$ in that case. Then we obtain $P(\bar{\nu}_e \to \bar{\nu}_e) = P(\widetilde{\nu}_2 \to \widetilde{\nu}_2)$. This expectation is confirmed by the numerical results plotted on figure 4.1. Such numerical results are obtained by solving

$$\imath \frac{d\psi}{dx} = H\,\psi, \tag{4.61}$$

with

$$\psi = \begin{pmatrix} \nu_e \\ \nu_\mu \end{pmatrix} \quad \text{and} \quad H = H^{\text{vac}} + H^{\text{mat}} + H^{\nu\nu}. \tag{4.62}$$

Here the flavor Hamiltonian H is composed of:
  – the vacuum Hamiltonian $H^{\text{vac}} = UKU^\dagger$ with $K = \text{diag}\left(m_1^2, m_2^2\right)$,
  – the matter induced potential $H^{\text{mat}} = \sqrt{2}G_F N_e\,\delta_{\alpha e}$,
  – the neutrino self-interaction Hamiltonian $H^{\nu\nu}$ in the single-angle approximation (see eq. (2.103)).

The calculations are done with the parameters $\Delta m_{21}^2 = -2.4 \times 10^{-3}\,\text{eV}^2$, $\theta_0 = 9°$ and equal luminosities $L_{\nu_e} = L_{\bar{\nu}_e} = L_{\nu_x} = 10^{51}\,\text{erg.s}^{-1}$.

In conclusion, we can use both basis to explain the complex behavior of the survival probabilities knowing that $\nu_e \equiv \widetilde{\nu}_1$ and $\bar{\nu}_e \equiv \widetilde{\nu}_2$. In the works we describe here, we indeed use the matter basis to extract more informations about the underlying effects.

---

3. We remind that the neutrino self-interaction effects only take place in inverted hierarchy when the equipartition of the luminosity among all flavors is assumed.
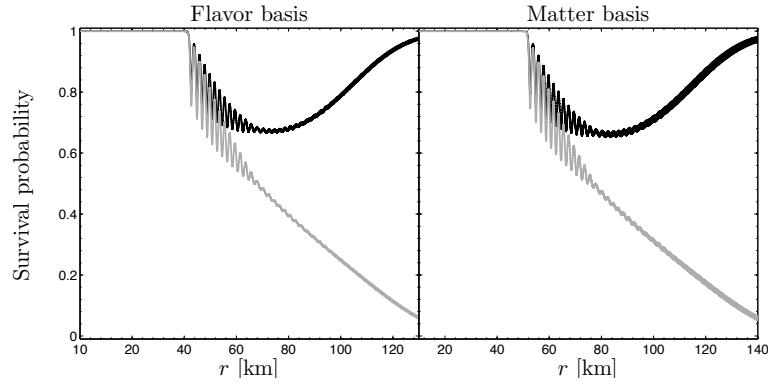
(a) Neutrino survival probability equivalence $P(\nu_e \to \nu_e) = P(\widetilde{\nu}_1 \to \widetilde{\nu}_1)$.
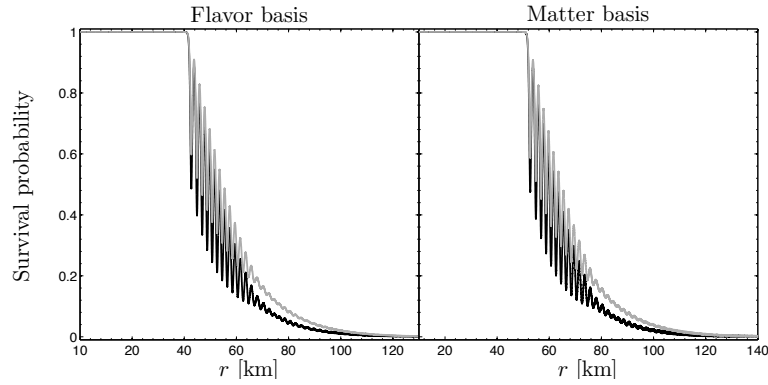
(b) Antineutrino survival probability equivalence $P(\bar{\nu}_e \to \bar{\nu}_e) = P(\widetilde{\bar{\nu}}_2 \to \widetilde{\bar{\nu}}_2)$.

Figure 4.1 – *Neutrino survival probabilities equivalence between the flavor and the matter basis in the neutrino self-interaction region ($x < 140$ km). The results are obtained with the parameters $\Delta m_{21}^2 = -2.4 \times 10^{-3}\,\mathrm{eV}^2$, $\theta_0 = 9°$ and equal luminosities $L_{\nu_e} = L_{\bar{\nu}_e} = L_{\nu_x} = 10^{51}\,erg.\mathrm{s}^{-1}$.*

4.2.2 Conditions for the end of the synchronization regime

To explain the different behaviors that we have identified in the neutrino and antineutrino survival probability patterns, we will often refer to the polarization vector formalism (see appendix B.1). Within this formalism, we define a magnetic field **B** and a polarization vector **P** which are in the flavor basis

$$\mathbf{B} = \begin{pmatrix} 2\,\Re\left(H_{e\mu}\right) \\ -2\,\Im\left(H_{e\mu}\right) \\ H_{ee} - H_{\mu\mu} \end{pmatrix} \quad \text{and} \quad \mathbf{P} = \begin{pmatrix} 2\,\Re\left(\nu_e\nu_\mu^*\right) \\ -2\,\Im\left(\nu_e\nu_\mu^*\right) \\ |\nu_e|^2 - |\nu_\mu|^2 \end{pmatrix}, \tag{4.63}$$

while the definition of the magnetic field $\widetilde{\mathbf{B}}$ and the polarization vector $\widetilde{\mathbf{P}}$ in the matter basis are

$$\widetilde{\mathbf{B}} = \begin{pmatrix} 2\,\Re\left(\widetilde{H}_{12}\right) \\ -2\,\Im\left(\widetilde{H}_{12}\right) \\ \widetilde{H}_{11} - \widetilde{H}_{22} \end{pmatrix} \quad \text{and} \quad \widetilde{\mathbf{P}} = \begin{pmatrix} 2\,\Re\left(\widetilde{\nu}_1\widetilde{\nu}_2^*\right) \\ -2\,\Im\left(\widetilde{\nu}_1\widetilde{\nu}_2^*\right) \\ |\widetilde{\nu}_1|^2 - |\widetilde{\nu}_2|^2 \end{pmatrix}. \tag{4.64}$$

Here we introduce for clarity two different frames which are defined to be
  – $\mathcal{R}_{\text{flavor}} = \{x, y, z\}$ for the flavor basis,
  – $\mathcal{R}_{\text{matter}} = \{X, Y, Z\}$ for the matter basis.

In the region between the neutrino-sphere radius that we take at $R_\nu = 10$ km and 50 km (see figure 2.22), the electron neutrino survival probability is stuck to 1 and no flavor conversion occurs, even partial. Indeed, the matter magnetic field $\widetilde{\mathbf{B}}$ is initially almost aligned with the Z-axis because the off-diagonal terms of $\widetilde{H}$ are tiny compared to the diagonal terms $\widetilde{k}_1$ and $\widetilde{k}_2$. Indeed at the beginning of the propagation, one of the eigenvalue is equal to the Hamiltonian term H_{ee} which is larger than the other terms by 3 order of magnitudes. So we have a magnetic field $\widetilde{\mathbf{B}}$ very close to the Z-axis and with a very small component in the XOY plane. The polarization vector $\widetilde{\mathbf{P}}$ representing the neutrino initially on the Z-axis i.e. $\widetilde{\mathbf{P}} = \widetilde{P}_Z \, \mathbf{e}_Z$, spins around the magnetic field with the angular velocity $|\widetilde{\mathbf{B}}|$. The smallness of the components $\widetilde{B}_{X,Y}$ implies that the oscillations of the Z component of $\widetilde{\mathbf{P}}$ are tiny too (figure 4.2). That is why, in the synchronized region, a good approximation is to consider

$$P(\widetilde{\nu}_1 \to \widetilde{\nu}_1) \simeq P(\widetilde{\nu}_2 \to \widetilde{\nu}_2) \simeq 1 \Rightarrow P(\nu_e \to \nu_e) \simeq P(\bar{\nu}_e \to \bar{\nu}_e) \simeq 1. \qquad (4.65)$$

(a) Vectors $\mathbf{B}$ and $\mathbf{P}$ in the flavor basis.   (b) Vectors $\widetilde{\mathbf{B}}$ and $\widetilde{\mathbf{P}}$ in the matter basis.
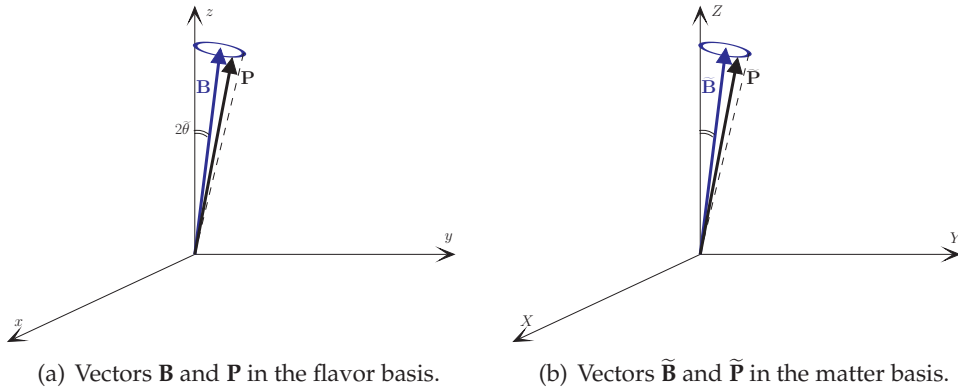
Figure 4.2 – *Polarization vectors spinning around the magnetic fields representing the Hamiltonians in the flavor and matter basis in the synchronization region. Due to the proximity of the magnetic fields with the z and Z axis, the oscillations of $\mathbf{P}$ and $\widetilde{\mathbf{P}}$ of the z and Z axis are tiny.*

To break the synchronization and enter in the bipolar regime, we need to reduce the difference between the off-diagonal and the diagonal terms of $\widetilde{H}$ to allow a connection between states 1 and 2. In other words, the X and Y component of $\widetilde{\mathbf{B}}$ have to be closer to the absolute value of $\widetilde{B}_Z$. Using eq. (4.64), one finds

$$\widetilde{\mathbf{B}} = \begin{pmatrix} -\frac{\delta\widetilde{k}_{12}+\delta Q_{12}}{\pi} \, \mathfrak{I}\left(\Gamma_{12}\right) \\ -\frac{\delta\widetilde{k}_{12}+\delta Q_{12}}{\pi} \, \mathfrak{R}\left(\Gamma_{12}\right) \\ \delta\widetilde{k}_{12} + \delta Q_{12} \end{pmatrix}. \qquad (4.66)$$

For neutrinos, we explicitly obtain

$$\widetilde{\mathbf{B}} = \begin{pmatrix} -\dot{\widetilde{\beta}} \sin 2\widetilde{\theta} \\ 2\dot{\widetilde{\theta}} \\ \delta\widetilde{k}_{12} - \dot{\widetilde{\beta}} \cos 2\widetilde{\theta} \end{pmatrix}. \qquad (4.67)$$

By looking at eq. (4.67), we have two possible choices to reduce the difference between the components of $\widetilde{\mathbf{B}}$. But in the region "close" to the PNS, the matter

angle does not change so much and $\dot{\tilde{\theta}} \simeq 0$. The significant effect coming from the variation of $\widetilde{\theta}$ are visible in the MSW resonance region, i.e. larger than 200 km. As a result, the only explanation is an effect coming from the variations of the matter Dirac phase $\widetilde{\beta}$.

In the expression of eq. (4.55), we remark that $\dot{\tilde{\beta}}$ is non-zero if the real or the imaginary part of $\dot{H}_{e\mu}$ is also non-zero. Let us see what is the trigger which authorizes the quantity $\dot{H}_{e\mu}$ to be non-zero at the neutrino-sphere. Using eq. (4.28), we can first say that the initial pure states at R_ν induces the fact that the $e\mu$ component of the matrix $G(\rho)$ (eq. (4.28)) is

$$G(\rho)_{e\mu} = 0. \tag{4.68}$$

So the only contribution comes from the other term of eq. (4.29), i.e. $\dot{G}(\rho)$. At the neutrino-sphere, the $e\mu$ component of H is solely the vacuum. The results of the commutators of eq. (4.31) are

$$\left[H, \rho_{\nu_{\underline{e}}}\right]_{e\mu} = -H_{e\mu}^{\text{vac}}, \tag{4.69}$$

$$\left[H, \rho_{\nu_{\underline{\mu}}}\right]_{e\mu} = H_{e\mu}^{\text{vac}}, \tag{4.70}$$

$$\left[\bar{H}, \rho_{\bar{\nu}_{\underline{e}}}\right]_{e\mu} = -\bar{H}_{e\mu}^{\text{vac}}, \tag{4.71}$$

$$\left[\bar{H}, \rho_{\bar{\nu}_{\underline{\mu}}}\right]_{e\mu} = \bar{H}_{e\mu}^{\text{vac}}, \tag{4.72}$$

where $\underline{\alpha}$ stands for a pure flavor $\alpha \in \{e, \mu\}$ at the neutrino-sphere. By taking the explicit vacuum terms in the context of two flavors

$$H_{e\mu}^{\text{vac}} = \bar{H}_{e\mu}^{\text{vac}} = \frac{\Delta m_{21}^2}{4q'} \sin 2\theta_0, \tag{4.73}$$

where q' is the neutrino energy and θ_0 the vacuum angle appearing in the mixing matrix U. The integration over the energy gives

$$\int dq' \left[H, \rho_{\nu_{\underline{e}}}\right]_{e\mu} F_{\nu_{\underline{e}}} = \frac{\Delta m_{21}^2}{4} \sin 2\theta_0 \int dq' \frac{F_{\nu_{\underline{e}}}}{q'}. \tag{4.74}$$

Now we replace the neutrino flux at the neutrino-sphere by e.g. the Fermi-Dirac distribution for the ν_e contribution (see eq. (2.10)) and we obtain

$$\int dq' \left[H, \rho_{\nu_{\underline{e}}}\right]_{e\mu} F_{\nu_{\underline{e}}} = -\frac{\Delta m_{21}^2 L_0}{4 \langle E_{\nu_e} \rangle^2} \sin 2\theta_0 \frac{F_3(\eta) F_1(\eta)}{F_2^2(\eta)}, \tag{4.75}$$

where L_0 is the initial luminosity, assuming an equipartition of the luminosity over each flavor, and $F_n(\eta_\nu)$ are the Fermi integral (without the Γ function normalization). We do exactly the same calculations for ν_μ, $\bar{\nu}_e$ and $\bar{\nu}_\mu$ and finally we have

$$\dot{H}_{e\mu} = -\imath \eth \sin 2\theta_0 \left(\frac{2}{\langle E_{\nu_\mu} \rangle^2} - \frac{1}{\langle E_{\nu_e} \rangle^2} - \frac{1}{\langle E_{\bar{\nu}_e} \rangle^2} \right), \tag{4.76}$$

where $\langle E_\nu \rangle$ indicates the neutrino average energies and we assume the equality $\langle E_{\nu_\mu} \rangle = \langle E_{\bar{\nu}_\mu} \rangle$. The function $\eth$ is defined as

$$\eth = \frac{\sqrt{2} G_F}{4\pi R_\nu^2} \frac{\Delta m_{21}^2}{4} L_0 \frac{F_3(\eta) F_1(\eta)}{F_2^2(\eta)}. \tag{4.77}$$

We first see in eq. (4.76) that the vacuum mixing angle θ_0 has to be non-zero to have $\dot{H}_{e\mu} \neq 0$. This statement was first pointed out in [15], with a toy model in the analogy with a pendulum. In addition to this condition, one must know if the term $\dot{H}_{e\mu}$ is stable or unstable to give rise to neutrino self-interaction effects.

By examining eq. (4.42), which gives the convexity of the off-diagonal terms of the Hamiltonian H, we distinguish three contributions at the neutrino-sphere:

1. $F(R_\nu)$ and $\ddot{G}(\rho)_{e\mu}$ are both constants and so $F(R_\nu)\ddot{G}(\rho)$ is a constant,
2. $\ddot{F}(R_\nu)$ tends to infinity and $G(\rho)_{e\mu}$ is strictly zero, so $\ddot{F}(R_\nu)G(\rho)_{e\mu}$ is zero,
3. $\dot{F}(R_\nu)$ tends to infinity and $\dot{G}(\rho)_{e\mu}$ is finite, so $\dot{F}(R_\nu)\dot{G}(\rho)$ tends to infinity.

Consequently we can say that we have two contributions of the second derivative $\ddot{H}^{\nu\nu}$ at the neutrino-sphere coming from the $\dot{F}(R_\nu)\dot{G}(\rho)$ term and the $F(R_\nu)\ddot{G}(\rho)$ term. Using the previous calculations, we find

$$\dot{F}(R_\nu)\dot{G}(\rho) = \dot{F}(R_\nu)\left[-\imath\frac{\Delta m_{21}^2}{4}L_0\frac{F_3(\eta)F_1(\eta)}{F_2^2(\eta)}\sin 2\theta_0\left(\frac{2}{\langle E_{\nu_\mu}\rangle^2} - \frac{1}{\langle E_{\nu_e}\rangle^2} - \frac{1}{\langle E_{\bar{\nu}_e}\rangle^2}\right)\right].$$
(4.78)

Because the quantity $\dot{F}(R_\nu)$ is real, the sign of eq. (4.78) define the convexity of the imaginary part of $H_{e\mu}$. Here we are interested in the convexity of the real part of $H_{e\mu}$ because at the neutrino-sphere, this term is pure real due to the contribution of the vacuum Hamiltonian. Let us focus on the second term $F(R_\nu)\ddot{G}(\rho)$.

At the neutrino-sphere, it is clear that the value of $F(R_\nu)$ is just $\sqrt{2}G_F/(4\pi R_\nu^2)$ which is positive. Now we calculate the value of the $e\mu$ component of the matrix $\ddot{G}(\rho)$ at the distance R_ν. The results of the double commutators of eq. (4.44) are

$$\left[H,\left[H,\rho_{\nu_{\underline{e}}}\right]\right]_{e\mu} = -H_{e\mu}(H_{ee} - H_{\mu\mu}), \tag{4.79}$$

$$\left[H,\left[H,\rho_{\nu_{\underline{\mu}}}\right]\right]_{e\mu} = H_{e\mu}(H_{ee} - H_{\mu\mu}), \tag{4.80}$$

$$\left[\bar{H},\left[\bar{H},\rho_{\bar{\nu}_{\underline{e}}}\right]\right]_{e\mu} = -\bar{H}_{e\mu}(\bar{H}_{ee} - \bar{H}_{\mu\mu}), \tag{4.81}$$

$$\left[\bar{H},\left[\bar{H},\rho_{\bar{\nu}_{\underline{\mu}}}\right]\right]_{e\mu} = \bar{H}_{e\mu}(\bar{H}_{ee} - \bar{H}_{\mu\mu}), \tag{4.82}$$

where $\underline{\alpha}$ stands for a pure flavor $\alpha \in \{e, \mu\}$ at the neutrino-sphere. By taking the explicit vacuum and matter potential terms and assuming that the fluxes follow Fermi-Dirac distributions, we find after integration over the energy

$$\begin{aligned}
\ddot{G}(\rho)_{e\mu} = {} & K_1 L_0\frac{F_3}{F_2^2}\left[K_2\frac{F_3 F_0}{F_2}\left(-\frac{1}{\langle E_{\nu_e}\rangle^3} + \frac{1}{\langle E_{\bar{\nu}_e}\rangle^3}\right)\right. \\
& \left. + \sqrt{2}G_F N_e F_1\left(\frac{1}{\langle E_{\nu_e}\rangle^2} + \frac{1}{\langle E_{\bar{\nu}_e}\rangle^2} - \frac{2}{\langle E_{\nu_\mu}\rangle^2}\right)\right] \\
& - \imath \dot{H}_{e\mu} L_0\left(-\frac{1}{\langle E_{\nu_e}\rangle} + \frac{1}{\langle E_{\bar{\nu}_e}\rangle}\right),
\end{aligned} \tag{4.83}$$

where the vacuum contribution are

$$K_1 = \frac{\Delta m_{21}^2}{4}\sin 2\theta_0, \tag{4.84}$$

$$K_2 = \frac{\Delta m_{21}^2}{2}\cos 2\theta_0. \tag{4.85}$$

Because the matter potential $\sqrt{2}G_F N_e$ is much larger than the vacuum contribution K_i. The eq. (4.83) can be reduced to

$$\ddot{G}(\rho)_{e\mu} \;=\; K_1 \, L_0 \frac{F_3}{F_2^2} \, \sqrt{2} G_F N_e \, F_1 \left(\frac{1}{\langle E_{\nu_e} \rangle^2} + \frac{1}{\langle E_{\bar{\nu}_e} \rangle^2} - \frac{2}{\langle E_{\nu_\mu} \rangle^2} \right). \tag{4.86}$$

Here, eq. (4.86) shows the convexity of the real part of the term $H_{e\mu}$ because all the parameters are reals.

Actually, we are not interested in the value but rather in the sign. We then have two scenarii, in normal hierarchy $K_1 > 0$ whereas it is negative in inverted hierarchy. The rest of the eq. (4.76) is guided by the the sign of

$$\frac{1}{\langle E_{\nu_e} \rangle^2} + \frac{1}{\langle E_{\bar{\nu}_e} \rangle^2} - \frac{2}{\langle E_{\nu_\mu} \rangle^2}, \tag{4.87}$$

where $\langle E_{\nu_e} \rangle$, $\langle E_{\bar{\nu}_e} \rangle$ and $\langle E_{\nu_\mu} \rangle$ are the degrees of freedom. With the typical hierarchy of the average energies in the cooling phase i.e. $\langle E_{\nu_e} \rangle < \langle E_{\bar{\nu}_e} \rangle < \langle E_{\nu_\mu} \rangle$, we have

$$\Re\left(\ddot{H}_{e\mu}\right) > 0 \text{ in normal hierarchy,}$$
$$\Re\left(\ddot{H}_{e\mu}\right) < 0 \text{ in inverted hierarchy.}$$

We conclude that the neutrino self-interaction can develop and give rise to new paradigm in inverted hierarchy because $H_{e\mu}$ is unstable ($\Re(\ddot{H}_{e\mu}^{\nu\nu}) < 0$) while it is not the case in normal hierarchy because $H_{e\mu}$ is stable ($\Re(\ddot{H}_{e\mu}^{\nu\nu}) > 0$). Here we recover, in an exact treatment, a result found in [15] about the fact that neutrino self-interaction (in the single-angle approximation) produces effects in inverted hierarchy and not in normal hierarchy. However we can go a bit further and add another condition on the neutrino average energy hierarchy. Neutrino self-interaction effects arise in inverted hierarchy if

$$\frac{1}{\langle E_{\nu_e} \rangle^2} + \frac{1}{\langle E_{\bar{\nu}_e} \rangle^2} - \frac{2}{\langle E_{\nu_\mu} \rangle^2} > 0. \tag{4.88}$$

While we have the opposite result, namely effects in normal hierarchy, if

$$\frac{1}{\langle E_{\nu_e} \rangle^2} + \frac{1}{\langle E_{\bar{\nu}_e} \rangle^2} - \frac{2}{\langle E_{\nu_\mu} \rangle^2} < 0. \tag{4.89}$$

To show that this is indeed the case, we have performed complete simulations by keeping $\langle E_{\nu_e} \rangle = 12 \, \text{MeV}$ and $\langle E_{\bar{\nu}_e} \rangle = 15 \, \text{MeV}$ and varying $\langle E_{\nu_\mu} \rangle$. We take three values

- $\langle E_{\nu_\mu} \rangle = 11 \, \text{MeV}$ to have $\dfrac{1}{\langle E_{\nu_e} \rangle^2} + \dfrac{1}{\langle E_{\bar{\nu}_e} \rangle^2} - \dfrac{2}{\langle E_{\nu_\mu} \rangle^2} < 0,$
- $\langle E_{\nu_\mu} \rangle = 13 \, \text{MeV}$ to have $\dfrac{1}{\langle E_{\nu_e} \rangle^2} + \dfrac{1}{\langle E_{\bar{\nu}_e} \rangle^2} - \dfrac{2}{\langle E_{\nu_\mu} \rangle^2} \simeq 0,$
- $\langle E_{\nu_\mu} \rangle = 16 \, \text{MeV}$ to have $\dfrac{1}{\langle E_{\nu_e} \rangle^2} + \dfrac{1}{\langle E_{\bar{\nu}_e} \rangle^2} - \dfrac{2}{\langle E_{\nu_\mu} \rangle^2} > 0.$

The results for both normal and inverted hierarchies are plotted on figure 4.3 and confirm our hypothesis. Indeed neutrino self-interaction effects arise in normal hierarchy when the quantity in eq. (4.87) is negative (figure 4.3 a) and in inverted hierarchy when the same quantity is positive (figure 4.3 f).

(a) $\langle E_{\nu_\mu} \rangle = 11\,\mathrm{MeV}$.

(b) $\langle E_{\nu_\mu} \rangle = 13\,\mathrm{MeV}$.

(c) $\langle E_{\nu_\mu} \rangle = 16\,\mathrm{MeV}$.

(d) $\langle E_{\nu_\mu} \rangle = 11\,\mathrm{MeV}$.

(e) $\langle E_{\nu_\mu} \rangle = 13\,\mathrm{MeV}$.

(f) $\langle E_{\nu_\mu} \rangle = 16\,\mathrm{MeV}$.
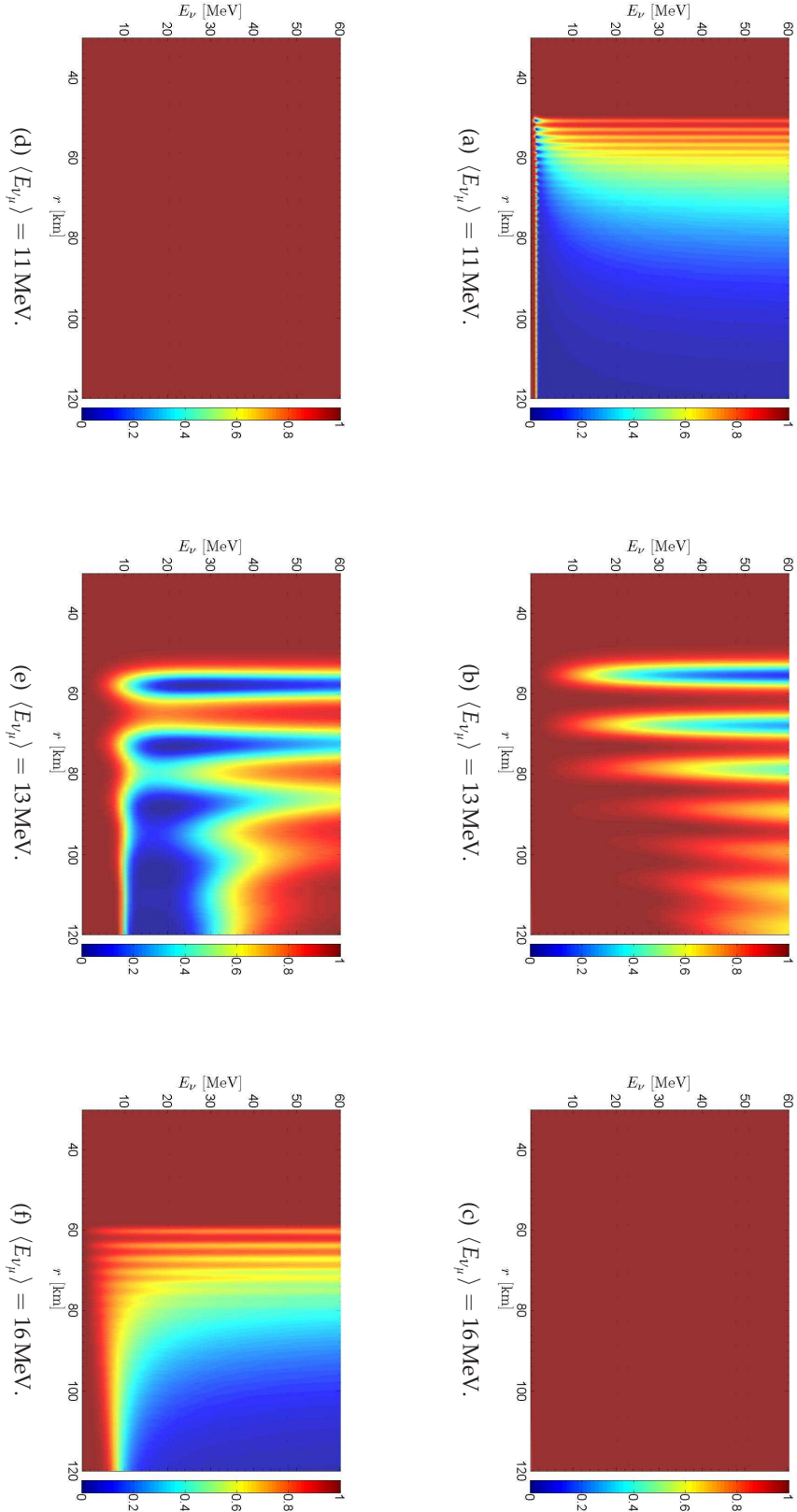
Figure 4.3 – Contour plots of the electron neutrino survival probability $P(\nu_e \to \nu_e)$ as a function of distance and energy obtained in a two flavor calculation including mixing, matter and neutrino self-interaction in a supernova environment. The distance r is from the neutrino-sphere set at $R_\nu = 10$ km. The cases shown correspond to normal (a, b and c) and inverted hierarchies (d, e and f). For the simulation, we consider an equipartition of the luminosity among all flavors and the oscillations parameters are $\Delta m^2_{21} = \pm 2.4 \times 10^{-3}\,\mathrm{eV}^2$ and $\theta_0 = 9°$. The average energies are fixed at $\langle E_{\nu_e} \rangle = 12\,\mathrm{MeV}$, $\langle E_{\bar{\nu}_e} \rangle = 15\,\mathrm{MeV}$ and $\langle E_{\nu_\mu} \rangle = \langle E_{\bar{\nu}_\mu} \rangle$. For the latter average energy, we study the sign modification of eq. (4.87) by taking three values $\langle E_{\nu_\mu} \rangle = 11, 13, 16\,\mathrm{MeV}$ to show the start of the bipolar oscillations.

We can extend eq. (4.87) to the case where both the equipartition is not assumed and $\langle E_{\nu_\mu} \rangle \neq \langle E_{\bar{\nu}_\mu} \rangle$. Then we find the extension of eqs. (4.88) and (4.89) to be

$$\frac{L^0_{\nu_e}}{\langle E_{\nu_e} \rangle^2} + \frac{L^0_{\bar{\nu}_e}}{\langle E_{\bar{\nu}_e} \rangle^2} - \frac{L^0_{\nu_\mu}}{\langle E_{\nu_\mu} \rangle^2} - \frac{L^0_{\bar{\nu}_\mu}}{\langle E_{\bar{\nu}_\mu} \rangle^2} \gtreqless 0. \tag{4.90}$$

In conclusion, we identified that the trigger to the onset of the bipolar oscillations (end of the synchronization) is related to the derivative of the Dirac $\widetilde{\beta}$ in matter. This derivative is directly connected to the value of the off-diagonal term of the flavor Hamiltonian $H_{e\mu}$ and its derivative. By calculating the value of the first and second derivative of $H_{e\mu}$ at the neutrino-sphere, we found two conditions for the trigger. We must have a non-zero vacuum mixing angle θ_0 and moreover we need specific combinations of the mass and average energy hierarchies.

4.2.3 Bipolar oscillations and the role of the matter phase

As we already mentioned, in the matter basis, the bipolar oscillations are possible if the difference between $\widetilde{B}_{X,Y}$ and the absolute value of $\widetilde{B}_Z$ is reduced (see eq. (4.67)). On figure 4.4, we present the numerical results obtained for neutrinos and antineutrinos using eqs. (4.52) and (4.53) for the calculation of the Q_i's and eq. (4.59) for $\delta \widetilde{k}_{12}$. For the simulations we use the following oscillation parameters: $\Delta m^2_{21} = \pm 2.4 \times 10^{-3}$ eV^2, $\theta_0 = 9°$. The average energies are fixed at $\langle E_{\nu_e} \rangle = 12$ MeV, $\langle E_{\bar{\nu}_e} \rangle = 15$ MeV and $\langle E_{\nu_\mu} \rangle = 18$ MeV and the luminosity at $L_0 = 10^{51}$ erg.s^{-1}. We see on figure 4.4 that the reduction between $\widetilde{B}_{X,Y}$ and $\widetilde{B}_Z$ is induced by the presence of the term $\delta Q_{12} \propto \dot{\widetilde{\beta}}$.
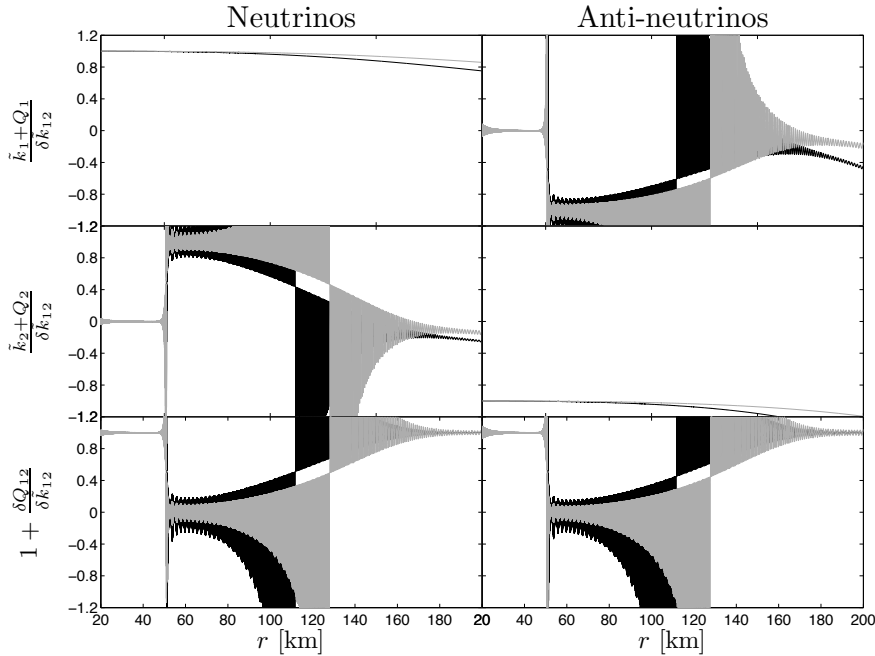
Figure 4.4 – *Diagonal entries of the Hamiltonian $\widetilde{H}$. Different associations are plotted: $(\widetilde{k}_1 + Q_1)/\delta\widetilde{k}_{12}$ (upper), $(\widetilde{k}_2 + Q_2)/\delta\widetilde{k}_{12}$ (middle) and $1 + \delta Q_{12}/\delta\widetilde{k}_{12}$ (lower panel). The curves correspond to a 5 (black) and 10 MeV (grey) neutrino energy for neutrinos (left) and antineutrinos (right figures).*

During the synchronization (from 10 to 50 km), the derivative of the Dirac phase $\widetilde{\beta}$ is zero and the Z component of $\widetilde{\mathbf{B}}$ is $\widetilde{B}_Z \simeq \delta \widetilde{k}_{12}$. To start the bipolar oscillations, one needs the addition of $\dot{\widetilde{\beta}}$ because it will increase the value of $\widetilde{B}_{X,Y}$ and, by its presence in the non-adiabaticity parameter Γ_{12}, it will decrease $\widetilde{B}_Z$. In fact, the definition of $\dot{\widetilde{\beta}}$ (see eq. (4.55)) tells us that the contribution from such a quantity is enormous when $|H_{e\mu}|^2$ approach zero. More explicitly, we need to have

$$|H_{e\mu}|^2 = |H_{e\mu}^{\text{vac}}|^2 + |H_{e\mu}^{\nu\nu}|^2 + 2\Re\left(H_{e\mu}^{\text{vac}} H_{e\mu}^{\nu\nu\,*}\right) \to 0. \qquad (4.91)$$

We extract from figure 4.5 that this condition occurs for the first time when

$$|H_{e\mu}^{\text{vac}}|^2 = |H_{e\mu}^{\nu\nu}|^2. \qquad (4.92)$$

This is due to the fact that the third term of eq. (4.91) varies very rapidly. The condition of eq. (4.92) we have discovered has been also postulated heuristically in [125] in a three flavor multi-angle calculation.
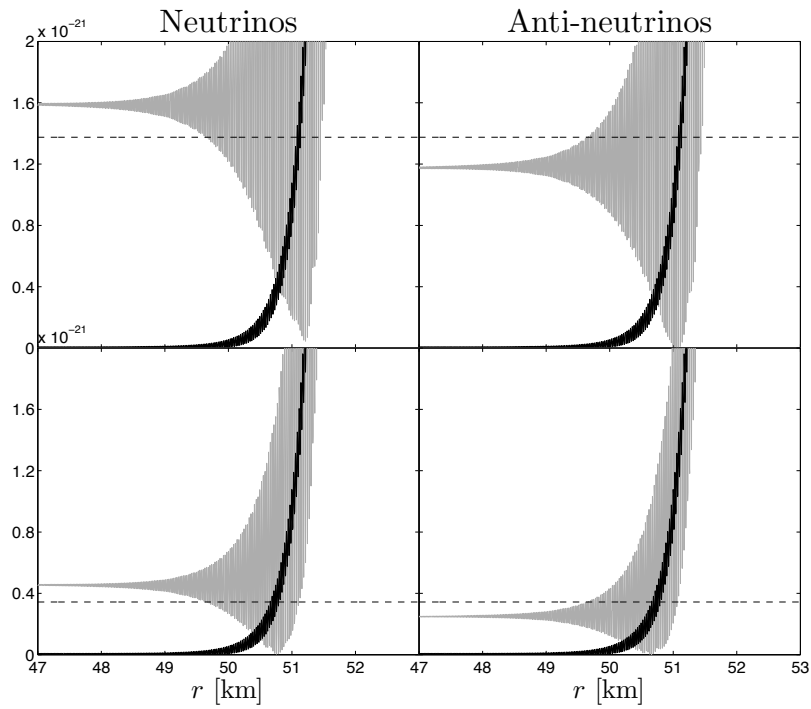
Figure 4.5 – *Contributions to the off-diagonal matrix element $|H_{e\mu}|$ (eq. (4.91)) of the two neutrino flavor Hamiltonian. The curves show: $|H_{e\mu}^{vac}|^2$ (dashed), $|H_{e\mu}^{\nu\nu}|^2$ (black) and the total $|H_{e\mu}|^2$ (grey) in units of eV^2 for neutrinos (left) and antineutrinos (right). Results for a 5 MeV neutrino are given in the upper figures and for a 10 MeV one in the lower figures.*

After that the end of the synchronization regime (~ 50 km) due to the fulfillment of the condition in eq. (4.92), we see on the lower panel of figure 4.4 that the quantity $1 + \delta Q_{12}/\delta\widetilde{k}_{12}$ decreases abruptly from 1 to 0. This is due to the fact that in the bipolar region, the derivative of the matter phase $\dot{\widetilde{\beta}}$ becomes large. Moreover, the derivative $\dot{\widetilde{\beta}}$ enters in the definition of the Q_i's namely $\delta Q_{12} = \dot{\widetilde{\beta}}\cos 2\widetilde{\theta}$. As a

result, the difference of the diagonal elements of $\widetilde{H}$ goes from $\delta\widetilde{k}_{12} + \delta Q_{12} \sim \delta\widetilde{k}_{12}$ to $\delta\widetilde{k}_{12} + \delta Q_{12} \sim 0$. So even if the off-diagonal entries of $\widetilde{H}$ remain small, they have an non-negligible impact on the neutrino propagation in the sense that they connect the states 1 and 2 leading to oscillations between these eigenstates.

These results make it clear that the Dirac phase $\widetilde{\beta}$ acquires a particularly significant role in the neutrino flavor conversion. It leads to an oscillatory degeneracy between the diagonal elements of $\widetilde{H}$, increasing significantly the importance of the off-diagonal entries of $\widetilde{H}$.

4.3 THE SPECTRAL SPLIT AND THE MAGNETIC RESONANCE PHENOMENON

The spectral split is the most striking phenomenon that the introduction of the neutrino self-interaction creates. It is represented by a complete swap of the fluxes (between e and μ flavor) at the end of the propagation before the MSW region. For antineutrinos, there is an almost complete exchange while for neutrinos there exists a sharp split in the flux at a critical energy E_C separating no swap and a complete swap (see figure 2.24). In our third work, we have established a connection between the spectral split phenomenon and the well known magnetic resonance phenomenon using the polarization vector formalism. This work has made the object of a publication [26].

4.3.1 Definitions of relevant quantities

First we define relevant quantities that we will use to establish this connection. Because of the equivalence between the Schrödinger-like equation and the gyroscopic equation

$$\iota\frac{d\psi}{dx} = H\,\psi \quad\Leftrightarrow\quad \frac{d\mathbf{P}}{dx} = \mathbf{B}\times\mathbf{P}, \tag{4.93}$$

the polarization vector spins around the magnetic field at the angular velocity

$$\omega_{\mathbf{P}} = |\mathbf{B}| \quad\text{and}\quad \widetilde{\omega}_{\widetilde{\mathbf{P}}} = |\widetilde{\mathbf{B}}|, \tag{4.94}$$

while the angle defining the evolution of $\widetilde{\mathbf{B}}$ with respect to the XOY plane is defined as

$$\tan\eta = \frac{\widetilde{B}_Z}{|\widetilde{B}_\perp|} = \frac{\delta\widetilde{k}_{12}}{|2\widetilde{H}_{12}|}. \tag{4.95}$$

In order to follow the evolution of the system, it is interesting to define the rate of change of the $\widetilde{\mathbf{B}}$ direction with respect to such a plane, namely the first derivative of the angle η

$$
\dot{\eta} = \frac{2}{4\left|\widetilde{H}_{12}\right|^2 + \delta\check{k}_{12}^2}
$$
$$
\left(\delta\dot{\check{k}}_{12}\left|\widetilde{H}_{12}\right| - \frac{\delta\check{k}_{12}}{\left|\widetilde{H}_{12}\right|}\left[\Re\left(\widetilde{H}_{12}\right)\Re\left(\dot{\widetilde{H}}_{12}\right) + \Im\left(\widetilde{H}_{12}\right)\Im\left(\dot{\widetilde{H}}_{12}\right)\right]\right) \tag{4.96}
$$

where we define for compactness the quantity

$$\check{k}_i = \widetilde{k}_i + Q_i. \tag{4.97}$$

Because of the relation $2\widetilde{H}_{12} = \frac{\delta \check{k}_{12}}{\pi}\Gamma_{12}$, we see in eq. (4.96) that the first derivative of both $\delta\check{k}_{12}$ and Γ_{12} (eq. (4.54)) are needed. For the former one gets

$$\delta\dot{\check{k}}_{12} = \delta\dot{\widetilde{k}}_{12} - \ddot{\widetilde{\beta}}\cos 2\widetilde{\theta} + 2\dot{\widetilde{\beta}}\dot{\widetilde{\theta}}\sin 2\widetilde{\theta}. \tag{4.98}$$

Now not only the first but also the second derivative of the Dirac phase $\widetilde{\beta}$ is needed

$$\ddot{\widetilde{\beta}} = \frac{1}{|H_{e\mu}|^2}\left(\Im\left(H_{e\mu}\right)\ \Re\left(\ddot{H}_{e\mu}\right) - \Re\left(H_{e\mu}\right)\ \Im\left(\ddot{H}_{e\mu}\right)\right)$$
$$-2\frac{1}{|H_{e\mu}|^2}\dot{\widetilde{\beta}}\left(\Re\left(H_{e\mu}\right)\ \Re\left(\dot{H}_{e\mu}\right) + \Im\left(H_{e\mu}\right)\ \Im\left(\dot{H}_{e\mu}\right)\right). \tag{4.99}$$

Finally the first derivative of the non-adiabaticity parameter is

$$\delta\widetilde{k}_{12}\delta\check{k}_{12}\dot{\Gamma}_{12} = -\left(\delta\dot{\check{k}}_{12}\delta\check{k}_{12} + \delta\widetilde{k}_{12}\delta\dot{\check{k}}_{12}\right) + 2\pi\left(\widetilde{U}^\dagger\dot{H}\widetilde{U} + \left[\widetilde{U}^\dagger H\widetilde{U}, \widetilde{U}^\dagger\dot{\widetilde{U}}\right]\right)_{12}, \tag{4.100}$$

which depends upon the first and second derivatives of the flavor Hamiltonian H that we already derived (see section 4.1.2.1 and 4.1.2.2).

4.3.2 Correspondence with the magnetic resonance phenomenon

In its simplest realization, the magnetic resonance phenomenon consists in a spin-flip occurring in presence of a constant and a time varying magnetics fields. Let us define three relevant frequencies that are useful to establish our connection. The magnetic field associated to the flavor Hamiltonian H can be developed on a Cartesian basis

$$\mathbf{B} = B_x\,\mathbf{e}_x + B_y\,\mathbf{e}_y + B_z\,\mathbf{e}_z. \tag{4.101}$$

Then we define three quantities for the polarization vector $\mathbf{P}$ that spins around $\mathbf{B}$ (see schematic picture on figure 4.6 a)
  – the rotation frequency around the z component of $\mathbf{B}$: $\omega_0 = |B_z|$,
  – the rotation frequency around the xOy plane component of $\mathbf{B}$, that we named $B^\perp$: $\omega_1 = |B^\perp|$,
  – the rotation frequency around the vector $\mathbf{B}$: $\omega_\mathbf{P} = |\mathbf{B}|$.
We also have the rotation of $B^\perp$ in the xOy plane which can be defined with an angle which is in our case the Dirac phase $\widetilde{\beta}$.

Now let us focus on the matter basis and see if this other basis gives more informations about the underlying phenomena. As for the flavor basis case, we develop the magnetic field $\widetilde{\mathbf{B}}$ associated to the matter Hamiltonian $\widetilde{H}$ on a Cartesian basis

$$\widetilde{\mathbf{B}} = \widetilde{B}_X\,\mathbf{e}_X + \widetilde{B}_Y\,\mathbf{e}_Y + \widetilde{B}_Z\,\mathbf{e}_Z. \tag{4.102}$$

We define three quantities for the polarization vector $\widetilde{\mathbf{P}}$ rotating around $\widetilde{\mathbf{B}}$ (see schematic picture on figure 4.6 b)
  – the rotation frequency around the Z component of $\widetilde{\mathbf{B}}$: $\widetilde{\omega}_0 = |\widetilde{B}_Z|$,
  – the rotation frequency around the XOY plane component of $\widetilde{\mathbf{B}}$, that we named $\widetilde{B}^\perp$: $\widetilde{\omega}_1 = |\widetilde{B}^\perp|$,
  – the rotation frequency around the vector $\widetilde{\mathbf{B}}$: $\widetilde{\omega}_{\widetilde{\mathbf{P}}} = |\widetilde{\mathbf{B}}|$.

In addition to these quantities, we define two angles which represent

  – the rotation of the vector $\widetilde{\mathbf{B}}$ in the *XOY* plane: $\tan\sigma = \dfrac{\widetilde{B}_Y}{\widetilde{B}_X}$,

  – the evolution of $\widetilde{\mathbf{B}}$ with respect to the *XOY* plane: $\tan\eta = \dfrac{\widetilde{B}_Z}{|\widetilde{B}^\perp|}$.

For the results that we will present, we use for the oscillation parameters: $\Delta m_{12}^2 = \pm 2.4 \times 10^{-3}\,\mathrm{eV}^2$, $\theta_0 = 9°$. The density profile is defined by $\rho_B = 1.5 \times 10^8 (10/x\,[\mathrm{km}])\,\mathrm{g.cm}^{-3}$. The average energies are $\langle E_{\nu_e}\rangle = 12\,\mathrm{MeV}$, $\langle E_{\bar\nu_e}\rangle = 15\,\mathrm{MeV}$ and $\langle E_{\nu_x}\rangle = 18\,\mathrm{MeV}$ and we assume an equipartition of energy with a total luminosity of 4×10^{51} erg.s^{-1}. In this case, single splits arise in the electron neutrino and antineutrino fluxes.

The plot of the angle η obtained after a complete simulation is shown on figure 4.7 in grey. We see that this angle undergoes fast oscillations in the range [50,115] km which is the region we are interested in. So we decided to check if the polarization vector $\widetilde{\mathbf{P}}$ perceives these fast oscillations or if it is only sensitive to the average motion of $\widetilde{\mathbf{B}}$. To do so, we need to look at the ratio of the two frequencies $\dot\eta$ and $\widetilde{\omega}_{\widetilde{\mathbf{P}}}$. The expression of the "speed " of the angle η is given by eq. (4.96).

We clearly see on figure 4.8, that the ratio $\dot\eta / \widetilde{\omega}_{\widetilde{\mathbf{P}}}$ is much larger than 1 which means that the magnetic field $\widetilde{\mathbf{B}}$ moves too rapidly and $\widetilde{\mathbf{P}}$ only sees its average $\langle\widetilde{\mathbf{B}}\rangle = (\langle\widetilde{B}_X\rangle, \langle\widetilde{B}_Y\rangle, \langle\widetilde{B}_Z\rangle)^T$. In order to check if such an approximation is reasonable, we have compared the motion of the polarization vector $\widetilde{\mathbf{P}}$ around $\widetilde{\mathbf{B}}$ and around its average $\langle\widetilde{\mathbf{B}}\rangle$. For the average of the magnetic field in the matter basis, we have averaged the components of $\widetilde{\mathbf{B}}$ over ± 5 km i.e.

$$\langle\widetilde{B}_i\rangle = \sum_{-5\,\mathrm{km}}^{+5\,\mathrm{km}} \widetilde{B}_i. \tag{4.103}$$

Then we constructed another code where we solve the gyroscopic equation in three dimensions with the average vectors $\langle\widetilde{\mathbf{B}}\rangle$ as input. We find out the results plotted on figure 4.9 where we see that the survival probabilities for electron neutrinos and antineutrinos (or the projection of $\widetilde{\mathbf{P}}$ on the Z-axis) follow the same behavior when we use $\langle\widetilde{\mathbf{B}}\rangle$ instead of $\widetilde{\mathbf{B}}$ in the range $[40, 120]$ km.

Therefore, because of the good agreement obtained when one follows the neutrino evolution using $\langle\widetilde{\mathbf{B}}\rangle$ instead of $\widetilde{\mathbf{B}}$, we decide to follow the motion of $\widetilde{\mathbf{P}}$ around $\langle\widetilde{\mathbf{B}}\rangle$. From now on we use $\langle\widetilde{\mathbf{B}}\rangle$ for our consideration so let us redefine some quantities defined before. The σ angle describing the evolution $\langle\widetilde{B}^\perp\rangle$ in the *XOY* plane is then

$$\tan\sigma = \frac{\langle\widetilde{B}_Y\rangle}{\langle\widetilde{B}_X\rangle}, \tag{4.104}$$

and its associated angular velocity $\dot\sigma$. In our numerical calculations, we obtain that $|\langle\widetilde{B}_Y\rangle| \sim 0$ and therefore the velocity $\dot\sigma$ is very close to zero. This result is related to the fact that the derivative of the matter angle $\dot{\widetilde\theta}$ is very small. Thus the average magnetic field is reduced to its motion in the *XOZ* plane (see figure 4.10 b).

We also redefine the η angle representing the evolution of $\langle\widetilde{\mathbf{B}}\rangle$ with respect to the *XOY* plane

$$\tan\eta = \frac{\langle\widetilde{B}_Z\rangle}{\sqrt{\langle\widetilde{B}_X\rangle^2 + \langle\widetilde{B}_Y\rangle^2}}. \tag{4.105}$$
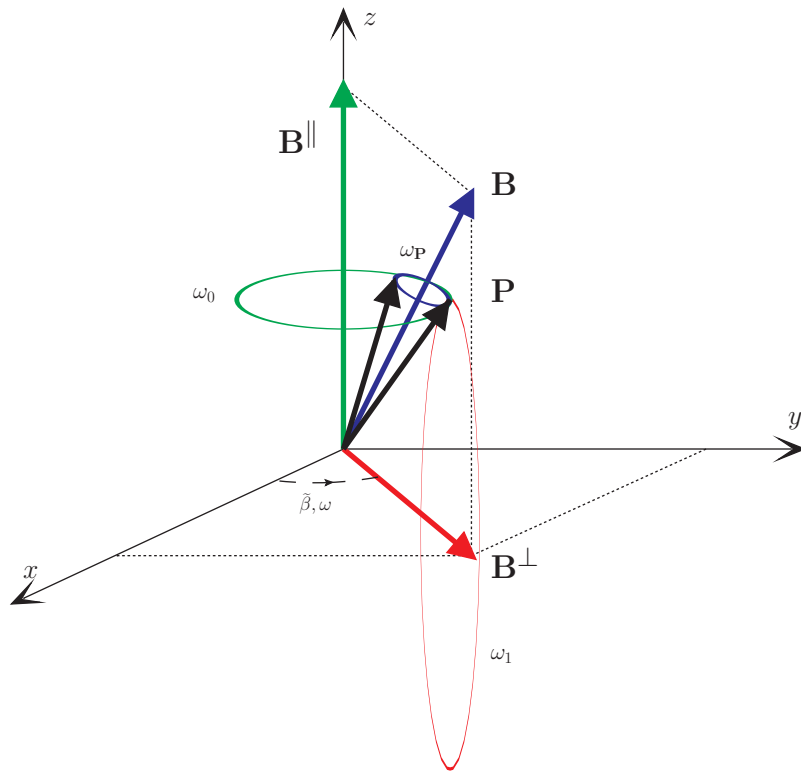
(a) Vectors **P** and **B** in the flavor basis.
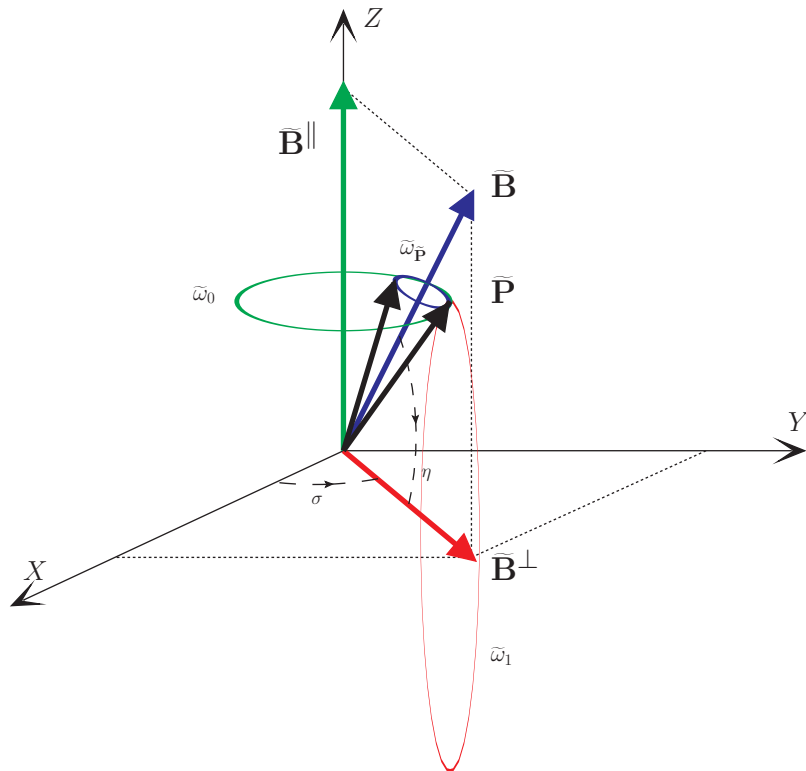
(b) Vectors $\widetilde{\mathbf{P}}$ and $\widetilde{\mathbf{B}}$ in the matter basis.

Figure 4.6 – *Polarization vectors spinning around the magnetic fields representing the Hamiltonians in the flavor and matter basis and the definitions of rotation frequencies and angles (see text).*
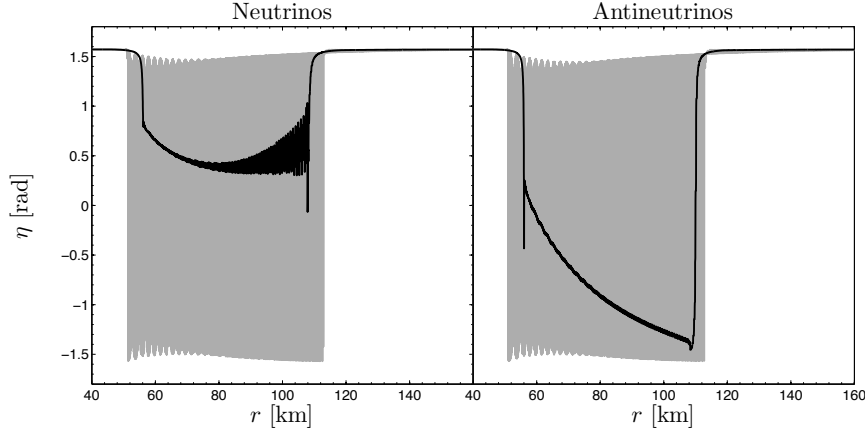
Figure 4.7 – *Evolution of the η angle defined between the magnetic field $\widetilde{\mathbf{B}}$ with respect to the XOY plane (see eq. (4.95)) as a function of the distance (see figure 4.6). The results are given for neutrinos (left) and antineutrinos (right) for the motion of $\widetilde{\mathbf{P}}$ around $\widetilde{\mathbf{B}}$ (grey) and $\langle\widetilde{\mathbf{B}}\rangle$ (black).*
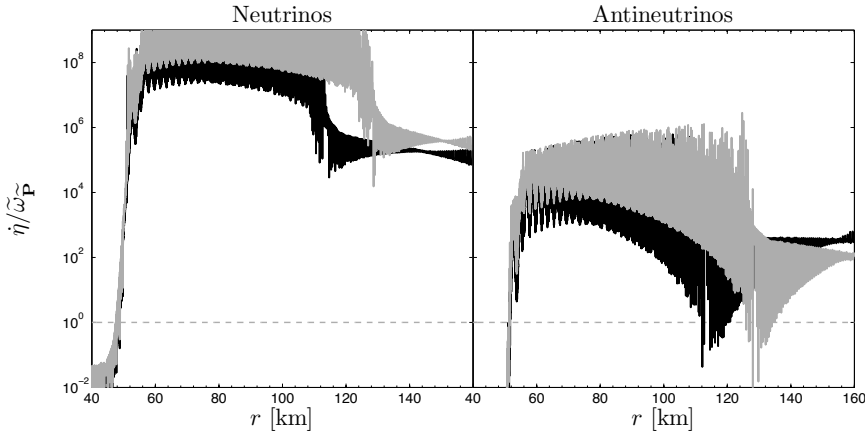
Figure 4.8 – *Evolution of the ratio of two frequencies $\dot{\eta}/\widetilde{\omega}_{\widetilde{\mathbf{P}}}$ as a function of the distance for neutrinos (left) and antineutrinos (right). The result are given for a 5 (black) and 10 MeV (grey) neutrino energy. These plots confirm that the magnetic field $\widetilde{\mathbf{B}}$ moves too rapidly and so the motion of $\widetilde{\mathbf{P}}$ around the average magnetic field $\langle\widetilde{\mathbf{B}}\rangle$ is a good approximation.*

With this new definition, we obtain for the η angle the solid black line plotted on figure 4.7. We see that now the variation of the angle is clearer with the average vector $\langle\widetilde{\mathbf{B}}\rangle$.

The frequencies are also changed. We have the precession of $\widetilde{\mathbf{P}}$ around $\langle\widetilde{B}_Z\rangle$ and around $\langle\widetilde{B}^\perp\rangle$ which are given respectively by the frequencies

$$\widetilde{\omega}_0 = |\langle\widetilde{B}_Z\rangle| = |\langle\widetilde{\delta k}_{12} - \dot{\widetilde{\beta}}\cos 2\widetilde{\theta}\rangle|, \tag{4.106}$$

$$\widetilde{\omega}_1 = |\langle\widetilde{B}^\perp\rangle| = \sqrt{\langle\widetilde{B}_X\rangle^2 + \langle\widetilde{B}_Y\rangle^2} = \sqrt{\langle\dot{\widetilde{\beta}}\sin 2\widetilde{\theta}\rangle^2 + \langle 2\dot{\widetilde{\theta}}\rangle^2}. \tag{4.107}$$

Since the contribution coming from $\dot{\widetilde{\theta}}$ comes out to be tiny, the quantity $\widetilde{\omega}_1$ is essentially determined by the phase derivative. Finally, we redefine the general frequency $\widetilde{\omega}_{\widetilde{\mathbf{P}}} = |\langle\widetilde{\mathbf{B}}\rangle|$.

By examining figure 4.10, we remark that the flavor basis is made of a magnetic field $\mathbf{B}$ with a strong component on the z-axis and small varying components on the x and y-axis. On the contrary, the matter basis consists in an average magnetic
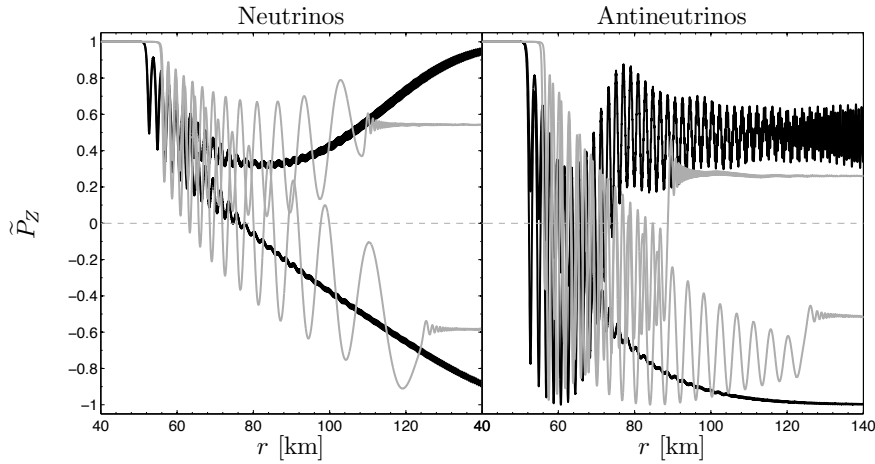
Figure 4.9 – *Projection of the polarization vector $\widetilde{\mathbf{P}}$ on the Z-axis for neutrinos (left) and antineutrinos (right) as a function of distance. The black curve corresponds to a complete simulation using $\widetilde{\mathbf{B}}$ and the grey curve is extracted from a code solving the gyroscopic equation with the average magnetic field $\langle \widetilde{\mathbf{B}} \rangle$ as input.*

field $\langle \widetilde{\mathbf{B}} \rangle$ moving in the *XOZ* plane with component that can become of the same order during the neutrino evolution. These two basis correspond exactly to the laboratory frame (for the flavor basis) and the corotating frame (for the matter basis) of the magnetic resonance phenomenon as we have been identifying in our work. The existence and importance of a corotating frame has been already discussed in the literature [18, 110, 81] where this frame was postulated in the context of a toy model. So let us see if the spectral split is the result of the fulfillment of the magnetic resonance criteria:

$$\Delta\omega = \omega - \omega_0 = 0 \qquad \Leftrightarrow \qquad \widetilde{\omega}_0 = 0, \tag{4.108}$$

$$\frac{\Delta\omega}{\omega_1} \ll 1 \qquad \Leftrightarrow \qquad \frac{\widetilde{\omega}_0}{\widetilde{\omega}_1} \ll 1, \tag{4.109}$$

where $\omega = \dot{\beta}$. The first criterion correspond to the location of the resonance and the second criterion ensure that we are on resonance. If $\widetilde{\omega}_0/\widetilde{\omega}_1 \gg 1$ we are off resonance. We emphasize that the magnetic resonance conditions can be calculated equivalently in the flavor basis where $B^\perp$ is a time varying field and in the comoving frame identified by $\langle \widetilde{\mathbf{B}} \rangle$ in the matter basis. In the former case, one should find the conditions $\omega - \omega_0 = 0$ with $(\omega - \omega_0)/\omega_1 \ll 1$, while in the latter case one should find $\widetilde{\omega}_0 = 0$ with $\widetilde{\omega}_0/\widetilde{\omega}_1 \ll 1$. In order to prove that our conjecture that the spectral split phenomenon is indeed a magnetic resonance phenomenon, we have been verifying that the magnetic resonance conditions are fulfilled when the spectral split occurs.

Figures 4.11 and 4.12 show the region where the magnetic resonance criterion $\widetilde{\omega}_0 = 0$ is fulfilled (solid black line) for neutrinos and antineutrinos respectively and also the region where its fulfillment has an impact i.e. $\widetilde{\omega}_0/\widetilde{\omega}_1 \ll 1$ (the blue region). The red region corresponds to $\widetilde{\omega}_0/\widetilde{\omega}_1 \gg 1$ where we are "off resonance". We first see that for neutrinos the resonance line is present and has an impact between 68 and 120 km whereas its part after 120 km has no effect because the second criterion is not fulfilled (the line is in the red region). We have the same result for antineutrinos but within the range [58,62] km.
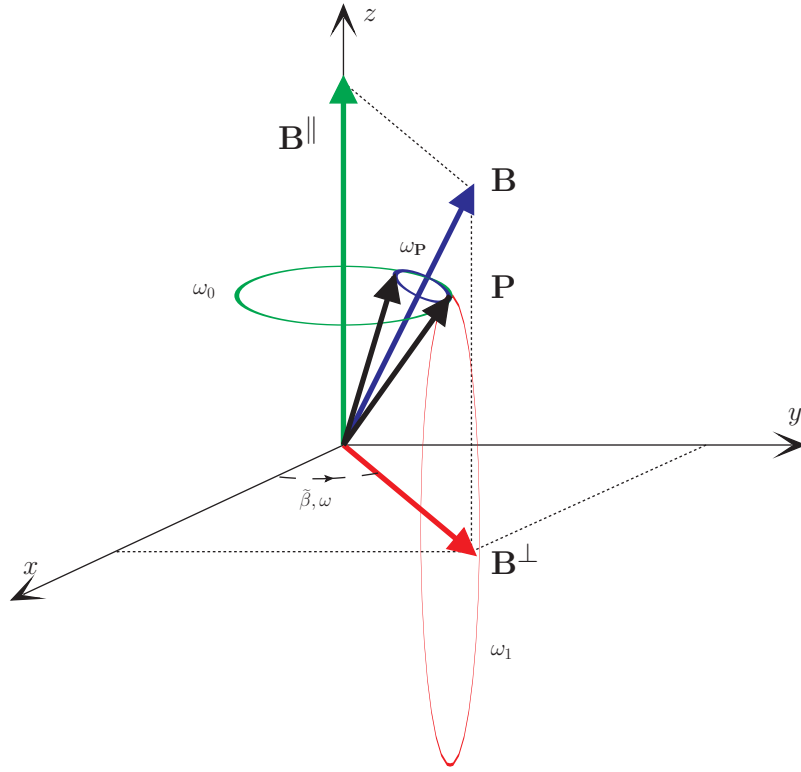
(a) Vectors **P** and **B** in the flavor basis.
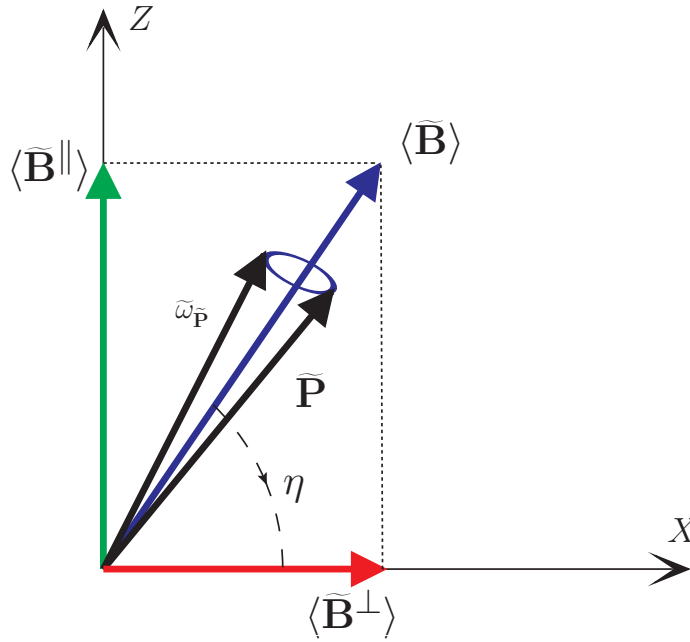
(b) Vectors $\widetilde{\mathbf{P}}$ and $\langle \widetilde{\mathbf{B}} \rangle$ in the matter basis.

Figure 4.10 – *Polarization vectors spinning around the magnetic field* **B** *for the flavor basis and around the average magnetic field* $\langle \widetilde{\mathbf{B}} \rangle$ *for the matter basis. Taking the average of* $\widetilde{\mathbf{B}}$ *makes the movement of the magnetic field bidimensional in the XOZ plane. Such a frame is the comoving frame of the magnetic resonance phenomenon.*

Now let us see if the magnetic resonance criteria have a relation with the spectral split phenomenon. For this, we combine the survival probabilities and the
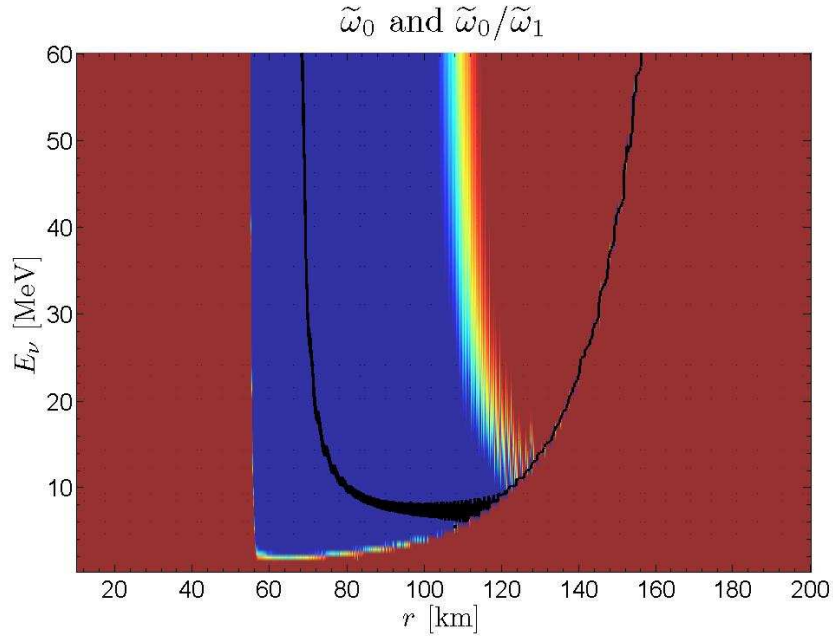
Figure 4.11 – *Fulfillment of the magnetic resonance criteria for neutrinos as a function of distance and energy. The neutrino-sphere is fixed at 10 km. The black curve corresponds to the first criterion $\widetilde{\omega}_0 = 0$ (eq. (4.108)). The blue region is defined by $\widetilde{\omega}_0/\widetilde{\omega}_1 \ll 1$ (second criterion) while the red one is for $\widetilde{\omega}_0/\widetilde{\omega}_1 \gg 1$. The results correspond to inverted hierarchy and $\theta_0 = 9°$. The average energies are $\langle E_{\nu_e} \rangle = 12$ MeV, $\langle E_{\bar{\nu}_e} \rangle = 15$ MeV and $\langle E_{\nu_x} \rangle = 18$ MeV and we assume an equipartition of energy with a total luminosity of 4×10^{51} erg.s^{-1}.*
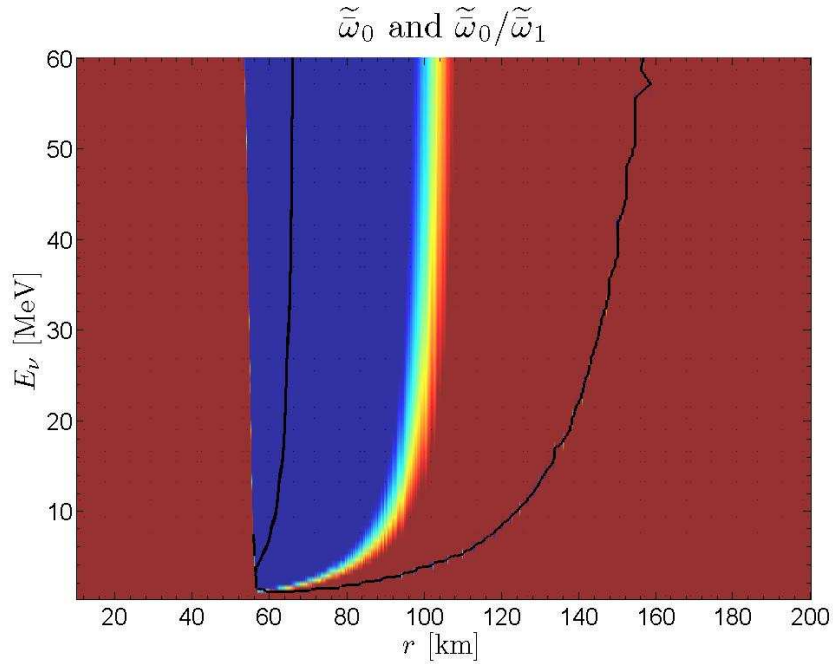
Figure 4.12 – *Fulfillment of the magnetic resonance criteria for antineutrinos as a function of distance and energy. The black curve corresponds to the first criterion $\widetilde{\omega}_0 = 0$. The blue region is defined by $\widetilde{\omega}_0/\widetilde{\omega}_1 \ll 1$ (second criterion) while the red one is for $\widetilde{\omega}_0/\widetilde{\omega}_1 \gg 1$. The results correspond to inverted hierarchy and the parameters are the same as figure 4.11.*

resonance line obtained in figures 4.11 and 4.12. Figures 4.13 and 4.14 present the contour plots of the survival probabilities with the resonance line (solid black

line) for neutrinos and antineutrinos respectively. The solid line representing the fulfillment of the first criterion (eq. (4.108)) is just plotted when the second criterion is also fulfilled ("on resonance"). These contour plots confirm our conjecture that the spectral split phenomenon is, in terms of polarization vectors, a magnetic resonance phenomenon: the fulfillment of the magnetic resonance criteria gives rise to the spectral split at exactly the same location and for the neutrino energies that undergo a spectral split. Indeed, on the energy axis of figures 4.13 and 4.14, we see that the lowest energy that is reached by the resonance line (solid black) corresponds exactly to the split energy. To conclude, our calculation explicitly shows for the first time that the spectral split phenomenon is indeed a magnetic resonance phenomenon.
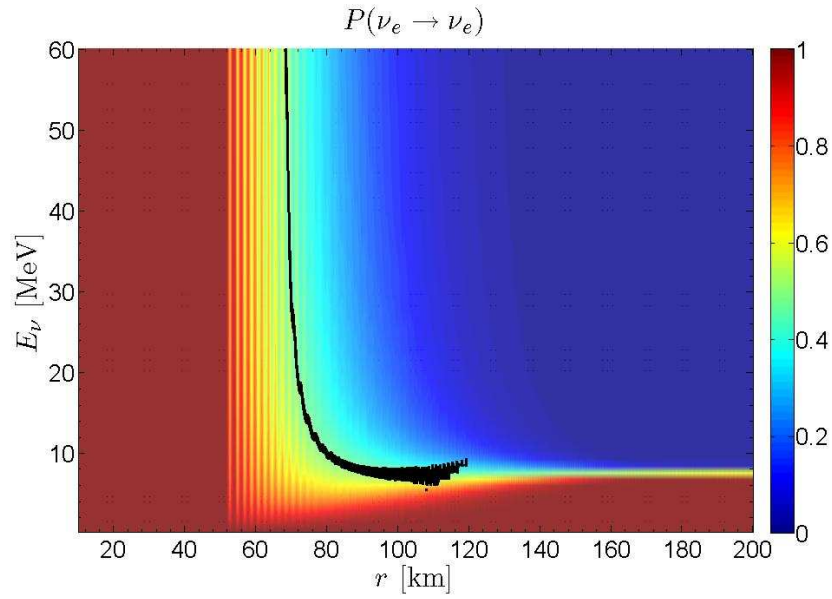
Figure 4.13 – *Contour plot of the electron neutrino survival probability as a function of distance and energy. The black curve shows the fulfillment of the magnetic resonance condition (fig 4.11). The magnetic resonance line and the spectral split coincide exactly in location in the Supernova and occur for the same neutrino energies.*

To ensure that the coincidence of the spectral split and the magnetic resonance phenomena is not a numerical artifact coming from the values of our parameters, we have varied the total luminosity that is distributed equivalently among all flavors and we also took three values for the vacuum mixing angle namely $\theta_0 \in \{9°, 10^{-3\,°}, 10^{-5\,°}\}$. The results for the inverted hierarchy are plotted on figure 4.15. For the calculations, we fix the values of the the average energies to $\langle E_{\nu_e} \rangle = 12\,\text{MeV}$, $\langle E_{\bar{\nu}_e} \rangle = 15\,\text{MeV}$ and $\langle E_{\nu_x} \rangle = 18\,\text{MeV}$ and we still assume an equipartition of the total luminosity. We see that the modifications of the total luminosity or the vacuum mixing angle do not modify our conclusion. In all cases, the resonance line (solid black) follows the spectral split which confirms the robustness of our results.
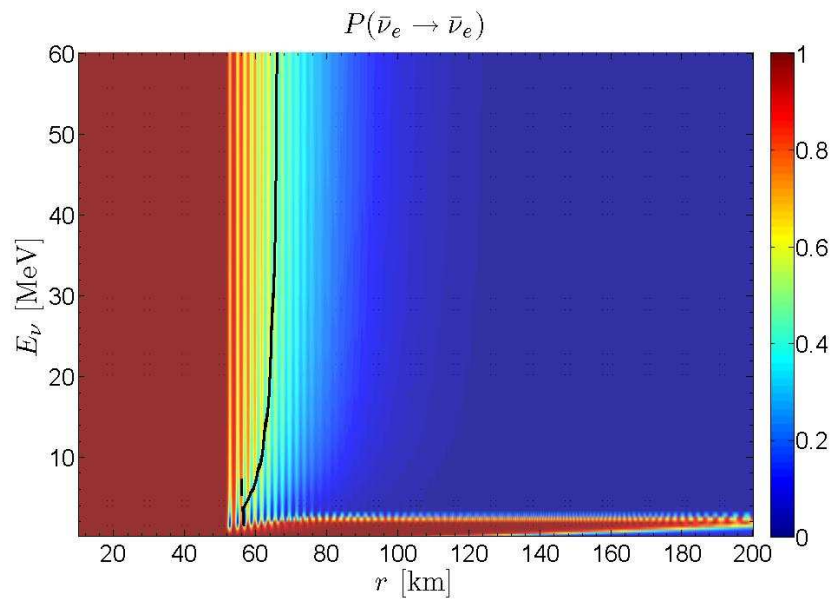
Figure 4.14 – *Contour plot of the electron antineutrino survival probability as a function of distance and energy. The black curve shows the fulfillment of the magnetic resonance condition (fig 4.12). The magnetic resonance line and the spectral split coincide exactly in location in the Supernova and occur for the same antineutrino energies.*

(a) $L_\nu = 10^{51}$ erg.s^{-1}, $\theta_0 = 9°$.

(b) $L_\nu = 10^{51}$ erg.s^{-1}, $\theta_0 = 10^{-3}°$.

(c) $L_\nu = 10^{51}$ erg.s^{-1}, $\theta_0 = 10^{-5}°$.

(d) $L_\nu = 1.25 \times 10^{51}$ erg.s^{-1}, $\theta_0 = 9°$.

(e) $L_\nu = 1.5 \times 10^{51}$ erg.s^{-1}, $\theta_0 = 9°$.
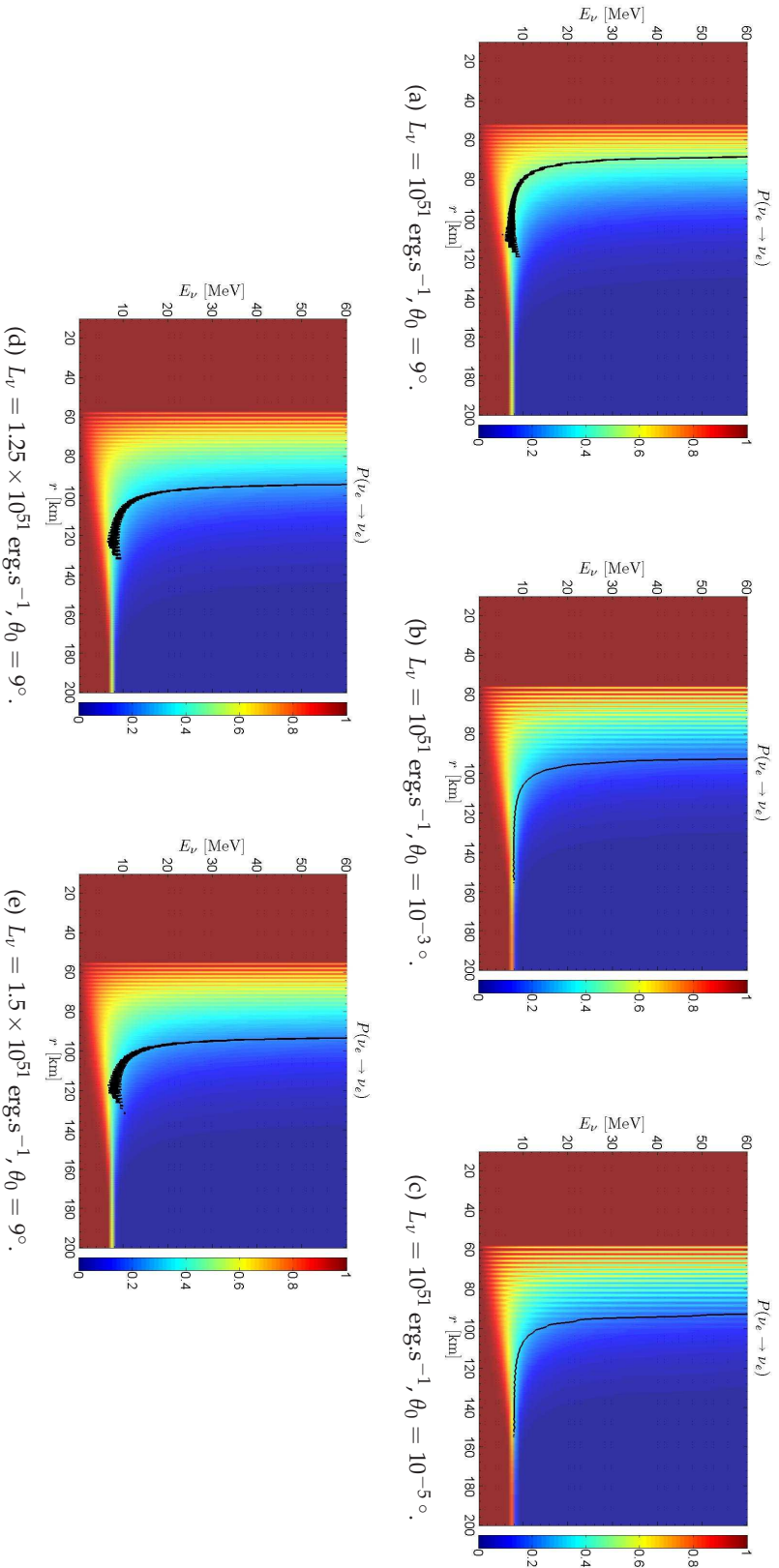
Figure 4.15 – Contour plot of the electron neutrino survival probability as a function of distance and energy. The black curve corresponds to the magnetic resonance line in the "on-resonance" region. We see that the magnetic resonance line and the spectral split coincide when we change the total luminosity or the angle θ_0. The results correspond to inverted hierarchy. The average energies are $\langle E_{\nu_e} \rangle = 12$ MeV, $\langle E_{\bar{\nu}_e} \rangle = 15$ MeV and $\langle E_{\nu_x} \rangle = 18$ MeV and we assume an equipartition of energy with a total luminosity.

4.4 SUMMARY OF THE PROPAGATION OF A NEUTRINO IN A SUPER-NOVA ENVIRONMENT USING THE POLARIZATION VECTOR FORMALISM

Here we give a summary of the whole propagation of a neutrino in the supernova in the region where the main effects come from the neutrino self-interaction using the polarization vector formalism. On figure 4.16, we show the neutrino (and antineutrino) propagation in the flavor (a, b and c) and the matter basis (d, e and f). We will only describe the motion of the polarization vector $\widetilde{\mathbf{P}}$ in the matter basis.

At the beginning of the propagation, in the synchronization regime, the magnetic field $\widetilde{\mathbf{B}}$ (representing the Hamiltonian in the matter basis) is almost stuck along the Z-axis due to the large difference existing between the diagonal and the off-diagonal terms of $\widetilde{H}$. At the neutrino-sphere, because we consider that neutrinos are emitted in a pure flavor state, the polarization vector has initially only a Z component. Then the rotation of the vector $\widetilde{\mathbf{P}}$ around the magnetic field $\widetilde{\mathbf{B}}$ engenders very small oscillations of the Z component due to the smallness of $\widetilde{\mathbf{B}}_{X,Y}$ (see figure 4.16 d). So in the first kilometers (< 50 km), because the projection of the polarization vector on the Z-axis is equivalent to the neutrino survival probability, a good approximation is to consider that the electron survival probability is equal to 1.

At ~ 50 km, the neutrino propagating in the supernova starts to enter in "resonance" i.e. the Z component of the average magnetic field $\langle\widetilde{\mathbf{B}}\rangle$ (see section 4.3.2 for the meaning of the average) decreases whereas its X component increases (figure 4.16 d). The reason of this evolution of the magnetic field $\langle\widetilde{\mathbf{B}}\rangle$ is the presence of the matter phase $\widetilde{\beta}$ which reduces significantly the difference between the diagonal and the off diagonal entries of the matter Hamiltonian $\widetilde{H}$. Because the polarization vector $\widetilde{\mathbf{P}}$ follows the magnetic field $\langle\widetilde{\mathbf{B}}\rangle$, $\widetilde{\mathbf{P}}$ also goes down which leads to a decrease of its projection on the Z-axis. Due to the direct relation between the projection on the Z-axis and the neutrino survival probability, the descent of $\widetilde{P}_Z$ corresponds to the bipolar oscillations visible in the neutrino survival probability.

If, in the on-resonance region (i.e. where the condition of eq. (4.109) is valid), the Z component of the magnetic field $\langle\widetilde{\mathbf{B}}\rangle$ cancels, then the magnetic resonance criteria are fulfilled and the spectral split phenomenon appears. After this phenomenon, the vector $\langle\widetilde{\mathbf{B}}\rangle$ continues to go down and the vector $\widetilde{\mathbf{P}}$ following $\langle\widetilde{\mathbf{B}}\rangle$ goes down until it aligns along the Z-axis (negative part). This motion from $\widetilde{P}_Z = 1$ to $\widetilde{P}_Z = -1$ is the mirror of the swap between the electron neutrino and the muon neutrino fluxes. This case where the spectral split phenomenon occurs is represented on the figure 4.16 e.

While, still in the on-resonance region, if the Z component of the magnetic field $\langle\widetilde{\mathbf{B}}\rangle$ does not cancel, then the first magnetic resonance criterion is not fulfilled and the spectral split phenomenon cannot appear. Actually, the polarization vector has entered the resonance region but has not reached the resonance "point" where $\langle\widetilde{B}_Z\rangle = 0$. In this case, the vector $\langle\widetilde{\mathbf{B}}\rangle$ goes up and the vector $\widetilde{\mathbf{P}}$ following $\langle\widetilde{\mathbf{B}}\rangle$ comes back to its initial position. This motion of return to $\widetilde{P}_Z = 1$ is the mirror of the absence of swapping between the electron neutrino and the muon neutrino fluxes for

the neutrino energies lower than the spectral split energy E_C. This case where the spectral split phenomenon does not occur is represented on the figure 4.16 f.

(a) Onset of the bipolar oscillations. The wiggles in the xOy plane are the spatial varying x and y components of the magnetic field **B**.

(b) Polarization vector evolution for energies which fulfill the magnetic resonance criteria. These energies have undergo the spectral split.

(c) Polarization vector evolution for energies which have not fulfilled the magnetic resonance criteria. These energies have not undergo the spectral split.

(d) Onset of the bipolar oscillations.

(e) Polarization vector evolution for energies which fulfill the magnetic resonance criteria.

(f) Polarization vector evolution for energies which have not fulfilled the magnetic resonance criteria.

Figure 4.16 – *Polarization vector evolution from the beginning of the bipolar oscillations to the spectral split (or not) phenomenon in the flavor basis (a, b and c) and the matter basis (d, e and f).*

4.5   ADIABATICITY OF THE PROPAGATION IN THE SELF-INTERACTION REGION

During the neutrino propagation in the supernova environment, we have seen in section 1.2.4 that the adiabaticity of the propagation is very important because it can lead to the presence/absence of resonant conversion. In this section, we make a comment about our definition of adiabaticity or actually non-adiabaticity. Using eq. (4.54), the non-adiabaticity is redefined with the average vector $\langle \widetilde{\mathbf{B}} \rangle$ as

$$|\Gamma_{12}| = \left| \frac{\pi}{\langle \widetilde{B}_Z \rangle} \right| \sqrt{\langle \widetilde{B}_X \rangle^2 + \langle \widetilde{B}_Y \rangle^2}. \tag{4.110}$$

The results of our calculation are plotted on figure 4.17. For the distance lower than 100 km, we first see that the spectral split phenomenon is identified by a spike in the $|\Gamma_{12}|$ function. Indeed, the first criterion of the magnetic resonance corresponds to $\langle \widetilde{B}_Z \rangle = 0$ which is related to a divergence in the $|\Gamma_{12}|$ function. The presence of these spikes corresponds to the location of the spectral split phenomenon because in that region where we are "on-resonance". The spikes that are visible after 100 km are not related to a magnetic resonance phenomenon because then we are "off-resonance" and so the magnetic resonance criteria are not fulfilled.
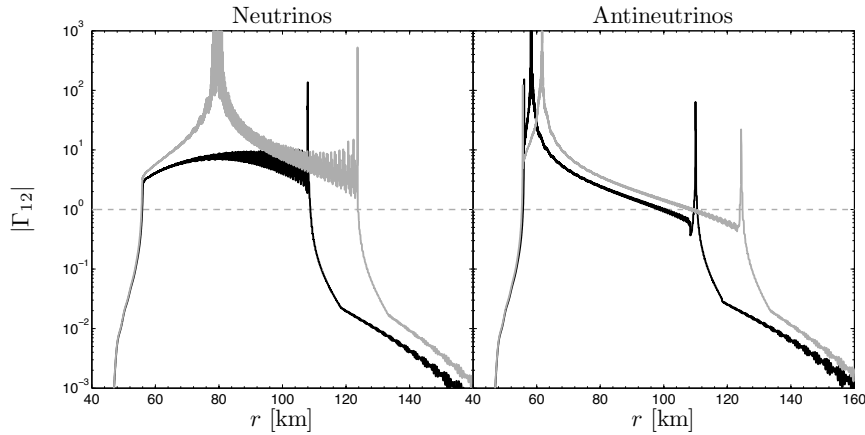
Figure 4.17 – *Non-adiabaticity parameter, in the two flavors case, as a function the distance from the neutrino-sphere fixed at 10 km.*

Another interesting result is that the increase of the non-adiabaticity parameter between 50 and $\sim$ 120 km is an indication of the fact that the neutrinos and antineutrinos are entering in resonance i.e. the Z component of $\langle \widetilde{\mathbf{B}} \rangle$ is decreasing while the X component increases. This radical change in the propagation is due to the presence of the non-zero matter phase $\widetilde{\beta}$ (section 4.2.3). This part of the propagation corresponds to the bipolar oscillations and the spectral split.

We also emphasize that our result about the magnetic resonance correspondence confirms the fact that the propagation of the neutrino before 200 km is adiabatic in the matter basis when the average of the magnetic field $\langle \widetilde{\mathbf{B}} \rangle$ is considered. Figures 4.13 and 4.14 show that the fulfillment of the magnetic resonance conditions, which are related to the motion of the magnetic field $\langle \widetilde{\mathbf{B}} \rangle$, exactly coincides with the location (in distance and energy) of the spectral split, which governs the movement of the polarization vector $\widetilde{\mathbf{P}}$. So we conclude that $\langle \widetilde{\mathbf{B}} \rangle$ and $\widetilde{\mathbf{P}}$ move similarly and are aligned (or anti-aligned). This behavior is characteristic of an adiabatic

propagation. Note that the fact that the propagation is adiabatic, in the matter basis, is a result of our calculations whereas the adiabaticity was considered as an hypothesis in the studies where schematic models are used [80, 81].

On the contrary, in the flavor basis, the neutrino propagation is non-adiabatic. As it is represented on the schematic figure 4.16 b, during the neutrino propagation, the magnetic field **B** is still very close to the z-axis. The magnetic resonance is engendered, in the flavor basis, by the fact that the rotation frequency of the polarization vector **P** around B_z defined as ω_0 becomes equal to the rotation frequency of the magnetic field in the xOy plane defined as $\omega = \dot{\tilde{\beta}}$. Moreover the x and y components of **B** stay tiny. So the angle between the vectors **B** and **P** increases progressively which is the characteristic of a non-adiabatic propagation.

4.6 EXTENSION OF THE MAGNETIC RESONANCE TO $SU(3)$

In the present section, we present preliminary results that we obtain by applying our calculations of section 4.1 to the three flavors case where the three families ν_e, ν_μ and ν_τ are considered. The results presented in this section use the following parameters:

- $\Delta m_{21}^2 = 7.65 \times 10^{-5} \, \text{eV}^2$ and $\Delta m_{31}^2 = -2.4 \times 10^{-3} \, \text{eV}^2$ (i.e. inverted hierarchy),
- $\theta_{12} = 33.46°$, $\theta_{13} = 9°$ and $\theta_{23} = 40°$,
- $\langle E_{\nu_e} \rangle = 12 \, \text{MeV}$, $\langle E_{\bar{\nu}_e} \rangle = 15 \, \text{MeV}$ and $\langle E_{\nu_x} \rangle = 18 \, \text{MeV}$,
- $L_\nu = 10^{51} \, \text{erg.s}^{-1}$ for each flavor.

By looking at figures 4.18, we see that in the matter basis the neutrino self-interaction effects correspond to a mixing between only two states. For neutrinos, only the eigenstates 2 and 3 mix whereas the conversion occurs between the eigenstates 1 and 3 for antineutrinos. Our expectation is that we can perform the same calculation as for the two flavors case (construction of a magnetic field, average, etc.) and show that the spectral split is still a magnetic resonance phenomenon occurring between two eigenstates.
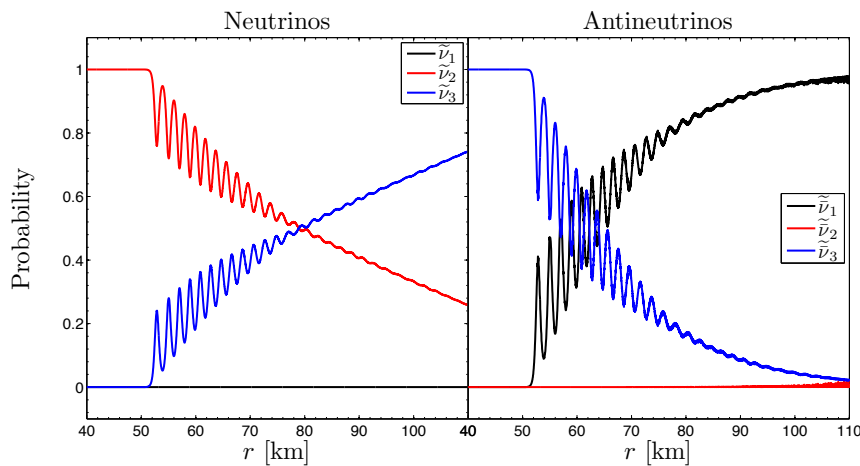
Figure 4.18 – *Eigenstate survival probabilities for neutrinos and antineutrinos as a function of the distance from the neutrino-sphere fixed at 10 km. The curves refer to the eigenstate 1 (black), 2 (blue) and 3 (red). It is clear that in the region where the neutrino self-interaction effects are dominant, the mixing is only between two eigenstates. The eigenstates which play a role are states 2 and 3 for neutrinos, and 1 and 3 for antineutrinos. See text for the parameters used.*

For the three flavors case, we cannot ignore that the three Dirac phases present in the unitary matrix $\widetilde{U}$ could reappear in matter. Consequently, we use our general parametrization of the mixing matrix $\widetilde{U}$ (see eq. (A.25))

$$
\widetilde{U} = \begin{pmatrix}
\widetilde{c}_{12}\widetilde{c}_{13} & \widetilde{s}_{12}\widetilde{c}_{13} & \widetilde{s}_{13} \\
(-\widetilde{s}_{12}\widetilde{c}_{23} e^{i\widetilde{\varepsilon}} - \widetilde{c}_{12}\widetilde{s}_{13}\widetilde{s}_{23})e^{i\widetilde{\delta}} & (\widetilde{c}_{12}\widetilde{c}_{23} e^{i\widetilde{\varepsilon}} - \widetilde{s}_{12}\widetilde{s}_{13}\widetilde{s}_{23})e^{i\widetilde{\delta}} & \widetilde{c}_{13}\widetilde{s}_{23}e^{i\widetilde{\delta}} \\
(\widetilde{s}_{12}\widetilde{s}_{23} e^{i\widetilde{\varepsilon}} - \widetilde{c}_{12}\widetilde{s}_{13}\widetilde{c}_{23})e^{i(\widetilde{\delta}+\widetilde{\beta})} & (-\widetilde{c}_{12}\widetilde{s}_{23} e^{i\widetilde{\varepsilon}} - \widetilde{s}_{12}\widetilde{s}_{13}\widetilde{c}_{23})e^{i(\widetilde{\delta}+\widetilde{\beta})} & \widetilde{c}_{13}\widetilde{c}_{23}e^{i(\widetilde{\delta}+\widetilde{\beta})}
\end{pmatrix},
$$

$$(4.111)$$

where $\widetilde{\beta}$, $\widetilde{\delta}$ and $\widetilde{\varepsilon}$ are the Dirac phases in matter, $\widetilde{c}_{ij} = \cos\widetilde{\theta}_{ij}$ and $\widetilde{s}_{ij} = \sin\widetilde{\theta}_{ij}$ are related to the matter angles $\widetilde{\theta}_{12}$, $\widetilde{\theta}_{13}$ and $\widetilde{\theta}_{23}$. For the Majorana phases, we are free to choose what we desire and decide to take $\widetilde{\alpha}_1 = \widetilde{\alpha}_2 = \widetilde{\alpha}_3 = 0$. That is why they do not appear in the definition of $\widetilde{U}$. With this parametrization of the mixing matrix, the full Hamiltonian in the matter basis $\widetilde{H}$ is

$$
\widetilde{H} = \begin{pmatrix}
\widetilde{k}_1 + Q_1 & \imath\frac{(\delta\widetilde{k}_{12}+\delta Q_{12})}{2\pi}\Gamma_{12} & \imath\frac{(\delta\widetilde{k}_{13}+\delta Q_{13})}{2\pi}\Gamma_{13} \\
-\imath\frac{(\delta\widetilde{k}_{12}+\delta Q_{12})}{2\pi}\Gamma_{12}^* & \widetilde{k}_2 + Q_2 & \imath\frac{(\delta\widetilde{k}_{23}+\delta Q_{23})}{2\pi}\Gamma_{23} \\
-\imath\frac{(\delta\widetilde{k}_{13}+\delta Q_{13})}{2\pi}\Gamma_{13}^* & -\imath\frac{(\delta\widetilde{k}_{23}+\delta Q_{23})}{2\pi}\Gamma_{23}^* & \widetilde{k}_3 + Q_3
\end{pmatrix},
$$

$$(4.112)$$

where the explicit values of the diagonal terms Q_i coming from the term $\left(\widetilde{U}^\dagger d\widetilde{U}/dx\right)_{ii}$ are

$$
\begin{aligned}
Q_1 &= \dot{\widetilde{\delta}}(1 - \widetilde{c}_{13}^2\widetilde{c}_{12}^2) + \dot{\widetilde{\beta}}(\widetilde{c}_{23}^2\widetilde{s}_{13}^2\widetilde{c}_{12}^2 + \widetilde{s}_{12}^2\widetilde{s}_{23}^2 - 2\widetilde{c}_{23}\widetilde{s}_{23}\widetilde{s}_{13}\widetilde{c}_{12}\widetilde{s}_{12}\cos\widetilde{\varepsilon}), \\
&\quad -2\dot{\widetilde{\theta}}_{23}\widetilde{s}_{13}\widetilde{c}_{12}\widetilde{s}_{12}\sin\widetilde{\varepsilon} + \dot{\widetilde{\varepsilon}}\widetilde{s}_{12}^2
\end{aligned}
$$

$$(4.113)$$

$$
\begin{aligned}
Q_2 &= \dot{\widetilde{\delta}}(1 - \widetilde{c}_{13}^2\widetilde{s}_{12}^2) + \dot{\widetilde{\beta}}(\widetilde{c}_{23}^2\widetilde{s}_{13}^2\widetilde{s}_{12}^2 + \widetilde{c}_{12}^2\widetilde{s}_{23}^2 + 2\widetilde{c}_{23}\widetilde{s}_{23}\widetilde{s}_{13}\widetilde{c}_{12}\widetilde{s}_{12}\cos\widetilde{\varepsilon}), \\
&\quad +2\dot{\widetilde{\theta}}_{23}\widetilde{s}_{13}\widetilde{c}_{12}\widetilde{s}_{12}\sin\widetilde{\varepsilon} + \dot{\widetilde{\varepsilon}}\widetilde{c}_{12}^2
\end{aligned}
$$

$$(4.114)$$

$$
Q_3 = \dot{\widetilde{\delta}}\widetilde{c}_{13}^2 + \dot{\widetilde{\beta}}\widetilde{c}_{23}^2\widetilde{c}_{13}^2,
$$

$$(4.115)$$

and we remind that the non-adiabaticity parameters are calculated using eq. (4.17) which is

$$
\Gamma_{ij} = \frac{2\pi}{\delta\widetilde{k}_{ij}(\delta\widetilde{k}_{ij} + \delta Q_{ij})}\left(\widetilde{U}^\dagger \dot{H} \widetilde{U}\right)_{ij}.
$$

$$(4.116)$$

We see that for the calculation of the full Hamiltonian in the matter basis $\widetilde{H}$, one needs to determine the values of the mixing angles and of the matter phases because they appear in the mixing matrix $\widetilde{U}$. To calculate numerically the values of the matter mixing angles and of the two phases $\widetilde{\beta}$ and $\widetilde{\delta}$, we use the following formulas taken from [103]

$$
\tan^2\widetilde{\theta}_{12} = -\frac{\delta\widetilde{k}_{13}\left[(H_{\mu\mu} - \widetilde{k}_2)(H_{\tau\tau} - \widetilde{k}_2) - |H_{\mu\tau}|^2\right]}{\delta\widetilde{k}_{23}\left[(H_{\mu\mu} - \widetilde{k}_1)(H_{\tau\tau} - \widetilde{k}_1) - |H_{\mu\tau}|^2\right]},
$$

$$(4.117)$$

$$
\sin^2\widetilde{\theta}_{13} = \frac{(H_{\mu\mu} - \widetilde{k}_3)(H_{\tau\tau} - \widetilde{k}_3) - |H_{\mu\tau}|^2}{\delta\widetilde{k}_{13}\,\delta\widetilde{k}_{23}},
$$

$$(4.118)$$

$$
\tan^2\widetilde{\theta}_{23} = \left|\frac{H_{\mu\tau}H_{\tau e} - H_{\mu e}(H_{\tau\tau} - \widetilde{k}_3)}{H_{\tau\mu}H_{\mu e} - H_{\tau e}(H_{\mu\mu} - \widetilde{k}_3)}\right|^2,
$$

$$(4.119)$$

$$
\tan\widetilde{\beta} = \frac{H_{\tau e}H_{e\mu} - H_{\mu e}H_{e\tau} - (H_{\tau\mu} - H_{\mu\tau})(H_{ee} - \widetilde{k}_3)}{H_{\tau e}H_{e\mu} + H_{\mu e}H_{e\tau} - (H_{\tau\mu} + H_{\mu\tau})(H_{ee} - \widetilde{k}_3)},
$$

$$(4.120)$$

$$\tan \widetilde{\delta} \quad = \quad \frac{H_{\mu\tau}H_{\tau e} - H_{e\tau}H_{\tau\mu} - (H_{\mu e} - H_{e\mu})(H_{\tau\tau} - \widetilde{k}_3)}{H_{\mu\tau}H_{\tau e} + H_{e\tau}H_{\tau\mu} - (H_{\mu e} + H_{e\mu})(H_{\tau\tau} - \widetilde{k}_3)}. \tag{4.121}$$

The problem is that a formula linking the matter phase $\widetilde{\varepsilon}$ to the eigenvalues $\widetilde{k}_i$ and the entries of the flavor Hamiltonian H does not exist, so we construct a function depending on $\widetilde{\varepsilon}$ to find its value. We use the following function

$$f(\widetilde{\varepsilon}) \quad = \quad \sum_{i,j=1}^{3} \left| H_{ij} - \left(\widetilde{U}(\widetilde{\varepsilon}) \widetilde{K} \widetilde{U}^\dagger(\widetilde{\varepsilon}) \right)_{ij} \right|^2, \tag{4.122}$$

which is normally equal to zero because the matrix $\widetilde{K}$ is the diagonalization of the Hamiltonian H and we have the relation $H = \widetilde{U}\widetilde{K}\widetilde{U}^\dagger$. As a result, by finding numerically the minimum [4] of the function $f(\widetilde{\varepsilon})$, we obtain the value of matter phase $\widetilde{\varepsilon}$.

Now if we look at eqs. (4.113) and (4.114), we see that we also need to know the value of the first derivative of the matter angles and phases. For the matter mixing angles and the matter phases $\widetilde{\beta}$ and $\widetilde{\delta}$, we perform the derivatives of eqs. (4.117), (4.118), (4.119), (4.120) and (4.121) with respect to the distance x. Again for the matter phase $\widetilde{\varepsilon}$, it is a bit more complex. We have to construct another function depending on $\dot{\widetilde{\varepsilon}}$ to find its value. So we construct the following function

$$f(\dot{\widetilde{\varepsilon}}) \quad = \quad \sum_{i \neq j; i,j=1}^{3} \left| \left(\widetilde{U}^\dagger \dot{\widetilde{U}}(\dot{\widetilde{\varepsilon}}) \right)_{ij} + \frac{1}{\delta \widetilde{k}_{ij}} \left(\widetilde{U}^\dagger \dot{H} \widetilde{U} \right)_{ij} \right|^2, \tag{4.123}$$

which is normally equal to zero because of the relation of eq. (4.9)

$$\left(\widetilde{U}^\dagger \dot{\widetilde{U}} \right)_{ij} = -\frac{1}{\delta \widetilde{k}_{ij}} \left(\widetilde{U}^\dagger \dot{H} \widetilde{U} \right)_{ij} \quad \text{for } i \neq j. \tag{4.124}$$

Then we find numerically the minimum of the function $f(\dot{\widetilde{\varepsilon}})$ and we obtain the value of the derivative of the matter phase $\dot{\widetilde{\varepsilon}}$.

With all these calculations, we are able now to construct the Hamiltonian in the matter basis $\widetilde{H}$ (eq. (4.112)) and its corresponding magnetic field in the matter basis $\widetilde{\mathbf{B}}$ which is given by

$$\widetilde{\mathbf{B}} = \sum_{i=1}^{8} \widetilde{B}_i \, \mathbf{e}_i = \begin{pmatrix} 2\,\Re\left(\widetilde{H}_{12}\right) \\ -2\,\Im\left(\widetilde{H}_{12}\right) \\ \widetilde{H}_{11} - \widetilde{H}_{22} \\ 2\,\Re\left(\widetilde{H}_{13}\right) \\ -2\,\Im\left(\widetilde{H}_{13}\right) \\ 2\,\Re\left(\widetilde{H}_{23}\right) \\ -2\,\Im\left(\widetilde{H}_{23}\right) \\ \frac{1}{\sqrt{3}}(\widetilde{H}_{11} + \widetilde{H}_{22} - 2\widetilde{H}_{33}) \end{pmatrix}. \tag{4.125}$$

As we mentioned, in the matter basis, the mixing only occurs between two eigenstates. As a consequence, we separate the magnetic field $\widetilde{\mathbf{B}}$ into three magnetic

---

4. We use the Nelder-Mead method of the simplex algorithm.

fields $\widetilde{B}_{ij}$, with $i, j = 1, 2, 3$ and $i \neq j$, which represent the connections existing between eigenstates i and j. The new three magnetic fields are

$$\widetilde{B}_{12} = \begin{pmatrix} \widetilde{B}_1 \\ \widetilde{B}_2 \\ \widetilde{B}_3 \end{pmatrix}, \quad \widetilde{B}_{13} = \begin{pmatrix} \widetilde{B}_4 \\ \widetilde{B}_5 \\ \frac{1}{2} \left(\sqrt{3}\widetilde{B}_8 + \widetilde{B}_3 \right) \end{pmatrix},$$

$$\widetilde{B}_{23} = \begin{pmatrix} \widetilde{B}_6 \\ \widetilde{B}_7 \\ \frac{1}{2} \left(\sqrt{3}\widetilde{B}_8 - \widetilde{B}_3 \right) \end{pmatrix}. \tag{4.126}$$

Then we perform the same procedure as for the two flavors and calculate the average of the magnetic fields over a distance of 10 km. The results are three average magnetic fields $\langle \widetilde{B}_{ij} \rangle$ which are given by

$$\langle \widetilde{B}_{12} \rangle = \begin{pmatrix} \langle \widetilde{B}_1 \rangle \\ \langle \widetilde{B}_2 \rangle \\ \langle \widetilde{B}_3 \rangle \end{pmatrix}, \quad \langle \widetilde{B}_{13} \rangle = \begin{pmatrix} \langle \widetilde{B}_4 \rangle \\ \langle \widetilde{B}_5 \rangle \\ \langle \frac{1}{2} \left(\sqrt{3}\widetilde{B}_8 + \widetilde{B}_3 \right) \rangle \end{pmatrix},$$

$$\langle \widetilde{B}_{23} \rangle = \begin{pmatrix} \langle \widetilde{B}_6 \rangle \\ \langle \widetilde{B}_7 \rangle \\ \langle \frac{1}{2} \left(\sqrt{3}\widetilde{B}_8 - \widetilde{B}_3 \right) \rangle \end{pmatrix}. \tag{4.127}$$

Now, we will check if the magnetic resonance criteria applied to one of these three magnetic fields lead to a coincidence with the spectral split phenomenon. For neutrinos, we know that the mixing is between the eigenstates 2 and 3 so we apply the magnetic resonance criteria to the magnetic field $\langle \widetilde{B}_{23} \rangle$ which are given by (see eqs. (4.108) and (4.109))

$$\left| \langle \frac{1}{2} \left(\sqrt{3}\widetilde{B}_8 - \widetilde{B}_3 \right) \rangle \right| = 0 \quad \text{and} \quad \frac{\left| \langle \frac{1}{2} \left(\sqrt{3}\widetilde{B}_8 - \widetilde{B}_3 \right) \rangle \right|}{\sqrt{\langle \widetilde{B}_6 \rangle^2 + \langle \widetilde{B}_7 \rangle^2}} \ll 1, \tag{4.128}$$

where the first criterion represents the fact that the "Z component" of the magnetic field $\langle \widetilde{B}_{23} \rangle$ is zero and the second criterion ensure that we are "on-resonance".

For antineutrinos, the mixing occurs between the eigenstates 1 and 3 so the magnetic resonance criteria are

$$\left| \langle \frac{1}{2} \left(\sqrt{3}\widetilde{B}_8 + \widetilde{B}_3 \right) \rangle \right| = 0 \quad \text{and} \quad \frac{\left| \langle \frac{1}{2} \left(\sqrt{3}\widetilde{B}_8 + \widetilde{B}_3 \right) \rangle \right|}{\sqrt{\langle \widetilde{B}_4 \rangle^2 + \langle \widetilde{B}_5 \rangle^2}} \ll 1. \tag{4.129}$$

On figures 4.19 a and b, we show the contour plots of the electron survival probabilities with the resonance line (solid black line) calculated with eqs. (4.128) and (4.129) for neutrinos and antineutrinos respectively. The solid line representing the fulfillment of the first criterion (eqs. (4.128) and (4.129)) is just plotted when the second criterion is also fulfilled to ensure that we are "on resonance". These contour plots tell us that in the three flavors case the spectral split phenomenon is, in terms of polarization vectors, a magnetic resonance phenomenon between two

eigenstates: the fulfillment of the magnetic resonance criteria gives rise to the spectral split at the same location and for the same neutrino energies. Indeed, on the energy axis of figures 4.19 a and b, we see that the lowest energy that is reached by the resonance line (solid black) corresponds exactly to the split energy. However a shift in the location of the resonance is apparent that needs further investigation before a decisive statement can be made. In conclusion, our calculation gives an indication for the first time that the spectral split phenomenon, within the three flavors case, can be as well understood as a magnetic resonance phenomenon occurring between two eigenstates.
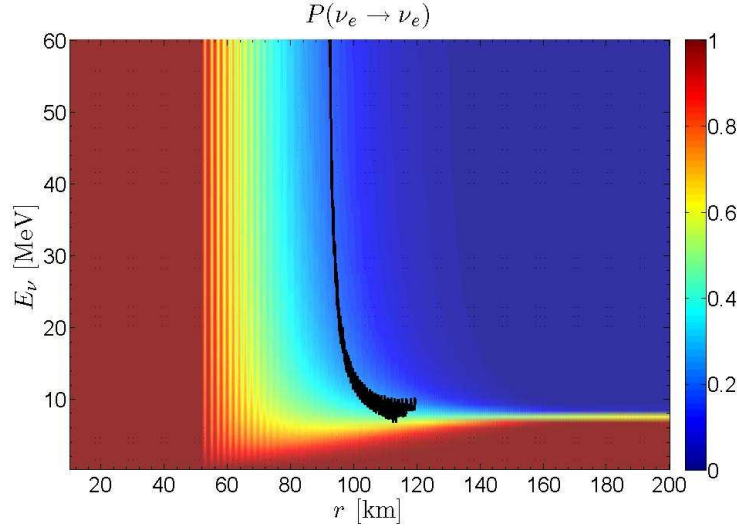
(a) Electron neutrino survival probability and the magnetic resonance line.
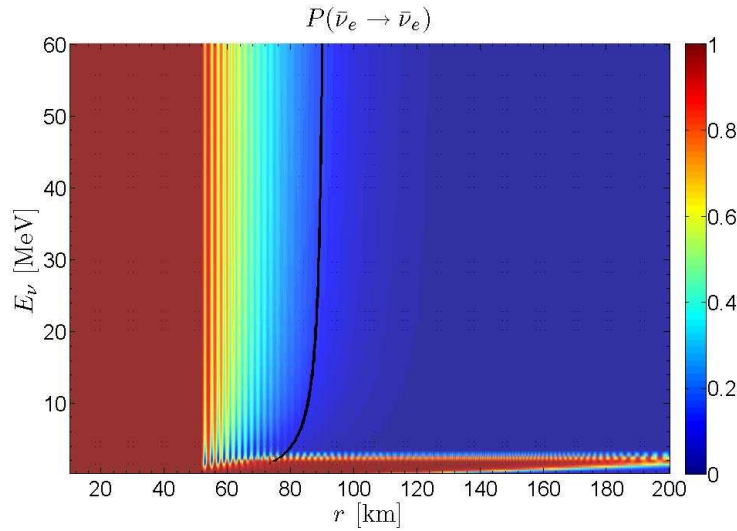
(b) Electron antineutrino survival probability and the magnetic resonance line.

Figure 4.19 – *Contour plots of the electron survival probabilities as a function of distance and energy within a three flavors treatment. The black curve shows the fulfillment of the magnetic resonance condition (eqs. (4.128) and (4.129)). The magnetic resonance line and the spectral split coincide in location in the supernova and occur for the same neutrino energies.*

CONCLUSION

In the present chapter, we have demonstrated that the use of the matter basis (which includes the neutrino self-interaction Hamiltonian) gives a new insight on the neutrino self-interaction effects. By applying the formal expressions of section 4.1 to the two flavors case, we have identified two conditions for the end of the synchronization regime. The first condition is a non-zero value of the vacuum mixing angle, confirming what was already mentioned in [15]. We emphasize that we recovered this first condition in an exact treatment i.e. with the matter induced Hamiltonian and within the single-angle approximation. In addition, we found a second condition which is related to the sign of the eq. (4.87) where the average energies play an important role. We have shown on figures 4.3 that the neutrino self-interaction effects can appear in normal or in inverted hierarchies if we change the sign of eq. (4.87).

Then we have underlined for the first time the important role played by the Dirac matter phase $\widetilde{\beta}$. Indeed the $\widetilde{\beta}$ phase is present in the mixing matrix $\widetilde{U}$ because of the complex contributions coming from the neutrino self-interaction Hamiltonian. In our calculations, we have shown that the $\widetilde{\beta}$ phase is the key point for the end of the synchronization regime and for the onset of the bipolar oscillations. We have identified a condition for the start of the bipolar oscillations (see eq. (4.92)) that leads to a divergence in the matter phase. Note that this condition has already been postulated heuristically in [125] while in our work we have identified the origin of this condition. Furthermore, we have found that non-zero value of the derivative of the matter phase $\dot{\widetilde{\beta}}$ reduces the difference between the X and the Z components of the magnetic field $\widetilde{\mathbf{B}}$ in the matter basis. It is this reduction that triggers the appearance of the mixing between the eigenstates known as the bipolar oscillations.

In section 4.3, we have identified that the spectral split phenomenon is actually a well known phenomenon in physics: the magnetic resonance. In our calculations, we found that the polarization vector $\widetilde{\mathbf{P}}$ evolving in the matter basis only sees the average of the magnetic field $\widetilde{\mathbf{B}}$. By performing the average of $\widetilde{\mathbf{B}}$, we realized that the motion of $\langle\widetilde{\mathbf{B}}\rangle$ takes place in the XOZ plane. So, on one hand we have the flavor basis where the magnetic field $\mathbf{B}$ has a strong z component and spatial varying components in the xOy plane with the rotation frequency $\dot{\widetilde{\beta}}$. We can identify the flavor basis with the laboratory frame of the magnetic resonance phenomenon. On the other hand, we have the matter basis where the average magnetic field $\langle\widetilde{\mathbf{B}}\rangle$ moves in the XOZ plane with components that become of the same order in the neutrino evolution. This is the comoving frame of the magnetic resonance phenomenon. From these observations, we conjectured that the spectral split is in terms of the polarization vector formalism a magnetic resonance phenomenon. To prove that our conjecture is right, we defined the two conditions (eqs. (4.108) and (4.109)) that have to be fulfilled to allow a magnetic resonance. We searched for the fulfillment of these conditions in the evolution of the magnetic field $\langle\widetilde{\mathbf{B}}\rangle$ and our numerical calculations (see figures 4.13 and 4.14) have confirmed that our conjecture is right. So we conclude that the spectral split phenomenon can be understood as a magnetic resonance phenomenon.

In the last section of this chapter, we have extended our results on the mag-

netic resonance correspondence to the three flavors case. Our preliminary numerical results have shown that the spectral split phenomenon is in that case as well a magnetic resonance phenomenon. Indeed, in the matter basis, the mixing induced by the neutrino self-interaction only occurs between two eigenstates. So we developed the magnetic field $\widetilde{\mathbf{B}}$ in 8 dimensions into three magnetic fields in 3 dimensions which represent the mixing between the eigenstates. By applying the magnetic resonance criteria of eqs. (4.108) and (4.109) to the three magnetic fields $\langle \widetilde{B}_{12} \rangle$, $\langle \widetilde{B}_{13} \rangle$ and $\langle \widetilde{B}_{23} \rangle$, our numerical calculations have shown (see figure 4.19) that the spectral split coincides with the fulfillment of the magnetic resonance criteria.

Conclusion

$\mathcal{I}$ N this PhD thesis, we have studied the shock wave and the neutrino self-interaction effects on the neutrino flavor conversion that occur in the environment of core-collapse supernova.

In the first work, we have performed the first dynamic calculations of the DSNB fluxes and event rates detected on Earth. In our theoretical model, we have included the last recent developments in neutrino astrophysics namely the neutrino self-interaction and the effects coming from the presence of the shock. Our calculations have shown that the presence of the shock waves induces significant effects if the third mixing angle θ_{13} is larger than the threshold $\sin^2 2\theta_{13} = 10^{-5}$. This is due to the fact that the shock waves imply multiple H-resonances which are only present if θ_{13} is sufficiently large. Our main results are:

1. the effects of the shock wave reduce the sensitivity to the third mixing angle θ_{13},

2. we found the surprising result that there is a loss of sensitivity to the collective effects introduced by the neutrino self-interaction for the electron antineutrinos in inverted hierarchy and for a large θ_{13}.

The first result is due to the presence of the shock which induces a modification of the density profile. Indeed, a forward and a reverse shock appear in the density profile that change the adiabaticity of the evolution. Consequently, the difference between the fluxes with a small θ_{13} and with a large θ_{13} is reduced.

Using a simplified model that we built, we have found that the loss of sensitivity to collective effects is due to the change of adiabaticity induced by the shock and to the fact that the neutrino self-interaction just swaps the electron and the muon antineutrino fluxes for all energies. So performing the integral in the calculation of the DSNB fluxes with or without neutrino self-interaction gives the same results, both cases are indistinguishable. With our simple model, we have also demonstrated the robustness of our results about the loss of sensitivity to collective effects and to θ_{13} by varying the cooling time τ and the details of the density profiles.

Our results have also proved that the use of analytical formulas without the shock effects can significantly overestimate (or underestimate) the fluxes and event rates which will be possibly detected in the future terrestrial experiments.

As we have seen at the end of the chapter 2, the neutrino self-interaction has a significant impact on the neutrino propagation. In the next two works, we decided to tackle the understanding of the neutrino self-interaction effects. To reach this aim, we studied the neutrino self-interaction effects from the point of another basis than the flavor basis: the matter basis. We also emphasize that we have performed our calculations in an exact treatment i.e. without the usual approximations of the schematic model proposed in [15] and which is often used. By applying our formal expressions of the matter basis to the two flavors case, we have identified two conditions for the end of the synchronization regime. The first condition is a

non-zero value of the vacuum mixing angle and the second condition is related to the sign of a relation where the average energies play a role.

Then we have shown for the first time the important role played by the matter phase $\widetilde{\beta}$ present in the mixing matrix $\widetilde{U}$. In our calculations, we have identified that the $\widetilde{\beta}$ phase is the key point for the end of the synchronization regime and consequently for the onset of the bipolar oscillations where a condition has been found. This condition involves a divergence in the matter phase. Moreover, we have demonstrated that the non-zero value of the derivative of the matter phase $\dot{\widetilde{\beta}}$ reduces the difference between the X and the Z components of the magnetic field $\widetilde{\mathbf{B}}$ in the matter basis which allows the presence of the bipolar oscillations i.e. the mixing between the eigenstates.

To complete the picture of the neutrino evolution in a supernova, we have found that the spectral split phenomenon is actually a well known phenomenon in physics: the magnetic resonance. Our calculations have shown that in the flavor basis we have a magnetic field $\mathbf{B}$ with a strong z component and spatial varying components in the xOy plane at the rotation frequency $\dot{\widetilde{\beta}}$ whereas in the matter basis we have an average magnetic field $\langle \widetilde{\mathbf{B}} \rangle$ moving in the XOZ plane with components that become to the same order with the neutrino evolution. So we identified the flavor basis with the laboratory frame and the matter basis with the comoving frame of the magnetic resonance phenomenon. From these observations, we conjectured that the spectral split is, in terms of the polarization vector formalism, a magnetic resonance phenomenon. Our full numerical calculations have shown that our conjecture is right. Indeed the fulfillment of the magnetic resonance conditions coincide exactly with the location (in distance and energy) of the spectral split phenomenon. The preliminary results of the extension to the $SU(3)$ group confirmed that the correspondence between the spectral split phenomenon and the magnetic resonance phenomenon is still valid.

The main topics of this PhD thesis are the effects on the neutrino flavor conversion coming from the shock and the neutrino self-interaction. Both have been treated in the perspective of calculations performed accurately. For the correspondence between the spectral split phenomenon and the magnetic resonance phenomenon, the formal expressions have been also given for the case of the multi-angle self-interaction Hamiltonian. Our expectation is that future numerical calculations will prove that this correspondence is still valid for the multi-angle treatment. Also recently it has been shown that the spectral split phenomenon can actually contain more than one split if one breaks down the assumption of equipartition of the total luminosity. We think that our theoretical model is enough general to also explain the presence of the other splits. Our preliminary results on the treatment of three flavors shows that we actually are on the right way.

A MASSIVE NEUTRINOS AND MIXING MATRICES

A.1 THE DIRAC MASS TERM

A Dirac neutrino mass can be generated with same Higgs mechanism that gives masses to quarks and charged leptons in the Standard Model [33]. The only extension we need is to consider that neutrinos also have right-handed components $\nu_{\alpha R}$. The right-handed neutrino fields are fundamentally different from the other fermion fields because they are singlets of $SU(3)_C \times SU(2)_L$ and have an hypercharge $Y = 0$. So these right-handed neutrinos are only sensitive to gravitational interaction.

The Higgs-lepton Yukawa lagrangian for leptons can be written as

$$\mathcal{L}^D_{\text{mass}} = -\frac{v}{\sqrt{2}}(\overline{l'_L}Y'^l l'_R + \overline{\nu'_L}Y'^\nu \nu'_R) + \text{h.c.,} \tag{A.1}$$

where Y'^l is a matrix containing the Yukawa couplings for charged leptons, Y'^ν contains the Yukawa couplings for Dirac neutrinos, v is the Higgs vacuum expectation value, ν'_L and ν'_R are the left and right-handed neutrino arrays

$$\nu'_{L,R} = \begin{pmatrix} \nu'_{eL,R} \\ \nu'_{\mu L,R} \\ \nu'_{\tau L,R} \end{pmatrix}. \tag{A.2}$$

The matrices Y'^l of charged leptons Yukawa couplings and Y'^ν of neutrino Yukawa couplings can be diagonalized in the following way

$$V_L^{l\dagger}Y'^l V_R^l = Y^l \quad \text{with} \quad Y^l_{\alpha\beta} = y^l_\alpha \delta_{\alpha\beta} \quad (\alpha, \beta = e, \mu, \tau), \tag{A.3}$$

$$V_L^{\nu\dagger}Y'^\nu V_R^\nu = Y^\nu \quad \text{with} \quad Y^\nu_{kj} = y^\nu_k \delta_{kj} \quad (k, j = 1, 2, 3), \tag{A.4}$$

with real and positive y^l_k and y^ν_k. $V_L^{\nu,l}$ and $V_R^{\nu,l}$ are four appropriates 3×3 matrices that satisfy $V_L^{\nu,l\dagger} = (V_L^{\nu,l})^{-1}$ and $V_R^{\nu,l\dagger} = (V_R^{\nu,l})^{-1}$. Now we define the chiral massive charged leptons arrays and the chiral massive neutrino arrays to be

$$l_{L,R} = \begin{pmatrix} l_{eL,R} \\ l_{\mu L,R} \\ l_{\tau L,R} \end{pmatrix} = V_{L,R}^{l\dagger} l'_{L,R} = V_{L,R}^{l\dagger} \begin{pmatrix} l'_{eL,R} \\ l'_{\mu L,R} \\ l'_{\tau L,R} \end{pmatrix}, \tag{A.5}$$

$$n_{L,R} = \begin{pmatrix} \nu_{1L,R} \\ \nu_{2L,R} \\ \nu_{3L,R} \end{pmatrix} = V_{L,R}^{\nu\dagger} \nu'_{L,R} = V_{L,R}^{\nu\dagger} \begin{pmatrix} \nu'_{eL,R} \\ \nu'_{\mu L,R} \\ \nu'_{\tau L,R} \end{pmatrix}. \tag{A.6}$$

149

Using the Dirac neutrino fields

$$\nu_k = \nu_{kL} + \nu_{kR},$$ (A.7)

and defining the charged lepton and neutrino masses as

$$m_\alpha = \frac{y_\alpha^l v}{\sqrt{2}} \quad \text{and} \quad m_k = \frac{y_k^\nu v}{\sqrt{2}},$$ (A.8)

we obtain the Dirac mass term

$$\mathcal{L}_{\text{mass}}^D = -\sum_{\alpha=e,\mu,\tau} m_\alpha \, \bar{l}_\alpha l_\alpha - \sum_{k=1}^3 m_k \, \bar{\nu}_k \nu_k.$$ (A.9)

The leptonic weak charged-current can be written as

$$j_{W,L}^\rho = 2\overline{\nu_L'}\gamma^\rho l_L = 2\overline{n_L}V_L^{\nu\dagger}V_L^l \gamma^\rho l_L,$$ (A.10)

where we recover the mixing matrix in the leptonic sector $U = V_L^{l\dagger}V_L^\nu$. It is customary to define the left-handed flavor neutrino fields as

$$\nu_L = \begin{pmatrix} \nu_{eL} \\ \nu_{\mu L} \\ \nu_{\tau L} \end{pmatrix} = U n_L = U \begin{pmatrix} \nu_{1L} \\ \nu_{2L} \\ \nu_{3L} \end{pmatrix}.$$ (A.11)

A.2   THE MAJORANA MASS TERM

From the left-handed flavor neutrino fields array in eq. (A.2), we can construct the Majorana mass term [33]

$$\mathcal{L}_{\text{mass}}^M = \frac{1}{2}\nu_L'^T \mathcal{C}^\dagger M^L \nu_L' + \text{h.c.},$$ (A.12)

where $\mathcal{C}$ is the charge conjugation which transforms the neutrino fields as $\nu'^C = \mathcal{C}\overline{\nu'}^T$ and $\overline{\nu'^C} = \nu'^T\mathcal{C}^\dagger$. As in the case of Dirac neutrinos, the fields of massive neutrinos are obtained by diagonalizing the Majorana mass term. We find

$$(V_L^\nu)^T M^L V_L^\nu = M \quad \text{with} \quad M_{kj} = m_k \delta_{kj} \quad (k,j = 1,2,3),$$ (A.13)

with an unitarity matrix V_L^ν and with real and positive m_k. We can then express the left-handed flavor fields as in

$$\nu_L' = V_L^\nu n_L = V_L^\nu \begin{pmatrix} \nu_{1L} \\ \nu_{2L} \\ \nu_{3L} \end{pmatrix}.$$ (A.14)

So the Majorana mass term in the diagonal form is

$$\mathcal{L}_{\text{mass}}^M = \frac{1}{2}\sum_{k=1}^3 m_k \nu_{kL}^T \mathcal{C}^\dagger \nu_{kL} + \text{h.c.} = -\frac{1}{2}\sum_{k=1}^3 m_k \overline{\nu_{kL}^C} \nu_{kL} + \text{h.c.}.$$ (A.15)

The Majorana mass term is not invariant under the global $U(1)$ gauge transformations $\nu_{kL} \to e^{i\alpha}\nu_{kL}$ with the same phase α for all massive neutrinos. This fact implies that with the presence of Majorana mass term we have to consider one phase α_k for each mass eigenstates k.

A.3 THE MIXING MATRIX U

In general, an unitary $N \times N$ matrix depends on N^2 independent real parameters. These parameters can be divided into

$$\frac{N(N-1)}{2} \quad \text{mixing angles,} \tag{A.16}$$

and

$$\frac{N(N+1)}{2} \quad \text{phases.} \tag{A.17}$$

In the most general case, one has to consider all the phases but they are not all physical observables because the only physical effect of the lepton mixing matrix occurs through its presence in the weak charged current

$$j^\rho_{W,L} = 2\overline{n_L} U^\dagger \gamma^\rho l_L. \tag{A.18}$$

If we only consider Dirac neutrinos, the lagrangian is invariant under the global phase transformations

$$n_k \to e^{i\psi^\nu_k} n_k \quad \text{and} \quad l_\alpha \to e^{i\psi^l_\alpha} l_\alpha. \tag{A.19}$$

Performing this transformation, the lepton current becomes

$$j^\rho_{W,L} = 2 \sum_{k=1}^N \sum_{\alpha=e,\dots N} \overline{n_{k,L}} e^{-i\psi^\nu_k} U^\dagger_{k\alpha} \gamma^\rho e^{i\psi^l_\alpha} l_{\alpha L}. \tag{A.20}$$

In this expression, we can factorize with an arbitrary phase, so this leaves $2N - 1$ phases that can be chosen to eliminate the $\dfrac{N(N+1)}{2}$ phases of the lepton mixing matrix. Thus the lepton mixing matrix contains

$$\frac{N(N+1)}{2} - (2N-1) = \frac{(N-1)(N-2)}{2} \quad \text{Dirac physical phases.} \tag{A.21}$$

In the case of Majorana neutrinos, because the Majorana mass term is not invariant under the global $U(1)$ gauge transformation, we only transform the N charged lepton fields and so it remains

$$\frac{N(N+1)}{2} - N = \frac{N(N-1)}{2} \quad \text{physical phases.} \tag{A.22}$$

Out of these physical phases, we still have $(N-1)(N-2)/2$ Dirac phases and the rest, $(N-1)$, are Majorana ones.

A.3.1 Two generations mixing

In the most general case (without redefinition of the fields) when we study the transformation between one basis to another (flavor to matter or the opposite), we will write the 2×2 unitary matrix as

$$U = \begin{pmatrix} 1 & 0 \\ 0 & e^{i\beta} \end{pmatrix} \begin{pmatrix} \cos\theta & \sin\theta \\ -\sin\theta & \cos\theta \end{pmatrix} \begin{pmatrix} e^{-i\alpha_1} & 0 \\ 0 & e^{-i\alpha_2} \end{pmatrix} = \begin{pmatrix} \cos\theta e^{-i\alpha_1} & \sin\theta e^{-i\alpha_2} \\ -\sin\theta e^{i(\beta-\alpha_1)} & \cos\theta e^{i(\beta-\alpha_2)} \end{pmatrix}. \tag{A.23}$$

The above expression contains 1 angle, 1 Dirac phase and 2 Majorana phases [1].

If we study the neutrino oscillations in vacuum, we can redefine the fields and in that case the mixing matrix is reduced to 1 angle and 1 Majorana phase. But because the Majorana phases do not lead to physical effects in neutrino oscillations, we can omit them. Then the matrix U is

$$U = \begin{pmatrix} \cos\theta & \sin\theta \\ -\sin\theta & \cos\theta \end{pmatrix}. \tag{A.24}$$

A.3.2 Three generations mixing

In the most general case, we will write the 3×3 unitary matrix as

$$U = \begin{pmatrix} c_{12}c_{13}e^{-\imath\alpha_1} & s_{12}c_{13}e^{-\imath\alpha_2} & s_{13}e^{-\imath\alpha_3} \\ (-s_{12}c_{23}\,e^{\imath\epsilon} - c_{12}s_{13}s_{23})e^{\imath(\delta-\alpha_1)} & (c_{12}c_{23}\,e^{\imath\epsilon} - s_{12}s_{13}s_{23})e^{\imath(\delta-\alpha_2)} & c_{13}s_{23}e^{\imath(\delta-\alpha_3)} \\ (s_{12}s_{23}\,e^{\imath\epsilon} - c_{12}s_{13}c_{23})e^{\imath(\delta+\beta-\alpha_1)} & (-c_{12}s_{23}\,e^{\imath\epsilon} - s_{12}s_{13}c_{23})e^{\imath(\delta+\beta-\alpha_2)} & c_{13}c_{23}e^{\imath(\delta+\beta-\alpha_3)} \end{pmatrix}, \tag{A.25}$$

where $c_{ij} = \cos\theta_{ij}$ and $s_{ij} = \sin\theta_{ij}$. In this definition of the mixing matrix, we have 3 angles, 3 Dirac phases and 3 Majorana phases [2]. This mixing matrix can be written as a product of six matrices

$$U = B\,T_{23}\,E\,T_{13}\,T_{12}\,A, \tag{A.26}$$

with

$$T_{12} = \begin{pmatrix} c_{12} & s_{12} & 0 \\ -s_{12} & c_{12} & 0 \\ 0 & 0 & 1 \end{pmatrix}, \quad T_{13} = \begin{pmatrix} c_{13} & 0 & s_{13} \\ 0 & 1 & 0 \\ -s_{13} & 0 & c_{13} \end{pmatrix}, \quad T_{23} = \begin{pmatrix} 1 & 0 & 0 \\ 0 & c_{23} & s_{23} \\ 0 & -s_{23} & c_{23} \end{pmatrix},$$

$$B = \begin{pmatrix} 1 & 0 & 0 \\ 0 & e^{\imath\delta} & 0 \\ 0 & 0 & e^{\imath(\beta+\delta)} \end{pmatrix}, \quad E = \begin{pmatrix} 1 & 0 & 0 \\ 0 & e^{\imath\epsilon} & 0 \\ 0 & 0 & 1 \end{pmatrix}, \quad A = \begin{pmatrix} e^{-\imath\alpha_1} & 0 & 0 \\ 0 & e^{-\imath\alpha_2} & 0 \\ 0 & 0 & e^{-\imath\alpha_3} \end{pmatrix}. \tag{A.27}$$

As for the two flavor case, If we study the neutrino oscillations in vacuum, we can redefine the fields and in that case the mixing matrix is reduced to 3 angles, 1 Dirac phase and 2 Majorana phases. But again because the Majorana phases do not lead to physical effects in neutrino oscillations, we can omit them. Then we recover the form of the U matrix as it is written is the Particle Data Group [126]

$$U = \begin{pmatrix} c_{12}\,c_{13} & s_{12}\,c_{13} & s_{13}\,e^{-\imath\delta} \\ -s_{12}\,c_{23} - c_{12}\,s_{23}\,s_{13}\,e^{\imath\delta} & c_{12}\,c_{23} - s_{12}\,s_{23}\,s_{13}\,e^{\imath\delta} & s_{23}\,c_{13} \\ s_{12}\,s_{23} - c_{12}\,c_{23}\,s_{13}\,e^{\imath\delta} & -c_{12}\,s_{23} - s_{12}\,c_{23}\,s_{13}\,e^{\imath\delta} & c_{23}\,c_{13} \end{pmatrix}, \tag{A.28}$$

where δ is the CP violating Dirac phase.

---

1. Actually we just need one Majorana phase but we decide to write the mixing matrix U knowing that the two Majorana phases are not independent.

2. As for the two flavors case, we just need two Majorana phases but we decide to write the mixing matrix U with three Majorana phases knowing that one Majorana phase depend on the others.

B Equivalent formalisms for neutrino propagation

B.1 Polarization vector formalism

Because the Hamiltonian in the Schrödinger-like equation that we want to solve is hermitian, it is always possible to express it in terms of a Bloch vector **B** [127, 99]. The generators of $SU(N)$ are a set of operators λ_i which satisfy

$$\lambda_i = \lambda_i^\dagger, \quad \mathrm{Tr}\left[\lambda_i\right] = 0, \quad \mathrm{Tr}\left[\lambda_i\lambda_j\right] = 2\delta_{ij}. \tag{B.1}$$

They are characterized by structure constants f_{ijk} (antisymmetric tensor) and g_{ijk} (symmetric tensor) of Lie algebra $\mathfrak{su}(N)$

$$\left[\lambda_i, \lambda_j\right] = \sum_{k=1}^{N^2-1} 2\imath f_{ijk}\lambda_k, \tag{B.2}$$

$$\left[\lambda_i, \lambda_j\right]_+ = \frac{4}{N}\delta_{ij}\mathbb{1}_N + \sum_{k=1}^{N^2-1} 2g_{ijk}\lambda_k. \tag{B.3}$$

If we choose the generators λ_i $(i = 1,\ldots,N^2-1)$ of $SU(N)$ for observables of interest, we have

$$H = \frac{1}{N}B_0\mathbb{1}_N + \frac{1}{2}\sum_{i=1}^{N^2-1} B_i\lambda_i, \tag{B.4}$$

where B_i $(i = 1,\ldots,N^2-1)$ are the expectation values. By using the inverse map of eq. (B.4), we also have

$$B_i = \mathrm{Tr}\left[H\lambda_i\right]. \tag{B.5}$$

So the the Bloch vector **B**, called the "magnetic field", is defined as

$$\mathbf{B} = \begin{pmatrix} B_1 \\ \vdots \\ B_{N^2-1} \end{pmatrix} \in \mathbb{R}^{N^2-1}. \tag{B.6}$$

We can also define a Bloch vector **P**, called the "polarization vector", corresponding to the density matrix $\rho = \psi \otimes \psi^\dagger$

$$\rho = \frac{1}{N}P_0\mathbb{1}_N + \frac{1}{2}\sum_{i=1}^{N^2-1} P_i\lambda_i, \tag{B.7}$$

and the inverse map

$$P_i = \mathrm{Tr}\left[\rho\lambda_i\right]. \tag{B.8}$$

153

We define $\mathbf{e}_i$ $(i = 1, \ldots, N^2 - 1)$ of $SU(N)$ as the unit vectors of the polarization vector $\mathbf{P}$ and we rewrite the Schrödinger-like equation in terms of the magnetic field and the polarization vector, then one obtains

$$i\frac{\partial \psi}{\partial t} = H\,\psi \quad \Longrightarrow \quad \frac{\partial \mathbf{P}}{\partial t} = \mathbf{B} \times \mathbf{P} = \sum_{i,j=1}^{N^2-1} f_{ijk} B_i P_j\, \mathbf{e}_k. \tag{B.9}$$

Then the Schrödinger-like equation corresponds to a generalized gyroscopic equation.

B.1.1 Two flavors

In a two flavor study, the generators of $SU(2)$ used are the Pauli matrices

$$\sigma_1 = \begin{pmatrix} 0 & 1 \\ 1 & 0 \end{pmatrix}, \quad \sigma_2 = \begin{pmatrix} 0 & -i \\ i & 0 \end{pmatrix}, \quad \sigma_3 = \begin{pmatrix} 1 & 0 \\ 0 & -1 \end{pmatrix}. \tag{B.10}$$

Using eqs. (B.4) and (B.7), we obtain the magnetic field and the polarization vector

$$\mathbf{B} = \begin{pmatrix} 2\,\Re\,(H_{12}) \\ -2\,\Im\,(H_{12}) \\ H_{11} - H_{22} \end{pmatrix} \quad \text{and} \quad \mathbf{P} = \begin{pmatrix} 2\,\Re\,(\psi_1\psi_2^*) \\ -2\,\Im\,(\psi_1\psi_2^*) \\ |\psi_1|^2 - |\psi_2|^2 \end{pmatrix}. \tag{B.11}$$

In the case of $SU(2)$, the structure constant is just $f_{123} = \epsilon_{123} = 1$ and we recover the standard cross product "$\times$" of the gyroscopic equation

$$\frac{\partial \mathbf{P}}{\partial t} = \mathbf{B} \times \mathbf{P}. \tag{B.12}$$

B.1.2 Three flavors

In a three flavor study, the generators of $SU(3)$ used are the Gell-Mann matrices

$$\lambda_1 = \begin{pmatrix} 0 & 1 & 0 \\ 1 & 0 & 0 \\ 0 & 0 & 0 \end{pmatrix}, \quad \lambda_2 = \begin{pmatrix} 0 & -i & 0 \\ i & 0 & 0 \\ 0 & 0 & 0 \end{pmatrix}, \quad \lambda_3 = \begin{pmatrix} 1 & 0 & 0 \\ 0 & -1 & 0 \\ 0 & 0 & 0 \end{pmatrix},$$

$$\lambda_4 = \begin{pmatrix} 0 & 0 & 1 \\ 0 & 0 & 0 \\ 1 & 0 & 0 \end{pmatrix}, \quad \lambda_5 = \begin{pmatrix} 0 & 0 & -i \\ 0 & 0 & 0 \\ i & 0 & 0 \end{pmatrix}, \quad \lambda_6 = \begin{pmatrix} 0 & 0 & 0 \\ 0 & 0 & 1 \\ 0 & 1 & 0 \end{pmatrix},$$

$$\lambda_7 = \begin{pmatrix} 0 & 0 & 0 \\ 0 & 0 & -i \\ 0 & i & 0 \end{pmatrix}, \quad \lambda_8 = \frac{1}{\sqrt{3}}\begin{pmatrix} 1 & 0 & 0 \\ 0 & 1 & 0 \\ 0 & 0 & -2 \end{pmatrix}. \tag{B.13}$$

Using eqs. (B.4) and (B.7), we obtain the magnetic field and the polarization vector

$$\mathbf{B} = \begin{pmatrix} 2\,\Re\,(H_{12}) \\ -2\,\Im\,(H_{12}) \\ H_{11} - H_{22} \\ 2\,\Re\,(H_{13}) \\ -2\,\Im\,(H_{13}) \\ 2\,\Re\,(H_{23}) \\ -2\,\Im\,(H_{23}) \\ \frac{1}{\sqrt{3}}(H_{11} + H_{22} - 2H_{33}) \end{pmatrix} \quad \text{and} \quad \mathbf{P} = \begin{pmatrix} 2\,\Re\,(\psi_1\psi_2^*) \\ -2\,\Im\,(\psi_1\psi_2^*) \\ |\psi_1|^2 - |\psi_2|^2 \\ 2\,\Re\,(\psi_1\psi_3^*) \\ -2\,\Im\,(\psi_1\psi_3^*) \\ 2\,\Re\,(\psi_2\psi_3^*) \\ -2\,\Im\,(\psi_2\psi_3^*) \\ \frac{1}{\sqrt{3}}(|\psi_1|^2 + |\psi_2|^2 - 2|\psi_3|^2) \end{pmatrix}. \tag{B.14}$$

In the case of $SU(3)$, the structure constants are

$$f_{123} = 1,$$

$$f_{458} = f_{678} = \frac{\sqrt{3}}{2},$$

$$f_{147} = f_{246} = f_{257} = f_{345} = -f_{156} = -f_{367} = \frac{1}{2},$$

$$g_{118} = g_{228} = g_{338} = -g_{888} = \frac{\sqrt{3}}{3},$$

$$g_{448} = g_{558} = g_{668} = g_{778} = -\frac{\sqrt{3}}{6},$$

$$g_{146} = g_{157} = g_{256} = g_{344} = g_{355} = -g_{247} = -g_{366} = -g_{377} = \frac{1}{2}. \quad \text{(B.15)}$$

B.2 DENSITY MATRIX FORMALISM AND THE LIOUVILLE-VON NEUMANN EQUATION

Just as the Schrödinger equation describes how wavefunctions evolve in time, the Liouville-Von Neumann equation describes how a density matrix evolves with time. A density matrix $\hat{\rho}$ is a Hermitian matrix, that describes the statistical state of a quantum system. Solving the Liouville-Von Neumann equation is another way to determine the neutrino propagation in supernovae environment.

In quantum mechanics, a system is described thanks to a state $|\psi(t)\rangle$ which can be expanded on a basis of a finite dimensional Hilbert space $\mathcal{B} = \{u_n\}$ with $n \in \mathbb{N}$. We have

$$|\psi(t)\rangle = \sum_n c_n(t)|u_n\rangle \quad \text{with} \quad \sum_n |u_n|^2 = 1. \quad \text{(B.16)}$$

The coefficients $c_n(t)$ are the probability amplitudes. It is well known that the evolution of the state is given by the Schrödinger-like equation

$$\imath \frac{d}{dt}|\psi(t)\rangle = \hat{H}|\psi(t)\rangle, \quad \text{(B.17)}$$

where $\hat{H}$ is the Hamiltonian of the system. The density matrices are represented by density operators which are the tensorial product of pure states

$$\hat{\rho}(t) = |\psi(t)\rangle\langle\psi(t)| = \sum_{n,l} c_l^* c_n |u_n\rangle\langle u_l|. \quad \text{(B.18)}$$

The density matrices obtained have the following properties:
 – they are hermitian matrices so $\hat{\rho} = \hat{\rho}^\dagger$. They can be diagonalized and their eigenvalues are real,
 – the total probability is conserved, i.e. $\text{Tr}\,[\hat{\rho}] = 1$,
 – for a pure state, the density operator is a projector $\hat{\rho}^2 = \hat{\rho}$.
The expectation value of an observable A can be calculated using the formula

$$\langle \hat{A} \rangle = \langle \psi | \hat{A} | \psi \rangle = \text{Tr}\,[\hat{\rho}\hat{A}]. \quad \text{(B.19)}$$

The time evolution of the density matrix is given by the Liouville-Von Neumann equation

$$\imath \frac{d\hat{\rho}}{dt} = [\hat{H}, \hat{\rho}]. \quad \text{(B.20)}$$

In neutrino physics, when considering three flavors, we define the state as

$$|\psi\rangle = \begin{pmatrix} \nu_e \\ \nu_\mu \\ \nu_\tau \end{pmatrix}. \tag{B.21}$$

Then the corresponding density matrix ρ is

$$\rho = \begin{pmatrix} |\nu_e|^2 & \nu_e \nu_\mu^* & \nu_e \nu_\tau^* \\ \nu_e^* \nu_\mu & |\nu_\mu|^2 & \nu_\mu \nu_\tau^* \\ \nu_e^* \nu_\tau & \nu_\mu^* \nu_\tau & |\nu_\tau|^2 \end{pmatrix}. \tag{B.22}$$

In conclusion, the neutrino evolution can be determined in an equivalent way with the wavefunctions and the Schrödinger-like equation or the density matrices and the Liouville-Von Neumann equation.

BIBLIOGRAPHY

[1] W. Pauli. Letter to "radioactive ladies and gentlemen" at the Tübingen conference. 1930. (Cited page 1.)

[2] C.L. Cowan F. Reines. *Phys. Rev.*, 92:830, 1953. (Cited page 1.)

[3] F.B. Harrison C.L. Cowan, F. Reines, H.W. Kruse, and A.D. McGuire. *Science*, 124:123, 1956. (Cited page 1.)

[4] B. Pontecorvo. *Sov. Phys. JETP*, 33:549, 1957. (Cited pages 1 et 6.)

[5] B. Pontecorvo. *Sov. Phys. JETP*, 34:247, 1958. (Cited page 1.)

[6] Ziro Maki, Masami Nakagawa, and Shoichi Sakata. Remarks on the unified model of elementary particles. *Prog. Theor. Phys.*, 28:870–880, 1962. (Cited pages 1 et 6.)

[7] M. Nakagawa, H. Okonogi, S. Sakata, and A. Toyoda. Possible existence of a neutrino with mass and partial conservation of muon charge. *Prog. Theor. Phys.*, 30:727–729, 1963. (Cited page 1.)

[8] B. Pontecorvo. *Chalk River Lab. PD–205 report*. (Cited page 1.)

[9] R. Davis. Solar neutrinos. II: Experimental. *Phys.Rev.Lett.*, 12:303–305, 1964. (Cited pages 1 et 29.)

[10] Jr. Davis, Raymond, Don S. Harmer, and Kenneth C. Hoffman. Search for neutrinos from the sun. *Phys.Rev.Lett.*, 20:1205–1209, 1968. (Cited pages 1 et 29.)

[11] J.N. Bahcall, William A. Fowler, Jr. Iben, I., and R.L. Sears. Solar neutrino flux. *Astrophys.J.*, 137:344–346, 1963. (Cited page 1.)

[12] Y. Fukuda et al. Evidence for oscillation of atmospheric neutrinos. *Phys. Rev. Lett.*, 81:1562–1567, 1998, hep-ex/9807003. (Cited pages 1, 6 et 32.)

[13] Sergio Pastor and Georg Raffelt. Flavor oscillations in the supernova hot bubble region: Nonlinear effects of neutrino background. *Phys. Rev. Lett.*, 89:191101, 2002, astro-ph/0207281. (Cited pages 2 et 44.)

[14] George M. Fuller and Yong-Zhong Qian. Simultaneous Flavor Transformation of Neutrinos and Antineutrinos with Dominant Potentials from Neutrino- Neutrino Forward Scattering. *Phys. Rev.*, D73:023004, 2006, astro-ph/0505240. (Cited pages 2 et 44.)

[15] Steen Hannestad, Georg G. Raffelt, Gunter Sigl, and Yvonne Y. Y. Wong. Self-induced conversion in dense neutrino gases: Pendulum in flavour space. *Phys. Rev.*, D74:105010, 2006, astro-ph/0608695. (Cited pages 2, 44, 79, 81, 82, 112, 119, 120, 144 et 147.)

[16] G. G. Raffelt and G. Sigl. Self-induced decoherence in dense neutrino gases. *Phys. Rev.*, D75:083002, 2007, hep-ph/0701182. (Cited pages 2 et 44.)

[17] Gianluigi L. Fogli, Eligio Lisi, Antonio Marrone, and Alessandro Mirizzi. Collective neutrino flavor transitions in supernovae and the role of trajectory averaging. *JCAP*, 0712:010, 2007, 0707.1998. (Cited pages 2, 44, 55 et 79.)

[18] Huaiyu Duan, George M. Fuller, and Yong-Zhong Qian. Collective Neutrino Flavor Transformation In Supernovae. *Phys. Rev.*, D74:123004, 2006, astro-ph/0511275. (Cited pages 2, 44, 55 et 129.)

[19] Huaiyu Duan, George M. Fuller, J Carlson, and Yong-Zhong Qian. Simulation of coherent non-linear neutrino flavor transformation in the supernova environment. I: Correlated neutrino trajectories. *Phys. Rev.*, D74:105014, 2006, astro-ph/0606616. (Cited pages 2, 44, 55, 75 et 78.)

[20] James P. Kneller, Gail C. McLaughlin, and Justin Brockman. Oscillation Effects and Time Variation of the Supernova Neutrino Signal. *Phys. Rev.*, D77:045023, 2008, 0705.3835. (Cited pages 2, 44, 69, 70, 85, 90, 91, 93, 95 et 98.)

[21] Basudeb Dasgupta and Amol Dighe. Phase effects in neutrino conversions during a supernova shock wave. *Phys. Rev.*, D75:093002, 2007, hep-ph/0510219. (Cited pages 2, 44, 69, 71 et 73.)

[22] Shunsaku Horiuchi, John F. Beacom, and Eli Dwek. The Diffuse Supernova Neutrino Background is detectable in Super-Kamiokande. *Phys.Rev.*, D79:083013, 2009, 0812.3157. (Cited pages 2 et 87.)

[23] D. Autiero, J. Aysto, A. Badertscher, Leonid B. Bezrukov, J. Bouchez, et al. Large underground, liquid based detectors for astro-particle physics in Europe: Scientific case and prospects. *JCAP*, 0711:011, 2007, 0705.0116. (Cited pages 2, 44, 61, 62 et 94.)

[24] Sebastien Galais, James Kneller, Cristina Volpe, and Jerome Gava. Shockwaves in Supernovae: New Implications on the Diffuse Supernova Neutrino Background. *Phys. Rev.*, D81:053002, 2010, 0906.5294. (Cited pages 3, 44, 55, 69, 85, 90 et 101.)

[25] S. Galais, J. Kneller, and C. Volpe. The neutrino-neutrino interaction effects in supernovae: the point of view from the matter basis. 2011, 1102.1471. (Cited pages 3, 44, 55, 82, 105, 106 et 115.)

[26] Sebastien Galais and Cristina Volpe. The neutrino spectral split in core-collapse supernovae: a magnetic resonance phenomenon. 2011, 1103.5302. (Cited pages 3, 44, 55, 82, 106, 111, 115 et 124.)

[27] B. Pontecorvo. Neutrino Experiments and the Problem of Conservation of Leptonic Charge. *Sov.Phys.JETP*, 26:984–988, 1968. (Cited page 6.)

[28] L. Wolfenstein. Neutrino oscillations in matter. *Phys. Rev.*, D17:2369–2374, 1978. (Cited pages 6 et 22.)

[29] S.P. Mikheev and A.Yu. Smirnov. Resonance Amplification of Oscillations in Matter and Spectroscopy of Solar Neutrinos. *Sov.J.Nucl.Phys.*, 42:913–917, 1985. (Cited pages 6, 22 et 24.)

[30] S. P. Mikheev and A. Yu. Smirnov. Resonant amplification of neutrino oscillations in matter and solar neutrino spectroscopy. *Nuovo Cim.*, C9:17–26, 1986. (Cited pages 6 et 22.)

[31] Thomas Schwetz, Mariam Tortola, and J.W.F. Valle. Global neutrino data and recent reactor fluxes: status of three-flavour oscillation parameters. *New*

J.Phys., 13:063004, 2011, 1103.0734. * Temporary entry *. (Cited pages 7, 34, 35, 40, 41 et 42.)

[32] Claude Amsler et al. Review of Particle Physics. *Phys.Lett.*, B667:1–1340, 2008. (Cited page 13.)

[33] C. Giunti and C. W. Kim. *Fundamentals of Neutrino Physics and Astrophysics.* 2007. (Cited pages 16, 149 et 150.)

[34] Rabindra N. Mohapatra and Palash B. Pal. *Massive neutrinos in physics and astrophysics.* 2004. (Cited page 16.)

[35] L. Landau. *Phys. Z. Sowjetunion*, 2:46, 1932. (Cited page 24.)

[36] C. Zener. *Proc. R. Soc. London*, Ser. A 137:696, 1932. (Cited page 24.)

[37] Tzee-Ke Kuo and James T. Pantaleone. Neutrino Oscillations in Matter. *Rev.Mod.Phys.*, 61:937, 1989. (Cited pages 26 et 27.)

[38] S.P. Mikheev and A.Yu. Smirnov. Resonance Oscillations of Neutrinos in Matter. *Sov.Phys.Usp.*, 30:759–790, 1987. (Cited page 27.)

[39] John N. Bahcall, Aldo M. Serenelli, and Sarbani Basu. New solar opacities, abundances, helioseismology, and neutrino fluxes. *Astrophys.J.*, 621:L85–L88, 2005, astro-ph/0412440. (Cited pages 29 et 38.)

[40] J.N. Abdurashitov et al. Measurement of the solar neutrino capture rate with gallium metal. *Phys.Rev.*, C60:055801, 1999, astro-ph/9907113. (Cited page 29.)

[41] W. Hampel et al. GALLEX solar neutrino observations: Results for GALLEX IV. *Phys.Lett.*, B447:127–133, 1999. (Cited page 29.)

[42] Y. Fukuda et al. Solar neutrino data covering solar cycle 22. *Phys.Rev.Lett.*, 77:1683–1686, 1996. (Cited page 29.)

[43] J. Hosaka et al. Solar neutrino measurements in Super-Kamiokande-I. *Phys. Rev.*, D73:112001, 2006, hep-ex/0508053. (Cited page 29.)

[44] B. Aharmim et al. Measurement of the nu/e and total B-8 solar neutrino fluxes with the Sudbury Neutrino Observatory phase I data set. *Phys. Rev.*, C75:045502, 2007, nucl-ex/0610020. (Cited page 30.)

[45] John N. Bahcall. Solar models and solar neutrinos: Current status. *Phys. Scripta*, T121:46–50, 2005, hep-ph/0412068. (Cited pages 30 et 39.)

[46] John N. Bahcall, P.I. Krastev, and A.Yu. Smirnov. Where do we stand with solar neutrino oscillations? *Phys.Rev.*, D58:096016, 1998, hep-ph/9807216. (Cited page 30.)

[47] T. Araki et al. Measurement of neutrino oscillation with KamLAND: Evidence of spectral distortion. *Phys. Rev. Lett.*, 94:081801, 2005, hep-ex/0406035. (Cited page 31.)

[48] Alessandro Strumia and Francesco Vissani. Neutrino masses and mixings and... 2006, hep-ph/0606054. (Cited pages 39 et 40.)

[49] T. K. Gaisser and M. Honda. Flux of atmospheric neutrinos. *Ann. Rev. Nucl. Part. Sci.*, 52:153–199, 2002, hep-ph/0203272. (Cited page 32.)

[50] M. Apollonio et al. Search for neutrino oscillations on a long baseline at the CHOOZ nuclear power station. *Eur.Phys.J.*, C27:331–374, 2003, hep-ex/0301017. (Cited page 34.)

[51] Xinheng Guo et al. A precision measurement of the neutrino mixing angle theta(13) using reactor antineutrinos at Daya Bay. 2007, hep-ex/0701029. (Cited page 34.)

[52] F. Ardellier et al. Double Chooz: A search for the neutrino mixing angle theta(13). 2006, hep-ex/0606025. (Cited page 34.)

[53] J. K. Ahn et al. RENO: An Experiment for Neutrino Oscillation Parameter theta_13 Using Reactor Neutrinos at Yonggwang. 2010, 1003.1391. (Cited page 34.)

[54] D. S. Ayres et al. NOvA proposal to build a 30-kiloton off-axis detector to study neutrino oscillations in the Fermilab NuMI beamline. 2004, hep-ex/0503053. (Cited page 34.)

[55] Y. Itow et al. The JHF-Kamioka neutrino project. 2001, hep-ex/0106019. (Cited page 34.)

[56] K. Abe et al. Indication of Electron Neutrino Appearance from an Accelerator-produced Off-axis Muon Neutrino Beam. 2011, 1106.2822. (Cited page 34.)

[57] A. B. Balantekin and D. Yilmaz. Contrasting solar and reactor neutrinos with a non-zero value of theta_13. *J. Phys.*, G35:075007, 2008, 0804.3345. (Cited page 34.)

[58] G. L. Fogli, E. Lisi, A. Marrone, A. Palazzo, and A. M. Rotunno. Hints of theta_13>0 from global neutrino data analysis. *Phys. Rev. Lett.*, 101:141801, 2008, 0806.2649. (Cited page 34.)

[59] A. B. Balantekin and H. Yuksel. Neutrino mixing and nucleosynthesis in core-collapse supernovae. *New J. Phys.*, 7:51, 2005, astro-ph/0411159. (Cited pages 44 et 59.)

[60] Yong-Zhong Qian. The origin of the heavy elements: recent progress in the understanding of the r-process. *Prog.Part.Nucl.Phys.*, 50:153–199, 2003, astro-ph/0301422. (Cited pages 44 et 55.)

[61] Margaret E. Burbidge, G.R. Burbidge, William A. Fowler, and F. Hoyle. Synthesis of the elements in stars. *Rev.Mod.Phys.*, 29:547–650, 1957. (Cited pages 44 et 55.)

[62] S.E. Woosley, J.R. Wilson, G.J. Mathews, R.D. Hoffman, and B.S. Meyer. The r process and neutrino heated supernova ejecta. *Astrophys.J.*, 433:229–246, 1994. (Cited pages 44 et 55.)

[63] K. Takahashi, J. Witti, and H.-T. Janka. Nucleosynthesis in neutrino-driven winds from protoneutron stars. 2. The R-process. *Astron.Astrophys.*, 286:857, 1994. (Cited pages 44 et 55.)

[64] Shinya Wanajo, Toshitaka Kajino, Grant J. Mathews, and Kaori Otsuki. The r-process in neutrino-driven winds from nascent, compact neutron stars of core-collapse supernovae. 2001, astro-ph/0102261. (Cited pages 44 et 55.)

[65] Alessandro Strumia and Francesco Vissani. Precise quasielastic neutrino/nucleon cross-section. *Phys.Lett.*, B564:42–54, 2003, astro-ph/0302055. (Cited pages 44, 55 et 57.)

[66] A. de Bellefon, J. Bouchez, J. Busto, Jean-Eric Campagne, C. Cavata, et al. MEMPHYS: A Large scale water Cerenkov detector at Frejus. 2006, hep-ex/0607026. (Cited pages 44, 59 et 93.)

[67] Michael Wurm et al. The next-generation liquid-scintillator neutrino observatory LENA. 2011, 1104.5620. (Cited pages 44, 59, 62, 93 et 94.)

[68] A. Rubbia. Experiments for CP violation: A Giant liquid argon scintillation, Cerenkov and charge imaging experiment? pages 321–350, 2004, hep-ph/0402110. (Cited pages 44, 59 et 93.)

[69] James T. Pantaleone. Neutrino oscillations at high densities. *Phys. Lett.*, B287:128–132, 1992. (Cited page 44.)

[70] Stuart Samuel. Neutrino oscillations in dense neutrino gases. *Phys. Rev.*, D48:1462–1477, 1993. (Cited pages 44 et 74.)

[71] G. Sigl and G. Raffelt. General kinetic description of relativistic mixed neutrinos. *Nucl.Phys.*, B406:423–451, 1993. (Cited page 44.)

[72] R. F. Sawyer. Speed-up of neutrino transformations in a supernova environment. *Phys. Rev.*, D72:045003, 2005, hep-ph/0503013. (Cited page 44.)

[73] Andreu Esteban-Pretel, Sergio Pastor, Ricard Tomas, Georg G. Raffelt, and Gunter Sigl. Decoherence in supernova neutrino transformations suppressed by deleptonization. *Nucl. Phys. Proc. Suppl.*, 188:121–123, 2009. (Cited page 44.)

[74] S. Pastor, A. Esteban-Pretel, G. G. Raffelt, G. Sigl, and R. Tomas. Mu-tau neutrino refraction and collective three-flavour transformations in supernovae. *J. Phys. Conf. Ser.*, 136:042076, 2008. (Cited page 44.)

[75] Basudeb Dasgupta, Amol Dighe, Alessandro Mirizzi, and Georg G. Raffelt. Spectral split in prompt supernova neutrino burst: Analytic three-flavor treatment. *Phys. Rev.*, D77:113007, 2008, 0801.1660. (Cited page 44.)

[76] V.Alan Kostelecky and Stuart Samuel. Selfmaintained coherent oscillations in dense neutrino gases. *Phys.Rev.*, D52:621–627, 1995, hep-ph/9506262. (Cited page 44.)

[77] Sergio Pastor, Georg G. Raffelt, and Dmitry V. Semikoz. Physics of synchronized neutrino oscillations caused by selfinteractions. *Phys.Rev.*, D65:053011, 2002, hep-ph/0109035. (Cited pages 44, 79 et 80.)

[78] Huaiyu Duan, George M. Fuller, J. Carlson, and Yong-Zhong Qian. Analysis of Collective Neutrino Flavor Transformation in Supernovae. *Phys. Rev.*, D75:125005, 2007, astro-ph/0703776. (Cited page 44.)

[79] A. B. Balantekin and Y. Pehlivan. Neutrino neutrino interactions and flavor mixing in dense matter. *J. Phys.*, G34:47–66, 2007, astro-ph/0607527. (Cited page 44.)

[80] Georg G. Raffelt and Alexei Yu. Smirnov. Adiabaticity and spectral splits in collective neutrino transformations. *Phys. Rev.*, D76:125008, 2007, 0709.4641. (Cited pages 44 et 139.)

[81] Huaiyu Duan, George M. Fuller, and Yong-Zhong Qian. A Simple Picture for Neutrino Flavor Transformation in Supernovae. *Phys. Rev.*, D76:085013, 2007, 0706.4293. (Cited pages 44, 129 et 139.)

[82] Huaiyu Duan and James P Kneller. Neutrino flavour transformation in supernovae. *J. Phys.*, G36:113201, 2009, 0904.0974. (Cited pages 44 et 55.)

[83] Basudeb Dasgupta and Amol Dighe. Collective three-flavor oscillations of supernova neutrinos. *J. Phys. Conf. Ser.*, 136:042072, 2008. (Cited pages 44 et 55.)

[84] Basudeb Dasgupta, Alessandro Mirizzi, Irene Tamborra, and Ricard Tomas. Neutrino mass hierarchy and three-flavor spectral splits of supernova neutrinos. *Phys. Rev.*, D81:093008, 2010, 1002.2943. (Cited page 44.)

[85] Basudeb Dasgupta, Amol Dighe, Georg G. Raffelt, and Alexei Yu. Smirnov. Multiple Spectral Splits of Supernova Neutrinos. *Phys. Rev. Lett.*, 103:051105, 2009, 0904.3542. (Cited pages 44, 55 et 82.)

[86] J. Gava and C. Volpe. CP violation effects on the neutrino degeneracy parameters in the Early Universe. *Nucl. Phys.*, B837:50–60, 2010, 1002.0981. (Cited page 44.)

[87] J. Gava and C. C. Jean-Louis. One-loop correction effects on supernova neutrino fluxes: a new possible probe for Beyond Standard Models. *JCAP*, 1005:029, 2010, 0912.5206. (Cited page 44.)

[88] J. Gava and C. C. Jean-Louis. SUSY radiative corrections on mu-tau neutrino refraction including possible R-parity breaking interactions. *Phys. Rev.*, D81:013003, 2010, 0907.3947. (Cited page 44.)

[89] J. Gava and C. Volpe. Core-collapse supernova neutrinos and neutrino properties. *AIP Conf. Proc.*, 1038:193–201, 2008, 0805.2717. (Cited pages 44, 54, 55 et 90.)

[90] Jerome Gava, James Kneller, Cristina Volpe, and G. C. McLaughlin. A dynamical collective calculation of supernova neutrino signals. *Phys. Rev. Lett.*, 103:071101, 2009, 0902.0317. (Cited pages 44, 69, 85, 89 et 93.)

[91] Jerome Gava and Cristina Volpe. Collective neutrinos oscillation in matter and CP- violation. *Phys. Rev.*, D78:083007, 2008, 0807.3418. (Cited pages 44, 54, 55 et 90.)

[92] R. Minkowski. *Publ. Astron. Soc. Pac.*, 53:224, 1941. (Cited page 47.)

[93] Stan Woosley and Thomas Janka. The Physics of Core-Collapse Supernovae. 2006, astro-ph/0601261. (Cited page 48.)

[94] H.T. Janka. Neutrinos from type II supernovae and the neutrino driven supernova mechanism. *Italian Phys.Soc.Proc.*, 40:345–374, 1993. (Cited page 50.)

[95] Mathias Thorsten Keil. Supernova neutrino spectra and applications to flavor oscillations. 2003, astro-ph/0308228. (Cited page 51.)

[96] T. Totani, K. Sato, H.E. Dalhed, and J.R. Wilson. Future detection of supernova neutrino burst and explosion mechanism. *Astrophys.J.*, 496:216–225, 1998, astro-ph/9710203. (Cited page 53.)

[97] R. Tomas et al. Neutrino signatures of supernova shock and reverse shock propagation. *JCAP*, 0409:015, 2004, astro-ph/0407132. (Cited page 54.)

[98] Akif Baha Balantekin, J. Gava, and C. Volpe. Possible CP-Violation effects in core-collapse Supernovae. *Phys. Lett.*, B662:396–404, 2008, 0710.3112. (Cited pages 54, 55 et 90.)

[99] Basudeb Dasgupta and Amol Dighe. Collective three-flavor oscillations of supernova neutrinos. *Phys. Rev.*, D77:113002, 2008, 0712.3798. (Cited pages 55 et 153.)

[100] Gianluigi Fogli, Eligio Lisi, Antonio Marrone, and Alessandro Mirizzi. Neutrinos self interactions in Supernovae. 2008, 0805.2530. (Cited page 55.)

[101] A.B. Balantekin and G.M. Fuller. Supernova neutrino - nucleus astrophysics. *J.Phys.G*, G29:2513–2522, 2003, astro-ph/0309519. (Cited page 55.)

[102] Hiroyuki Sekiya. Solar neutrino results from Super-Kamiokande. *PoS*, ICHEP2010:330, 2010. (Cited page 60.)

[103] James P. Kneller and Gail C. McLaughlin. Three Flavor Neutrino Oscillations in Matter: Flavor Diagonal Potentials, the Adiabatic Basis and the CP phase. *Phys. Rev.*, D80:053002, 2009, 0904.3823. (Cited pages 63 et 140.)

[104] Amol S. Dighe and Alexei Yu. Smirnov. Identifying the neutrino mass spectrum from the neutrino burst from a supernova. *Phys.Rev.*, D62:033007, 2000, hep-ph/9907423. (Cited pages 66, 67 et 68.)

[105] C. Lunardini and A.Yu. Smirnov. The Minimum width condition for neutrino conversion in matter. *Nucl.Phys.*, B583:260–290, 2000, hep-ph/0002152. (Cited page 68.)

[106] Phillip Colella and Paul R. Woodward. The Piecewise Parabolic Method (PPM) for Gas Dynamical Simulations. *J.Comput.Phys.*, 54:174–201, 1984. (Cited page 69.)

[107] S. Nussinov. Solar Neutrinos and Neutrino Mixing. *Phys.Lett.*, B63:201–203, 1976. (Cited page 73.)

[108] Hajime Anada and Haruhiko Nishimura. Coherence Condition for Resonant Neutrino Oscillation. *Phys.Rev.*, D41:60, 1989. (Cited page 73.)

[109] James T. Pantaleone. Dirac neutrinos in dense matter. *Phys. Rev.*, D46:510–523, 1992. (Cited page 74.)

[110] Georg G. Raffelt and Alexei Yu. Smirnov. Self-induced spectral splits in supernova neutrino fluxes. *Phys. Rev.*, D76:081301, 2007, 0705.1830. (Cited pages 79 et 129.)

[111] Y. Pehlivan, A.B. Balantekin, Toshitaka Kajino, and Takashi Yoshida. Invariants of Collective Neutrino Oscillations. 2011, 1105.1182. (Cited pages 81 et 82.)

[112] Meng-Ru Wu and Yong-Zhong Qian. Resonances Driven by a Neutrino Gyroscope and Collective Neutrino Oscillations in Supernovae. 2011, 1105.2068. (Cited pages 81 et 82.)

[113] Georg G. Raffelt. N-mode coherence in collective neutrino oscillations. *Phys.Rev.*, D83:105022, 2011, 1103.2891. (Cited pages 81 et 82.)

[114] M. Malek et al. Search for supernova relic neutrinos at SUPER-KAMIOKANDE. *Phys.Rev.Lett.*, 90:061101, 2003, hep-ex/0209028. (Cited pages 87 et 94.)

[115] Cecilia Lunardini and Orlando L.G. Peres. Upper limits on the diffuse supernova neutrino flux from the SuperKamiokande data. *JCAP*, 0808:033, 2008, 0805.4225. (Cited page 87.)

[116] B. Aharmim et al. A Search for Neutrinos from the Solar hep Reaction and the Diffuse Supernova Neutrino Background with the Sudbury Neutrino Observatory. *Astrophys.J.*, 653:1545–1551, 2006, hep-ex/0607010. (Cited page 87.)

[117] John F. Beacom. The Diffuse Supernova Neutrino Background. *Ann.Rev.Nucl.Part.Sci.*, 60:439–462, 2010, 1004.3311. (Cited page 88.)

[118] Hasan Yuksel, Matthew D. Kistler, John F. Beacom, and Andrew M. Hopkins. Revealing the High-Redshift Star Formation Rate with Gamma-Ray Bursts. *Astrophys. J.*, 683:L5–L8, 2008, 0804.4008. (Cited pages 89 et 90.)

[119] Ivan K. Baldry and Karl Glazebrook. Constraints on a universal IMF from UV to near-IR galaxy luminosity densities. *Astrophys.J.*, 593:258–271, 2003, astro-ph/0304423. (Cited page 89.)

[120] Shin'ichiro Ando and Katsuhiko Sato. Supernova relic neutrinos and observational implications for neutrino oscillation. *Phys.Lett.*, B559:113, 2003, astro-ph/0210502. (Cited pages 94 et 95.)

[121] Richard C. Schirato and George M. Fuller. Connection between supernova shocks, flavor transformation, and the neutrino signal. 2002, astro-ph/0205390. (Cited page 95.)

[122] G. L. Fogli, E. Lisi, D. Montanino, and A. Mirizzi. Analysis of energy- and time-dependence of supernova shock effects on neutrino crossing probabilities. *Phys. Rev.*, D68:033005, 2003, hep-ph/0304056. (Cited page 95.)

[123] Vernon D. Barger, K. Whisnant, S. Pakvasa, and R. J. N. Phillips. Matter effects on three-neutrino oscillations. *Phys. Rev.*, D22:2718, 1980. (Cited page 107.)

[124] Tommy Ohlsson and Hakan Snellman. Three flavor neutrino oscillations in matter. *J. Math. Phys.*, 41:2768–2788, 2000, hep-ph/9910546. (Cited page 107.)

[125] Huaiyu Duan and Alexander Friedland. Self-induced suppression of collective neutrino oscillations in a supernova. *Phys.Rev.Lett.*, 106:091101, 2011, 1006.2359. (Cited pages 123 et 144.)

[126] W. M. Yao et al. Review of particle physics. *J. Phys.*, G33:1–1232, 2006. (Cited page 152.)

[127] G. Kimura. The bloch vector for n-level systems. *Phys. Lett.*, A314:339, 2003, 0301152. (Cited page 153.)

NOTATIONS

$\Re(z)$	Real part of the complex z
$\Im(z)$	Imaginary part of the complex z
H	Hamiltonian in the flavor basis
K	Diagonal matrix containing the eigenvalues of H
ψ_α, ν_α	Flavor states
ψ_i, ν_i	Vacuum mass eigenstates
$\widetilde{H}$	Hamiltonian in the instantaneously diagonalized or 'matter' basis
$\widetilde{K}$	Diagonal matrix containing the eigenvalues of $\widetilde{H}$
$\widetilde{\psi}_i, \widetilde{\nu}_i$	Matter eigenstates
$P(\nu_\alpha \to \nu_\beta)$	Transition probability between the flavors α and β if $\alpha \neq \beta$ or survival probability if $\alpha = \beta$ in the flavor basis
$P(\nu_i \to \nu_j)$	Transition probability between the mass states i and j if $i \neq j$ or survival probability if $i = j$ in the mass basis
$P(\widetilde{\nu}_i \to \widetilde{\nu}_j)$	Transition probability between the matter states i and j if $i \neq j$ or survival probability if $i = j$ in the matter basis
Δm^2_{ij}	Mass squared difference
θ_0, θ_{ij}	Vacuum mixing angles
$\widetilde{\theta}_{ij}$	Matter mixing angles or effective angles
$\widetilde{\beta}, \widetilde{\delta}, \widetilde{\varepsilon}$	Dirac matter phases
$\widetilde{\alpha}_i$	Majorana matter phases
$F_\nu, F_{\bar{\nu}}$	Neutrino and antineutrino fluxes
R_ν	Neutrino-sphere
ρ	Density matrix
Γ_{ij}	Non-adiabaticity parameters
$\mathbf{P}$	Polarization vector in the flavor basis
$\mathbf{B}$	Magnetic field in the flavor basis
$\widetilde{\mathbf{P}}$	Polarization vector in the matter basis
$\widetilde{\mathbf{B}}$	Magnetic field in the matter basis

Titre: Effets de l'onde de choc et de l'auto-interaction des neutrinos sur la conversion de saveur des neutrinos dans l'environnement des supernovae

Résumé: Depuis la découverte du phénomène d'oscillation des neutrinos par l'expérience Super-Kamiokande et de l'effet de résonance MSW comme solution au déficit de neutrinos solaires, l'étude de la propagation des neutrinos et de leur conversion de saveur dans un contexte astrophysique est un domaine très actif. La présente thèse se focalise sur les phénomènes de conversion de saveur des neutrinos de supernova. Dans un premier travail, nous avons réalisé le premier calcul complet incluant l'onde de choc et l'auto-interaction des neutrinos pour estimer le flux du fond diffus de neutrinos de supernovae (DSNB) arrivant sur Terre. Ce flux de neutrinos provient de toutes les supernovae qui ont explosé dans l'Univers visible. En variant la valeur du troisième angle θ_{13} de la matrice de mélange U_{MNSP}, nos résultats numériques ont montré que l'onde de choc a un impact significatif sur le flux du DSNB. Nous avons par la même occasion proposé un modèle simplifié qui prend en compte les effets de l'onde de choc et qui pourrait être utilisé pour des calculs futurs de flux du DSNB. Le deuxième travail de cette thèse s'est concentré sur la première dérivation analytique exacte de l'Hamiltonien de matière en présence de l'auto-interaction des neutrinos. Nous avons souligné, pour le cas à deux saveurs, le rôle important tenu par la phase de Dirac $\widetilde{\beta}$ apparaissant dans la base de matière et nous avons établi une condition sur les éléments de l'Hamiltonien de saveur pour le début des oscillations bipolaires. Dans le troisième travail, utilisant le formalisme des vecteurs polarisations, nous avons identifié une correspondance entre les phénomènes de "spectral split" et de résonance magnétique: les énergies pour lesquelles les critères de résonance magnétique sont remplis subissent une conversion de saveur à l'endroit où le "spectral split" a lieu. Une étude préliminaire du cas à trois saveurs nous indique que la correspondance entre le "spectral split" et la résonance magnétique est toujours présente.

Mots-clés: neutrinos de supernova, oscillation, résonance, conversion de saveur, phénomènes collectifs, auto-interaction, supernovae à effondrement gravitationnel, fond diffus de neutrinos de supernova, onde de choc, base de matière, adiabaticité, résonance magnétique

Title: Shock wave and neutrino self-interaction effects upon neutrino flavor conversion in the supernovae environment

Abstract: Since the discovery of the neutrino oscillation phenomenon by the Super-Kamiokande experiment and of the MSW effect as the solution of the solar neutrino deficit, the study of the neutrino propagation and of their flavor conversion in astrophysical environments is a very active field. This PhD thesis focuses upon flavor conversion phenomena of supernova neutrinos. In a first work, we performed the first complete calculation including the shock wave and the neutrino self-interaction to estimate the diffuse supernova neutrino background (DSNB) flux arriving on Earth. This neutrino flux comes from all the supernovae that exploded in the visible Universe. By varying the value of the third angle θ_{13} of the mixing matrix U_{MNSP}, our numerical results have shown that the shock wave has a significant impact on the DSNB flux. At the same time, we have proposed a simplified model that accounts for the shock wave effects to be used in future calculations of the DSNB flux. The second work of this thesis is focused on the first exact analytical derivation of the matter Hamiltonian in the presence of the neutrino self-interaction. We have underlined, in the two flavors case, the important role of the Dirac phase $\widetilde{\beta}$ appearing in the matter basis and established a condition on the elements of the flavor Hamiltonian for the onset of bipolar oscillations. In the third work, using the polarization vector formalism, we have identified a correspondence between the "spectral split" and the magnetic resonance phenomena: the neutrino energies for which the magnetic resonance criteria are fulfilled undergo a flavor change at the location where the "spectral split" occurs. A preliminary study of the three flavors case indicates us that the correspondence between the "spectral split" and the magnetic resonance holds in this case as well.